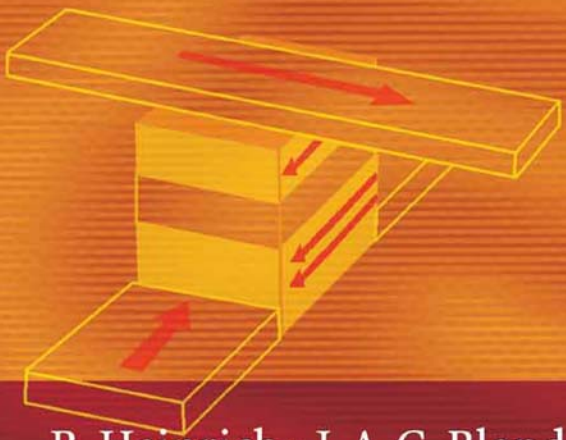

B. Heinrich · J. A. C. Bland
Editors

ULTRATHIN MAGNETIC STRUCTURES IV

Applications of Nanomagnetism

Springer

Ultrathin Magnetic Structures IV

B. Heinrich · J.A.C. Bland (Eds.)

Ultrathin Magnetic Structures IV

Applications of Nanomagnetism

With 198 Figures, Including 117 in Color

Springer

Bretislav Heinrich
Physics Department
Simon Fraser University
Burnaby, BC, V5A 1S6
Canada
e-mail: bheinric@sfu.ca

J. Anthony C. Bland
The Cavendish Laboratory
Department of Physics
University of Cambridge
Madingley Road
CB3 0HE Cambridge
United Kingdom
e-mail: jacb1@phy.cam.ac.uk

Library of Congress Control Number: 2004104844

ISBN 3-540-21954-4 Springer Berlin Heidelberg New York

Production and typesetting: LE-TEX Jelonek, Schmidt & Vöckler GbR, Leipzig
Cover production: Erich Kirchner, Heidelberg

Printed on acid-free paper 57/3141/YL - 5 4 3 2 1 0

Preface

The field of magnetic nanostructures is now an exciting and central area of modern condensed matter science, which has recently led to the development of a major new direction in electronics – so called 'spintronics'. This is a new approach in which the electron spin momentum plays an equal role to the electrical charge, and these radical ideas have galvanised the efforts of previously disparate research communities by offering the promise of surpassing the limits of conventional semiconductors. Clearly the world of magnetism has now entered electronics in a very fundamental manner. This is a very fast growing and exciting field which attracts a steadily increasing number of researchers, bringing a constant stream of new ideas. Both spintronics and magnetic nanostructures are already household names in the broad scientific community and we are now, as a result, at the important stage of beginning to develop entirely new approaches to electronics and information technology. 50 Gigabyte/sq inch storage densities in hard drive disks are now a reality. Magnetic Random Access Memories are being introduced commercially and they will soon change the operation of PC's and laptops. Computer logic architectures based on spintronics are already being widely discussed.

Spintronics spreads beyond the traditional boundaries of physics research, device applications and electronics. Researchers in biology and the medical sciences find this approach equally exciting. In this background it is obvious that a deplorable absence of magnetism teaching within University curricula, which started with the advent of an enormous growth of semiconductor physics, and electronics in the early sixties, is now a complete anachronism. There is a pressing need to have books suitable for lecturers in advanced undergraduate and postgraduate courses. Teaching staff at Universities need such literature to quickly incorporate the field of magnetic nanostructures and spintronics into the University teaching program. Scientists working in spintronics applications come from a very broad science and technology background. They also need access to literature which addresses fundamentals and which helps to achieve a broader understanding of this field.

We addressed the basic topics of magnetic multilayers in Volumes I and II which still underpin many of these developments today. In the early nineties, Giant Magnetoresistance and new materials based on the unique properties of interfaces of

ultrathin films structures were already in place, but applications were only a promise and the 'engineering' of new magnetic materials using nanostructures was still not well known to the wider community. Since that time the field has moved way ahead and undergone a complete transformation. This is indeed a true success story of modern materials science based on nanostructures, which has led to very powerful and far reaching developments in information storage and device technologies. In view of these developments we have been encouraged by our fellow scientists to update the information base started by the earlier volumes and to provide in Vols. III and IV a new perspective on both nanomagnetism and spintronics, aiming at the reader who needs a concise coverage of the underlying phenomena. These volumes have been written keeping in mind that the prime purpose of these books is to educate and help to eliminate gaps in the understanding of the complex phenomena which magnetic nanostructures manifest. This is highly multidisciplinary science where the enormous and rapid growth currently occurring is hard to follow without having access to a treatment which aims to encompass both the present knowledge and direction of the field, so providing insight into its likely future development.

In preparing these volumes we were fortunate to be able to enlist many of the leading experts in this field. Not only have authors come from leading scientific Institutions and made pioneering contributions but they have often played a role as scientific ambassadors of this fast developing science and technology, often encouraging young scientist to bring their talents to this exciting and demanding research endeavour. We hope that this treatment, based at it is on such wide experience, will therefore be particularly attractive to readers already working in, or planning a career in nanoscience.

We would like to express our thanks to all participating authors for their willingness to put aside an appreciable amount of time to write and keep updating their chapters and to cross-correlate their writing with other contributions. We appreciate all the authors' sharing the experience and expertise which has allowed them to contribute so successfully and fundamentally to magnetic nanostructures and spintronics. Finally we hope that the reader will find these two new volumes a pleasure to read and that the material presented will enrich the reader's understanding of this truly fascinating and revolutionary field of science.

Burnaby and Cambridge *B. Heinrich*
September 2004 *J. A.C. Bland*

Contents

Contributors

A. S. Arrott
Department of Physics
Simon Fraser University
Burnaby, BC, V5A 1S6
Canada

J. A. C. Bland
University of Cambridge
Department of Physics
The Cavendish Laboratory
Madingley Road
CB3 0HE Cambridge
UK

M. Carey
Hitachi Global Storage Technologies
San Jose Research Center
650 Harry Road,
San Jose, CA 95120
USA

R. Fontana, Jr.
Hitachi Global Storage Technologies
San Jose Research Center
650 Harry Road
San Jose, CA 95120
USA

E. Grochowski
Hitachi Global Storage Technologies
San Jose Research Center
650 Harry Road
San Jose, CA 95120
USA

B. Gurney
Hitachi Global Storage Technologies
San Jose Research Center
650 Harry Road
San Jose, CA 95120
USA

B. Heinrich
Physics Department
Simon Fraser University
8888 University Drive
Burnaby, BC, V5A 1S6
Canada

B. T. Jonker
Magnetoelectronic Materials & Devices Section
Naval Research Laboratory
4555 Overlook Ave SW
Washington, DC 20375-5000
USA

R. R. Katti
Honeywell International, Inc.
Solid State Electronics Center
12001 State Highway 55
Plymouth, Minnesota 55441
USA

T. Lin
Hitachi Global Storage Technologies
San Jose Research Center
650 Harry Road
San Jose, CA 95120
USA

D. Mauri
Hitachi Global Storage Technologies
San Jose Research Center
650 Harry Road
San Jose, CA 95120
USA

S. Parkin
Hitachi Global Storage Technologies
San Jose Research Center
650 Harry Road
San Jose, CA 95120
USA

M. Pirnabasi
Hitachi Global Storage Technologies
San Jose Research Center
650 Harry Road
San Jose, CA 95120
USA

G. A. Prinz
Code 6300.1
Naval Research Laboratory
Washington, DC 20375
USA

J. Shi
Department of Physics
University of Utah
115 South 1400 East, #201 JFB
Salt Lake City, UT 84112.
USA

T. Taniyama
University of Cambridge
Department of Physics
The Cavendish Laboratory
Madingley Road
CB3 0HE Cambridge
UK

C. Tsang
Hitachi Global Storage Technologies
San Jose Research Center
650 Harry Road
San Jose, CA 95120
USA

M. Williams
Hitachi Global Storage Technologies
San Jose Research Center
650 Harry Road
San Jose, CA 95120
USA

Acronyms

$P_{\mathbf{spin}}$	electron spin polarization
$\tau_{\mathbf{s}}$	electron spin relaxation time
1R0T	one resistor, zero transistor
2DEG	two dimensional electron gas
2R2T	two resistor, two transistor
ABS	air bearing surface
AFM	atomic force microscopy
AF	antiferromagnetic
AGM	alternating gradient magnetometer
AMR	anisotropic magnetoresistance
AP	antiparallel
CB	conduction band
CIP	current in plane
CPP	current perpendicular to the plane
DMS	diluted magnetic semiconductor
DOS	density of states
DRAM	dynamic RAM
DRO	destructive readout
e-beam	electron-beam
EEPROM	electrically erasable programmable read only memory
EL	electroluminescence
FET	field effect transistor
FM	ferromagnet
FRAM	ferroelectric RAM
FeRAM	ferroelectric RAM
GMRAM	giant magneto-resistive random-access memory
GMR	giant magnetoresistance
HDD	hard disk drives
HH	heavy hole
LED	light emitting diode
LEED	low energy electron diffraction

LH	light hole
LLG	Landau-Lifshitz-Gilbert
MBE	molecular beam epitaxy
MCD	magnetic circular dichroism
ML	monolayer
MOKE	magneto-optic Kerr effect
MOKE	surface magneto-optic Kerr effect
MOS	metal-oxide-semiconductor
MRAM	magnetic RAM
MR	magnetoresistance
MTJ	magnetic tunnel junction
NDRO	non-destructive readout
OHE	oblique Hanle effect
PEM	photo-elastic modulator
PSV	pseudo-spin-valve
QW	quantum well
RAM	random access memories
RHEED	reflection high energy electron diffraction
RTD	resonant tunnelling diode
RT	room temperature
SAL	soft-adjacent layer
SC	semiconductor
SFs	stacking faults
SOI	silicon-on-insulator
spin-FET	spin-polarized field effect transistor
spin-LED	spin-polarized light emitting diode
spin-RTD	spin-dependent resonant tunneling diode
SQUID	superconducting quantum interference device
SRAM	static RAM
STM	scanning tunneling microscopy
SV	spin-valve
TAA	track averaged amplitude
TEM	transmission electron microscopy
TMR	tunneling magnetoresistance
UHV	ultrahigh vacuum
VB	valence band
VMRAM	vertical MRAM
XPS/XPD	X-ray photoelectron spectroscopy/diffraction

1

Introduction

J.A.C. Bland and B. Heinrich

Since the publication of volumes I and II in this series 10 years ago, there has been an explosion of interest and activity in the subject of thin film magnetism. Much of this activity has been stimulated by the use of giant magnetoresistance read heads in hard disc drives and by the continuing advances in storage densities achievable in thin film media. Such applications are now almost as familiar as those of the semiconductor transistor, while 10 years ago, the phenomenon of giant magnetoresistance was largely unknown outside the research laboratory.

As early as the 1950s, researchers had already recognised the enormous technological potential of thin magnetic films for use as sensors and information storage devices. Louis Néel identified the importance of the surface in leading to modified switching fields, the role of finite thickness in modifying the domain structure of a thin ferromagnetic film and the role of interface roughness in mediating interlayer dipole coupling. Many researchers recognised the possibilities of using such modified magnetic properties to create technologically useful devices. However it was soon recognised that difficulties in controlling sample quality, often due to the inevitable chemical contamination resulting from the inadequate vacuum available for thin film growth, frustrated attempts to control thin film properties and to perform reliable experiments in the search for modified properties. Despite advances in surface science techniques and the widespread use of MBE in the 1980s it was only in the late 1990s that the early dreams of a new technology have begun to be truly fulfilled.

The very success of the giant magnetoresistance spin valve structure has led to increased efforts to develop magnetic tunnel junction devices based on metal/insulator/metal structures. Spintronic devices based on spin polarised electron injection and detection in all semiconductor or hybrid metal/semiconductor structures are now being very actively developed. Such devices rely for their operation on the manipulation of the electron spin rather the electron charge and momentum as in conventional SC (Semiconductor) devices. Ultimately it is believed that by controlling the spin polarised transport channels it may be possible to engineer complete suppression of one of the spin conduction channels in the presence of an applied magnetic or

electric field, leading to infinite MR (Magneto Resistance) ratios in future spintronic devices Advances in our understanding of spin polarised electron transport in magnetic multilayers have emphasised the role of the microscopic spin polarised electron scattering processes in magnetotransport and have led to the beginnings of a theoretical understanding of the reciprocal effect, current induced magnetic reversal, in which the electron current induces a reversal of the magnetisation in magnetic nanostructures. This phenomenon would allow magnetic switching in nanoscale devices by all electrical means without the need to apply external magnetic fields.

In the earlier two volumes, UMS (Ultrathin Magnetic Structures) I and II, we described many of the fundamental properties of thin magnetic films and techniques used to investigate them. These properties largely underpin the remarkable technological developments of the last decade. However the last decade has seen considerable progress and refinement in our understanding of magnetotransport and interlayer coupling but also the blurring of the boundaries between metals and semiconductors research in the quest for new spin polarised phenomena: it is largely these developments which form the focus of the present volumes. In volume III, the first of the two new volumes, we presented further advances in the fundamental understanding of thin film magnetic properties and of methods for characterising thin film structure which underpin the present spintronics revolution. Here in volume IV we deal with the fundamentals of spintronics: magnetoelectronic materials, spin injection and detection, micromagnetics and the development of magnetic random access memnory based on GMR and tunnel junction devices.

The possibility of realising practical devices based on spin dependent transport has become a reality in a very short period. In the second chapter Prinz reviews the whole field of magnetoelectronics, surveying the developments in thin film materials and the understanding of thin film properties which first led to spin valve devices based on GMR (Giant Magneto Resistance), the subsequent developments which have led to the realisation of MRAM (Magnetic Random Access Memory) , the problem of efficient spin injection into semiconductors and the materials challenges which need to be overcome to realise future devices. The issue of how to efficiently inject polarised electrons into a SC is one of the key challenges of spintronics. Very recently the efficient injection of spin polarised electrons into GaAs was demonstrated at low temperature using an all semiconductor structure. Currently there is great interest in how to achieve the same efficiency using a ferromagnetic metal injector at room temperature. In the second Jonker discusses recent experiments which use optical luminescence techniqes to probe electrical spin injection into semiconductors. In the Chap. 4 Bland, Taniyama, Hirohata and Steinmuller describe optical studies of electron spin transmission at the ferromagnet/semiconductor interface based on photo-excitation measurements. This approach essentially corresponds to the reverse of the polarised luminescence approach and allows polarised electrons to be optically generated in the semiconductor at room temperature. The transmission of the optically pumped polarised electrons into the metal under an applied bias is found to be strongly spin dependent and the authors conclude with a discussion of spin valve/semiconductor structures and the outlook for hybrid metal devices. A crucial aspect of nanoscale magnetic devices is the requirement to control the spin configura-

tions with the structure so that the magnetic switching and stable magnetic states can be optimised for such applications as magnetic memory elements in MRAM arrays. The initial magnetic states and switching processes are, of course, intimately linked and both are strongly materials and geometry dependent. Until recently experiment and computation were often at variance. As computational techniques and efficiency have rapidly evolved in the last few years guided by the increasing availability of high quality magnetic images on well defined nanostructures, the possibility of accurately predicting the micromagnetic states of magnetic nanostructures has become a reality. In Chap. 5 Arrott introduces the subject of micromagnetics and the discusses the underlying basis for the computation of micromagnetic properties and the dynamical switching process. The spin valve is the quintiessential magnetoelectronic device and is used in the giant magnetoresistance read head as well as providing the basis for magnetic memory elements. The development and refinement of the spin valve for such applications is now at an advanced stage and builds on many fundamental advances in the early 90s. In Chap. 6 Gurney et al describe spin valve giant magnetoresistance sensor materials used for hard disk drive read heads. They describe the fundamental physics of spin valves and a quantum view of their operation, materials and structural properties and explain the observed performance characteristics. Finally the outlook for future performance is considered in the context of 100 Gb/square inch data densities. In Chap. 7 Shi describe an approach to MRAM based on pseudo spin valves and tunnelling. First the existing semiconductor memory technology is reviewed followed by a review of different modes of MRAM. Then the switching process and the effect of switching on reading/writing selectivity is discussed. Finally the issues for magnetic switching in high density MRAM are considered. In Chap. 8 Katti describes an approach to realising MRAM based on GMR pseudo spin valve devices. The current status of GMR technology is discussed and demonstrations of switching with short cycle times are presented for GMR arrays. The bit architecture is decribed and the writing and reading steps and bit selectivity are considered in detail. Measurements of the actual switching performance of GMR pseudo spin valve devices are related to the fundamental switching process and the requirements for GMR MRAM.

The reader is encouraged to use these volumes not only as an introduction to recent developments in thin film magnetism and to the new field of spintronics but to see this work as part of a continuing evolution in a subject which continues to grow in importance, both technologically and scientifically. By focusing on fundamental issues we hope that the material we have covered will continue to be of value as a tutorial guide for some time. Inevitably we have not been able to cover all important topics in the present volumes, many of which are still in a rapid state of rapid development. Nevertheless we hope that the present volumes will serve to help interest grow still further in a fascinating field.

2

Magnetoelectronics

G.A. Prinz

2.1 Background

Before the critical discovery of the giant magnetoresistance effect [2.1], the study of electrical transport in magnetic materials was confined to a very small community of researchers. Now, slightly more than a decade later, it has become one of the dominant themes of condensed matter physics and materials science involving thousands of scientists, worldwide. This is driven both by the fact that the subject of spin-polarized transport is an interesting and challenging field of study, and also by the technological opportunities which may lie in electronic devices, which have a new degree of functionality based upon the spin of the carrier. The initial work, centered around the giant magnetoresistance (GMR) effect, dealt with layered materials which were all metallic. This attracted considerable attention from the electronic band structure community, since the largest effects were seen in those systems which were both structurally matched (e.g. bcc Fe/Cr or fcc Co/Cu multilayers) and exhibited electronic band matching preferentially for one spin state at the interfaces [2.2]. This is illustrated schematically in Fig. 2.1. The next important breakthrough came with the observation of spin-polarized tunneling from one magnetic metal to another, through an insulating barrier [2.3]. This attracted an additional community of researchers, many of whom had previously worked in the field of superconductivity and Josephson junctions. The focus now shifted from the bulk electronic states of the metal, to the interface states responsible for tunneling through the barrier.

Most recently, the focus has shifted again now to include the injection of spin polarized current from a ferromagnet into a semiconductor [2.4]. This focus again changes the issues of the electronic states involved in the transport, since in semiconductors one is generally concerned with low k momentum states with low effective mass, while ferromagnetic metals generally have high k and high effective mass. This mismatch has raised concerns about the likelihood of success in observing useful effects in such layered materials. Indeed, the mismatch in conductivity alone

would suggest that since most of the voltage drop in a device would be across the semiconductor layer, the small changes in resistance due to the ferromagnetic metals, would result in vanishingly small observed effects [2.5]. This, in turn, has led to considerable activity to develop ferromagnetic semiconductors ordered at room temperature, which would be electronically better matched to other semiconductor materials for device applications [2.6]. Most recently, however, something of a grand convergence has been suggested, when it was realized that the interface between ferromagnetic metals, and most semiconductors, forms a Schottky tunneling barrier, and this implies that the mismatch in conductance is less an issue [2.7]. There are, therefore, opportunities for devices, which include metallic ferromagnetism, spin polarized conductance through a barrier and spin-polarized transport in semiconductors. These developments have drawn in the even larger community of semiconductor researchers, and potential applications to many more devices.

The introduction of semiconductor layers brings a powerful new element to this field, since they can be doped to vary their conductance from insulating to highly conducting and, perhaps more importantly, they can be exploited for their optical properties. All of the early work involving seminconductors, has in fact, utilized the optical absorption of circularly polarized light to generate spin-polarized carriers [2.8]. Also, spin injection has been detected by monitoring the circularly polarized light emitted by the recombination of spin polarized electrons and holes [2.9]. When the optical properties are combined with the very long effective path lengths for spin polarized carriers in semiconductors, one has the basis for signal processing and computation.

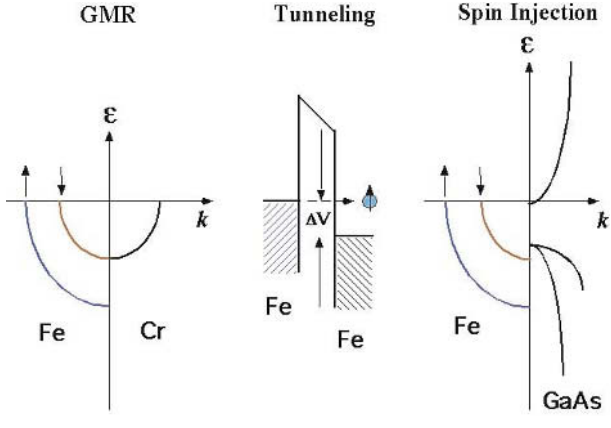

Fig. 2.1. Schematic representation of the bulk electronic states involved in: (**a**) giant magnetoresistance; (**b**) magnetic tunnel junction; (**c**) ferromagnetic metal/compound semiconductor

2.2 Commercialized Applications

The earliest application, following closely on the discovery of GMR, was a magnetic field sensor for use in the read head for hard disc storage drives [2.10]. This application, first announced in 1994, is now used throughout the industry. It is useful to recognize that insertion of this development was facilitated by the fact that the hard disc storage industry had already moved from inductive pick-up coils to thin film sensors, which exploited the anisotropic magnetoresistance (AMR) in NiFe films. AMR provided approximately a 1% effect, so the 9% effect seen for GMR was an immediate improvement with very little further investment in either manufacturing (film deposition, lithography, etc.) or engineering changes in ancillary components (motor drives, disc media, etc.).

Additional applications of GMR sensors have had less impact. This is generally because they have to create a new market, or as is more often the case, they must displace existing technology that performs comparably at very low cost. A good example of this is the Hall sensor. This is a mature technology (the leading manufacturer has produced over 10^9 of them), which sells sensors as low as a few cents a piece. Although not having the narrow spacial resolution of a thin-film read head, for a large variety of mechanical motion sensing, it is cost-effective. Nevertheless, the higher sensitivity of GMR sensors are beginning to obtain a market approaching 10^6 units per year, largely in the automotive industry (as brake sensors) and machine industry (for rotary motion sensing).

A more sophisticated application has developed as a signal isolator in information and communications systems. A common problem that arises when transmitting electrical signals from one electronic device to another through a connecting cable, is that ground loops can be generated which pick-up external noise. This can be avoided by converting the signal information from electrical to optical, by modulating a light source, then transmitting the optical signal to the second device, and finally reconverting the optical signal from a detector back into an electrical signal. This is commonly called an optical coupler. A replacement device is now marketed which converts the original signal to a modulated magnetic field, which then acts upon a GMR sensor [2.11]. The modulation of the GMR sensor resistance is then converted to electrical signal in the second device. This coupling through magnetic fields, rather than optical devices, has proved to be cheaper and have better high frequency response. It is beginning to displace the optical technology of the leading manufacturer.

2.3 Developing Technology

The most important area, where advanced product development is underway, that has very high potential for new commercialized products is magnetic random access memory (MRAM).

The original small computers, manufactured in the 1960's had MRAM in the form of small toroidal ferrite elements which were used to store bits of information

based upon the (circular) direction of magnetization, and the information was read in or out inductively via wires threaded through the center of these ferrite transformer cores (hence the name "core memory"). The replacement of magnetic memory by thin film, lithographically fabricated semiconductor memory in the 1970's provided RAM which was much faster, cheaper and higher in density. Unfortunately, the ability to retain the information, without power supplied to the memory, was lost. The current developments in thin-film MRAM promise to provide all of the advantages of semiconductor memory, plus return the advantage of non-volatility when power is removed.

There are two principal approaches to memory architecture currently being pursued from MRAM. One is called "sense line" [2.12] and the other is "cross-point array" [2.13]. These are illustrated in Fig. 2.2. The former is suitable for low resistance memory elements, while the latter is appropriate for high resistance elements. This distinction is based upon the need to sense the information in the elements using common semiconductor electronics, which are best suited to match resistances of 1 kΩ to 10 kΩ. Low resistance elements are therefore wired together in series into what is termed a "sense line", whose total resistance lies in the acceptable range of 1 kΩ to 10 kΩ. If the individual resistance of a device exceeds this range, then the sense line is reduced to essentially one element, and the concept of a sense line is no longer useful. For elements whose resistance are in this high range, it is convenient to locate them at the intersection of two conducting lines which can provide a classic four point probe connection to the device. Two of the lines carry current in and out of the element, while the other two serve to measure the voltage drop. An economical arrangement of these elements can be achieved if a square array of $n \times n$ elements are commonly served by n parallel top leads and orthogonally oriented n parallel bottom leads, the elements located between them at the n^2 intersections, forming a "cross-point array". Unfortunately, such an array has infinite connectivity between any pair of top and bottom leads, through all of the elements of the array. This can be corrected by placing a diode in each element, but attempts to do this by developing thin film diode have not been reported as successful. An alternative solution, which has been adopted, is to insert a transistor switch in each element, which is independently controlled so that only the element being interrogated can conduct current. The crossed array of conductors serves the additional purpose of generating magnetic fields, which can act on the magnetic layers of the elements. A half-select addressing scheme is used such that the field from one conductor is not sufficient to switch an element, but the combined effect of the fields from two conductors which cross above and below the magnetic element, is sufficient to reverse the magnetization in that element only where they intersect. Generally, the two addressing signals are applied in sequence, the first applying torque to orient the magnetization perpendicular to the easy axis, and the second is applied along the easy axis to set the moment in the desired direction. Similarly in the sense-line architecture, there is an array of addressing conductors, above and below the elements, that serve to provide a half-select addressing system. Both of these approaches are functional. The sense-line is seen as being suitable for low resistance GMR elements, and the cross-point array for high resistance MTJ elements.

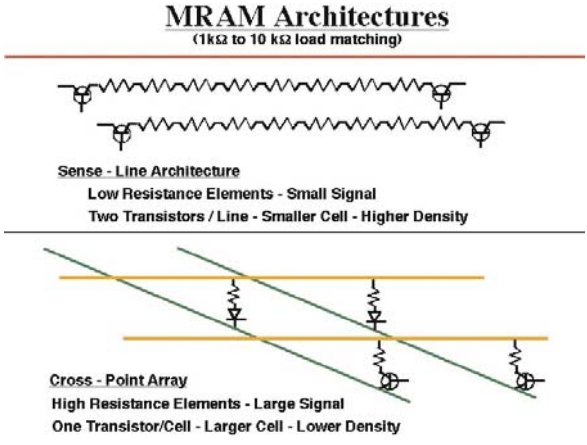

Fig. 2.2. Schematic illustration of two principal approaches to MRAM memory architecture

There is one other reported information storage element under development, which would also utilize a cross-point array architecture, namely, the hybrid-Hall device [2.14]. This device, illustrated in Fig. 2.3, utilizes a Hall cross patterned in the supporting semiconductor underlayer as its sensor, and the information is stored in a soft magnetic layer immediately above it. The magnetic layer is patterned into a longitudinal element, whose one end is centered at the intersection of the Hall cross. The fringing field, from the end poles, passes through the plane of the cross generating a Hall voltage when current is passed through the device. Reversing the magnetization of the magnetic element, reverses the sign of the fringing field, and therefore, the sign of the Hall voltage. In terms of circuit architecture, a hybrid-Hall device array has many of the same requirements of an MTJ array. A half-select addressing network to switch the magnetic elements is required, and instead of leads to the switching transistor, one needs leads to the Hall device to supply current and read the Hall voltage.

The single most challenging issue to be resolved in MRAM technology has been magnetic switching of the elements. That is the reversal of the magnetoresistance between the high and low value states. Although this may always be accomplished for any given element in sufficiently high applied fields, the challenge is to be able to accomplish this repeatedly, for each element in an array, using the fields generated by the addressing lines operated at acceptable current levels. Specifically, this means repeating the operation $10^{12}-10^{15}$ times, on $10^{6}-10^{9}$ elements, at current levels < 10 mA. Furthermore, the values of the applied current must be the same for every element, within a narrow range, so that $1/2$ of the field necessary to switch the hardest element is not sufficient by itself to switch the softest element. Finally, the values for the magneto-resistance obtained, must also fall within a narrow range to match the design requirements of the supporting semiconductor electronics.

Of course, meeting this challenge has placed demands upon both materials fabrication and lithographic processing, but intelligent design of the elements themselves

can have a large impact on the latitude of control needed in those steps. The switching behavior of one element is determined by the properties of its constituent films themselves (coercivity and anisotropy), the micromagnetic behavior of the element (determined by its shape), the magnetic coupling of the individual components of an element to each other, and the coupling of elements to their neighboring elements. The most commonly chosen material is permalloy ($Ni_{0.78}Fe_{0.22}$) because of its low coercivity and low anisotropy as well as low magnetostriction. It does not exhibit the largest magnetoresistance effects, however, and to enhance this Co may be added as an alloy or at the interface between layers. This can, however, have a deleterious effects on the other properties, such as the anisotropy or the magnetostriction. Although the original element shape was often chosen to be a rectangle, in order to provide a longitudinal shape anisotropy, it is now generally recognized that if the ends of the element are square, magnetic singularities are formed in the element by the demagnetizing effects of the end poles. These singularities cause irregularities in the switching, which are difficult to control and lead to variations in the switching fields and multidomain structure within the element [2.15]. Therefore, the elements are generally given tapered ends or the elements are rounded to approximate elipses. This lowers the pole density at the ends, lowering the demagnetizing fields and creating quasi-single domain elements with reproducible behavior. This is achieved at the expense of requiring larger switching fields to be generated by the addressing lines, and there are still pole-created magnetic fields, which can couple to other layers in an element, or to neighboring elements.

An alternative approach is to shape the element into a toroid where the magnetization closes on itself leaving no poles, and therefore, no demagnetizing fields or coupling fields [2.16]. This solves the problems encountered with linear devices, but requires an addressing scheme, which can generate switching fields reflecting the

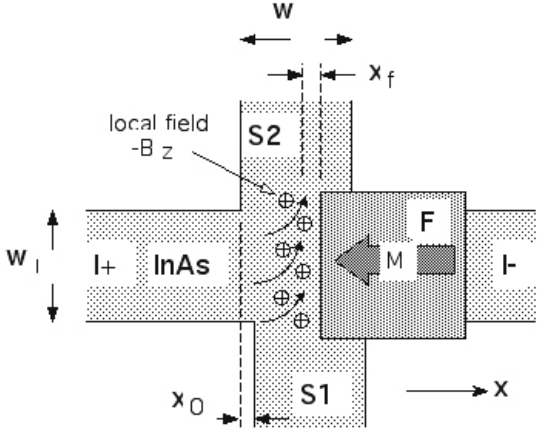

Fig. 2.3. Schematic illustration of hybrid-Hall device, showing edge of ferromagnetic pad (F) located near center of Hall cross. The fringing field from the end poles, B_z, acts on the carriers to create the Hall voltage across S1-S2

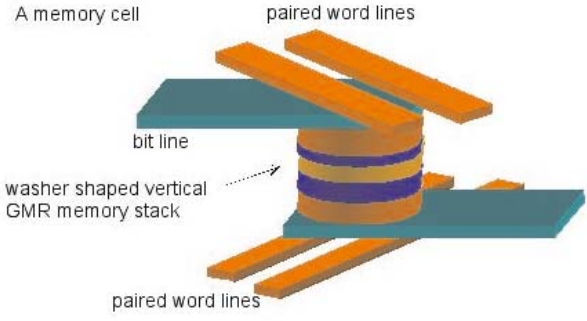

Fig. 2.4. Schematic illustration of a toroidal MRAM element to utilize CPP-GMR. The dual addressing lines are located above and below the element and insulated from it

circular symmetry of the element, as shown in Fig. 2.4 [2.17]. This can be achieved by pairs of addressing lines located above and below the element. With the proper choice of current direction in these lines, a radial magnetic field is generated at the element. If a vertical current is then passed down through the element itself, a circular magnetic field is generated, which can reverse the magnetization of the toroid. This scheme is suitable for conducting devices, such as an all-metal GMR element. For an MTJ device, unless sufficient tunneling current can be obtained, an insulated conductor passing through the center hole, would be required.

There are two approaches to deal with the controlling of the magnetic orientation between the magnetic layers of an element, called respectively the spin-valve or pseudo spin-valve. The spin valve, commonly used with MTJ devices, pins one magnetic layer by placing it in contact with an antiferromagnetic layer, which is itself immune to the magnitude of the applied fields provided by the addressing lines. This layer is effectively "infinitely hard" and remains magnetically fixed. The information is stored in the soft layer, which can be switched to be either parallel or antiparallel with the fixed layer, placing the device in either the low resistance or high resistance state. Since the spacing between the two magnetic layers in a MTJ is generally < 10 Å, there can still be strong dipolar coupling between them due to end poles of the element. This can be considerably reduced by making the fixed layer itself a double layer which is strongly antiferromagneticallly coupled together so that its own fringing fields due to the end poles are self-contained. The operation of the device is still maintained but the only remaining fringing fields are from the soft layer. These still are a cause for coupling between neighboring elements, but will not destabilize the switching properties of a given element.

The pseudo spin-valve, commonly used in GMR devices in sense-line arrays, stores the information in a magnetically hard layer and uses a magnetically soft layer to interrogate the element nondestructively. The soft layer is cycled through two reversals of known direction and the magnetoresistance of the device is measured. The relative change in resistance during this cycle reveals the orientation of the magnetization in the hard storage layer. The difference in coercive fields between

the hard and soft layers must be sufficient to avoid altering the hard layer during interrogation. Magnetic coupling between the layers via the fringing fields from the end poles, can be a major source of unreliability in this device. The final cause for troublesome coupling between magnetic layers is coupling between the interfaces, either through exchange coupling or interface roughness Néel coupling. The former is an important consideration for GMR based devices, and demands either using an exchange-breaking material between the layers, or increasing the spacing to make the coupling negligible. For a NiFe/Cu/NiFe structure, the latter approach requires Cu thickness > 30 Å. Interface roughness coupling can be a serious problem. If the interface roughness is correlated between successive layers, this generally results in "ferromagnetic" coupling. For MTJ devices due to the close layer proximity demanded by the thin tunneling barrier, and near-atomic smoothness can be required. Thus, control of layer thickness and interface roughness across a total wafer area (which may approach 12" diameter in modern fabrication plants) is one of the most serious materials challenges facing this technology.

The hybrid-Hall storage element, in contrast to the GMR and MTJ devices, exploits the fringing field from the magnetic layer, and therefore the device design issues center on shaping the magnetic element to obtain optimum switching behavior, while retaining maximum flux passing through the Hall sensor. Although this may require a soft magnetic "keeper" layer beneath the sensor, in general the magnetics issues of this device are much simpler than either the GMR or MTJ devices.

In order to compare these different approaches to MRAM, the most useful criteria are those of manufacturability, speed, and scalability. All these are not entirely independent issues and we shall consider them in turn.

Manufacturability includes all of the steps required to reliably and inexpensively fabricate MRAM on a scale comparable with modern integrated electronics. All of these approaches are essentially "back-end" fabrication, in that all of the required clocks, amplifiers, multiplex switching networks, etc. are first fabricated using silicon technology, and then the magnetic memory elements are added on top, without compromising the underlying silicon circuitry. This has now been demonstrated for both MTJ and GMR devices. Since Hall devices demand a high mobility layer in the element itself, this may represent a separate case and has not yet been demonstrated. In layer fabrication, thickness control and interface roughness control over the whole wafer are paramount. The MTJ tunnel barrier is the most critical example of the former and research results look promising [2.18]. Interface roughness will compromise both GMR and MTJ devices, where again the MTJ devices may be the most demanding, but results from small wafers look acceptable. Vertical GMR multilayer devices, in which roughness increases with the number of layers, must also solve this problem. Current lithographic patterning tools and processes seem adequate for all of these approaches, probably down to $0.10\,\mu$m dimensions; however alignment of the sequential lithographic levels is more demanding in the vertical devices (MTJ and VGMR) than in the in-plane devices (in-plane GMR and hybrid Hall).

An important issue in MRAM technology is signal strength, or more properly, signal-to-noise (S/N). This quality ultimately determines the speed of the device, since inadequate S/N generally demands averaging over time. The largest signals

have been demonstrated in the high impedance devices. Specifically the MTJ and the Hall elements. For example, MTJ devices of 0.7 μm^2 area, operated at 200 mV bias, exhibiting a 23% $\Delta R/R$, yielded a 50 mV signal. Applying larger bias generally causes $\Delta R/R$ to decrease [2.19]. Hybrid Hall devices of 3 μm^2 have exhibited 40 mV signals, using InAs for the Hall sensor, and 1 mA through the 500 Ω device [2.19]. The low impedance in-plane GMR devices have demonstrated a 4% change at 2 mA through a 60 Ω device yielding a 5 mV signal [2.20]. Since 8% is seen in unpattered GMR material, if the loss of signal caused by patterning can be recovered, one might expect 10 mV signals in this technology. Finally, the vertical GMR devices have the smallest resistance and give the smallest signals. A 0.3 μm diameter element of 0.2 Ω resistance passing 10 mA, exhibits a 12.5% effect, yielding at 0.25 mV signal [2.21]. It is generally agreed that signal levels in the range 1 mV to 10 mV are the best match to existing Si electronics. All of these, except the vertical GMR, meet this criteria. Since 100% changes in vertical GMR have been reported a low temperature [2.22], which should scale to 50% [2.23] changes at room temperature, devices at this scale should be capable of meeting the 1 mV criteria. Of course at smaller scale, R increases as 1/area, and the signal level will similarly scale, so decreasing size improves the vertical GMR signal.

Scalability, that is, the ability for a technology to remain functional as the device dimensions shrink, is an important consideration, since it determines the ultimate memory capacity of an MRAM chip and its ability to provide multiple generation products for a commercial manufacturer. The factors involved are not identical for the different approaches under discussion. For the MTJ-based MRAM, the cell size is completed dominated by the use of transistor, as is also the case in commonly used DRAM. It therefore faces the same approaching barrier, recognized by the semiconductor industry as the "0.1 μm barrier". For reference, a $(0.1\ \mu m)^3$ of Si changes its resistivity from 10^5 Ω-cm to 5Ω-cm with the addition of one phosphorous atom as a dopant [2.24]. This raises the question of fabricating transistors at this scale, and any reduction of the magnetic element below size this dimension would be irrelevant. The hybrid Hall device, which also depends upon a functional semiconductor as its transduction material, faces a similar limitation for scaling. In contrast, the sense line architecture, which only uses transistors at the ends, does not have its cell size limited by the transistor dimension.

However, all magnetic devices face ultimate limits based upon the occurrence of superparamagnetism. Superparamagnetic behavior is a well-known phenomena in magnetic materials when a particle size gets sufficiently small so that, even though the spin system is ordered, and a net magnetic moment exists, there is insufficient magnetic anisotropy to keep it oriented in one direction against thermal fluctuations. For an application such as MRAM this is especially troublesome, since a half-select scheme is generally used to reverse an element's magnetic moment either for reading or writing. When the element size is sufficiently small that thermal instability obtains, all of the elements on a single half-select addressing line may be at risk of reversing, even though they do not lie at the intersection with the other energized addressing line [2.25]. For an unpinned permalloy device layer 15 Å thick, of 0.1 μm × 0.4 μm dimension, it has been calculated that thermal upset at 125 °C will make it unusable

under normal operating conditions [2.26]. Using this result for a typical permalloy-based device as a metric, the in-plane GMR sense line technology, with a cell size of $32l^2$ [2.27], terminates at approximately $3 \cdot 10^8$ bits/cm^2 for $l = 0.1\,\mu$m and the reported [2.28] $20l^2$ for MTJ cells, terminates at approximately $5 \cdot 10^8$ bits/cm^2. The vertical GMR sense-line using toroidal elements of several multilayers has a cell size of $16l^2$ determined by the center hole being the smallest lithographic dimension l. In addition, the larger shape anisotropy of the toroids, for the same thickness of the permalloy soft layer, stabilizes the magnetic orientation against thermal upset at 125 °C down to a dimension of $l = 0.01\,\mu$m [2.29], which implies a terminal density of $60 \cdot 10^9$ cm^2. Thus, the vertical GMR sense line architecture offers the highest ultimate density of all the approaches, 200 times that of in-plane GMR and 100 times that of MTJ, once lithography tools are suitable to reach $l = 0.01\,\mu$m. For reference, the minimum planar cell for any technology which has elements of square dimension ($l \times l$) separated by a space of l in each direction is $4l^2$. For $l = 0.1\,\mu$m this yields a memory density of $2.5 \cdot 10^9$ bits/cm^2, and for $l = 0.01\,\mu$m yields $250 \cdot 10^9$ bits/cm^2 or 10^{12} bits/inch^2.

2.4 Future Opportunities

Presently available sensors and prototype MRAM elements, exploit the commonly available materials Co, Ni and Fe and their alloys. This is understandable, since these materials magnetically order well above room temperature and their properties from a physics and materials point-of-view, are well understood. Furthermore, the magneto-transport effects which they demonstrate are sufficient to satisfy the engineering requirements of these technologies. If one would like to move beyond this, to perhaps challenge and replace other electronic technology, the observed effects would have to be considerably enhanced. This is illustrated, in Fig. 2.5 which shows ΔR/R for a tunneling device as a function of the % polarization of the carriers at the Fermi level of the ferromagnetic conductors used. As shown, the 3-d transition metals with their $\sim$ 50% polarization, can provide at best a factor of two change in the magnetoresistance. Polarizations exceeding 90% are required to significantly improve this. If, however, one can obtain a factor of $\sim$10 change in the magnetoresistance, one can seriously begin to challenge, say, a semiconductor device used as a logic gate. This is a particularly important application, since a magnetoresistive logic gate would be reprogrammable at very fast speeds and could lead to an entirely new technology based upon software-driven reprogrammable logic circuits.

At present there appear to be several opportunities for materials whose polarization approaches 100%: transition metal oxides; Heusler alloys, and ferromagnetic semiconductors. The electronic basis for 100% spin polarization in transport is illustrated in Fig. 2.6 for CrO_2. One observes that the majority spin states lie below the Fermi level and are all filled. The minority spin states contain the Fermi level and are only partially filled, but since the Fermi level lies in a gap in the majority spin density of states there are no majority spin carriers at the Fermi level, thus creating 100% spin polarization of the carriers. These materials are also referred to as half-metallic,

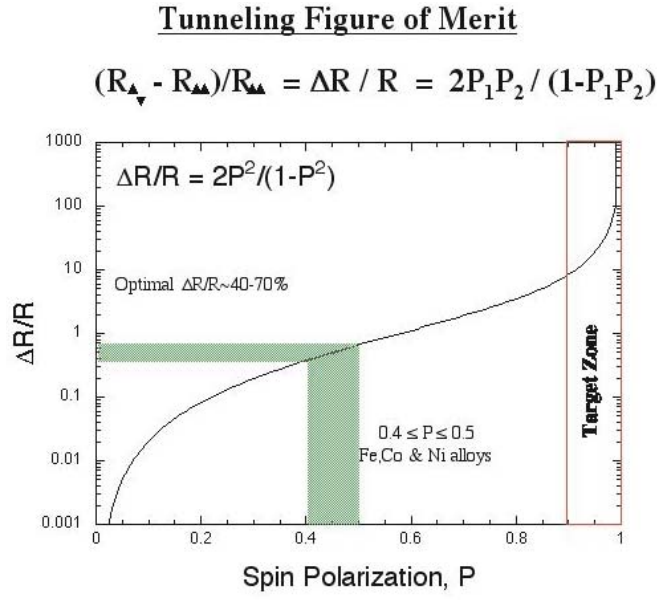

Fig. 2.5. ΔR/R for a tunneling device as a function of the polarization, using the Julliere [2.30] criterion and assuming P1 = P2 for the metallic contacts

since they are only metallic for the minority carriers, and are either insulating or semiconducting for the majority carriers, depending upon the size of the band gap.

Work on CrO_2 dates back to 1961 [2.32], and it remains today one of the few examples of a material that actually exhibits transport properties approaching half-metallic behavior. Recent work [2.33], using Andreev point contact spectroscopy at low temperature has yielded a value of 96%, with the remaining discrepancy probably attributable to the contact interface effects. Although its Curie temperature is 115 °C, room temperature half-metallicity has not been reported. Large effects have been seen for the mixed valence manganites $La_{0.7}Sr_{0.3}MnO_3$, but they order at too low a temperature ($T_c \sim 360$ K), and are therefore not of interest for applications.

Finally Fe_3O_4 (magnetite) is predicted to be a half-metal and has a high Curie temperature of 850 K. Some large effects have been seen in tunneling [2.34] and small nanocontacts [2.35], but no robust room temperature electronic device has yet been demonstrated which exhibits 100% spin polarization.

The Mn-alloyed III-V compound semiconductors In(Mn)As [2.36] and Ga(Mn)As [2.37] also have calculated density of states which predict them to be half metallic [2.30]. Although they have yielded large tunnel junction magnetoresistances (~70%), they have not yet displayed 100% polarization and their low ordering temperatures does not yet make them suitable for applications.

Other half-metallics, as predicted by their calculated electronic structure, are listed in Table 2.1. None of these, in transport experiments, have proven to have polarizations as high as CrO_2. It should be understood that these are predicted bulk properties

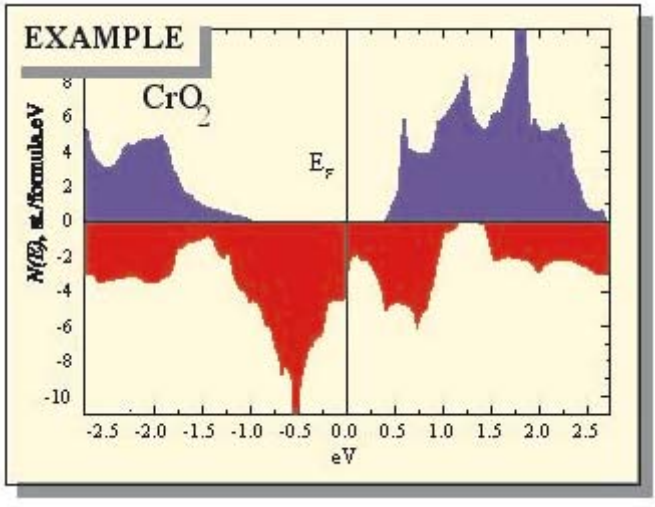

Fig. 2.6. The calculated spin-polarized density of states (DOS) for CrO_2 [2.31]

Table 2.1. Predicted Half Metallic Ferromagnets

Half Heuslers	Oxides	Full Heuslers	
(C1b structures)	CrO_2 (rutile)	(L21 Structures)	Pd_2MnAl
NiMnSb	Fe_3O_4	Co_2MnAl	Pd_2MnSn
PtMnSb	$La_xSr_{1-x}MnO_3$	Co_2MnSn	Pd_2MnGa
CoMnSb		Co_2MnGa	Pd_2MnSi
FeMnSb (ferri-)		Co_2MnSi	Pd_2MnGe
CrMnSb		Ni_2MnAl	
UniSb		Ni_2MnSn	
		Ni_2MnGa	
		Ni_2MnSi	
		Ni_2MnGe	

and often depend crucially upon details of the crystalline and chemical order being precisely met. For example, the so-called "half Heuslers" have received a great deal of attention in the research community, because of their being highlighted in the seminal theoretical treatment of "half-metallic " ferromagnets [2.38]. Unfortunately, the C1b unit cell contains a vacancy at the X1 site. This vacancy is mobile, making it very difficult to obtain long-range chemical order from cell to cell throughout a crystal. In the absence of chemical ordering, the half-metallic electronic structure does not

obtain. The situation is considerably better in the so-called "Full Heuslers" where the vacancy is filled by another ion yielding the L21 unit cell. Unfortunately, even here, there can be interchange between transition metal ions (i.e. Co^{2+}, Mn^{2+}) which leads to a more suble chemical disorder (often called phase disorder) from cell to cell which can again alter the electronic structure away from half-metallic. Finally, even given a single crystal not subject to chemical disorder issues (such as CrO_2) one still must deal with interfaces, since in any real application, one is likely to require that carriers pass from the interior (where 100% spin polarization may obtain) through an interface to another conductor. The interface states themselves are likely not to be half-metallic. They may offer the opportunity to introduce carriers of the opposite polarity, or even spin-flip scatter the carriers passing through.

2.5 Conclusion

The future of magnetoelectronics ultimately lies in the development of new materials. The early stages of the field moved rapidly, largely because it was exploiting established materials supported by a large body of work, both in the basic research and the applied worlds. Films of Fe, Ni, Co and permalloy had been studied for decades, before the discovery of GMR. Similarly, spin polarized tunneling through oxidized aluminum films had a long history. This field is now faced with the expensive and time-consuming work of determining the fabrication procedures and resulting characteristics of new materials, including the ferromagnetic semiconductors and highly spin polarized alloys and compounds. Good fortune may provide rapid breakthroughs, but it is more likely that the solutions will yield to careful, systematic research. Both the pleasures that these discoveries will give to the researchers, and the new technology that they will enable, will make the enterprise well worth the effort.

References

2.1. M.N. Baibich, J.M. Broto, A. Fert, F. Nguyen Van Dau, F. Petroff, P. Etienne, G. Creuzet, A. Friederich, and J. Chazelas. *Phys. Rev. Lett.*, 61:2472, 1988.
2.2. K.B. Hathaway and J.R. Cullen. *J. Magn. Magn. Mat.*, 104–107:1840, 1992.
2.3. J. Moodera, L. Kinder, T. Wong, and R. Meservey. *Phys. Rev. Lett.*, 74:3273, 1995.
2.4. S. Datta and B. Das. *Appl. Phys. Lett.*, 56:665, 1990.
2.5. G. Schmidt, D. Ferrand, L.W. Molenkamp, A.T. Filip, and B.J. van Wees. *Phys. Rev. B*, 62:4790, 2000.
2.6. Y. Ohno, D.K. Young, B. Beschoten, F. Matsukura, H. Ohno, and D.D. Awschalom. *Nature*, 402:790, 1999.
2.7. A. Fert and H. Jaffres. *Phys. Rev. B*, 64:184420, 2001.
2.8. D.D. Awschalom and N. Smorth. *J. Magn. Magn. Mater.*, 200:130, 1999.
2.9. R. Fiederling, M. Kleim, G. Reuscher, W. Ossau, G. Schmidt, A. Waag, and L.W. Molenkamp. *Nature*, 402:787, 1999.

2.10. C. Tsang, R.E. Fontana, T. Lin, D.E. Heim, V.S. Speriosu, B.A. Gurney, and M. L. Manson. *IEEE Trans. Magn.*, 30:3801, 1994.
2.11. J.M. Daughton. *IEEE Trans. Magn.*, 36:2773, 2000.
2.12. M. Dax. *Semicond. Int.*, 20:84, 1997.
2.13. R.E. Scheuerlein. 1998. Paper presented at the IEEE Int. Conf. On Nonvolatile Memory Technology, Albuquerque, NM 22–24 June.
2.14. M. Johnson, B.R. Bennet, M.J. Yang, M.M. Miller, and B.V. Shanabrook. *Appl. Phys. Lett.*, 71:1699, 1993.
2.15. T.-N. Fang and J.-G. Zhu. *IEEE Trans. Mag.*, 37:1963, 2001.
2.16. K. Bussmann, G.A. Prinz, S.F. Cheng, and D. Wang. *Appl. Phys. Lett.*, 75:2476, 1999.
2.17. J.-G. Zhu, Y. Zheng, and G. A. Prinz. *J. Appl. Phys.*, 87:6668, 2000.
2.18. S. Tehrani, J.M. Slaughter, E. Chen, M. Durlam, J. Shi, and M. Deherra. *IEEE Trans. Magn.*, 35:2814, 1999.
2.19. M. Johnson, B.R. Bennet, M.J. Yang, M.M. Miller, and B.V. Shanabrook. *IEEE Trans. Magn.*, 34:1054, 1998.
2.20. R.R. Katti, A. Arrott, J. Drewes, W. Larson, H. Liu, Y. Lu, T. Vogt, and T. Zhu. *IEEE Trans. Mag.*, 37:1967, 2001.
2.21. K. Bussmann, G.A. Prinz, R. Bass, and J.G. Zhu. *Appl. Phys. Lett.*, 78:2029, 2001.
2.22. E.E. Fullerton, M.J. Conover, J.E. Mattson, C.H. Sowers, and S.D. Bader. *Appl. Phys. Lett.*, 63:1699, 1993.
2.23. M.A.M. Gijs, J.B. Giesbers, M.T. Johnson, J.B.F. aan de Stegge, H.H.J.M. Janssen, S.K.J. Lenczowski, R.J.M. van de Veerdonk, and W.J.M. de Jonge. *J. Appl. Phys.*, 75:6709, 1994.
2.24. R.K. Cavin III, D.J.C. Herr, and V. Zhirnov. *Semiconductor Research Needs in the Basic Physical Sciences*. Semiconductor Research Corp., 2000.
2.25. R.H. Koch, G. Grinstein, G.A. Keefe, Yu Lu, P.L. Trouilloud, W.J. Gallagher, and S. S. P. Parkin. *Phys. Rev. Lett.*, 84:5419, 2000.
2.26. R.S. Beech, J.A. Anderson, A.V. Pohm, and J. M. Daughton. *J. Appl. Phys.*, 87:6403, 2000.
2.27. J. Gadbois, J.-G. Zhu, W. Vavra, and A. Hurst. *IEEE Trans. Magn.*, 34:1066, 1998.
2.28. S. Tehrani, B. Engel, J.M. Slaughter, E. Chen, M. DeHerrera, M. Durlam, P. Naji, R. Whig, J. Janesky, and J. Calder. *IEEE Trans. Magn.*, 36:2752, 2000.
2.29. J. Zhu. Number DA-04, Seattle, Washington, 2001. 46th Annual Conference on Magnetism and Magnetic Materials.
2.30. T.C. Schulthess and W.H. Butler. *J. Appl. Phys.*, 89:7021, 2001.
2.31. M. Julliere. *Phys. Lett. A*, 54:225, 1975.
2.32. B. Kubota and E. Hirota. *J. Phys. Soc. Japan*, 16:345, 1961.
2.33. Y. Ji, G.J. Strijkers, F.Y. Yang, C.L. Chien, J.M. Byers, A. Angelouch, G. Xiao, and A. Gupta. *Phys. Rev. Lett.*, 86:5585, 2001.
2.34. P. Seneor, A. Fert, J.L. Maurice, F. Montaigne, F. Petroff, and A. Vaures. *Appl. Phys. Lett.*, 674:4017, 1999.
2.35. J.J. Versluijs, M.A. Bari, and J.M.D. Coey. *Phys. Rev. Lett.*, 87:026601, 2001.
2.36. H. Ohno, H. Munekatta, T. Penny, S. von Molnar, and L.L. Chang. *Phys. Rev. Lett.*, 68:2664, 1992.
2.37. H. Ohno, A. Shen, F. Matsukura, A. Oiwa, A. Endo, S. Katsumot, and Y. Iye. *Appl. Phys. Lett.*, 69:363, 1996.
2.38. R.A. de Groot, F.M. Mueller, P.G. van Engen, and K.H.J. Buschow. *Phys. Rev. Lett.*, 50:2024, 1983.

3

Electrical Spin Injection into Semiconductors

B.T. Jonker

3.1 Introduction

The basic approach to improve performance in modern semiconductor electronics to date has been to reduce the minimum feature size to increase circuit density. According to Moore's Law, which extrapolates the number of transistors per unit area due to such scaling, this approach is expected to reach practical and fundamental physical limits by the year 2010 [3.1]. Consequently, there is keen interest in developing a new paradigm for future electronic technologies.

Spintronics, or the use of carrier spin as a new degree of freedom in an electronic device, represents one of the most promising candidates for this paradigm shift. Commercial success has already been realized in all-metal structures based on giant magnetoresistance (GMR), a new and entirely spin-derived functionality. The GMR effect is due to spin transport between two ferromagnetic metals separated by a non-magnetic spacer metal, and refers to the increase in resistance which occurs when the relative orientation of the magnetic moments of the two magnetic layers is switched from parallel to anti-parallel [3.2, 3]. In a simple model, this change in resistance is ascribed to the availability of states of the correct spin in the collector ferromagnet. A "majority spin" electron from the source ferromagnet, FM1 (i.e. an electron whose moment is parallel to the magnetization of FM1), is easily transmitted through the nonmagnetic spacer metal and into the collector ferromagnet, FM2, if the magnetizations of FM1 and FM2 are parallel. In this case, the electron is also a majority spin carrier in FM2 and the appropriate spin states are available. However, if the magnetization of FM2 is aligned anti-parallel to that of FM1, fewer states of the appropriate spin are available, and it is less likely that the carrier will be transmitted into FM2, resulting in a higher resistance. Applications of this remarkably simple effect include GMR-based sensors, recording heads and nonvolatile memory [3.4]. More recent work has extended this basic effect to metal/insulator/metal tunnel junctions to increase the relative change in resistance and thereby the performance of the end product [3.5–7]. GMR recording heads, first introduced in 1998, now com-

pletely dominate the hard disk industry, and are responsible in part for the remarkable performance to cost ratio ($\sim$ 1 GB/$1) enjoyed in the consumer electronics market.

Semiconductor-based spintronics offers many new avenues and opportunities which are inaccessible to metal-based structures. This is due to the characteristics for which semiconductors are so well known: the existence of a band gap which can often be tuned over a significant range in ternary compounds, the accompanying optical properties on which a vast opto-electronic industry is based, and the ability to readily control carrier concentrations and transport characteristics via doping, gate voltages and band offsets. Coupling the new degree of freedom of carrier spin with the traditional band gap engineering of modern electronics offers new functionality and performance for semiconductor devices, [3.8–11] as well as an avenue to circumvent the dielectric breakdown and capacitive limits which are major near-term concerns in existing electronics [3.1].

3.2 Device Concepts

A number of semiconductor-based spin dependent device concepts have been proposed and discussed which offer exciting new properties. The seminal proposal by Datta and Das of a spin-polarized field effect transistor, or spin-FET [3.8], with ferromagnetic source and drain contacts for spin injection and detection (Fig. 3.1a), has stimulated a great deal of effort to better understand the behavior of spin-polarized carriers in semiconductor hosts under conditions of dynamic transport. In the proposed operation of this device, spin-polarized electrons are injected from the FM source and into the high mobility two dimensional electron gas (2DEG) channel. The electric field in the channel under the gate region causes the orientation of the moving carrier spin to change by some amount which is controlled by the gate voltage. When these carriers reach the drain contact, they will be transmitted or reflected with some probability which depends on the relative orientation of carrier spin and drain magnetization, similar to GMR. Thus the conductance of the device is controlled in part by the orientation of the carrier spin in the 2DEG channel. This device concept has stimulated a tremendous amount of theoretical and experimental effort addressing the various facets of operation of spin-polarized devices.

A variety of other semiconductor spintronic devices of varying complexity have been discussed in the literature. These include a spin-polarized light emitting diode (spin-LED, Fig. 3.1b) [3.12–15], tunable optical isolators, spin-dependent resonant tunneling diodes (spin-RTDs, Fig. 3.1c) [3.16–21], and gated spin coherent devices [3.22, 23]. The spin-LED is based on radiative recombination of spin polarized carriers, resulting in the emission of circularly polarized light. This relatively simple structure provides a testbed for examining the fundamentals of spin injection and transport, and will be discussed in detail in later sections.

The spin-RTD is more complex in structure and operation, and is based on resonant tunneling of carriers through quantum confined levels in the quantum well. The standard RTD is a two terminal device [3.24, 25] which cannot readily be gated, a critical disadvantage limiting its application [3.26]. Hybrid GMR/RTD device structures

have been reported which enable programming the RTD operating characteristics in a nonvolatile manner [3.27, 28]. However, the addition of spin transport in the semiconductor heterostructure enables a *spin-gated* mode of operation in which the conductance of the device may be determined by the relative alignment of emitter and quantum well states in both energy and spin. If both emitter and quantum well are ferromagnetic or exhibit spin-split states, when the energy resonance condition is met, changing the relative orientation of the emitter and quantum well spin systems gates the current through the device. Note that if the emitter is non-magnetic, the structure then serves as a tunable spin filter – at a given bias, resonant tunneling occurs through only one spin state in the well, and the output current exhibits the corresponding polarization. The opposite polarization is realized by changing either the bias or switching the magnetization of the quantum well.

Some degree of success has been realized in each of the devices described above. However, more significant progress towards a practical device has been thwarted by the lack of one or more of the components essential to the intended operation.

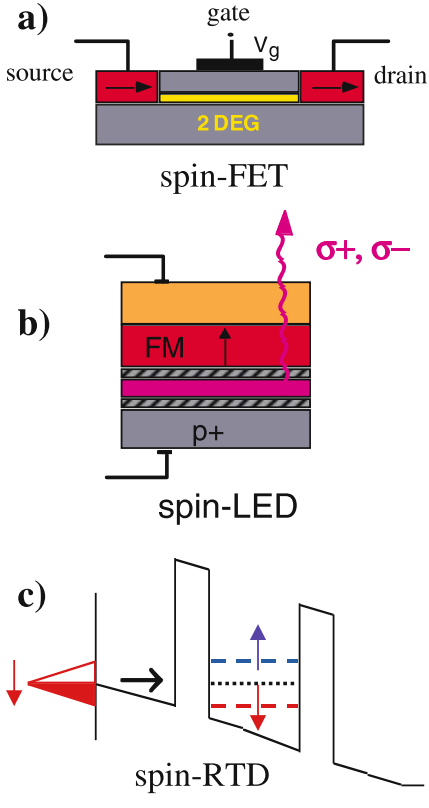

Fig. 3.1. Schematic diagrams of a number of semiconductor spintronic device concepts: (**a**) the spin-FET of reference [3.8], (**b**) the spin-LED, and (**c**) a band diagram of the spin-RTD

A semiconductor-based spintronics technology has at least four essential requirements for implementation, as can be seen by inspection of any of the devices shown in Fig. 3.1:

(i) efficient *electrical injection* of spin-polarized carriers from an appropriate contact into the semiconductor heterostructure,
(ii) efficient spin *transport* and sufficiently long spin *lifetimes* within the semiconductor host medium,
(iii) effective *control/manipulation* of the spin carriers to provide the desired functionality, and
(iv) effective *detection* of the spin-polarized carriers to provide the output.

Optical pumping has routinely been used to "inject" spin polarized carrier populations in semiconductor heterostructures, and has provided tremendous insight into their behavior [3.29]. A number of experiments have convincingly demonstrated requirement (ii) of long spin lifetimes and efficient spin transport in materials such as GaAs [3.30–32]. Spin diffusion lengths of many microns have been reported in optically pumped GaAs [3.32], for example, demonstrating that a spin-polarized mode of operation is certainly feasible for every modern transport device, where sub-micron length scales are the norm. Corresponding measurements revealed surprisingly long spin lifetimes (> 100 ns) [3.31], which are much longer than typical transit times in existing devices.

The particular mechanism used to effectively control and manipulate carrier spin (iii) depends upon the details of the device, and several successful avenues have been demonstrated. In 2DEG systems, several experiments have shown that a gate voltage can be used to control the spin precession via the Rashba effect [3.33, 34]. In spin-RTDs, modeling has shown that the energy separation of spin states and relative orientation of the corresponding magnetization in a ferromagnetic quantum well determine the transport through the structure [3.19].

A number of detection mechanisms (iv) are known and have been employed, including GMR-like behavior in planar transport [3.35] or at a Schottky contact [3.36], the emission of circularly polarized radiation resulting from the recombination of spin-polarized carriers [3.12, 30], the so-called spin Hall effect [3.37, 38], or spin-split features in tunneling spectra [3.17].

Efficient and practical spin injection (i), however, has been an elusive goal. Although injection from a scanning tunneling microscope tip has been reported [3.39–41], *electrical spin injection via a discrete contact* is highly desirable, since it provides a very simple and direct means of implementing spin injection compatible with existing device fabrication technology in which the contact area defines the spin source. A number of groups have attempted to inject spin polarized carriers from a ferromagnetic metal contact into a semiconductor, and reported measured effects on the order of 0.1–1% [3.35, 42–44]. An estimate of actual injection efficiency can be extracted from a particular transport model based on assumptions believed appropriate for a given experiment. Such small effects, however, make it difficult to either unambiguously confirm spin injection or successfully implement new device concepts. In addition, these experiments typically measured a change in resistance

or potential, which some argue may be compromised by possible contributions from anisotropic magnetoresistance or a local Hall effect [3.45–47]. These latter effects can easily result in a contribution of a few percent to the measured signal, and care must be taken in the experimental design to eliminate their role. This experimental approach has been discussed extensively in the literature, and will not be reviewed further here.

An alternative approach to measure electrical spin injection takes advantage of one of the distinguishing characteristics of semiconductors – radiative recombination of carriers and the consequent emission of light. The spin-polarized light emitting diode, or spin-LED shown in Fig. 3.2, [3.12] provides an accurate and *quantitative* measure of the carrier spin polarization in a semiconductor in a *model independent* manner. In a normal LED, electrons and holes recombine in the vicinity of a *p-n* junction or quantum well to produce light when a bias current flows. This light is unpolarized, because all carrier spin states are equally populated, and all dipole-allowed radiative transitions occur with equal probability. In a *spin*-LED, carriers are electrically injected from a contact with a net spin polarization across the heterointerface and into the semiconductor. If these carriers retain their spin polarization when they reach the quantum well, radiative recombination results in the emission of right ($\sigma-$) or left ($\sigma+$) circularly polarized light along the surface normal as given by well known selection rules.

The quantum selection rules which govern radiative recombination in cubic semiconductors in the Faraday geometry are illustrated in Fig. 3.3 [3.29, 48]. They permit a simple analysis of the electroluminescence data which provides a quantitative measure of the spin polarization of the carriers involved. In bulk zincblende semiconductors such as GaAs, the conduction band (CB) is two-fold degenerate at the center of the Brillouin zone, corresponding to spin-up and spin-down electrons ($m_j = \pm 1/2$). In the semiconductor community, "spin-up" by convention means that the electron's spin is parallel to an applied magnetic field or the surface normal (note that the *opposite* convention is used in the magnetic metals community [3.49, 50]), and the sign of the g-factor determines whether that state is at higher or lower energy in an applied magnetic field. The valence band (VB) is four-fold degenerate (Fig. 3.3a), and consists of heavy hole (*HH*) and light hole (*LH*) bands with large and small effective mass, respectively, which are each two-fold spin degenerate ($m_j = \pm 3/2$, $\pm 1/2$). Radiative electron-hole recombination is allowed for interband transitions which obey the selection rule $\Delta m_j = \pm 1$. The probability of a given transition is weighted by the matrix element connecting the levels involved, so that transitions to *HH* states are 3 times more likely than those to *LH* states, as indicated in the figure.

The net circular polarization P_{circ} of the light emitted can readily be calculated for a given occupation of the carrier states. Assuming a spin-polarized electron population and an unpolarized degenerate hole population (i.e. all of the hole states are at the same energy and thus have the same probability of being occupied), a general expression for the degree of circular polarization in the Faraday geometry follows directly from Fig. 3.3a – P_{circ} can be written in terms of the relative populations of the electron spin states $n\uparrow$ ($m_j = +1/2$) and $n\downarrow$ ($m_j = -1/2$), where $0 \leq n \leq 1$,

and $n\uparrow + n\downarrow = 1$:

$$\begin{aligned} P_{\text{circ}} &= [\mathrm{I}(\sigma+) - \mathrm{I}(\sigma-)] \,/\, [\mathrm{I}(\sigma+) + \mathrm{I}(\sigma-)] \\ &= 0.5\,(n\downarrow - n\uparrow) \,/\, (n\downarrow + n\uparrow) \\ &= 0.5 P_{\text{spin}}\ . \end{aligned} \tag{3.1}$$

The optical polarization is directly related to the electron spin polarization $P_{\text{spin}} = (n\downarrow - n\uparrow)/(n\downarrow + n\uparrow)$, and has a maximum value of 0.5 due to the bulk degeneracy of the *HH* and *LH* bands.

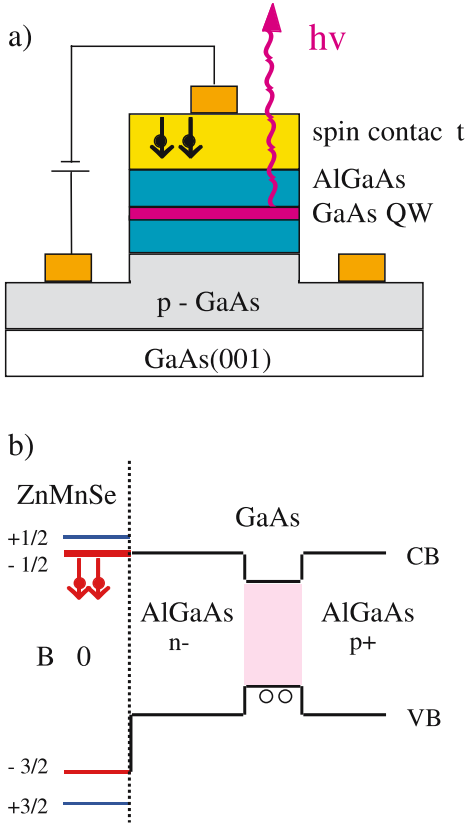

Fig. 3.2. (**a**) Schematic cross section of a spin-LED for electron injection based on an AlGaAs/GaAs quantum well (QW). A spin contact injects spin-polarized electrons into the GaAs QW where they radiatively recombine with unpolarized holes from the substrate. The circular polarization of the light emitted along the surface normal may be analyzed using the quantum selection rules to determine the net spin polarization of the electrons in the QW. (**b**) Flat band diagram of the spin-LED in which a ZnMnSe contact is used. A magnetic field applied along the surface normal splits the ZnMnSe conduction band (CB) edge, forming a spin-polarized electron population which can be injected into the QW

In a quantum well (QW), however, the *HH* and *LH* bands are separated in energy by quantum confinement, which modifies (3.1) and significantly impacts the analysis. The *HH/LH* band splitting is typically several meV even in shallow quantum wells, and is much larger than the thermal energy at low temperature (~ 0.36 meV at 4.2 K), so that the *LH* states are at higher energy and are not occupied (Fig. 3.3b). For typical $Al_xGa_{1-x}As/GaAs$ quantum well structures with Al concentration $0.03 \leq x \leq 0.3$ and a 150 Å QW, a simple calculation yields a value of 3–10 meV for the *HH/LH* splitting [3.51]. In this case, only the *HH* levels participate in the radiative recombination process, as shown in Fig. 3.3b, and P_{circ} is calculated as before:

$$\begin{aligned} P_{\text{circ}} &= (n\downarrow - n\uparrow) \,/\, (n\downarrow + n\uparrow) \\ &= P_{\text{spin}} \,. \end{aligned} \tag{3.2}$$

In this case, P_{circ} is equal to the electron spin polarization in the well, and can be as high as 1.0.

The use of a quantum well offers several distinct advantages over a *p-n* junction in this approach. The QW provides a specific spatial location within the structure where the spin polarization is measured, and hence depth resolution. Varying the

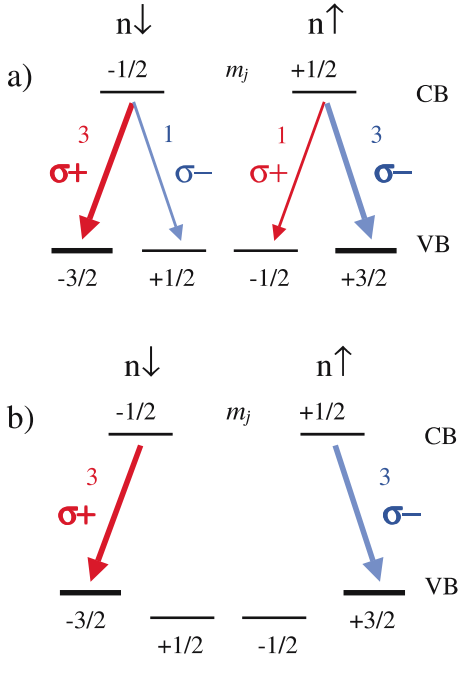

Fig. 3.3. Radiative interband transitions and corresponding optical polarizations allowed by the selection rules $\Delta m_j = \pm 1$ (Faraday geometry) for the cases of (**a**) bulk material in which the hole bands are degenerate, and (**b**) a quantum well in which the reduced symmetry lifts the degeneracy, so that the heavy hole states ($m_j = \pm 3/2$) are at lower energy than the light hole states ($m_j = \pm 1/2$), as is the case for an AlGaAs/GaAs QW

distance of the QW from the injecting interface may then provide a measure of spin transport lengths. This feature was utilized by Hagele et al. to obtain a lower bound of 4 μm for spin diffusion lengths in optically pumped GaAs at 10 K [3.30]. In addition, the light emitted from the QW has an energy characteristic of the QW structure, and may therefore be easily distinguished from spectroscopic features arising from other areas of the structure or impurity related emission. Since the quantum selection rules apply only to the free exciton or free carrier recombination features, it is critical to spectroscopically resolve and unambiguously identify these features using standard spectroscopic techniques [3.52]. Further details on the behavior of various components which might appear in an electroluminescence spectrum and their impact on quantifying electrical spin injection may be found elsewhere [3.52].

Thus standard polarization analysis of the electroluminescence (EL) effectively interrogates the spin polarization of the carriers involved. The existence of circularly polarized EL demonstrates successful electrical spin injection, and an analysis of the circular polarization using these fundamental selection rules provides a quantitative assessment of carrier spin polarization in the QW without resorting to a specific model.

3.3 Spin Injection from Semimagnetic Semiconductors

The relatively small effects measured with transport techniques and attributed to spin injection for ferromagnetic metals in intimate contact with a semiconductor, and the potential complications of interpretation discussed earlier, lead some groups to investigate all-semiconductor heterostructures. This avoided the poorly understood issues of spin transport across an interface between such dissimilar materials (metal *vs* semiconductor), and enabled design of the spin-injecting interface based on the familiar principles of band gap engineering between materials of similar structure and properties.

Semimagnetic (or diluted magnetic) semiconductors are well-studied materials [3.53, 54], and offer a convenient source of spin-polarized carriers, albeit at relatively low temperatures and high applied magnetic fields (> 1 T). Typical examples include the II-VI compounds $Zn_{1-x}Mn_xSe$ and $Cd_{1-y}Mn_yTe$. These materials are Brillouin paramagnets, and are especially noted for the very large band edge spin splitting they exhibit in an applied magnetic field (giant Zeeman effect). For modest fields, the spin splitting significantly exceeds k_BT at low temperature. For example, the splitting of the spin-up ($m_j = +1/2$) and spin-down ($m_j = -1/2$) electron states in $Zn_{0.94}Mn_{0.06}Se$ is ~ 10 meV at 3 Tesla and 4.2 K, so that the conduction band effectively forms a completely polarized source of spin-down electrons. This same effect has been used in the past to create a static spin superlattice, in which carriers of opposite spin occupy alternating layers of a multilayer structure [3.55, 56].

Oestreich et al. initially proposed the use of a semimagnetic semiconductor as the spin injecting contact which would serve to align the spins of the electrons on a picosecond time scale in an applied magnetic field [3.57]. They used time-resolved photoluminescence to demonstrate that *optically* excited carriers became spin aligned

in a $Cd_{1-x}Mn_xTe$ layer, and that spin polarized electrons were transferred into an adjacent CdTe layer with little loss in spin polarization.

The first demonstrations of *electrical* spin injection from a semimagnetic semiconductor contact were reported by Fiederling et al. [3.13] and Jonker et al. [3.15] using very similar LED structures and either a BeMgZnSe/$Be_{0.07}Mn_{0.03}Zn_{0.9}Se$ composite contact or a simpler $Zn_{0.94}Mn_{0.06}Se$ contact, respectively. In each case, the raw EL data exhibited a circular polarization of $\sim 50\%$, providing striking evidence for injection of spin polarized electrons from the contact and into the QW. Some considerations of device design, and details of fabrication, operation and data analysis of Jonker et al. [3.15] follow.

The $Al_xGa_{1-x}As$/GaAs system is one of the most well-studied III-V heterostructures. The existing growth and doping technology, type I band alignment and known band offsets offer a versatile system for device design, and the close lattice match to ZnSe makes it a natural choice for the QW LED spin detector. A closely related system, GaAs/$In_xGa_{1-x}As$, shares many of these attributes, and the lower bandgap of $In_xGa_{1-x}As$ enables transmission of the QW emission through a GaAs substrate for analysis. However, the addition of In is likely to result in stronger spin-orbit effects and shorter spin lifetimes in the QW. In addition, the larger g-factor of $In_xGa_{1-x}As$ leads to larger magnetic field dependent background effects, all of which complicate interpretation of the data [3.58].

$Zn_{1-x}Mn_xSe$ is attractive as a contact material for a number of reasons. It can readily be doped *n*-type, [3.59, 60] allowing one to focus on *electron* transport, which is the basis for modern high frequency device technology. This *n*-type doping and the giant Zeeman splitting described above provide an essentially 100% spin-polarized electron population, a highly desirable feature for the injecting contact. While ferromagnetic semiconductors such as $Ga_{1-x}Mn_xAs$ potentially provide a source of spin-polarized *holes* [3.61], the higher hole mass and exceedingly short spin lifetimes due to strong spin-orbit coupling are serious drawbacks for device operation [3.62]. Both ZnSe and GaAs are zincblende with a lattice mismatch of only 0.25%, and a great deal of epitaxial growth effort has been devoted to perfecting the structure of this heterointerface due to the interest in ZnSe-based blue-green lasers [3.63]. The lattice mismatch and conduction band offset at the $Zn_{1-x}Mn_xSe/Al_yGa_{1-y}As$ interface may be controlled by selecting appropriate Al and Mn concentrations.

The samples studied were grown on semi-insulating GaAs(001) substrates by molecular beam epitaxy (MBE) in a multichamber system. The III-V layers were grown under standard As-rich conditions at a substrate temperature and growth rate of 585 °C and 1 µm/hr, respectively. The growth sequence (see Fig. 3.2b) consisted of a 1 µm *p*-type GaAs buffer layer, a 2000 Å *p*-doped AlGaAs barrier, an undoped 150 Å GaAs quantum well, and an *n*(Si)-doped 500 Å AlGaAs barrier. Dopant setbacks of 250 Å were used on either side of the well, and $p(\mathrm{Be}) = 10^{18}\ \mathrm{cm}^{-3}$. A 2000 Å epilayer of *n*(Cl)-doped $Zn_{0.94}Mn_{0.06}Se$ was grown in a second attached MBE chamber at a rate of 0.25 µm/hr. This growth was initiated by exposing the (2×4)-As reconstructed surface of the AlGaAs to the Zn flux for 60 s at the growth temperature of 300 °C to minimize the formation of defects near the interface [3.63].

For these growth conditions, the ZnSe/GaAs conduction band (CB) offset is reported to be 100 meV, with the ZnSe band edge at higher energy [3.64]. The band gap of $Zn_{0.94}Mn_{0.06}Se$ is nearly equal to that of ZnSe (2.8 eV at 4.2 K) due to bandgap bowing, while that of AlGaAs increases with Al concentration. An Al concentration of 0.1 was chosen for the barrier to minimize the ZnMnSe/AlGaAs CB offset, which is calculated to be $\sim$ 10 meV, and the depth of the GaAs CB quantum well is $\sim$ 100 meV. The resultant lattice mismatch is 0.5%. A doping level of $n = 10^{17}$ cm^{-3} was used for both the AlGaAs and the ZnMnSe to minimize band bending. A simplified flat band diagram is shown in Fig. 3.2b. The use of multiple quantum wells and an asymmetric single quantum well (with an $Al_{0.3}Ga_{0.7}As$ barrier nearest the GaAs substrate) were also investigated to increase the probability that an electron injected from the ZnMnSe would be collected in the QW. A single asymmetric QW was found to provide the highest optical efficiency.

The samples were processed into surface-emitting LED mesas 200–400 μm in diameter using standard photolithographic techniques, and electrical contacts were made to the ZnMnSe and *p*-GaAs buffer layer via Ti/Au liftoff. Figure 3.4 shows a schematic cross-section and photograph of the final devices. Mesa isolation of the active QW region is not necessary if *p*-doped GaAs substrates and a backside contact are used. The top mesa metallization consists of concentric Au rings to help insure current distribution, leaving most of the mesa surface optically transparent.

The electroluminescence (EL) was measured by placing the LED samples in a magnetic cryostat with optical access along the field direction, and electrically biasing them to inject electrons from the ZnMnSe into the GaAs quantum well at current densities of ~ 0.01 A/cm^2. The light emitted along the surface normal and field direction (Faraday geometry) was analyzed for left ($\sigma+$) and right ($\sigma-$) circular polarization and spectroscopically resolved using a quarter wave plate and fixed linear polarizer followed by a spectrometer.

Representative spectra of the light emitted from such a structure (in this case with a multiple quantum well LED ($3\times$(200 Å $Al_{0.08}Ga_{0.92}As$/100 Å GaAs)) are shown in Fig. 3.5a for selected values of the applied field. The spectra are displaced vertically to facilitate comparison. At zero field, no optical polarization is observed, as expected, since $Zn_{0.94}Mn_{0.06}Se$ is a Brillouin paramagnet which acquires a net magnetization only in a magnetic field. The emission peaks near 1.547 eV, attributed to recombination with heavy holes, confirming that radiative recombination occurs in the GaAs quantum well. Corresponding photoreflectance measurements confirm this feature to be the *HH* exciton, with the *LH* exciton appearing at $\sim$ 10 meV higher energy. The *LH* feature appears in the EL spectrum at higher temperatures as the *LH* levels are thermally populated. The polarization of the *HH* feature rapidly increases with applied field, saturating at a value of 83% (Fig. 3.5b) as the spin polarized electron population is created in the ZnMnSe and injected into the LED structure. The corresponding spectra reveal a significant difference in intensity between the $\sigma+$ and $\sigma-$ components of the EL even at 0.5 T. This large difference in intensity is the *signature of spin polarized carrier injection* into the quantum well, as the selection rules of Fig. 3.3b clearly show. Thus a simple inspection of the raw data confirm successful electrical spin injection.

Other effects which might contribute to the optical polarization were carefully considered and found to be inconsequential. For example, the Faraday rotation resulting from transmission through the ZnMnSe is negligible due to the very short path length (2000 Å), and because the GaAs emission wavelength is very far from that corresponding to the band gap of $Zn_{0.94}Mn_{0.06}Se$. Photoluminescence data from the GaAs quantum well excited with linearly polarized light from the same LED mesa structures used for the EL studies show little polarization, providing a very effective built-in reference for each mesa LED. Such dichroism effects could be much larger for emission energies very near the ZnMnSe band gap, and must be considered when designing the LED structure.

3.4 Spin Injection across an Air-Exposed Semiconductor Interface

The results described above [3.15] and in reference [3.13] utilized samples which were grown entirely under a carefully controlled ultra high vacuum (UHV) environment to insure a pristine interface between the spin contact and the semiconductor

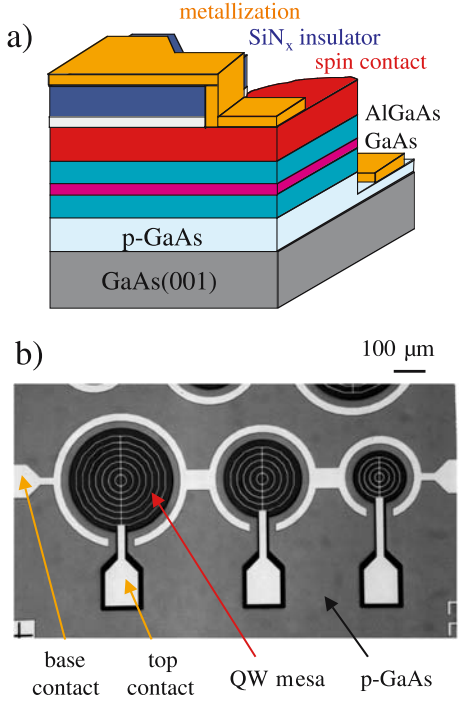

Fig. 3.4. (**a**) Schematic cross section of spin-LED illustrating the structure and processing steps. (**b**) Photograph of completed surface-emitting devices. The active mesa areas (dark circular regions) are 200, 300 and 400 µm in diameter

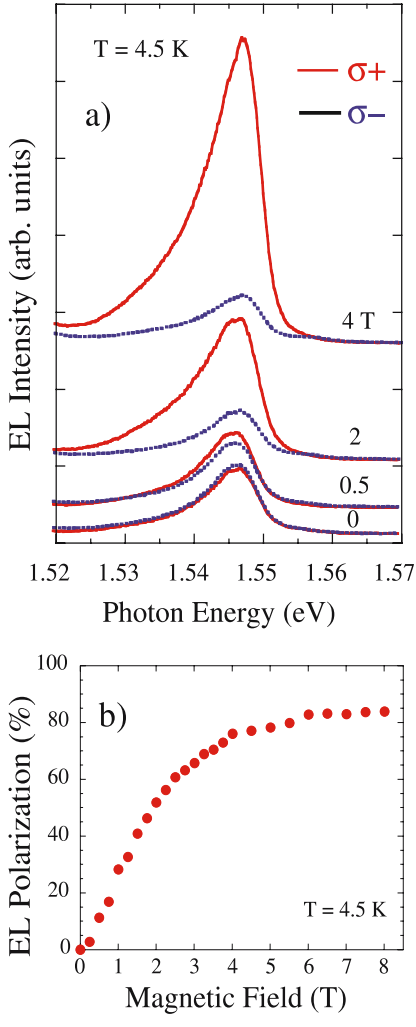

Fig. 3.5. (**a**) Electroluminescence (EL) spectra from a surface-emitting spin-LED with a $Zn_{0.94}Mn_{0.06}Se$ contact for selected values of applied magnetic field, analyzed for left ($\sigma+$) and right ($\sigma-$) circular polarization. The magnetic field is applied along the surface normal (Faraday geometry). The spectra are dominated by the heavy hole exciton. (**b**) Magnetic field dependence of the EL circular polarization

LED structure. This necessitated interconnected MBE machines, with the tacit assumption that an air-exposed interface would negatively impact spin injection. This assumption has indeed been confirmed for the growth of spin-dependent metal tunnel junctions [3.65]. As a first step towards assessing the effect of contamination or defects at the semiconductor spin-injecting interface, spin-LED structures were fabricated in which the surface of the top $Al_{0.1}Ga_{0.9}As$ barrier was exposed to air

for several months prior to the growth of the $Zn_{0.94}Mn_{0.06}Se$ spin injecting contact [3.66]. It was anticipated that this should represent a worst-case scenerio and test the robustness of electrical spin injection across a heterointerface.

The III-V single quantum well LED structure was grown as described above. At the end of the III-V layer growth, the surface exhibited a clear As-stabilized c(4×4) reflection high energy electron diffraction (RHEED) pattern. No arsenic passivation layer of any kind was deposited. After growth, the wafer was simply removed from the MBE system, exposed to atmosphere, and stored in a nitrogen-flow plexiglas storage box.

After storage of up to six months, a wafer was cleaved into quarters which were mounted on an indium-free holder. No surface preparation of any kind was performed before the sample was introduced into the II-VI MBE chamber. The sample was heated in UHV until the surface oxide was desorbed as indicated by the appearance of a RHEED pattern at approximately 585 °C (a procedure identical to that used for a conventional epi-ready substrate). A rather poor, spotty 1×1 RHEED pattern resulted which did not improve with further heating. A 2200 Å thick *n*-type (Cl, $n \sim 10^{17}$ cm^{-3}) epilayer of $Zn_{0.94}Mn_{0.06}Se$ was grown on this surface at a substrate temperature of 300 °C and growth rate of 0.25 µm/hr to serve as the spin injecting contact. The sample surface was first exposed to the Zn flux alone, following the growth procedure described in Sec. 3.3. After opening the Se and Mn shutters, the RHEED pattern immediately improved to a much sharper, streaky 1×1 pattern after two minutes of growth, and exhibited a faint 2×1 reconstruction characteristic of a Se-terminated surface as the growth progressed, as expected for these conditions.

Surface-emitting LED mesas were again fabricated, and arrays of LEDs were wire-bonded to chip carriers and placed in a magnetic cryostat with optical access along the field direction (Faraday geometry). A representative EL spectrum analyzed for left ($\sigma+$) and right ($\sigma-$) circularly polarized light is shown in Fig. 3.6 at an applied magnetic field of 4 T at 4.2 K. The spectrum is again dominated by the *HH* exciton feature – reflectance measurements confirm that the light hole excitons are shifted 6 meV to higher energy by quantum confinement, so that they are not occupied at the measurement temperature ($k_BT \sim 0.36$ meV) and do not participate in the EL process. The 5-fold difference in intensity between these two components corresponds to a circular polarization of 65%. This direct spectroscopic signature of spin injection provides a quantitative measure of the electron spin polarization in the GaAs QW of 65% based only on the fundamental selection rule analysis of (3.2) and Fig. 3.3b.

Thus efficient spin transport occurs even across the air-exposed $Al_{0.1}Ga_{0.9}As$ interface with the epitaxially regrown $Zn_{0.94}Mn_{0.06}Se$ spin-injecting contact. These results attest to the robustness of the spin injection process in the diffusive transport regime. Since all existing device structures operate in this regime, it is clear that the use of carrier spin as a parameter complementary to charge is a viable avenue towards new functionality and performance. These results further attest to the practicality of manufacturing semiconductor-based spintronic devices – a basic device structure can be obtained from a commercial epi-wafer vendor, and magnetic semiconductor layers deposited at a second location for research or device fabrication purposes.

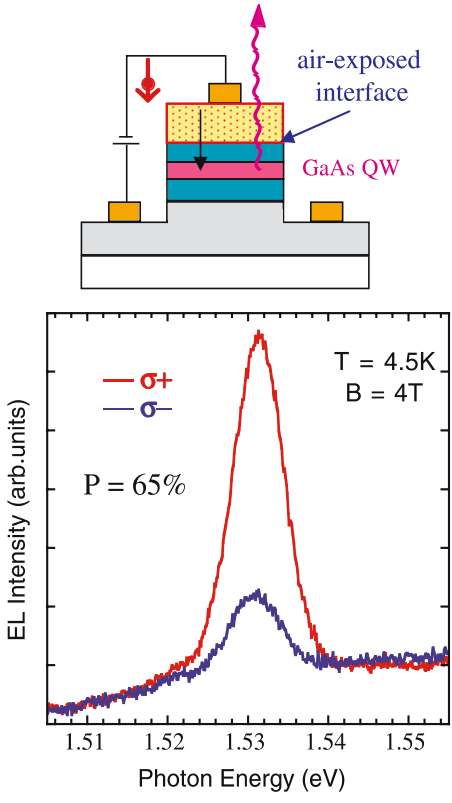

Fig. 3.6. Electroluminescence (EL) spectrum as in Fig. 3.5 at H = 4T from a surface-emitting spin-LED. The $Zn_{0.94}Mn_{0.06}Se$ contact was regrown on the AlGaAs/GaAs QW LED structure *after* prolonged exposure of the top AlGaAs layer to atmosphere and storage for six months in a nitrogen-flow drybox. The spin-polarized electrons are successfully injected from the ZnMnSe across the air exposed interface, resulting in an electron spin polarization in the GaAs QW of 65%

3.5 Role of Interface Structure in Spin Injection

The use of the spin-LED in demonstrating electrical spin injection and quantifying the resulting electron spin polarization achieved in the semiconductor heterostructure provides a large and unambiguous signature of spin injection. The difference in intensity between the $\sigma+$ and $\sigma-$ *HH* exciton components observed in EL can be over an order of magnitude, in contrast to the 0.1–1 % signals attributed to spin injection in pure transport experiments [3.35, 42–44]. This large measurable parameter enables one to systematically examine the role of more subtle contributions which play a role in the spin injection process.

In the ZnMnSe/AlGaAs/GaAs LEDs, spin polarized electrons from the ZnMnSe are injected across the II-VI / III-V heterointerface, diffuse through the $Al_{0.1}Ga_{0.9}As$

"drift" region, and are captured in the GaAs QW where they radiatively recombine with an unpolarized hole population from the p-GaAs buffer. Little spin relaxation is expected to occur in the 500 Å thick $Al_{0.1}Ga_{0.9}As$ drift region based on the strong experimental evidence for spin diffusion lengths of many microns (in GaAs) [3.30, 31] Similarly, little spin relaxation is expected to occur as the injected electrons thermalize to the lowest confined state in the GaAs QW – photoluminescence measurements have shown that the circular polarization of the emitted light shows little dependence on the energy of the circularly polarized pump beam until the pump energy is high enough to excite the spin-orbit split off band over 300 meV above the fundamental gap [3.67]. This energy is significantly higher than the energy of the electrons injected from the ZnMnSe relative to the GaAs QW ground state. Therefore, it is likely that some parameter of the heterointerface is a limiting factor, and it is natural to ask what role the interface itself or related defects play as potential sources of spin scattering.

Transmission electron microscopy (TEM) was used to examine the microstructure of a number of ZnMnSe / AlGaAs / GaAs spin-LEDs in an effort to correlate any defects observed with the spin polarization as measured from the electroluminescence [3.68]. Cross-sectional samples in $[1\bar{1}0]$ orientations for TEM studies were prepared by hand grinding and argon-ion milling. Bright-field / dark-field image pairs were collected in order to reveal the defect type and concentration, using a Philips CM30 300 kV TEM. High-resolution images of the interface microstructures were obtained using a Hitachi H9000 300 kV TEM.

The most prevalent defects observed were stacking faults (SFs) in ⟨111⟩ directions, nucleating at or near the ZnMnSe-AlGaAs interface. The SFs were easily observed in dark-field images ($g = (2\bar{2}0)$) as diagonal lines extending from the heterointerface to the ZnMnSe film surface (Fig. 3.7a). The number density of these SFs was determined from a series of dark field images by counting the SFs per unit length along the [110] direction. An equivalent number of such defects lie in the perpendicular direction, but are not visible in this cross section. These SFs are a well-known problem in ZnSe/GaAs epitaxy [3.69, 70], and are attributed to both lattice strain [3.71] and the formation of Se dimers at the interface [3.72]. No secondary phases, Mn clusters, or defects in the AlGaAs-GaAs LEDs were found. Away from the immediate vicinity of a SF, high-resolution lattice images (Fig. 3.7b) reveal a structurally well-ordered interface.

The electron spin polarization in the GaAs QW of the ZnMnSe/AlGaAs-GaAs spin-LEDs correlates inversely with the observed SF density, as shown in Fig. 3.8, demonstrating a link between the spin injection efficiency and interface microstructure. It is remarkable to note that polarized injection efficiencies as high as 85% can be realized across the II-VI/III-V heterointerface despite moderately high (10^4–$10^5\,cm^{-1}$) SF densities, attesting to the robust nature of the spin injection process. Complete suppression of the spin polarized injection was only achieved for a sample (not included here) in which the AlGaAs surface was exposed to air and then chemically treated using an ammonium sulfide surface passivation procedure prior to the growth of the ZnMnSe. This resulted in a very rough interface in addition to the highest SF density.

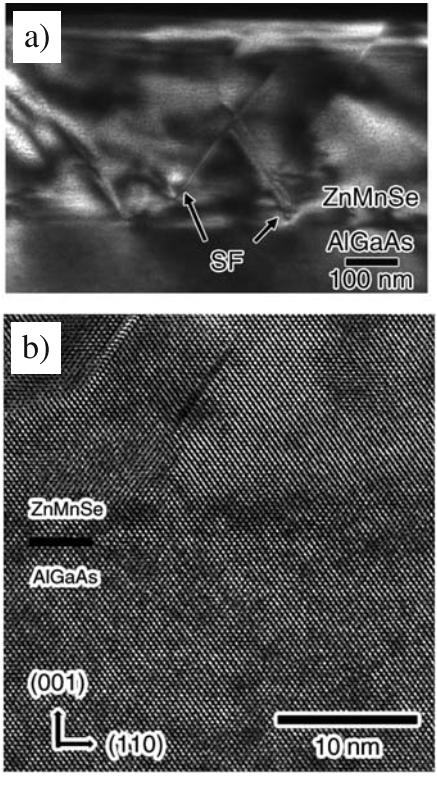

Fig. 3.7. (**a**) Dark-field cross-sectional transmission electron micrograph of a ZnMnSe spin-LED. Stacking faults in ⟨111⟩ directions are observed to nucleate at the ZnMnSe/AlGaAs interface. This sample had a stacking fault concentration of 9×10^4 cm^{-1} and an electron spin polarization of 49% in the GaAs QW. (**b**) High-resolution lattice image of a ZnMnSe/AlGaAs/GaAs spin-LED. The ZnMnSe/AlGaAs interface (*black line*) is structurally well-ordered in areas between the interface-nucleated stacking faults

To theoretically analyze the relationship between spin polarization and defects, a model of the scattering properties of defects with non-spherical symmetry was adapted that includes spin-orbit interactions [3.68]. As an extended planar defect, a SF may cause spin-flip scattering anywhere within the ZnMnSe layer. However, Oestreich et al. [3.57] have noted that in a semimagnetic semiconductor, the minority spin lifetime is exceedingly short ($\sim$ 1 ps) on the time scale of diffusive transport when the conduction band edge is split by a sufficiently large magnetic field. If a spin-flip scattering event occurs far above the ZnMnSe/AlGaAs interface, the minority carrier spin quickly relaxes to the majority spin channel in the ZnMnSe before reaching the interface and being injected. If, however, the scattering event occurs at the interface, the spin-flipped carrier may cross the interface into the AlGaAs, where both spin states are equally favored. These carriers then diffuse to the GaAs QW where the net spin polarization is determined via the resultant EL. Therefore, the

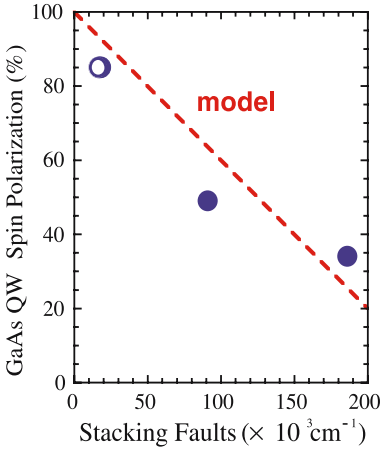

Fig. 3.8. Correlation of electron spin polarization in the GaAs QW (resulting from spin injection) with the stacking fault density. Two data points nearly overlap at 85% spin polarization. The dashed line is the result calculated from the model (3.7) and uses no adjustable parameters

relevant spin scattering in the spin-LED occurs at the interface, and we need only consider scattering from the line defect associated with the intersection of each SF plane with the interface plane (Fig. 3.9). These line defects lie in the interface plane and extend along the [110] and [1$\bar{1}$0] directions, referred to as the defect axes. The density of such line defects is simply equal to twice the SF density observed in the [1$\bar{1}$0] cross section as defined above (expressed in units of cm^{-1}).

The spin-orbit Hamiltonian associated with the potential of a lattice defect can be written from Kane's model [3.74, 75]:

$$H_{SO} = \frac{\hbar\Delta}{3mE_g^2}\boldsymbol{\sigma}\left[\nabla U(\boldsymbol{r}) \times \boldsymbol{p}\right], \tag{3.3}$$

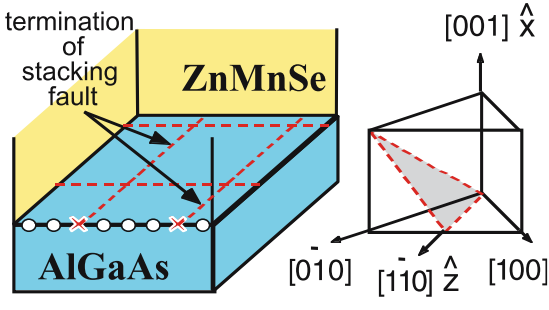

Fig. 3.9. Diagrams illustrating the linear interface defects resulting from the intercept of (111)-type stacking fault (SF) planes and the ZnMnSe/AlGaAs interface plane. Only one of the four possible (111)-type SF planes is shown in (*the diagram on the right*) for clarity. Both orientations of the interface line defects are shown in (*the diagram on the left*)

where Δ is the spin-orbit splitting in the valence band, E_g is the band gap, m is the effective mass, $\frac{\hbar}{2}\boldsymbol{\sigma}$ is the spin operator, $\boldsymbol{p}$ is the momentum operator, and $U(\boldsymbol{r})$ is the potential of the defect. The Hamiltonian (3.3) is responsible for the Elliot-Yafet spin-scattering mechanism in bulk III-V or II-VI semiconductors [3.74].

The potential for the line defect associated with the intersection of the stacking fault with the interface plane described above, can be written [3.76–78]:

$$U(\boldsymbol{r}) = (A/\rho) f(\rho) \sin\varphi, \tag{3.4}$$

where the conventional polar coordinate system is used with the x, y and z axes chosen along the [001], [$1\bar{1}0$], and [$1\bar{1}0$] directions, respectively (see Figs. 3.9 and 3.10). This potential describes a line dipole with the defect axis along [$1\bar{1}0$] and the dipole moment parallel to the [110] axis. The distance from a probe point to the axis of the linear defect is ρ, φ is the azimuthal angle, $f(\rho)$ is a Thomas-Fermi screening function such that $f(0) = 1$ and $f(\infty) = 0$, and A is a constant combining several material parameters such as deformation potential, dielectric constant, and the Poisson ratio [3.76–78]. Plane-wave matrix elements of $U$and H_{SO} determine the scattering matrix, which can be written in the Born approximation as follows:

$$\begin{aligned} S(\boldsymbol{k},\boldsymbol{k}') &= i(\langle \boldsymbol{k}|U|\boldsymbol{k}'\rangle + \langle \boldsymbol{k}|H_{SO}|\boldsymbol{k}'\rangle) \\ &\equiv g(\boldsymbol{k},\boldsymbol{k}') + ih(\boldsymbol{k},\boldsymbol{k}')\boldsymbol{\sigma}\cdot\hat{n}(\boldsymbol{k},\boldsymbol{k}'). \end{aligned} \tag{3.5}$$

Here $g(\boldsymbol{k},\boldsymbol{k}')$ and $h(\boldsymbol{k},\boldsymbol{k}')$ are the regular (non-spin-flip) and spin-flip scattering amplitudes, respectively [3.79, 80], and $\hat{n}(\boldsymbol{k},\boldsymbol{k}')$ is a unit pseudovector depending on the mutual orientation of the incident wave vector $\boldsymbol{k}$, scattered wave vector $\boldsymbol{k}'$, and the defect axis z. In the case $\boldsymbol{k}\perp z$, $\hat{n}(\boldsymbol{k},k')$ is normal to the scattering plane formed by $\boldsymbol{k}$ and $\boldsymbol{k}'$.

For spherical defects, the amplitudes $g(\boldsymbol{k},\boldsymbol{k}')$ and $h(\boldsymbol{k},\boldsymbol{k}')$ have similar angular dependencies. As a result, the regular scattering amplitude always exceeds the spin-flip amplitude due to the weakness of the spin-orbit coupling. For a *non-spherical* defect such as the line dipole considered here, however, these quantities have different angular dependencies, and the amplitude for spin-flip scattering can be comparable to or exceed the regular scattering amplitude.

The spin polarization can be calculated straightforwardly from the scattering matrix following Merzbacher, [3.79] and Landau and Lifschitz [3.80]. We are primarily concerned with electrons moving towards the GaAs quantum well ($\boldsymbol{k}$|| [$00\bar{1}$]) and having a large longitudinal component of the initial spin polarization $\boldsymbol{P}_0(\boldsymbol{k})$|| $\boldsymbol{k}$. This corresponds to the experimental conditions for spin injection across the interface with an out-of-plane applied magnetic field. Calculating the final spin polarization $\boldsymbol{P}(\boldsymbol{k}')$ of the electron scattered in the direction of $\boldsymbol{k}'$, we introduce the function

$$\begin{aligned} \pi(\boldsymbol{k},\boldsymbol{k}') &= \frac{1}{2} + \frac{\boldsymbol{k}\boldsymbol{P}(\boldsymbol{k}')}{2\boldsymbol{k}\boldsymbol{P}_0(\boldsymbol{k})} \\ &= \frac{1}{2} + \frac{\left|g(\boldsymbol{k},\boldsymbol{k}')\right|^2 - \left|h(\boldsymbol{k},\boldsymbol{k}')\right|^2 + 2\left|h(\boldsymbol{k},\boldsymbol{k}')\right|^2 \boldsymbol{k}\cdot\hat{n}(\boldsymbol{k},\boldsymbol{k}')/k}{2\left(|g(\boldsymbol{k},\boldsymbol{k}')|^2 + |h(\boldsymbol{k},\boldsymbol{k}')|^2\right)}, \end{aligned} \tag{3.6}$$

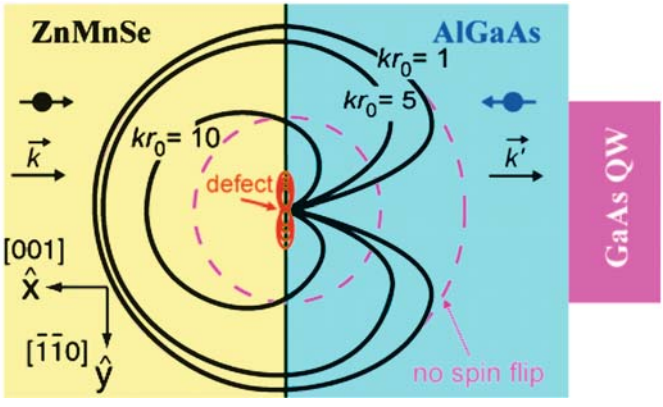

Fig. 3.10. Angular distributions of the electron spin polarization about the axis of the linear interface defect (the [110] direction) for different values of electron energy kr_0 following scattering from the defect. The outer dashed circle corresponds to 100% spin polarization (no spin-flip), the origin corresponds to the opposite spin polarization (all spin-flip), and the inner circle divides the regions of negative and positive polarizations. The dipole moment is oriented along the [110] direction in the interface plane. Spin-flip scattering dominates for all electrons scattered in the forward direction towards the GaAs quantum well, where they are detected

describing the angular distribution of the spin polarization. This function is a natural measure of the probability of spin-flip processes. Its value lies between 0 (all spin-flip) and 1 (no spin-flip), with $\pi(\boldsymbol{k}, \boldsymbol{k}') = 0.5$ corresponding to zero net spin polarization. When $\pi(\boldsymbol{k}, \boldsymbol{k}')$ is close to zero the spin-flip processes dominate and result in significant degradation of the spin polarization.

The angular distribution of the spin polarization $\pi(\boldsymbol{k}, \boldsymbol{k}')$ about the defect axis is presented in Fig. 3.10 (solid lines) for electrons incident normal to the interface, and for different values of the electron energy expressed as the dimensionless parameter kr_0 ($kr_0 \sim 1$ corresponds to electrons at the Fermi level). The Thomas-Fermi screening distance r_0 is approximately 100 Å for the carrier densities considered experimentally (10^{16}–$10^{17}\,\mathrm{cm}^{-3}$). The outer dashed circle corresponds to 100 % spin polarization (*no* spin-flip scattering), while the origin corresponds to *all* spin-flip scattering (opposite polarization). The inner dashed circle indicates zero spin polarization, where one half of the carriers have flipped their spin due to interaction with the defect potential.

The most striking characteristic of the plot is that spin-flip scattering dominates for forward scattering for all electron energies – interaction with the defect potential has a very high probability for spin-flip, and results in a significant reduction of the spin polarization when averaged over all the interface sites. Thus the longitudinal component of the spin polarization of the electrons scattered forward at small angles (towards the GaAs quantum well) will be significantly reduced as a result of such scattering. While spin-orbit scattering is normally a small effect, it is strongly enhanced due to the non-spherical character of the defect potential. A spherically symmetric defect would not produce such a dramatic increase in spin-flip scattering.

Figure 3.10 also clearly shows that the effects of spin depolarization become dominant for hot electrons with $kr_0 \gg 1$ for all directions. Qualitatively similar results are obtained for other orientations of the dipole moment. This angular distribution and energy dependence are clearly important factors to consider when attempting to measure spin polarization in any given structure.

The theoretical conclusion that spin-flip scattering completely dominates in the forward scattering direction enables a particularly simple prediction of the net electron spin polarization in the GaAs quantum well, P_{spin} , in the single scattering limit for direct comparison with experiment. Since the preceding analysis has shown that forward scattering is clearly accompanied by spin flip (Fig. 3.10), we adopt a 100% spin flip for any electron interacting with such a defect. The spatial extent of the defect potential is approximated by the Thomas-Fermi screening radius, r_0 , which depends upon the electron density, and is $r_0 \approx 100$ Å for the electron densities of the ZnMnSe and AlGaAs layers in the spin-LEDs studied ($10^{16}-10^{17}\text{cm}^{-3}$). Thus, all electrons crossing the interface within r_0 on either side of the defect will be spin-flipped. The spin polarization of the incident current (assumed to be 100% polarized) is reduced by a factor proportional to the measured defect density m, and P_{spin} is given by

$$P_{\text{spin}} \approx 1 - (2r_0)2m \tag{3.7}$$

where the factor of $2m$ accounts for the contribution of the line defects along both [110] and [1$\bar{1}$0]. This calculated behavior is shown as the dashed line in Fig. 3.8, and shows remarkably good agreement with the experimental data in both slope and magnitude. Note that (3.7) contains *no* adjustable parameters $-r_0$ is known from the carrier density, and m is directly measured. These data provide the first direct evidence identifying a particular structural defect as a spin scattering site and correlating spin injection efficiency across a heteroepitaxial interface with the interface structure [3.68]. Because interface defects such as stacking faults are generic to heteroepitaxial systems, these results have implications for all spin transport heterostructures.

3.6 Ferromagnetic Metals as Spin Injecting Contacts

As shown in the preceding sections, semimagnetic semiconductors such as ZnMnSe provide excellent electrical spin injection into another semiconductor, producing electron populations with a spin polarization exceeding 80%. However, these materials are not ferromagnetic, and such large measurable effects are produced only at low temperature (< 10 K) and high magnetic field (> 1 T) due to their intrinsic Brillouin paramagnetic character. Ferromagnetic semiconductors such as GaMnAs appear very promising [3.81], but are typically p-type and generally exhibit Curie temperatures well below 300 K.

Ferromagnetic *metals* offer most of the properties desired for a practical spin injecting contact material: a source of electrons rather than holes, high Curie temperatures, low coercive fields, fast switching times, and a well developed materials

technology due to decades of research and development driven in large part by the recording industry. In addition, metallization is a standard process in any semiconductor device fabrication line, so that the use of a ferromagnetic metallization could easily be incorporated into existing processing schedules. However, the 0.1–1 % effects which have been measured and attributed to spin injection from a FM metal in intimate contact with a semiconductor have not been very encouraging [3.35, 42, 44].

Recent model calculations by several groups [3.82–84] provided some insight into the issues which effect spin transport at the metal / semiconductor interface. These authors extended the work of van Son et al. [3.85] and Valet and Fert [3.86] to calculate the spin polarization achieved in a semiconductor due to transport of spin polarized carriers from the ferromagnet. The results of Schmidt et al. [3.82] are shown in Fig. 3.11 for selected values of the ratio of the conductivity of the semiconductor and ferromagnet, σ_{sc} and σ_{fm}. In the diffusive transport regime, successful spin injection occurs only for two conditions: either the conductivities of the FM and SC are closely matched, or the FM is 100% polarized. If neither condition is satisfied, the spin polarization in the SC is expected to be very low ($< 1\%$). No FM metal has been realized at present which meets either of these two conditions, offering a possible explanation for the experimental results referenced above. Since all current electronic devices operate in the diffusive transport regime, these results appear to preclude FM metals as viable candidates for spin contacts in such devices. It is interesting to note that ZnMnSe satisfies both criteria at low temperature and high magnetic field.

While tunnel barriers have been commonly used in metal/insulator/metal spin transport structures [3.5, 6], Rashba first elucidated their potential for implementing

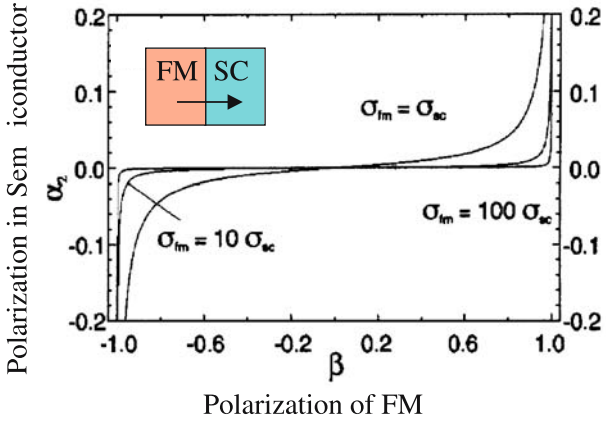

Fig. 3.11. The results of the model calculations of Schmidt et al. (reference [3.82]) showing the spin polarization of the current density (α_2) realized in the semiconductor as a function of the polarization of the ferromagnetic injecting contact for different ratios of the conductivities of the ferromagnet and semiconductor, σ_{fm} and σ_{sc}, respectively. Significant carrier spin polarization is realized in the semiconductor if the two conductivities are similar, or if the ferromaget is 100% polarized

spin injection from a FM metal into a semiconductor [3.87]. He pointed out that inserting a tunnel barrier between the metal and semiconductor provided a means of controlling the interface resistance and supporting a difference in electrochemical potentials between the spin-up and spin-down bands. This approach circumvents the issues revealed by Schmidt et al. [3.82]. This seemingly simple solution thus enables the use of common FM metals with robust magnetization, although accompanied by rather modest Fermi level spin polarizations of typically $\sim 50\%$.

Aluminum oxide is the canonical tunnel barrier material, and has been used successfully in spin-dependent tunnel junction structures such as Co / Al_2O_3 / NiFe [3.5–7]. However, for a metal contact on a semiconductor, the band bending accompanying Schottky barrier formation provides a very natural potential barrier [3.88], as shown in Fig. 3.12. In the case of an n-type semiconductor, electrons are transferred into the metal, depleting the semiconductor interfacial region and causing the CB to bend upwards, forming a pseudo-triangular shaped barrier with a quadratic falloff with distance into the semiconductor. For moderately doped semiconductors ($n \sim 10^{16}-10^{18}$), the depletion width is hundreds of angstroms [3.89]. However, this width can be readily controlled by an appropriate doping profile – heavily doping the surface of the semiconductor during MBE growth reduces the depletion width to tens of angstroms, so that tunneling from the metal into the semiconductor becomes a highly probable process under reverse bias.

Hanbicki et al. [3.90] utilized this approach and fabricated spin-LEDs designed to provide efficient tunnel barrier injection of spin-polarized electrons from epitaxial Fe film contacts into an AlGaAs/GaAs QW LED structure. The LED heterostructures were grown by MBE using interconnected growth chambers. A 100–125 Å thick Fe(001) film was grown with the substrate at 10–15 °C to minimize potential intermixing at the $Al_{0.08}Ga_{0.92}As$ interface. The doping profile of this top 800 Å thick n-type $Al_{0.08}Ga_{0.92}As$ layer included a heavily doped 150 Å surface layer ($n = 1 \cdot 10^{19}$ cm^{-3}, Si) so that the resulting Schottky contact had a narrow depletion width, thus forming a triangular shaped tunnel barrier, as shown in Fig. 3.12. The width of the undoped GaAs quantum well was chosen to be 100 Å to insure separation of the light and heavy hole levels and corresponding excitonic spectral features, an important consideration for quantitative interpretation of the data [3.52]. Dopant setbacks of 100–250 Å were

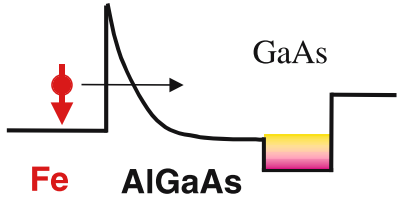

Fig. 3.12. Schematic diagram of the Schottky barrier which forms at the interface between the Fe contact and the AlGaAs layer (conduction band edge shown), and of the $Al_{0.08}Ga_{0.92}As/GaAs/Al_{0.3}Ga_{0.7}As$ QW detector. The n-type doping profile at the AlGaAs surface controls the width of the depletion region, enabling tunneling to occur through this triangular shaped potential under reverse bias

used on either side of the QW, as before. A higher Al concentration was used on the p-doped side (500 Å $Al_{0.3}Ga_{0.7}As$), forming a higher potential barrier (an asymmetric QW) to improve the capture of injected electrons into the GaAs quantum well.

The samples were processed to form surface emitting LEDs (Figs. 3.3 and 3.4), and the light emitted along the surface normal (Faraday geometry) analyzed for left ($\sigma+$) and right ($\sigma-$) circular polarization and spectroscopically resolved as a function of applied magnetic field and temperature, as described previously. Electroluminescence spectra obtained from the LED structures are shown in Fig. 3.13 at low temperature. The EL spectrum is dominated by a feature at 1.535 eV with a full width at half maximum of 17 meV, due to the heavy hole exciton in the GaAs QW. With no applied magnetic field, the Fe magnetization (easy axis) and corresponding electron spin orientation are entirely in the plane of the thin film. Therefore, the average electron spin along the z-axis is zero, and the $\sigma+$ and $\sigma-$ components are nearly coincident, as expected. The small difference observed corresponds to less than 2% polarization, and is treated as a background in subsequent data analysis (it is not uncommon to see a small apparent polarization of $\pm 1\%$ at zero field, an artifact attributed to subtracting the two spectra of nearly equal intensity). A magnetic field is

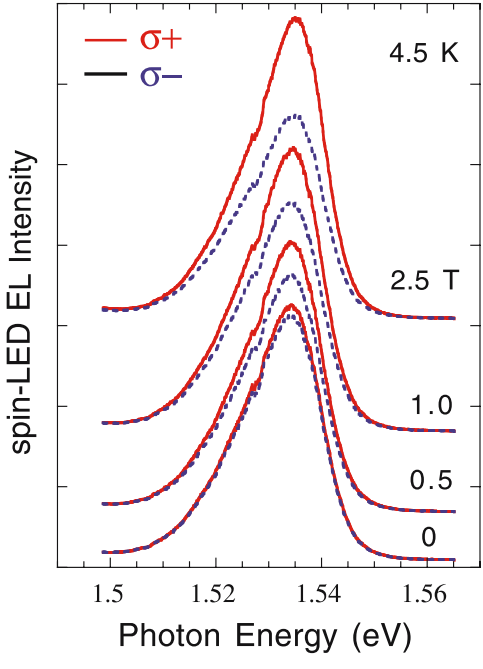

Fig. 3.13. Electroluminescence (EL) spectra at selected magnetic fields and T = 4.5 K, analyzed for $\sigma+$ and $\sigma-$ circular polarization. The magnetic field is oriented out of plane, i.e. along the sample surface normal. The large difference in intensity between these components indicates successful spin injection from the Fe and into the GaAs QW. The full width at half maximum is 17 meV. Typical operating parameters are 10 mA and 1.8 V

applied along the surface normal to align the electron spins in the Fe along the z-axis to satisfy the conditions for the quantum selection rule analysis. A simple inspection of the raw data reveals that carrier spin injection indeed occurs – as the magnetic field increases, the component of Fe magnetization and electron spin polarization along the z-axis continuously increase, and the corresponding spectra exhibit a substantial difference in intensity of the $\sigma+$ and $\sigma-$ components which rapidly increases with field.

The circular polarization data $P_{\rm circ}$ = [I(σ+) - I(σ-)] / [I($\sigma+$) + I($\sigma-$)] (where I($\sigma+$) and I($\sigma-$) are the EL component peak intensities when analyzed as $\sigma+$ and $\sigma-$, respectively – see (3.1)) for an identical Fe/AlGaAs/GaAs spin-LED are summarized in Fig. 3.14 as a function of magnetic field. $P_{\rm circ}$ rapidly increases in magnitude until the Fe moment is saturated out-of-plane. This occurs at a field value determined by the magnetic properties of Fe, $4\pi M$ = 2.2 T (indicated by the fiducial marks on the top axis in the figure), where M is the Fe magnetization. The polarization continues to increase at higher fields, but at a much slower rate of $\sim$ 1 %/T, which is attributed to a combination of Zeeman splitting in the GaAs and an instrumental background – this uniform linear background has been subtracted from the data of Fig. 3.14 and all subsequent data presented here.

Note that $P_{\rm circ}$ changes sign as the field direction is reversed – the field dependence of $P_{\rm circ}$ mirrors that of the out-of-plane magnetization of the Fe film, obtained by independent superconducting quantum interference device SQUID magnetometry measurements and shown as a dot-dashed line. The slight field asymmetry observed in the data is attributed to instrumental effects. $P_{\rm circ}$ saturates at a value of 16%, and the quantum selection rules again provide a quantitative and model-independent link between the measured $P_{\rm circ}$ and the spin polarization of the carriers which radiatively recombine in the QW, $P_{\rm spin}$, as described above (3.2). Thus electrical spin injection from the Fe contact produces a net electron spin polarization in the GaAs quantum well $P_{\rm spin}$ = 16%.

The sign of the optical polarization is the same as that observed for spin injection from a ZnMnSe contact (cf. Fig. 3.5, – the $\sigma+$ component is systematically larger than the $\sigma-$ component when the applied field and Fe magnetization are along the surface normal). This demonstrates that injection of $m_j = -1/2$ electrons dominates when the magnetic field is applied along the surface normal, as shown in Figs. 3.2 and 3.3 [3.91]. Using the nomenclature of the magnetic metals community [3.50], this corresponds to *majority* spin injection from the Fe Schottky contact, i.e. that the polarization of the injected current reflects majority electron spin in the Fe [3.92]. By convention in the magnetic metals community, the terms "majority spin" and "spin-up" (designated here as $n_{\rm m}\uparrow$) refer to electrons whose *moment* (rather than spin) is in the direction of the applied field or magnetization, and therefore have a lower energy than the "spin-down" or "minority spin" electrons ($n_{\rm m}\downarrow$) whose *moment* is antiparallel to the field [3.50]. Since the electron's spin and moment are antiparallel [3.93]. the spin of a "spin-up" or "majority spin" ($n_{\rm m}\uparrow$) electron is therefore antiparallel to the field or magnetization. The subscript "m" is used here to unambiguously indicate the convention used in this community.

As noted in Sect. 3.2, the opposite convention is used in the semiconductor community [3.49], where "spin-up" ($n_s\uparrow$) designates an electron whose *spin* is parallel to the field. Thus $n_m\uparrow = n_s\downarrow$ and (3.2) can be written

$$\begin{aligned} P_{\text{circ}} &= (n\downarrow - n\uparrow)/(n\downarrow + n\uparrow) \\ &= (n_s\downarrow - n_s\uparrow)/(n_s\downarrow + n_s\uparrow) \\ &= (n_m\uparrow - n_m\downarrow)/(n_m\uparrow + n_m\downarrow) \\ &= P_{\text{spin}} \, . \end{aligned} \tag{3.8}$$

This is consistent with the familiar definition of spin polarization in the magnetic metals community. The observation that the tunneling current is dominated by majority spin carriers is consistent with the model proposed by Stearns [3.94] and the tunneling experiments of Meservey and Tedrow [3.50].

A number of control experiments were performed to rule out spurious effects. LED structures fabricated with the Fe contact removed showed little circular polarization and very weak field dependence. Possible contributions to the measured P_{circ} arising

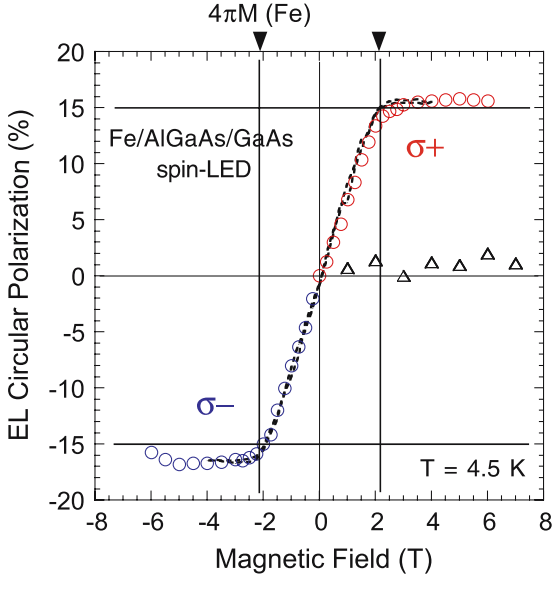

Fig. 3.14. The field dependence of P_{circ} (open circles) and the out-of-plane component of the Fe film magnetization obtained from SQUID magnetometry measurements (dot-dashed line, normalized to the maximum value of P_{circ}). The fiducial marks on the top axis indicate the value at which the Fe magnetization is saturated out of plane ($4\pi M = 2.2$ T). The sign of P_{circ} changes as the Fe magnetization is reversed, and reflects majority electron spin injection from the Fe contact. Positive (negative) field values correspond to the applied field and Fe magnetization parallel (antiparallel) to the sample surface normal. The triangles show the contribution to P_{circ} due to magnetic dichroism in the Fe film measured with photoluminescence under identical experimental conditions. This contribution is $\sim 1\% \pm 1\%$

from magnetic dichroism as the light emitted from the QW passes through the Fe film were determined both analytically and directly measured, and found to be less than 1%. This contribution was calculated to be 0.9% using well established models at the appropriate wavelength for the thickness of the Fe film [3.95]. This contribution was also directly measured for the samples included here by measuring the circular polarization of the GaAs QW photoluminescence excited by linearly polarized light and emitted along the surface normal (through the Fe film). Since linearly polarized optical excitation produces zero net carrier spin polarization in the GaAs QW, the emitted light is unpolarized, and any measured circular polarization is derived from Faraday rotation produced by the Fe film. These results are shown as open triangles in Fig. 3.14, and are $\sim 1\%$. Note that the effect measured due to electron spin injection is over an order of magnitude larger.

Zhu et al. have also utilized this approach to examine spin injection from Fe films grown epitaxially on a GaAs/InGaAs quantum well based structure [3.96]. Although they observe no large differences in electroluminescence intensity when analyzed as $\sigma+$ and $\sigma-$, by examining the wings of the Gaussian-like intensity distribution to distinguish the heavy hole exciton contribution, they concluded that an injected spin polarization of $\sim 2\%$ had been realized which was independent of temperature. The reasons for the smaller effect are not clear, although it may be due to a wider depletion region in the GaAs at the Fe interface due to a lower surface doping of the GaAs, resulting in a wider barrier and reduced probability for tunneling [3.97].

It is interesting to note that the EL linewidths reported to date from these Fe spin-LED structures are surprisingly broad – Zhu et al. [3.96] reported a full with at half maximum (FWHM) of 33 meV at zero field and low temperature, and Hanbicki et al. [3.90] reported a corresponding value of 17 meV, as noted above and seen in Fig. 3.13. In contrast, photoluminescence linewidths reported in the literature for similar (undoped) 100 Å wide AlGaAs/GaAs quantum wells are typically on the order of 1 meV. The source of the broadening is difficult to pinpoint, but is probably due to a combination of QW interface roughness, electric field and doping profile effects, and the energy distribution of the electrically injected carriers.

Very recent efforts to improve the GaAs QW and optimize the doping profile in the AlGaAs contact layer have resulted in much narrower EL linewidths, as shown in Fig. 3.15. The doping profile used here was as follows: the top 150 Å of the $Al_{0.1}Ga_{0.9}As$ was doped at $n = 1 \cdot 10^{19}\,cm^{-3}$ to minimize the depletion width. This was followed by a 150 Å transition region where the n-doping was increased from $1 \cdot 10^{16}\,cm^{-3}$ to $1 \cdot 10^{19}\,cm^{-3}$ during growth. The remaining 550 Å of the $Al_{0.1}Ga_{0.9}As$ layer was doped $n = 1 \cdot 10^{16}\,cm^{-3}$, with a 100 Å dopant setback at the GaAs QW. The data for an $Fe/Al_{0.1}Ga_{0.9}As/GaAs/Al_{0.3}Ga_{0.7}As$ spin-LED sample are similar to those of Fig. 3.13, but the surface-emitted EL spectra exhibit much narrower linewidths of ~ 5 meV and a significantly higher degree of circular polarization. The field dependence of the polarization is summarized in Fig. 3.16. P_{circ} tracks the out-of-plane magnetization of the Fe contact, as seen in Fig. 3.14, but now saturates at a much higher value of 32%. Thus electrical spin injection from a reverse-biased Fe Schottky contact results in an electron spin polarization in the GaAs quantum well of $P_{spin} = P_{circ} = 32\%$. It is noteworthy that such a high value is obtained for

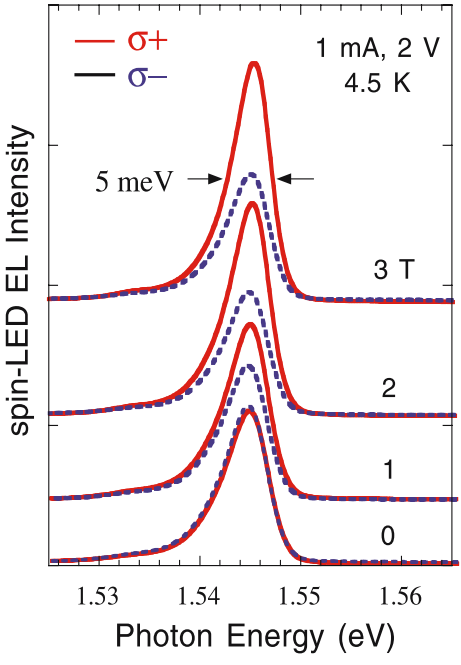

Fig. 3.15. EL spectra at selected magnetic fields and T = 4.5 K for an Fe/$Al_{0.1}Ga_{0.9}As$/GaAs/$Al_{0.3}Ga_{0.7}As$ spin-LED sample, analyzed for $\sigma+$ and $\sigma-$ circular polarization. The magnetic field is oriented out of plane. These data are similar to those of Fig. 3.13, but the surface-emitted EL spectra exhibit much narrower linewidths of $\sim$ 5 meV and a significantly higher degree of circular polarization. Typical operating parameters are 0.2–3 mA and 1.8–2.2 V

injection from a contact which has a Fermi level polarization of 44% [3.98]. Further improvements in the design and material quality are likely to lead to even higher QW polarizations.

The bias dependence of $P_{\text{circ}} = P_{\text{spin}}$ is shown in Fig. 3.17. P_{circ} initially increases very rapidly with current or bias voltage to a maximum value, and then decreases slightly by a few percent and retains a fairly uniform value. This pronounced dependence on injected current is observed for all spin-LED devices studied, and provides further convincing evidence that the circular polarization observed is due to electrical spin injection into the GaAs quantum well. The detailed dependence on bias voltage is not well understood at present and requires further investigation – one ideally would prefer to measure the bias across only the tunnel barrier to examine the transport process rather than across the entire device (which includes the $n - i - p$ LED structure), as presented here. A number of authors have reported intial results at more detailed modeling of such structures [3.99–102]

Successful spin injection suggests that tunneling is a significant contribution to the current flowing through the reverse biased Schottky barrier based on the model calculations discussed earlier [3.82, 83, 87]. However, other measurements are more

typically used to determine the dominant transport process. The Rowell criteria are commonly employed to confirm tunneling in a nominal tunnel structure [3.103]. Two of these criteria are very familiar: the conductance should exhibit an exponential dependence on the thickness of the tunnel barrier, and a parabolic dependence on the bias voltage. It has been argued, however, that neither can reliably distinguish tunneling from contributions due to pinholes or other spurious effects [3.104, 105]. Jonsson-Akerman et al. [3.104] have presented convincing evidence that the *third* Rowell criterion is a definitive confirmation of tunneling and can reliably be applied: the conductance should exhibit a weak insulating-like temperature dependence. This criterion has therefore been applied to the $Fe/Al_{0.08}Ga_{0.92}As$ Schottky barrier fabricated using the identical doping profile as for the spin-LEDs, but grown instead on an *n*-doped GaAs buffer layer rather than on the quantum well heterostructure. The results are shown in Fig. 3.18, where the zero-bias resistance exhibits a weak, linear decrease with increasing temperature. These data are very similar to those presented in reference [3.104], and provide convincing evidence that tunneling is the dominant transport process in the Fe Schottky barrier spin-LEDs of Figs. 3.13 – 3.17.

One of the primary advantages offered by FM metals over magnetic semiconductors is their high Curie temperature, a requirement for practical device applications. To assess the efficacy of spin injection from Fe at higher temperatures, the temperature dependence of the measured circular polarization, P_{circ}, is shown in Fig. 3.19a.

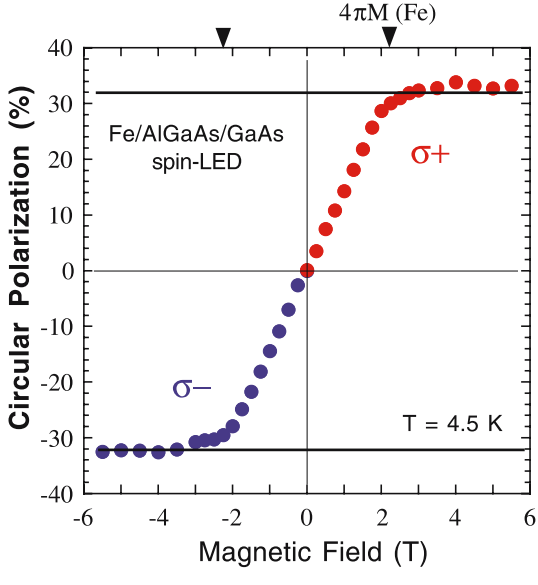

Fig. 3.16. The field dependence of the EL polarization and the spin polarization in the GaAs QW, $P_{circ} = P_{spin}$, for the data shown in Fig. 3.15. The polarization saturates at a value of $\sim$ 32%. The fiducial marks on the top axis indicate the field value 4πM(Fe) = 2.2 T. Positive (negative) field values correspond to the applied field and Fe magnetization parallel (antiparallel) to the sample surface normal

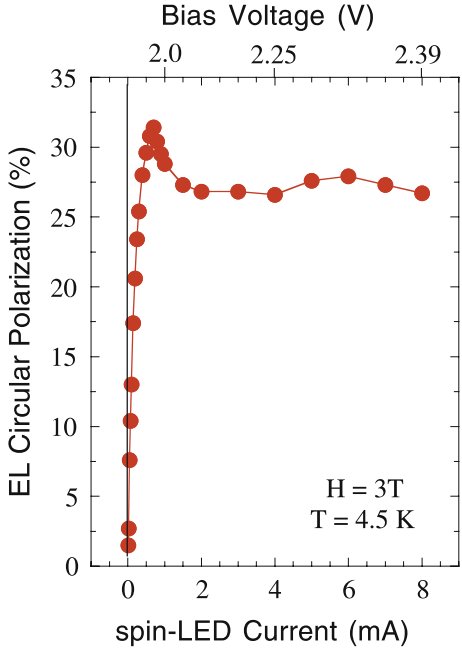

Fig. 3.17. The bias dependence of the EL polarization and the spin polarization in the GaAs QW, $P_{\mathrm{circ}} = P_{\mathrm{spin}}$ for the sample of Fig. 3.15. The bias voltage is measured across the entire device, which includes the $n-i-p$ AlGaAs/GaAs/AlGaAs LED heterostructure, and therefore includes the voltage necessary to bring this portion of the device into a flat-band condition

For this particular sample, $P_{\mathrm{circ}} = 13\%$ at 4.5 K and decreases with temperature. EL spectra obtained at 90 K and 240 K at a field of 3 T (Fe magnetization saturated normal to the surface) are shown as insets. They exhibit a significant difference in intensity between the $\sigma+$ and $\sigma-$ components, with polarizations of 8.5% at 90 K and 4% at 240 K, and corresponding linewidths of 20 and 25 meV, respectively.

It is important to recognize that there are two potential contributions to the observed temperature dependence: that of the spin injection process itself occurring at the Schottky barrier, and that of the GaAs QW detector (Fig. 3.19b). It is known that electron spin relaxation in the GaAs QW generally occurs more rapidly with increasing temperature, suppressing the measured circular polarization – the GaAs(001) QW is simply an imperfect detector, since it has a strong temperature response of its own. This effect is completely independent of the spin injection process, and must be corrected for to obtain values for the electron spin polarization before this effect occurs. These corrected values will then more accurately reflect the efficacy of the spin injection process itself at elevated temperature, as desired. Adachi et al. [3.106] report experimental values for the electron spin relaxation time, τ_{s} , for the full temperature range considered here. We use these values to provide a first order correction for the spin relaxation occurring in the QW by weighting our measured circular polarization at 90 and 240 K by the ratio of the corresponding value of τ_{s} to that at

low temperature. (Note that this procedure does *not* correct for the effect of QW spin relaxation at the lowest temperature studied, and therefore the experimental value P_{circ} =13% at 4.5 K is probably an underestimate and lower bound for P_{spin}). This yields values of 14% and 13% at 90 and 240 K, respectively, as shown by the square symbols in Fig. 3.19a. Thus the spin injection efficiency exhibits little temperature dependence. Since tunneling is known to be independent of temperature [3.103], these data provide further evidence that the spin injection is dominated by tunneling.

These results have demonstrated that electrical spin injection from the reverse biased Fe Schottky contact produces a net electron spin polarization in the GaAs quantum well P_{spin} = 32% for the best samples studied to date. Note that this represents a lower bound for the electron spin polarization – since the spin relaxation time in a GaAs(001) QW is typically less than the radiative lifetime, the spin polarization decays before radiative recombination occurs. This is significantly less than the carrier polarizations reported using ZnMnSe contacts, but persists to much higher temperatures due to the higher Curie temperature of Fe. Furthermore, it is achieved in a non-optimized structure for spin transport across an interface between dissimilar materials, and from a contact which is only 44% spin polarized [3.98]. Higher values of P_{spin} can be expected upon optimization of the doping profile and other device parameters. Several groups have recently modeled spin transport through a Schottky contact, and discuss the various parameters which effect the spin injection efficiency [3.97, 99–102] These results further demonstrate that spin injecting contacts can be formed using a very familiar and widely employed contact methodology, and provide a ready pathway for the integration of spin transport into semiconductor processing. This is a critically important and enabling contribution towards a semiconductor-based spintronics technology which will have broad appli-

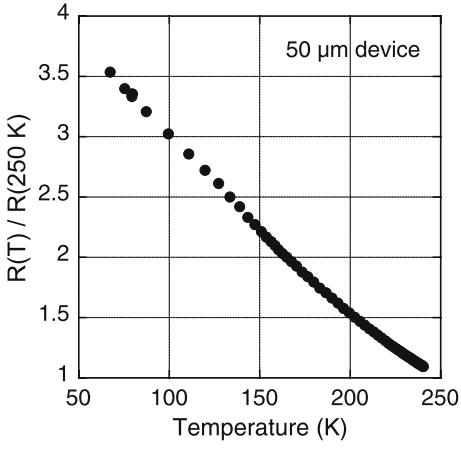

Fig. 3.18. Temperature dependence of the zero-bias resistance measured across the Fe/n+-AlGaAs Schottky interface (4-point measurement). The weak insulating-like temperature dependence satisfies the third Rowell criterion (as described in [3.104]), confirming that tunneling is the dominant process

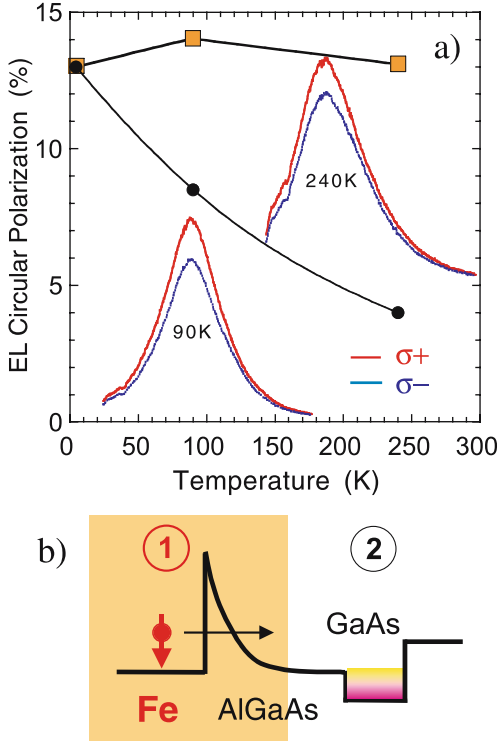

Fig. 3.19. (**a**) Temperature dependence of P_{circ} measured for an Fe/AlGaAs/GaAs spin-LED structure (same device as for Fig. 3.13). The insets show the EL spectra obtained at the temperatures indicated, analyzed for $\sigma+$ and $\sigma-$, at H = 3 T where the Fe magnetization is saturated out of plane. A significant difference in intensity is observed even near room temperature. The square symbols show the spin polarization achieved in the GaAs QW due to electrical injection from the Fe contact through the Schottky tunnel barrier after correction for the unrelated process of spin relaxation in the GaAs QW. (**b**) Conduction band diagram of the spin-LED illustrating two potential sources of the observed temperature dependence

cation and interest. Promising results have also been recently reported using a discrete Al_2O_3 tunnel barrier in an CoFe/Al_2O_3/AlGaAs/GaAs structure, where an injected spin polarization in excess of 9% at 80 K was determined using the oblique Hanle effect [3.107].

3.7 Characteristics of the Fe/AlGaAs(001) Interface

The Fe/GaAs epitaxial system has been very well-studied [3.108–112]. No effort will be made here to provide a comprehensive review. However, a few observations relevant to the spin injection achieved from the Fe Schottky tunnel barrier contact into the AlGaAs/GaAs LED will be presented.

The initial work on the epitaxy of Fe on GaAs addressed growth on GaAs(110) – the cleavage plane facilitates the preparation of a clean substrate surface [3.113], and each of the three principle crystallographic axes of bcc Fe lie in this plane, making it attractive to study the magnetic properties [3.114]. More recent work has focused on the GaAs(001) surface due to its technological relevance. In most cases, some outdiffusion of Ga, and outdiffusion and surface segregation of As have been reported.

One of the principal concerns of these studies has been the degree of interdiffusion at the interface and its impact on the magnetic and electronic properties, specifically the potential presence of "magnetic dead layers" or non-ferromagnetic Fe-alloy layers at the interface. While some groups have reported gross interdiffusion occurring over tens of monolayers, others have reported interfaces which are relatively abrupt, with interdiffusion limited to a monolayer or so. Differences in substrate surface preparation certainly contribute to these seemingly contradictory claims – GaAs surfaces prepared by sputter annealing, thermal desorption of the surface oxide, or MBE growth are likely to exhibit vastly different stoichiometry, defect structure, average roughness and step edge density, all of which are important parameters in chemical interaction and thin film growth. The substrate temperature during Fe film growth is another critical parameter, and work by Filipe and Schuhl [3.115] highlighted the potential sensitivity of interdiffusion to the measured substrate temperature – growth at substrate temperatures below 175 °C produced significantly more abrupt interfaces than at temperatures above 175 °C. This temperature was reported to result in the best RHEED and narrowest ferromagnetic resonance linewidths in the pioneering work of epitaxial Fe growth on GaAs(110) [3.114], and has been commonly adopted as the "standard" substrate temperature. Since the actual substrate temperature is likely to be different than the indicated temperature, it is easy to see that Fe films grown at an indicated 175 °C under nominally the same conditions in one laboratory may exhibit quite different degrees of interdiffusion than for similar samples grown in another laboratory.

A detailed study of the initial nucleation, interface formation and magnetic properties of Fe films grown on the As-dimer terminated GaAs(001) 2×4 and c(4×4) surfaces with 0.25 μm wide surface terraces was presented by Kneedler et al. [3.116–118] and Thibado et al [3.119] using in situ scanning tunneling microscopy (STM), x-ray photoelectron spectroscopy / diffraction (XPS/XPD), RHEED and the surface magneto-optic Kerr effect (MOKE). Subsequent work addressed Fe growth on the Ga-dimer terminated 4×6 surface [3.120]. These studies are particularly relevant to the Fe-based spin-LED heterostructures described above because the same MBE growth facilities and procedures were used in each case. The STM data demonstrated that the initial GaAs surface reconstruction profoundly effects the Fe adsorption and island nucleation, with initial adsorption occurring preferentially on the As-dimer sites. However, the general conclusion was that the interface which was ultimately formed after a few monolayers of Fe deposition was remarkably independent of the initial GaAs surface reconstruction. The interface is planar with little intermixing and characterized by Fe-As bonding (Fig. 3.20), with half of the Fe atoms in the first monolayer occupying Ga substitutional sites, while the remaining half monolayer of

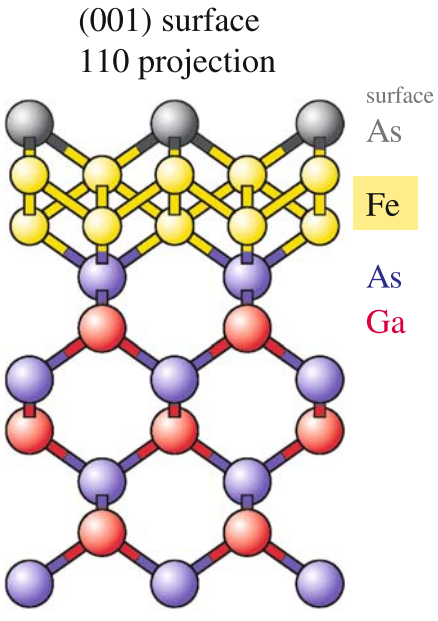

Fig. 3.20. A ball and stick model (from reference [3.123]) illustrating the bonding at the Fe/AlGaAs interface and surface segregation of As as described in [3.116–121]

Fe is accommodated in sites above the underlying Ga atoms to form a square surface net [3.116, 118, 119] rapidly transitioning the zincblende GaAs structure to that of bcc Fe [3.121]. Excess As diffuses through the Fe film and segregates to the surface, occupying both surface and bcc subsurface sites.[3.116, 118] Complementary studies further indicated that the electrical character of the Fe/GaAs interface was not dominated by As antisite defects.[3.121, 122] Although these studies were performed using a nominal substrate temperature of 175 °C, the abruptness of the final interface suggests that the "indicated 175 °C" was below the transition temperature for gross interdiffusion noted by Filipe and Schuhl [3.115]. It is then reasonable to assume that the interface realized for Fe film growth near room temperature (as for growth of the Fe contacts on the spin-LEDs described in the preceeding sections) should not be significantly more interdiffused.

A first principles study of the formation and structure of the Fe/GaAs interface was performed using density functional theory by Erwin et al.[3.123] They conclude that atomically abrupt interfaces are energetically favored for films several monolayers thick, and surface segregation of As reduces the film's formation energy. A model of one of the energetically favored structures is shown in Fig. 3.20, and illustrates several of the characteristics described above as derived by independent experiment. This structure also provides essentially the full moment of $\sim 2.2\,\mu_B$ per Fe atom.

A cross-sectional TEM image of the Fe/AlGaAs interface of the spin-LED device from which the data of Fig. 3.13 were obtained is shown in Fig. 3.21 [3.124]. The interface appears to be well-ordered and epitaxial, and there is no gross disruption

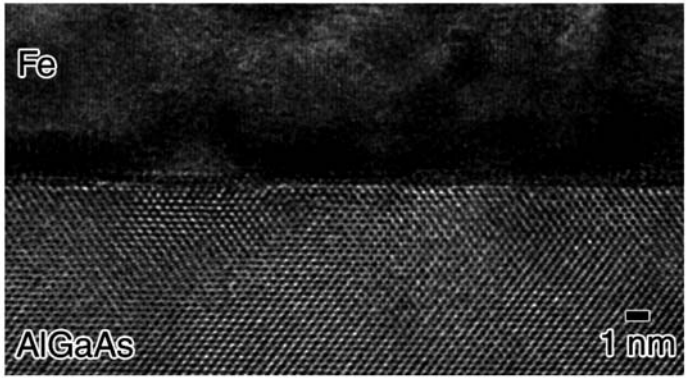

Fig. 3.21. High resolution cross-sectional transmission electron micrograph showing the Fe/AlGaAs interface from the spin-LED structure of Fig. 3.13

of the substrate itself. There appears to be some structure at the interface which is consistent with either electron beam transmission effects arising from monolayer thickness fluctuations over the specimen thickness (perpendicular to the plane of the figure), or intermixing at the monolayer level. Higher resolution work is in progress to further elucidate the atomic structure of this spin-injecting interface with the goal of correlating this structure with the spin injection efficiency as measured from the electroluminescence of the spin-LED itself.

The magnetic properties as determined by in situ MOKE were found to be remarkably similar for growth on the As-2 $\times$ 4, As-c(4 $\times$ 4) and Ga-4 $\times$ 6 surface reconstructions [3.116–118, 120] supporting the conclusion that a very similar interface and Fe film structure were achieved in each case. A summary of these data are shown in Fig. 3.22, where the room temperature remanence is plotted as a function of Fe film thickness for growth on these three reconstructed surfaces. The data are normalized to the signal at 16 monolayers (MLs) of bcc Fe(001). Regardless of the initial GaAs surface reconstruction, the onset of FM order at room temperature occurs at 5–6 ML, attributed to a reduction in Curie temperature for thinner films. At 6 ML, the Curie temperature was determined to be 80 °C. A least squares fit to the data for 6–16 ML intercepts the coverage axis at about 0.5 ML, demonstrating that essentially all of the Fe layers contribute equally once this critical thickness of 6 ML is reached, but potentially leaving 0.5 ML unaccounted for. The 0.5 ML is within the error bar of intercepting the origin, and it is therefore difficult to assess its significance from these data. If one assumes this 0.5 ML is at the *surface* of the Fe film, it is bonded with the surface segregated As which is known to exist [3.116–119] This would readily account for a reduction in net moment, and would have little impact on spin injection at the semiconductor interface. However, if this 0.5 ML is at the Fe/GaAs *interface* in non-ferromagnetic form, it is very likely to produce spin scattering and reduce the spin polarization of the electron current injected into the semiconductor. Hence detailed knowledge of the interface is critical in semiconductor spintronic het-

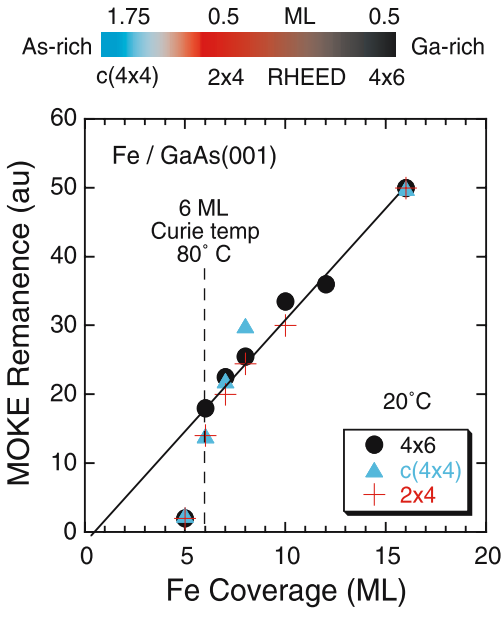

Fig. 3.22. Magnetic remanence obtained from *in situ* magneto-optic Kerr effect measurements *vs* Fe film coverage for growth of Fe(001) films on the three reconstructed surfaces of MBE-grown GaAs(001) indicated. The relative surface coverage and corresponding RHEED pattern of the three initial GaAs surface reconstructions are indicated in the bar graph. The data were obtained at 20 °C, and the Fe films were deposited at a nominal 175 °C. The data are normalized at a coverage of 16 monolayers (ML)

erostructures, just as it is in conventional semiconductor, GMR and magnetic tunnel junction devices.

3.8 Summary

Remarkable progress has been realized in the last few years towards achieving the basic requirements for a practical semiconductor spintronics technology. The development of the surface emitting spin-LED has enabled quantitative analysis and detailed study of spin injection and transport in semiconductor heterostructures. The very large spin injection efficiencies and correspondingly large measured effects in all-semiconductor structures have afforded an analysis of the role of generic interface defects in spin scattering, and the development of a simple predictive model. The use of a ferromagnetic metal Schottky contact as a tunnel barrier for spin injection takes advantage of an intrinsic property of the metal/semiconductor interface (avoiding the concerns of pinholes associated with a discrete barrier layer), as well as the many desirable attributes of FM metals, such as high Curie temperatures. Electron populations with a spin polarization of 32% produced by spin injection from such an Fe Schottky

tunnel contact into a GaAs QW demonstrate that efficient spin injecting contacts can be formed using a very familiar and widely employed contact methodology. Since metallization is a standard process in any semiconductor device fabrication line, the use of a ferromagnetic metallization could readily be incorporated into existing processing schedules. Future work is needed to develop a FM Schottky contact which has a perpendicular magnetization with a low coercive field, *i.e.* in which the easy magnetic axis is out-of-plane, for applications which require such a spin orientation. As noted above, the heterointerface plays a critical role in spin injection, and future work is required to understand the structural, magnetic and electronic properties, and their correlation with spin transport.

Acknowledgement. The author gratefully acknowledges the many people who have contributed significantly to the recent work presented here. These include S.C. Erwin, A.T. Hanbicki, Y.D. Park (now at Seoul National University), A. Petukhov (South Dakota School of Mines and Technology, on sabbatical at NRL), and R. Stroud at the Naval Research Laboratory, and the group of Prof. A. Petrou at the State University of New York at Buffalo, including his graduate students (past and present) G. Itskos, G. Kioseoglou, R. Mallory and M. Yasar. The author also gratefully acknowledges financial support for this work by the Office of Naval Research (Dr. L. Cooper), the Defense Advanced Research Project Agency's program *Spins in Semiconductors* (Dr. S. Wolf), and core programs at the Naval Research Laboratory.

References

3.1. H.S.P. Wong, D.J. Frank, P.M. Solomon, C.H.J. Wann and J.J. Welser. Proceedings of the IEEE 87, 537 (1999).
3.2. M.N. Baibich, J.M. Broto, A. Fert, F. Nguyen van Dau, F. Petroff, P. Etienne, G. Creuzet, A. Friederich, and J. Chazelas Phys. Rev. Lett. 61, 2472 (1988).
3.3. G. Binasch, P. Grunberg, F. Saurenbach, and W. Zinn. Phys. Rev. B 39, 4828 (1989).
3.4. J. Daughton. J. Magn. Magn. Materials 192, 334 (1999).
3.5. J.S. Moodera, L.R. Kinder, T.M. Wong, and R. Meservey. Phys. Rev. Lett. 74, 3273 (1995).
3.6. W.J. Gallagher, S.S.P. Parkin, Y. Lu, X.P. Bian, A. Marley, K.P. Roche, R.A. Altman, S.A. Rishton, C. Jahnes, T.M. Shaw, and G. Xiao. J. Appl. Phys. 81, 3741 (1997).
3.7. J.M. Daughton. J. Appl. Phys. 81, 3758 (1997).
3.8. S. Datta, and B. Das. Appl. Phys. Lett. 56, 665 (1990).
3.9. For recent reviews, see G.A. Prinz, Science 282, 1660 (1998); S.A. Wolf, D.D. Awschalom, R.A. Buhrman, J.M. Daughton, S. von Molnar, M.L. Roukes, A.Y. Chtchelkanova, and D.M. Treger, Science 294, 1488 (2001).
3.10. I. Zutic, J. Fabian and S. Das Sarma, Phys. Rev. B 64, 121201 (2001).
3.11. M.E. Flatte and G. Vignale, Appl. Phys. Lett. 78, 1273–75 (2001).
3.12. B.T. Jonker, U.S. Patent No. 5,874,749 (filed 23 June 1993, awarded 23 February 1999 to U.S. Navy).
3.13. R. Fiederling, M. Kelm, G. Reuscher, W. Ossau, G. Schmidt, A. Waag and L.W. Molenkamp. Nature **402**, 787 (1999).
3.14. Y. Ohno, D.K. Young, B. Beschoten, F. Matsukura, H. Ohno, and D.D. Awschalom. Nature 402, 790 (1999).
3.15. B.T. Jonker, Y.D. Park, B.R. Bennett, H.D. Cheong, G. Kioseoglou, and A. Petrou. Phys. Rev. B 62, 8180 (2000).
3.16. P. Bruno and J. Wunderlich. J. Appl. Phys. 84, 978, (1998).
3.17. H. Ohno, N. Akiba, F. Matsukura, A. Shen, K. Ohtani, and Y. Ohno. Appl. Phys. Lett. 73, 363 (1998).
3.18. E.A. de Andrada e Silva and G.C. La Rocca. Phys. Rev. B 59, R15583 (1999).
3.19. T. Hayashi, M. Tanaka, and A. Asamitsu. J. Appl. Phys. 87, 4673 (2000).
3.20. Th. Gruber, M. Keim, R. Fiederling, G. Reuscher, W. Ossau, G. Schmidt, L.W. Molenkamp, and A. Waag. Appl. Phys. Lett. 78, 1101 (2001).
3.21. T. Koga, J. Nitta, H. Takayanagi, and S. Datta. Phys. Rev. Lett. 88, 126601 (2002).
3.22. A.F. Morpurgo, J.P. Heida, T.M. Klapwijk, B.J. van Wees, and G. Borghs. Phys. Rev. Lett. 80, 1050 (1998).
3.23. J. Nitta, F. Meijer, Y. Narita and H. Takayanagi, Phyica E 6, 318 (2000).
3.24. T. Whitaker. Compound Semiconductor 4, 36 (1998).
3.25. P. Mazumder, S. Kulkarni, M. Bhattacharya, J.P. Sun, and G.I. Haddad. Proc. IEEE 86, 664 (1998).
3.26. W.B. Kinard, M.H. Weichold, and W.P. Kirk. J. Vac. Sci. Technol. B8, 393 (1990).
3.27. B.T. Jonker and R. Magno. U.S. Patent No. 6.316.965 (awarded 13 November 2001 to U.S. Navy).
3.28. A.T. Hanbicki, R. Magno, S.-F. Cheng, Y.D. Park, A.S. Bracker, and B.T. Jonker. Appl. Phys. Lett. 79, 1190 (2001).
3.29. F. Meier and B.P. Zakharchenya, *Optical Orientation* (North-Holland, Amsterdam, 1984), vol. 8.
3.30. D. Hagele, M. Oestreich, W.W. Ruhle, N. Nestle, and K. Eberl. Appl. Phys. Lett. **73**, 1580 (1998).

3.31. J.M. Kikkawa and D.D. Awschalom. Phys. Rev. Lett. **80**, 4313 (1998).
3.32. J.M. Kikkawa and D.D. Awschalom. Nature 397, 139 (1999).
3.33. J. Nitta, T. Akazaki, H. Takayanagi, and T. Enoki. Phys. Rev. Lett. 78, 1335 (1997).
3.34. G. Engels, J. Lange, Th. Schapers, and H. Luth. Phys. Rev. B 55, R1958 (1997).
3.35. Y.Q. Jia, R.C. Shi, and S.Y. Chou. IEEE Trans. Magn. **32**, 4707 (1996).
3.36. A. Hirohata, Y.B. Xu, C.M. Guertler, J.A.C. Bland, and S.N. Holmes. Phys. Rev. B 63, 104425 (2001).
3.37. J.E. Hirsch. Phys. Rev. Lett. 83, 1834 (1999)
3.38. S. Zhang. Phys. Rev. Lett. 85, 393 (2000)
3.39. S.F. Alvarado and P. Renaud. Phys. Rev. Lett. 68, 1387 (1992).
3.40. V.P. Labella, D.W. Bullock, Z. Ding, C. Emery, A. Venkatesan, W.F. Oliver, G.J. Salamo, P.M. Thibado. Science 292, 1518 (2001).
3.41. W.F. Egelhoff, M.D. Stiles, D.P. Pappas, D.T. Pierce, J.M. Byers, B.T. Jonker, S.F. Alvarado, J.F. Gregg, J.A.C. Bland, and R.A. Buhrman, Science 296, 1195a (2002).
3.42. P.R. Hammar, B.R. Bennett, M.J. Yang, and M. Johnson. *Phys. Rev. Lett.* **83,** 203 (1999).
3.43. C.-M. Hu, J. Nitta, A. Jensen, J.B. Hansen, and H. Takayanagi, *Phys. Rev. B* **63,** 125333 (2001).
3.44. S. Gardelis, C.G. Smith, C.H.W. Barnes, E.H. Linfield, and D.A. Ritchie, *Phys. Rev. B* **60,** 7764 (1999).
3.45. F.G. Monzon, H.X. Tang, M.L. Roukes, *Phys. Rev. Lett.* **84,** 5022 (2000).
3.46. B.J. van Wees. *Phys. Rev. Lett.* **84,** 5023 (2000).
3.47. A.T. Filip, B.H. Hoving, F.J. Jedema, B.J. van Wees, B. Dutta and S. Borghs, *Phys. Rev. B* **62,** 9996 (2000).
3.48. C. Weisbuch and B. Vinter. *Quantum Semiconductor Structures* (Academic Press, New York, 1991), sec. 11.
3.49. There is an unfortunate clash of nomenclature between the semiconductor and magnetic metals communities. In the latter, the convention is that a "spin-up" electron has its *moment* parallel to the field or magnetization (see [3.50]). This is also called a "majority spin" electron, since this state is at lower energy and therefore more heavily populated. Since the electron's spin and moment are antiparallel, the spin of a "spin-up" electron is thus antiparallel to the field. This will be an important distinction in Section VI which deals with spin injection from ferromagnetic metals into semiconductors.
3.50. R. Meservey and P.M. Tedrow. Phys. Rep. 238, 173–234 (1999). See pp. 200–202.
3.51. G. Bastard, *Wave Mechanics Applied to Semiconductor Heterostructures* (Halsted, New York, 1988) p. 109.
3.52. B.T. Jonker, A.T. Hanbicki, Y.D. Park, G. Itskos, M. Furis, G. Kioseoglou and A. Petrou, Appl. Phys. Lett. 79, 3098 (2001). See also the *Nature* Physics Portal web site: "Spintronics Quantified" http://www.nature.com/physics/highlights/6860-3.html
3.53. J.K. Furdyna and J. Kossut. *Diluted Magnetic Semiconductors*, vol. 25 of *Semiconductors and Semimetals* (series editors: R.K. Willardson and A.C. Beer, Academic Press, New York, 1988).
3.54. M. Jain, *Diluted Magnetic Semiconductors* (World Scientific, Singapore, 1991).
3.55. W.C. Chou, A. Petrou, J. Warnock and B.T. Jonker, Phys. Rev. Lett. 67, 3820 (1991); X. Liu et al. Phys. Rev. Lett. 63, 2280 (1989)
3.56. N. Dai et al. Phys. Rev. Lett. 67, 3824 (1991).
3.57. M. Oestreich, J. Hubner, D. Hagele, P.J. Klar, W. Heimbrodt, W.W. Ruhle, D.E. Ashenford, and B. Lunn. Appl. Phys. Lett. 74, 1251 (1999).
3.58. A.F. Isakovic, D.M. Carr, J. Strand, B.D. Schultz, C.J. Palmstrom, and P.A. Crowell. Phys. Rev. B 64, 161304(R) (2001).

3.59. H. Abad, B.T. Jonker, W.Y. Yu, S. Stolz, and A. Petrou. Appl. Phys. Lett. 66, 2412 (1995).
3.60. I. Smorchkova and N. Samarth. Appl. Phys. Lett. 69, 1640 (1996).
3.61. H. Ohno. Science 281, 951 (1998).
3.62. Y. Ohno, D.K. Young, B. Beschoten, F. Matsukura, H. Ohno, and D.D. Awschalom. Nature 402, 790 (1999).
3.63. L.H. Kuo et al. Appl. Phys. Lett. **67**, 3298 (1995); J. Vac. Sci. Technol. **13**, 1694 (1995).
3.64. R. Nicolini et al. Phys. Rev. Lett. **72**, 294 (1994).
3.65. J. Moodera, J. Nowak, and R.J.M. van de Veerdonk. Phys. Rev. Lett. **80**, 2941 (1998).
3.66. Y.D. Park, B.T. Jonker, B.R. Bennett, G. Itskos, M. Furis, G. Kioseoglou, and A. Petrou. Appl. Phys. Lett. 77, 3989 (2000).
3.67. M.I. Dyakonov and V.I. Perel in reference 29, p. 11–71 (1984).
3.68. R.M. Stroud, A.T. Hanbicki, Y.D. Park, G. Kioseoglou, A.G. Petukhov, B.T. Jonker, G. Itskos, and A. Petrou. Phys. Rev. Lett. 89, 166602 (2002).
3.69. K.K. Fung, N. Wang, and I.K. Suo. Appl. Phys. Lett. **71**, 1225 (1997).
3.70. T. Walter and D. Gerthsen, Ultramicroscopy **81**, 279 (2000).
3.71. M.A. Vidal, et al. *in Defects and Diffusion Forum* **173–174**, 32 (1999).
3.72. C. Gianni, et al., J. Phys. D **32,** A51 (1999).
3.73. M.S. Carpenter, et al. Appl. Phys. Lett. **53**, 66 (1988).
3.74. G.E. Pikus and A.N. Titkov. in reference 29 p. 73 (1984).
3.75. M.I. D'yakonov et al. Zh. Exp. Teor. Fiz. **90**, 1123 (1986) [Sov. Phys. JETP **63**, 655 (1986)].
3.76. J.S. Koehler. Phys. Rev. **60**, 397 (1941).
3.77. R. Landauer. Phys. Rev. **82**, 520 (1951).
3.78. D.L. Dexter. Phys. Rev. **85,** 936 (1952); D.L. Dexter and F. Seitz, Phys. Rev. **86**, 964 (1952).
3.79. E. Merzbacher. *Quantum Mechanics* (John Wiley, New York, 1998), p. 402.
3.80. L.D. Landau and E.M. Lifshitz. *Quantum Mechanics* (Addison-Wesley, Reading, MA, 1958)
3.81. T. Dietl, H. Ohno, F. Matsukura, J. Cibert, and D. Ferrand. Science 287, 1019 (2000); M. Kohda, Y. Ohno, K. Takamura, F. Matsukura, and H. Ohno. Jpn. J. Appl. Phys. 40, L1274 (2001); E. Johnston-Halperin et al. Phys. Rev. B 65, R041306 (2002).
3.82. G. Schmidt, D. Ferrand, L.W. Molenkamp, A.T. Filip, and B.J. van Wees. Phys. Rev. B 62, R4790 (2000).
3.83. D.L. Smith and R.N. Silver. Phys. Rev. B 64, 045323 (2001).
3.84. A. Fert and H. Jaffres. Phys. Rev. B 64, 184420 (2001).
3.85. P.C. van Son, H. van Kempen, and P. Wyder. Phys. Rev. Lett. 58, 2271 (1987)
3.86. T. Valet and A. Fert. Phys. Rev. B 48, 7099 (1993)
3.87. E.I. Rashba. Phys. Rev. B 62, R16267 (2000).
3.88. E.H. Rhoderick and R.H. Williams. *Metal-Semiconductor Contacts*(second edition, Clarendon, Oxford, 1988)
3.89. M. Ilegems. in *The Technology and Physics of Molecular Beam Epitaxy*, p. 119 (edited by E.H.C. Parker, Plenum, New York, 1985).
3.90. A.T. Hanbicki, B.T. Jonker, G. Itskos, G. Kioseoglou, and A. Petrou. Appl. Phys. Lett. 80, 1240 (2002).
3.91. For the ZnMnSe/AlGaAs spin-LED system described in Section III and reference [3.15], $m_j = -1/2$ electrons are injected from the ZnMnSe contact when the magnetic field is applied along the surface normal. These would be described as "spin-down" electrons using the nomenclature of the semiconductor community.

3.92. Note that this was incorrectly labeled minority spin in the Fe in [3.90].
3.93. See, for example C. Kittel. *Introduction to Solid State Physics* (5^{th} edition, Wiley, New York, 1976) p 438–439; N.W. Ashcroft and N.D. Mermin, *Solid State Physics* (Holt, Rinehart and Winston, New York, 1976) p. 654, 661.
3.94. M.B. Stearns. *J. Magn. Magn. Mater.* **5,** 167–171 (1977).
3.95. J.J. Krebs and G.A. Prinz. *NRL Memo Rep. 3870* (Naval Research Lab, Washington, 1978).
3.96. H.J. Zhu, M. Ramsteiner, H. Kostial, M. Wassermeier, H.-P. Schonherr, and K.H. Ploog. *Phys. Rev. Lett.* **87,** 016601 (2001).
3.97. J.D. Albrecht and D.L. Smith. Phys. Rev. B 66, 113303 (2002).
3.98. R.J. Soulen et al. Science 282, 85 (1998).
3.99. H. Jaffres and A. Fert. private communication and preprint.
3.100. E.I. Rashba. Appl. Phys. Lett. 80, 2329 (2002).
3.101. G. Schmidt and L.W. Molenkamp. Semicond. Sci. Technol. 17, 310 (2002).
3.102. Z.G. Yu and M.E. Flatte. cond/mat-0206321
3.103. *Tunneling Phenomena in Solids*, edited by E. Burnstein and S. Lundqvist (Plenum, New York, 1969).
3.104. B.J. Jonsson-Akerman, R. Escudero, C. Leighton, S. Kim, I.K. Schuller, and D.A. Rabson. Appl. Phys. Lett. 77, 170 (2000).
3.105. U. Rudiger, R. Calarco, U. May, K. Samm, J. Hauch, H. Kittur, M. Sperlich, and G. Guntherodt. Appl. Phys. Lett. 89, 7573 (2001).
3.106. S. Adachi, T. Miyashita, S. Takeyama, Y. Takagi, and A. Tackeuchi. *J. Lumin*. **72**, 307 (1997).
3.107. V.F. Motsnyi, J. De Boeck, J. Das, W. Van Roy, G. Borghs, E. Goovaerts, and V.I. Safarov. Appl. Phys. Lett. 81, 265 (2002).
3.108. G.A. Prinz. *Ultrathin Magnetic Structures II*, p. 1 (edited by B. Heinrich and J.A.C. Bland, Springer-Verlag, Berlin, 1994).
3.109. T.A. Moore, J. Rothman, Y.B. Xu, and J.A.C. Bland. J. Appl. Phys. 89, 7018 (2001).
3.110. T.L. Monchesky, R. Urban B. Heinrich, M. Klaua, and J. Kirschner. J. Appl. Phys. 87, 5167 (2000).
3.111. H.-P. Schonherr, R. Notzel, Ma Wenquan, and K.H. Ploog. J. Appl. Phys. 89, 169 (2001).
3.112. R. Moosbuehler, F. Bensch, M. Dumm, and G. Bayreuther. J. Appl. Phys. 91, 8757 (2002).
3.113. J.R. Waldrop and R.W. Grant. Appl. Phys. Lett. 34, 630 (1979).
3.114. G.A. Prinz and J.J. Krebs. Appl. Phys. Lett. 39, 397 (1981).
3.115. A. Filipe and A. Schuhl. J. Appl. Phys. 81, 4359 (1997).
3.116. E.M. Kneedler, P.M. Thibado, B.T. Jonker, B.R. Bennett, B.V. Shanabrook, R.J. Wagner, and L.J. Whitman. J. Vacuum Science and Technol. B14, 3193 (1996).
3.117. E.M. Kneedler and B.T. Jonker. J. Appl. Phys. 81, 4463 (1997).
3.118. E.M. Kneedler, B.T. Jonker, P.M. Thibado, R.J. Wagner, B.V. Shanabrook, and L.J. Whitman. Phys. Rev. B 56, 8163 (1997).
3.119. P.M. Thibado, E.M. Kneedler, B.T. Jonker, B.R. Bennett, B.V. Shanabrook, and L.J. Whitman. Phys. Rev. B 53, 10481 (1996).
3.120. E.M. Kneedler and B.T. Jonker. unpublished.
3.121. B.T. Jonker, O.J. Glembocki, R.T. Holm, and R.J. Wagner. Phys. Rev. Lett. 79, 4886 (1997).
3.122. C.S. Gworek, P. Phatak, B.T. Jonker, E.R. Weber, and N. Newman. Phys. Rev. B 64, 045322 (2001).
3.123. S.C. Erwin, S.-H. Lee, and M. Scheffler. Phys. Rev. B 65, 205422 (2002).
3.124. R.M. Stroud et al. unpublished.

4

Optical Studies of Electron Spin Transmission

J.A.C. Bland, S.J. Steinmüller, A. Hirohata and T. Taniyama

4.1 Introduction to Spin Electronics

4.1.1 Concept

The birth of spin electronics heralds a new era of integration in semiconductor electronics, in which the electron charge, the electron spin and the photon helicity are controlled, leading to the prospect of a vastly expanded range of design possibilities for electronic devices [4.1, 2]. In particular, significant improvements in data storage, processing, and communications are already in sight. Figure 4.1 schematically illustrates the concept of spin electronics. Giant magnetoresistance (GMR) sensors are a now familiar example of the integration of electron charge and electron spin manipulation; on the other hand the integration of spin polarised electron transport with polarised photon manipulation is still in development. For the electron spin to be successfully employed in a spin electronic device, the spin degree of freedom must be handled most delicately, because the spin will rapidly depolarise in the device: the spin lifetime is ~ 10 ns at most in GaAs [4.3].

The basic concept of a "notional" spin polarised device is schematically shown in Fig. 4.2. Spin polarised electrons/holes are injected from a source electrode and detected electrically (or optically) at a drain electrode. The device functionality is based on the manipulation of the electron spin during propagation from the source to the drain electrode. The device relies on three different key processes: (1) spin injection (2) spin manipulation (control) and (3) spin detection. The spin field effect transistor (FET) as proposed by Datta and Das [4.5] is an example of a spin electronic device based on this concept. For the spin FET, electron (or hole) spins are injected from a source, modulated by the gate bias and finally detected electrically at a drain. In order to successfully implement such a device, however, there are still obstacles to overcome. Since the spin-orbit interaction is relatively weak, a long device length would be needed to manipulate the spin via the Rashba effect, as was originally proposed [4.5]. To achieve efficient spin control in the transistor base, therefore a more effective mechanism, such as Larmor precession, may be necessary. Furthermore,

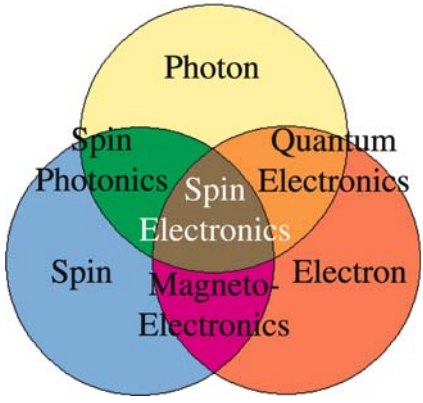

Fig. 4.1. Concept of spin electronics. Modified after [4.4]

spin injection and detection efficiencies at room temperature reported to date are too low to be practical. However, while the concept of the spin FET has yet to be successfully realised, it has nevertheless been very stimulating to the field. In the spin light emitting diode (LED) [4.6, 7], the modulation of the electron spin polarisation is converted to an optical polarisation signal. The spin LED is therefore closely related to the spin FET, but in this case the output signal is detected as circularly polarised electroluminescence (EL). In general, efficient spin dependent transport depends on achieving both efficient spin injection and detection of electrons passing from the source to the drain. Both of these processes crucially depend on the electronic properties of the interfaces which are elusive and difficult to control. In this context, the most critical issue in the development of spin electronic devices is that of efficiently injecting and detecting spin polarised electrons at room temperature.

While spin electronic devices do not necessarily have to be semiconductor (SC) based, the implementation of semiconductors offers a variety of new opportunities due to their extraordinary properties, such as the tunability of the charge transport parameters by carrier doping and the possibility of exciting or detecting spin polarised charge carriers optically. To date, two different approaches have been reported for spin injection and detection in ferromagnet (FM)/SC structures, namely the use of (1) a diluted magnetic semiconductor (DMS) and (2) a FM metal as a spin aligner.

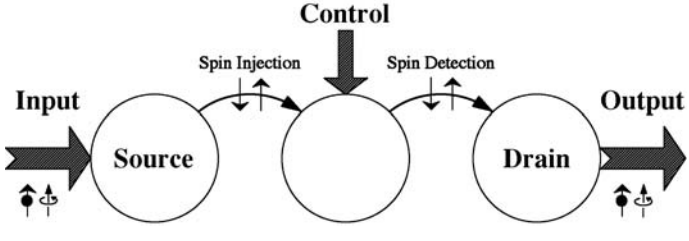

Fig. 4.2. Schematic diagram of a spin polarised three-terminal device

Several studies of spin LED structures using magnetic semiconductors have been carried out, and a high spin injection efficiency of $\sim 90\%$ has been observed at 2 K [4.6]. A basic obstacle for the application in spin electronic devices, which need to be operated at room temperature (RT), is the relatively low Curie temperature T_C of most existing ferromagnetic semiconductors. There has been extensive effort to increase the T_C of DMS with some reports of RT ferromagnetism. In order to achieve a large spin polarisation, however, T_C has to be considerably larger than RT and this remains a challenging goal in current research. Furthermore, in the case of giant g-splitting paramagnetic SC (e.g. BeMnZnSe [4.6]), the application of a very high magnetic field is required for conduction electrons to be spin polarised. Ferromagnetic metals such as Fe, Co and Ni, on the other hand, have a high enough T_C for RT operation and low saturation fields, as required for applications. However, Schmidt et al. pointed out that the conductivity mismatch between a ferromagnetic metal and a semiconductor introduces another obstacle for highly efficient spin injection [4.8]. According to the theoretical predictions, the spin injection coefficient γ is proportional to the ratio of the conductivity of the semiconductor σ_{SC} to that of the ferromagnet σ_{FM}, i.e., $\gamma \propto \sigma_{SC}/\sigma_{FM} \ll 1$ in the diffusive regime (details are given in the following section). It is expected, however, that efficient spin injection can be achieved via electron tunnelling at the FM/SC interface [4.9], provided an appropriate tunnel barrier (e.g., an insulating layer or a Schottky barrier) is introduced. If the tunnelling process is spin dependent, and the tunnel barrier contact resistance is larger than the resistance of the SC, spin injection efficiencies of up to 100% can be expected. In fact, experimental demonstrations of electrical spin injection at Fe/AlGaAs [4.10], Fe/GaAs [4.11], and CoFe/AlO_x/AlGaAs [4.12] interfaces support these theoretical predictions. Consequently, significant efforts are now being made to develop possible spin injection and detection devices using thin FM metal films. In this article, our focus is on demonstrating an optical approach to the study of electron spin transmission at the FM metal/SC interface with an emphasis on spin detection processes. Related studies on spin injection can be found in Chap. 3 of this book.

4.1.2 Optical Spin Orientation in GaAs

Optical spin orientation provides a basis for quantifying spin injection and is a powerful approach to research studies of spin transport. Optical spin orientation was first demonstrated in 1968 by Lampel and the spin polarisation was detected using nuclear magnetic resonance [4.13]. Subsequently, the optical detection of spin oriented electrons in p-GaSb was carried out by Parsons et al. [4.14, 15]. Pierce and Meier also developed an approach for detecting optically spin oriented photoelectrons emitted from GaAs into the vacuum using a Mott detector [4.16]. These pioneering studies of optical spin orientation underpin a variety of current experimental approaches used in spin electronics research. Recently, in a highly sophisticated approach, the control of local electron spin orientation in GaAs using a pump laser pulse and simultaneous recording of the spin orientation using a second probe laser pulse was successfully demonstrated by measuring time resolved Faraday rotation [4.17]. A detailed review

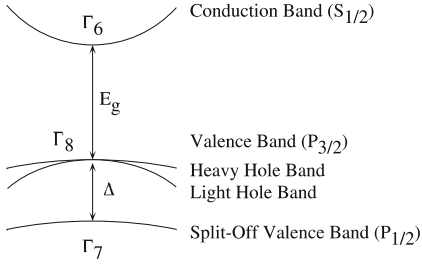

Fig. 4.3. Schematic band structure of GaAs in the vicinity of the Γ-point (the centre of the Brillouin zone) in $\boldsymbol{k}$-space. The energy gap E_g between the conduction band and the valence bands for both heavy and light holes is shown. The spin-orbit splitting Δ introduces a split in the P bands. After [4.19]

of this approach can be found in [4.15]. In this section, the basic concepts underlying optical spin orientation are introduced for the direct band gap semiconductor GaAs.

In GaAs, the valence band maximum and the conduction band minimum are at the Γ-point, the centre of the Brillouin zone ($\boldsymbol{k} = 0$), with an energy gap $E_g = 1.43\,\text{eV}$ at room temperature, indicating that the only transition induced by photons occurs at Γ (direct gap SC) [4.16, 18]. The valence band (p-symmetry) splits into four-fold degenerate $P_{3/2}$ states at Γ_8 and two-fold degenerate $P_{1/2}$ states at Γ_7, which lie $\Delta = 0.34\,\text{eV}$ below $P_{3/2}$, whereas the conduction band (s-symmetry) is two-fold degenerate $S_{1/2}$ at Γ_6, as schematically shown in Fig. 4.3. The $P_{3/2}$ band consists of two-fold degenerate bands: heavy hole and light hole subbands.

When circularly polarised light with an energy of $h\nu = E_g$ illuminates GaAs, electrons are excited from $P_{3/2}$ to $S_{1/2}$. According to the selection rule ($\Delta m_j = \pm 1$), two transitions for each photon helicity ($\boldsymbol{\sigma}^+$ and $\boldsymbol{\sigma}^-$) are possible; however, the relative transition probabilities for light and heavy holes are different, resulting in a net spin polarisation of excited electrons in the GaAs [4.16]. Since transitions from the heavy hole band ($m_j = \pm 3/2$) are three times more likely than those from the light hole band ($m_j = \pm 1/2$) for each light polarisation (Fig. 4.4), theoretically a maximum spin polarisation of 50% can be expected.[1] Experimentally, the spin polarisation was found to be slightly smaller ($\sim 40\%$), as shown in Fig. 4.5, due to limitations, such as spin depolarisation within the GaAs layer and at the interfaces [4.16].

Let us consider what occurs for illumination with the photon energy satisfying $E_g + \Delta < h\nu$. The polarisation clearly decreases with increasing $h\nu$ due to simultaneous excitation of electrons from light and heavy hole states and the split-off valence band states, giving electron excitation with the opposite spin sign [4.16] (see Fig. 4.4). With further increase in the energy of the light ($E_g + \Delta \ll h\nu$), the spin-orbit interaction becomes negligible and spin depolarisation during cascade processes can be significant, causing the absence of electron spin polarisation in this energy range [4.19].

[1] In strained GaAs, the heavy and light hole bands are split, leading to even 100% spin polarisation for an appropriate choice of photon energy.

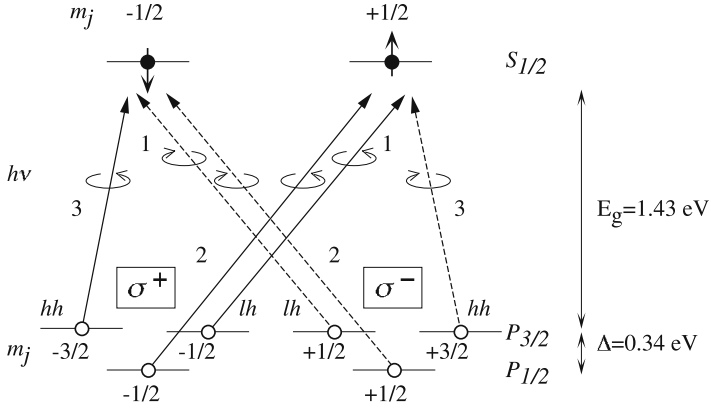

Fig. 4.4. Schematic diagram of the allowed transitions for right (σ^+, solid lines) and left (σ^-, dashed lines) circularly polarised light with GaAs. The selection rule is $\Delta m_j = +1$ for σ^+ and $\Delta m_j = -1$ for σ^-. The numbers near the arrows represent the relative transition probabilities. The magnetic quantum numbers are also indicated at the energy levels. The heavy and light holes are abbreviated to *hh* and *lh*, respectively. After [4.16]

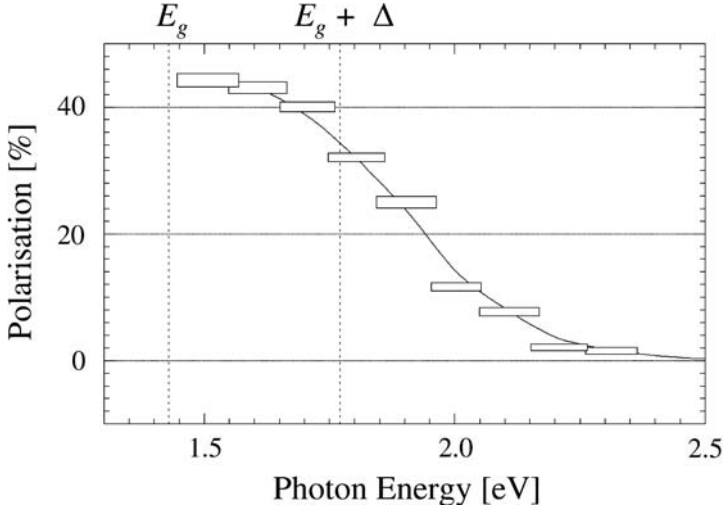

Fig. 4.5. Photoemission spectrum of spin polarisation from GaAs + CsOCs at $T \leq 10$ K. After [4.16]

In this way, provided that the energy of the circularly polarised light is tuned to the band gap of GaAs, electrons with a spin polarisation of up to about 50% can be generated in the GaAs – this is termed optical spin orientation.

4.1.3 Demonstration of Optical Spin Injection and Detection

One approach to investigating spin detection in FM/GaAs structures employs optical spin orientation, as described in the previous section (see Table 4.1). This method allows for a direct study of spin detection, since the process of spin orientation is well understood. In this section several experimental examples are reviewed.

Photoexcited spin dependent electron transport through thin film tunnel junctions of both Co/Al_2O_3/GaAs and Co/τ-MnAl/AlAs/GaAs was first discussed by Prins et al. [4.20]. For the former structure, the tunnelling current showed a spin dependence, while for the latter structure only magnetic circular dichroism (MCD, i.e., magneto-optical effects in the FM layer, see Sect. 4.3.1) was observed. In their experiment, the samples with a 2 nm Al_2O_3 tunnel barrier showed the largest helicity dependence of the photoexcited current of approximately 1.2% at $h\nu = 1.5$ eV (near the GaAs band gap). Accordingly, many studies of spin dependent tunnelling through metal-oxide-semiconductor (MOS) junctions have been carried out, such as [4.21]. Recently, an effort to observe spin dependent transport of photoexcited electrons through FM/SC interfaces with quantum well (QW) structures has also been made by Isakovic et al. [4.22]. They fabricated structures based on various combinations of materials, including *n*-, *p*-type GaAs, Fe and CoFe ferromagnetic metals, and measured the helicity dependent photocurrent as a function of photon energy, bias voltage, and magnetic field. They conclude that for the front pumping geometry through the top ferromagnetic layer — although the MCD background signals dominate the polarised photocurrent due to the thick CoFe and Fe films used — at most 0.5% of the photocurrent may be a true spin dependent signal in a *p*-type sample at 10 K with an excitation energy of 1.96 eV. On the other hand, a spin dependent contribution to the photocurrent of up to 10% was observed at the first QW transition from the ground state excitation after subtracting the MCD effects of the QW and the ferromagnetic layer, suggesting that the energy dependence of the photocurrent is useful for understanding the spin transport. They also measured the photocurrent in the side-pumping geometry, in which the MCD effect can be eliminated, and 1% of spin dependent photocurrent was detected at the first QW transition from the ground state. These results are suggestive of spin transport, but not conclusive, and highlight the issues which need to be addressed in such experiments. We will discuss our experimental results using a closely related experimental approach in the following sections.

After the first photoexcitation experiments by Prins et al., Sueoka et al. demonstrated the possibility of detecting spin polarised signals using a Ni scanning tunnelling microscope (STM) tip scanned over a GaAs/AlGaAs membrane with circularly polarised light illumination from the back AlGaAs side [4.24]. Although optically excited electrons scatter at the SC surface with such a back illumination geometry [4.27], Suzuki et al. performed similar measurements by scanning a *p*-GaAs STM tip over a Co film with back illumination through mica/Au/Co, and successfully obtained magnetic domain images [4.25]. In order to avoid the MCD effect and possible light scattering within the sample structure, Kodama et al. passed polarised light directly into a GaAs tip in the vicinity of the sample, in an arrangement equivalent

Table 4.1. Recent optical spin detection studies. Circularly polarised photons are injected and spin polarised electrons/holes are detected

Structures	Spin polarisation	Refs.
FM/SC hybrid structures:		
(NiFe, Co and Fe)/*n*-GaAs	2±1% (RT)	[4.23]
(FeCo and Fe)/GaAs QW	∼0.5% (10 K)	[4.22]
MOS junctions:		
$Co/Al_2O_3/p$-GaAs	∼1.2% (RT)	[4.20]
(Ni and Co)/Al_2O_3/p-GaAs	∼2.5 and 1.0% (RT)	[4.21]
SP-STM:		
Ni STM tip/GaAs	<10% (RT)	[4.24]
p-GaAs STM tip/Co/mica	∼10% (RT)	[4.25]
p-GaAs STM tip/NiFe/Si	∼7% (RT)	[4.26]

to front illumination and measured the I-V response [4.26]. They detected a change of approximately 7% between the current obtained for right and left circularly polarised light with NiFe films. However, the main problem of spin polarised STM is the difficulty of separating spin dependent information (∼ 1 pA) from the topographical current signal (∼ 1 nA), and this approach has therefore not been widely used. Nevertheless, the success of these pioneering experiments illustrates the possibility of using spin orientation to probe spin dependent tunnelling processes.[2]

When spin polarised electrons (holes) are electrically injected into GaAs, they recombine with holes (electrons), resulting in the emission of circularly polarised light. Applying the optical selection rules described above, it is then possible to determine the spin polarisation of the injected charge carriers from the degree of polarisation of the emitted light. Based on this approach, a great number of studies of spin injection into SC has been carried out using spin LEDs. In these experiments, the electron (or hole) spin injection efficiency is estimated from the electroluminescence of a QW (see Table 4.2) [4.6, 7, 30].

As discussed above, to date two types of spin aligner materials have been used successfully for electrically injecting spin polarised electrons (or holes) into a SC, namely DMS and FM metals. For the former, spin polarised hole injection has been recently reported at low temperature with FM *p*-GaMnAs as a spin aligner used in conjunction with a QW structure so that the recombination process is spatially confined [4.7]. At forward bias, spin polarised holes from the *p*-GaMnAs layer are injected into an InGaAs QW, where they recombine with unpolarised electrons

[2] A great progress in terms of resolution has been reported recently without using optical methods [4.28, 29].

Table 4.2. Recent optical spin injection studies. Spin polarised electrons/holes are injected and circularly polarised photons are detected. The spin polarisation in the table is defined as the circular polarisation of the emitted photons

Structures	Spin polarisation	Refs.
spin LED (spin polarised *electron* injection):		
BeMgZnSe+BeMnZnSe/*n*-AlGaAs/ *i*-GaAs QW/.../*p*-GaAs	∼42% (<5 K)	[4.6]
CdMnTe/CdTe	∼30% (5 K)	[4.32]
n-ZnMnSe/AlGaAs/GaAs QW/AlGaAs	∼83% (4.5 K)	[4.30, 33]
Fe/GaAs/InAs QW/GaAs	∼2% (RT)	[4.11]
Fe/AlGaAs/GaAs QW/AlGaAs	∼13% (4.5 K) ∼4% (240 K)	[4.10]
NiFe+CoFe/AlO_x/AlGaAs/GaAs QW/AlGaAs	∼9.2% (80 K)	[4.12]
(Co, Fe and NiFe)/Al_2O_3/*n*-AlGaAs/ GaAs QW/.../GaAs	∼0.8, 0.5 and 0.2% (RT)	[4.39]
spin LED (spin polarised *hole* injection):		
p-GaMnAs/GaAs/InAs QW	∼1% (<31 K)	[4.7]
SP-STM:		
Ni STM tip/GaAs	∼30% (RT)	[4.40]

provided by a *n*-GaAs layer, resulting in circularly polarised light emission. However, as the spin relaxation time for holes is much shorter than that for electrons [4.31], the measured spin polarisation was relatively small (about ±1%). On the other hand, highly efficient electron spin injection (spin polarisation of about 90% [4.6]) has been achieved at an applied field of ∼ 3 T using paramagnetic *n*-BeMnZnSe (exhibiting giant Zeeman splitting) as a spin aligner, since the spin diffusion length of electrons has been reported to be above 100 µm in GaAs [4.3]. Similar results have been obtained using CdMnTe [4.32], ZnSe [4.17], ZnMnSe [4.30, 33] and MnGe [4.34] but only at low temperature (typically below 80 K). Since RT ferromagnetism has been theoretically predicted in several DMS compounds [4.35] and experimentally observed in $Cd_{1-x}Mn_xGeP_2$ [4.36], spin injection at RT with DMS should be possible. However, in order to achieve a large spin polarisation, a T_C that is significantly larger than RT is necessary, as has been pointed out above. This aim has yet to be realised experimentally.

The spin resonant tunnelling diode (RTD) represents an interesting approach to controlling the spin polarisation of electrons injected into a SC. In the RTD, a magnetic semiconductor QW (exhibiting giant Zeeman splitting), situated between two insulating barrier layers, is used as a spin switch [4.37, 38]. By applying a magnetic field to the device, the degeneracy of the up- and down-spin subbands in the QW is lifted. When unpolarised electrons are injected into the diode structure, the spin

orientation of the states available in the QW can be changed by shifting the energy of the spin subbands via an applied gate voltage. In this way, the spin polarisation of the current transmitted through the device is altered. The RTD has been realised experimentally, using AlAs/GaMnAs/AlAs [4.37] and BeTe/ZnMnSe/BeTe structures [4.38].

Successful spin injection in FM metal/SC structures has recently been demonstrated by several groups. Fe (20 nm)/GaAs/InGaAs QW LED structures were investigated by Zhu et al. [4.11]. By measuring the degree of polarisation of the EL light they determined the spin polarisation of the injected electron current (about 2%, independent on temperature). However, a clear difference between the right and left circularly polarised EL was only observed at the tails of the Gaussian-like EL intensity distribution, but not in the center of the peaks. Hanbicki et al. carried out similar experiments with Fe (12.5 nm)/AlGaAs/GaAs QW LEDs and found a spin injection efficiency of 30% [4.10] – see Chap. 3 by Jonker. In their case, a significant polarisation of the emitted light was seen in the whole EL energy range. The spin polarisation was estimated to be 13% at 4.5 K and was found to decrease to 4% at 240 K, which was attributed to the decreased spin relaxation time at elevated temperatures. In order to enhance the spin injection efficiency in a spin LED following Rashba's prediction, Manago et al. used FM/Al_2O_3/(Al,Ga)As/GaAs structures (MOS spin LED), for which they reported circular light polarisation values of 0.8% (Co), 0.5% (Fe) and 0.2% (NiFe) at RT [4.39].

Motsnyi et al. also used an AlO_x insulator layer inserted between a FM metal and GaAs [4.12] and measured the spin polarisation of electrons injected across the FM/SC interface relying on the oblique Hanle effect (OHE). Figure 4.6 shows a schematic diagram of the OHE. A magnetic field is applied at an angle ϕ with respect to the plane normal of the magnetic film which has an in-plane easy axis. The field strength is chosen to be small enough not to pull the sample magnetisation

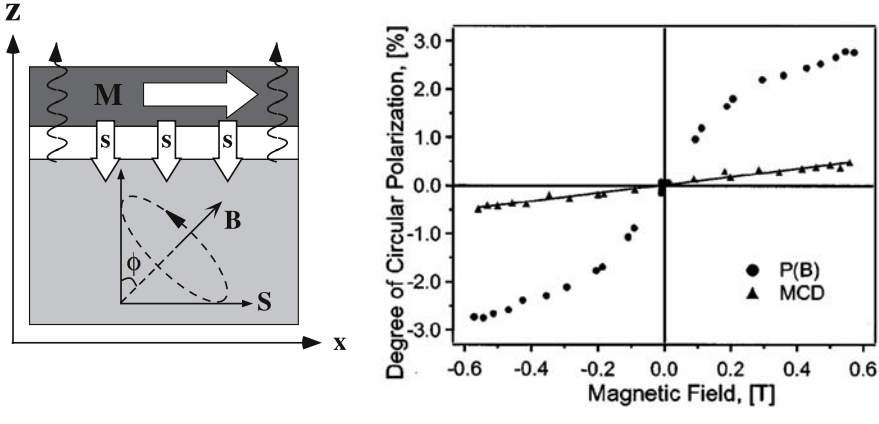

Fig. 4.6. Schematic diagram of the oblique Hanle effect in a SC (left) and electrical spin injection signal at 80 K (right). The solid line is a fit to the MCD. After [4.12]

appreciably out of plane. When spin polarised electrons are injected from the FM into the SC, the average electron spin $\mathbf{S} = \Sigma s_i/n$ of all individual electron spins s_i precesses about the applied magnetic field in the SC with the Larmor frequency $\Omega = (g\mu_B/\hbar)\boldsymbol{B}$, following (4.1):

$$\frac{d\boldsymbol{S}}{dt} = \frac{\boldsymbol{S}_0}{\tau} - \frac{\boldsymbol{S}}{T_S} + \Omega \times \boldsymbol{S}, \tag{4.1}$$

where g is the effective Landé factor, μ_B is the Bohr magneton, $\boldsymbol{S}_0$ is the average electron spin of injected electrons, τ is the lifetime of electrons due to electron-hole recombination, and T_S is the spin lifetime. The last term in (4.1) describes the precession of an ensemble of spins in a magnetic field. The first two terms take into account the electron and spin transport properties, respectively, in the SC. In the steady condition of $d\boldsymbol{S}/dt = 0$, (4.1) is reduced to

$$S_z(B) = S_{0x}\frac{T_S}{\tau}\frac{(\Omega T_S)^2 \cos\phi \sin\phi}{1 + (\Omega T_S)^2}. \tag{4.2}$$

Since the out of plane component $S_z(B)$ is equal to the degree of circular polarisation of light emitted in the recombination process, the spin polarisation of electrons injected into the GaAs ($\Pi = 2S_{0x} = 4S_{z\max}\tau/T_S$ for $\phi = \pi/4$) can be estimated by fitting (4.2) to the experimental EL data shown in Fig. 4.6 (parameters used: $S_{0x}T_S/\tau = 2.3\%$, $T_S = 0.20$ ns). In this ingenious approach, the spin polarisation of electrons injected into the GaAs was obtained to be $\Pi = (\tau/T_S) \times 9.2\%$ at 80 K in a CoFe/AlO_x/(Al,Ga)As/GaAs structure, with $\tau/T_S > 1$.

4.1.4 Theoretical Issues in Designing Spin Electronic Devices

As mentioned in the introduction to this chapter, Schmidt et al. have suggested that there may be a fundamental obstacle to achieving efficient spin transmission across a FM metal/SC interface via a diffusive process [4.8]. Using a two-current model, they show that the spin polarisation of the current in the semiconductor injected through the FM/SC interface is expected to be of the order 10^{-4} or smaller, due to the large conductivity mismatch between FM metals and SC, as is illustrated in Fig. 4.7. Since the conductivity of the FM is much larger than that of the SC, only a small fraction of the electrons in the FM can enter the SC and the number of electrons propagating into the SC is almost the same for each spin channel (Fig. 4.7a). This corresponds to the fact that the voltage drop occurs mainly in the SC and therefore, the same (small) current enters the SC independently of the electron spin. The total spin polarisation of the current in the SC is thus strongly decreased and expressed by $\gamma = (i^{\uparrow} - i^{\downarrow})/(i^{\uparrow} + i^{\downarrow}) = R_{FM}/R_{SC} \sim 10^{-4}$, where $i^{\uparrow}$, $i^{\downarrow}$, R_{FM}, and R_{SC} are up- and down-spin currents and the resistances of the FM and the SC, respectively. In this simple model of spin injection, any spin flip scattering between the two channels is neglected, although spin flip processes are likely to occur in the SC within a spin diffusion length of the order of micrometers. Nevertheless, a more detailed description of the electrochemical potentials of the two spin channels, in which the spin flip

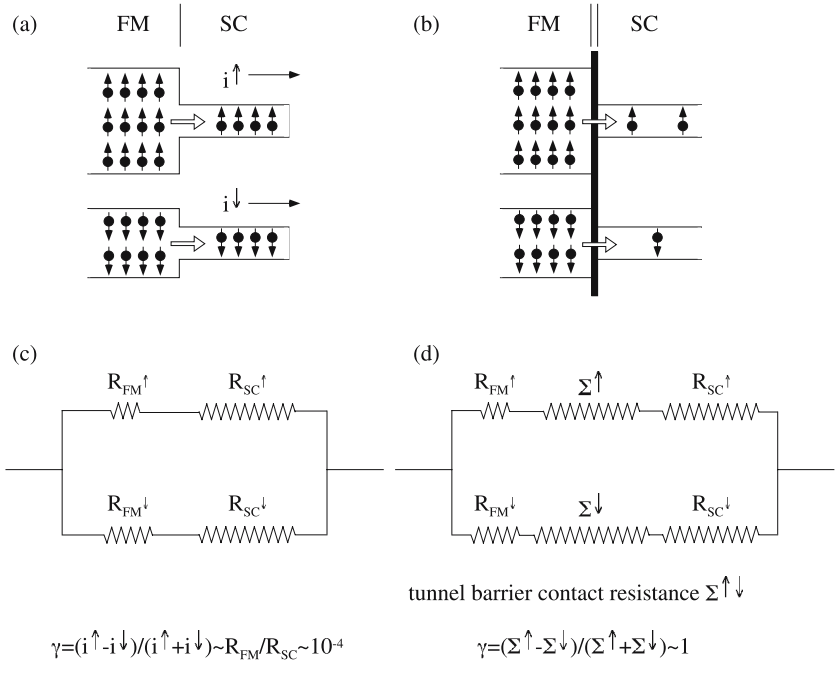

Fig. 4.7. Two-current model of (**a**) ferromagnetic metal/semiconductor and (**b**) ferromagnetic metal/oxide/semiconductor devices, schematically demonstrating spin polarisation in the SC. The conductivities of the FM and the SC are represented by the width of the electron path. Schematics (**c**) and (**d**) are the corresponding resistor equivalents

process is taken into account using the diffusion equation, confirms the prediction of the model.

It has been proposed by Rashba that the conductivity mismatch can be overcome by introducing a spin dependent tunnel barrier between the FM and the SC [4.9]. In such a structure, the electron transmission probability from the FM into the SC is principally governed by the barrier, as shown in Fig. 4.7b. When the contact resistance of the tunnel barrier is comparable to or larger than the resistance of the SC, electrons tunnelling through the barrier can enter spin channels of the SC with the spin information preserved. The spin polarisation is then expressed by $\gamma \sim (\Sigma^{\uparrow} - \Sigma^{\downarrow})/(\Sigma^{\uparrow} + \Sigma^{\downarrow})$ where $\Sigma^{\uparrow}$ and $\Sigma^{\downarrow}$ are the tunnel barrier contact resistances for each spin channel, resulting in spin injection efficiencies of up to 100%.

Besides the tunnelling process, ballistic electron transport is also likely to provide a high spin injection efficiency as described by Tang et al. [4.41, 42]. Recently, Yu et al. have theoretically investigated the spin injection efficiency from a FM into a SC in a high electric field regime using the drift-diffusion equation [4.43]. In this regime, the spin diffusion length can be different, depending on the direction of the diffusion with respect to the electric field, leading to a spin diffusion behaviour that is different from that ocurring in low fields. The electric field effects then increase

the spin injection efficiency by orders of magnitude, suggesting that the conductivity mismatch can also be overcome in the high electric field regime. For the realisation of efficient spin injection between a FM and a SC, fully spin polarised materials are likely to be essential. The half metallic Heusler alloy NiMnSb [4.44] and the half metallic double perovskites Sr_2FeMoO_6 [4.45], Fe_3O_4 [4.46], and CrO_2 [4.47] are promising candidates.

The other crucially important issue in designing novel spin electronic devices is that of spin transport within the SC. Recent photoluminescence experiments reveal that there is a very long spin coherence length in GaAs (above 100 μm in *n*-GaAs at 5 K [4.3, 48]). The spin lifetime for electrons in GaAs is found to be about 10 ns and has a peak at a critical doping density, which is reported to be around 10^{24} m^{-3} [4.49]. Flatté et al. theoretically explained spin transport within a SC based on a local perturbation of the spin polarised carriers produced for example by circularly polarised photons [4.31]. For an undoped SC, a local imbalance of conduction electron spins implies a local increase in hole density. The mobility of the spin packet is dominated by that of the valence band holes, since the hole motion in a SC is in general much slower than the electron motion. With an *n*-type SC, on the other hand, a spin imbalance can be created purely within the conduction band, due to the substantial background of conduction electrons. As a consequence the spin packet mobility is considerably larger in doped SC, which is consistent with the observed long spin coherence length in *n*-type SC [4.3].

4.2 Spin Filtering Experiments in Ferromagnet/ Semiconductor Hybrid Structures

Spin injection from FM into SC has been the subject of numerous studies, as has been shown in the previous section. Another key step required for the development of spin electronic devices is that of achieving efficient detection of spin polarised electrons passing from a SC into a FM. In this section, we introduce a promising approach to detecting the spin polarisation of electrons optically excited in GaAs, i.e., spin filtering, based on the photoexcitation technique, which we have used in our recent experimental studies of spin detection.

4.2.1 Spin Filtering

Before introducing the spin filtering model, it is helpful to first review the principal photoexcited charge carrier transport processes expected in a FM metal/SC structure. We shall then consider how these processes can contribute to the spin filtering effects observed in our photoexcitation experiments.

As illustrated in Fig. 4.8a and b, most of the electrons optically generated in the GaAs flow into the bulk of the SC due to the band bending at the Schottky interface present at reverse and zero bias, while some of the excited electrons can travel into the FM metal via tunnelling or thermionic emission. The number of the electrons propagating into the FM metal increases with increasing forward bias (Fig.

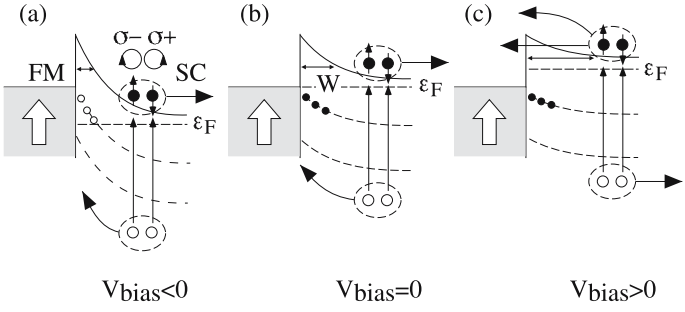

Fig. 4.8. Schematic diagram of principal photoexcited carrier transport processes at the FM metal/SC Schottky interface at reverse (**a**), zero (**b**) and forward (**c**) bias. Electrons and holes are represented by the large solid and empty circles, respectively. Recombination centres are represented by the small solid and empty circles in the vicinity of the interface

4.8c). All of these transport processes (electron tunnelling, thermionic emission, hole diffusion) could, in principle, be spin dependent. Our discussion of the spin dependent transmission process will, however, focus just on the tunnelling of electrons through the Schottky barrier. In this case it is clear that a significant spin dependence could arise, due to the large difference in spin dependent density of states (DOS) in the FM metal, as will be discussed in detail below. We will present in section 4.4 experimental evidence that electron tunnelling is the transport process responsible for the observed spin filtering effects. The probability of tunnelling through the FM metal/SC interface is determined by the Schottky barrier height and depletion layer width. The depletion layer width W is given by

$$W = \sqrt{\frac{2\varepsilon_S}{qN_D}(V_{bi} - V)}, \tag{4.3}$$

where N_D, ε_S and V_{bi} stand for the doping density, the static dielectric constant and the built-in potential across the depletion layer, respectively. For GaAs, $\varepsilon_S = 13.1\varepsilon_0$ ($\varepsilon_0 = 8.85419 \times 10^{-12}$ F/m) and $V_{bi} \approx 1.3$ eV. At zero bias, W is estimated to be in the range 3.4 nm ($N_D = 10^{25}$ m^{-3}) to 34 nm ($N_D = 10^{23}$ m^{-3}). When W is large, the electron tunnelling process is reduced due to the wide tunnel barrier, while tunnelling does not occur for very small W because of tunnel barrier breakdown.

Let us now consider the spin dependence of the transport of optically excited electrons into the FM metal. When light with right ($\boldsymbol{\sigma}^+$) or left ($\boldsymbol{\sigma}^-$) helicity excites electrons from the valence band to the conduction band in GaAs as shown in Fig. 4.9, the spin polarisation of the photoexcited electrons is opposite for $\boldsymbol{\sigma}^+$ and $\boldsymbol{\sigma}^-$, since the two helicity values correspond to opposite spin angular momentum values of the incident photon [4.16]. We shall assume that the magnetisation $\boldsymbol{M}$ in the FM is aligned perpendicular to the plane of the film or in-plane using an external field, as in our experiments. For $\boldsymbol{\sigma} \parallel \boldsymbol{M}$ (or antiparallel), the electrons in the FM and the SC share the same spin quantisation axis, while for $\boldsymbol{\sigma} \perp \boldsymbol{M}$ the two possible spin states created by the circularly polarised light are equivalent when projected

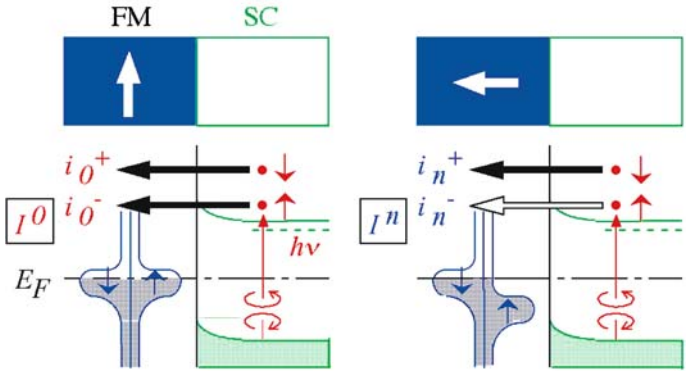

Fig. 4.9. Schematic diagrams illustrating the spin filtering mechanism for photoexcited electron transport at the FM/SC interface. I^0 and I^n correspond to the helicity dependent photocurrents for $\boldsymbol{\sigma} \perp \boldsymbol{M}$ and $\boldsymbol{\sigma} \parallel \boldsymbol{M}$, respectively; $i_0^{\pm}$ and $i_n^{\pm}$ correspond to the current components for right and left circularly polarised light illumination, respectively, for each magnetisation configuration

along the magnetisation direction in the FM. Therefore, when the magnetisation $\boldsymbol{M}$ is orthogonal to the photoexcited spin polarisation, both up- and down-spin electrons can flow from the SC into the FM with equal probabilities (Fig. 4.9 left). When $\boldsymbol{\sigma} \parallel \boldsymbol{M}$, on the other hand, the electron current across the FM/SC interface is filtered, depending on the direction of the electron spin, due to the spin split DOS in the FM [4.50–52], i.e., mainly minority spin electrons contribute to the transmitted current from the SC to the FM (Fig. 4.9 right) – this is called spin filtering. The spin filtering effect is turned on or off by controlling the relative orientations of $\boldsymbol{\sigma}$ and $\boldsymbol{M}$, and is detected as the helicity dependent photocurrent, measured by modulating the photon helicity from right to left.

It should also be noted that photoexcited electron transport from the SC into the FM includes both thermionic emission and tunnelling contributions, so that the photoexcited current across the FM/SC interface is not equal to the tunnelling current. At zero bias most of the photoexcited electrons will be pushed away from the interface due to the potential gradient (Fig. 4.8b), as mentioned above, and the net measured photocurrent will flow into the bulk of the GaAs. In other words, only a fraction of the excited electrons propagates into the FM metal (see Sect. 4.5.2). Therefore, the helicity dependent photocurrent normalised by the total photocurrent is artificially small and the spin polarisation measured in our experiments is not the simple inverse of that measured in EL experiments.

4.2.2 Spin Filtering Using Photoexcitation Techniques

In this section we describe the photoexcitation technique that we used in our spin detection studies. In order to investigate the spin dependence of the photoexcited electron current in Schottky diodes, MOS junctions, and spin and band gap engineered samples, the helicity dependent photocurrent I was measured using a circularly

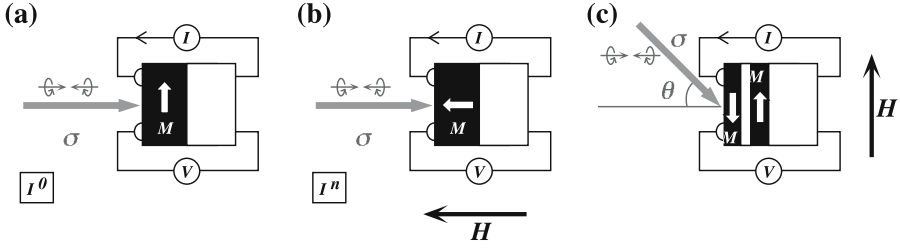

Fig. 4.10. Schematic configuration of the photoexcitation experiment used to study spin filtering. The magnetisation $\boldsymbol{M}$ in the FM and the photon helicity $\boldsymbol{\sigma}$ are shown (**a**) without applied field $\boldsymbol{H}$ (I^0), (**b**) with the field $\boldsymbol{H}$ applied normal to the film (I^n), and (**c**) with the field $\boldsymbol{H}$ applied parallel to the film in a spin valve sample

polarised laser beam together with an external applied magnetic field $\boldsymbol{H}$. The light polarisation was modulated from right to left circular using a photo-elastic modulator (PEM) operated at a frequency of 50 kHz.

The measured helicity dependent photocurrent is proportional to the difference between the current components for right and left circularly polarised light illumination: $I = p|i^+ - i^-|$, where p is a phase factor. Since the auto-phase mode of the lock-in amplifier is used in our measurements of I, the phase factor p is adjusted to be 1. As illustrated in Fig. 4.9, $i_0^+ = i_0^-$ is expected for $\boldsymbol{\sigma} \perp \boldsymbol{M}$, as there is no spin splitting in the DOS in the FM, since the magnetic quantisation axis is perpendicular to the photon helicity, while $i_n^+ \neq i_n^-$ for $\boldsymbol{\sigma} \parallel \boldsymbol{M}$ due to the spin polarisation of the DOS in the FM. In principle, the helicity dependent photocurrent I^0 should be zero and I^n should reflect the spin polarisation both in the SC and the FM. A bias voltage was applied between one Al (or Au) contact on the surface of the sample and an ohmic contact attached to the back of the GaAs substrate for FM metal/SC diode samples. The current flowing through these two pads was measured (both with and without photoexcitation), while the voltage drop across the sample was also measured using a separate top contact as shown in Fig. 4.10 [4.53, 54] (for MOS junction samples, a different planar electrode geometry was used, see Sect. 4.2.3). From the I-V curves without photoexcitation, the Schottky characteristics were studied. This set-up is basically the reverse experiment of the EL measurements at the FM/SC interface made by Alvarado and Renaud for example [4.40]. Since the laser beam enters from the Au capping layer side, laser absorption at the bottom surface of the SC, as occurs under back illumination [4.27], is avoided. Temperature dependent measurements (Sect. 4.4.4) of band gap engineered FM/AlGaAs barrier/SC structures were carried out in a constant flow liquid helium cryostat with the magnetic field applied along the plane of the FM film. The light $h\nu = 1.58$ eV was shone on the sample at an angle θ of 22.5° with respect to the plane normal. In this case the photon helicity has an in-plane component and therefore electrons with an in-plane spin polarisation component are excited in the SC. All electrical measurements, i.e., I-V characteristics, photocurrent and helicity dependent photocurrent measurements, were performed in

the same contact geometry as described above for the case of the FM/SC Schottky barrier structures.

An in-plane photoexcitation set-up was also employed to measure the spin dependent photocurrent across spin valve structures (Sect. 4.5), as shown in Fig. 4.10c. The magnetic field was applied parallel to the sample plane along the easy axis. Electrons were photoexcited in the GaAs by laser front illumination ($h\nu = 1.58$, 1.85 and 1.96 eV) incident at an angle $\theta = 45°$ from the sample plane normal. The same contact geometry as used for the FM/SC Schottky barrier samples was applied for all electrical measurements.

4.2.3 Sample Preparation

The samples used in our studies were prepared in a variety of ways, according to their structure, as described here in detail. For the FM/SC Schottky diodes, $Ni_{80}Fe_{20}$, Co and Fe layers with thicknesses of 2.5, 5.0 and 7.5 nm were directly deposited onto GaAs ($n = 3.0\times10^{23}$ and $1.5 \times 10^{24}\,m^{-3}$) substrates by molecular beam epitaxy (MBE) and capped with 3 nm thick Au layers to prevent oxidation. An antiferromagnetic (AF) Cr (5.0 nm)/GaAs sample was also prepared as a reference. The ohmic contacts on the back of the *n*-type substrates were prepared by evaporating 100 nm thick GeAuNi and then annealed at 770 K for two minutes prior to the film deposition. The GaAs substrates were cleaned for two minutes using an oxygen plasma followed by cleaning with acetone and isopropanol, and then loaded into the ultrahigh vacuum (UHV) chamber [4.55]. The FM films were grown at a rate of approximately one monolayer (ML) per minute by electron-beam (e-beam) evaporation.[3] The substrate temperature was held at 300 K and the pressure was approximately 7×10^{-10} mbar during growth. The deposition rate was monitored by a quartz microbalance which was calibrated using atomic force microscopy (AFM). After the film growth, two Al (or Au) electrical contacts (0.5 mm×0.5 mm×550 nm) were evaporated onto the Au capping layer.

In addition, a set of MOS junctions was also prepared: an Fe (3 nm)/GaAs(100) sample for comparison (1) and two samples with nominal structure Fe (3 nm)/AlO_x (5 nm)/GaAs(100) (2-a and 2-b) [4.56]. For the two latter structures, Fe layers were deposited in a UHV chamber at $\sim10^{-10}$ mbar on AlO_x (5 nm)/GaAs(100) ($n = 1\times 10^{24}\,m^{-3}$). Prior to the Fe deposition, the AlO_x layers were sputtered with an Ar plasma and annealed at 500 °C to obtain flat surfaces. Low energy electron diffraction (LEED) observations revealed that the Fe layer of sample (1) was grown epitaxially and those of samples (2-a) and (2-b) were polycrystalline. Cross-sectional transmission electron microscopy (TEM) showed that the AlO_x layer of sample (2-a) has a rough morphology compared with sample (2-b). Contacts for the electrical measurements were made using a planar electrode geometry, which enables us to probe the voltage drop at the interface only and to exclude the voltage drop associated with the electrical current flowing through the bulk of the GaAs substrate [4.56].

The FM/AlGaAs tunnel barrier/SC structures were grown by combined SC and metal MBE in two distinct UHV growth chambers. The SC part of the structure was

[3] No special preparation procedures were adopted and the film growth was polycrystalline.

grown on an n-GaAs(100) substrate under a background pressure in the low 10^{-10} mbar range at 580°C after oxide desorption at 620°C in As_2-flux. The layer sequence consists of a 200 nm GaAs buffer (Si doped, 10^{22} m^{-3}), a 2 nm undoped AlGaAs barrier, and a 2 nm GaAs spacer (Si doped, 10^{24} m^{-3}). An amorphous As layer was deposited for protection against surface oxidation during transfer, and PdGe was deposited at the back of the substrate as a contact. The metal growth took place at room temperature under a background pressure in the low 10^{-10} mbar range after first desorbing the As cap by annealing at 450 °C for 30 min and checking the surface reconstruction by LEED. A 5 nm thick NiFe magnetic layer was deposited followed by 3 nm Au to prevent oxidation.

Samples with a spin valve structure, such as Au (2 nm)/Co (2 nm)/Cu (3 nm)/NiFe (4 nm)/GaAs ($n = 10^{24}$ m^{-3}) and Au (2 nm)/Co (2 nm)/Cu (5 nm)/NiFe (3 nm)/GaAs ($n = 10^{24}$ m^{-3}), were also fabricated by MBE in a UHV system. The spin valves are polycrystalline but show a growth induced in-plane uniaxial anisotropy. The fabrication of the ohmic contacts on the bottom of the GaAs substrates, the substrate cleaning and the metal growth were performed using the same procedures as described in the preparation of the FM/SC Schottky diodes.

4.3 Spin Filtering in Ferromagnet/ Semiconductor Schottky Diodes

Four key experiments were carried out in order to verify spin polarised electron transport across FM/GaAs Schottky barrier interfaces at room temperature: the dependence of the spin filtering effect on (i) the applied magnetic field strength, (ii) the applied bias, (iii) the GaAs doping density, and (iv) the FM metal composition. Experiment (i) shows that the helicity dependent photocurrent is controlled by the magnetic properties of the FM film and that a SC related background can be ruled out in our measurements. This finding is further supported by the fact that no magnetic field dependent effects were seen in AF Cr/GaAs structures. Experiment (ii) enables us to separate MCD from the measured signal and to isolate the true spin filtering effect. We find that spin dependent electron transport from the SC into the FM occurs at forward bias, whereas at reverse bias only magneto-optical effects are observed. Varying the GaAs doping density in experiment (iii), shows that this spin filtering mechanism strongly depends on the details of the Schottky barrier, suggesting that electron tunnelling is the relevant transport process. Significant spin filtering effects were found for both NiFe/GaAs and Fe/GaAs (experiment (iv)), while MCD dominates the helicity dependent photocurrent in Co/GaAs structures.

For a basic characterisation of the samples, the I-V curves without photoexcitation were measured. Representative results for NiFe (2.5, 5.0 and 7.5 nm)/GaAs ($n = 10^{23}$ m^{-3}) are shown in Fig. 4.11. All curves show a typical Schottky behaviour, i.e., a low current level at reverse bias and a sharp increase in current once a certain onset voltage at forward bias is overcome. Furthermore, weak linear ohmic components can be identified, indicating that the samples behave as leaky Schottky diodes. However, since we use a three-contact geometry (Sect. 4.2.2) rather than

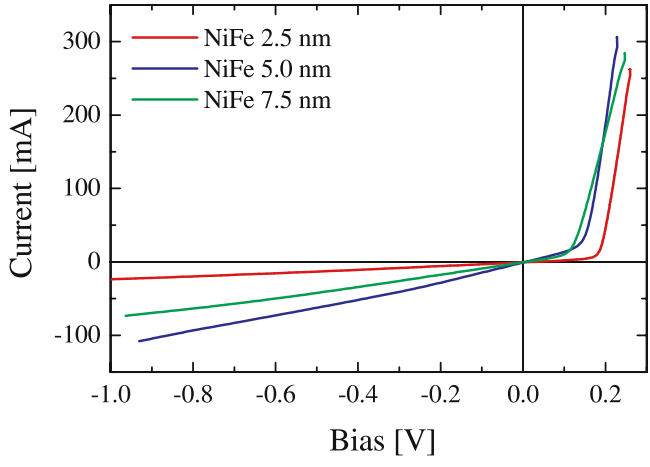

Fig. 4.11. Current-voltage characteristics without photoexcitation for the NiFe (2.5, 5.0 and 7.5 nm)/GaAs samples

a four-contact geometry, the observed ohmic behaviour could also originate from the contact resistance.

4.3.1 Applied Magnetic Field Dependence

In order to confirm that the helicity dependent photocurrent is determined by the magnetic properties of the FM layer, we carried out magnetic field dependent measurements at zero bias. Figure 4.12a shows the results for the NiFe (2.5, 5.0 and 7.5 nm)/GaAs ($n = 10^{23}$ m^{-3}) samples and the AF Cr (5.0 nm)/GaAs ($n = 10^{23}$ m^{-3}) structure. At zero magnetic field the magnetisation of the FM layer is aligned in-plane (since the easy magnetic axes lie in the plane of the sample), perpendicular to the photon helicity, and the helicity dependent photocurrent I is approximately zero, as expected (Sect. 4.2.2). With increasing applied magnetic field, I increases until it reaches saturation. A comparison of I with polar magneto-optic Kerr effect (MOKE) measurements[4] (Fig. 4.12b) shows that the saturation fields for I correspond to the saturation fields of the magnetisation, proving that the helicity dependent photocurrent is controlled by the magnetic properties of the FM layer. This is confirmed by the fact that I shows no significant applied magnetic field dependence for the AF Cr/GaAs sample. Only a small constant offset is observed, which is likely to be due to optical effects. For Cr, the net magnetisation is zero in the whole applied field range, as evidenced by MOKE (Fig. 4.12b). Any magnetic field dependent contribution to I could only arise from Zeeman splitting of the electron energy levels in the GaAs [4.11, 22]. This is, however, not observed. We can therefore conclude that there is no SC related magnetic background in our helicity dependent photocurrent measurements and that I is determined only by the magnetic properties of the FM.

[4] The MOKE loops were normalised to the saturation value of the NiFe (7.5 nm) sample.

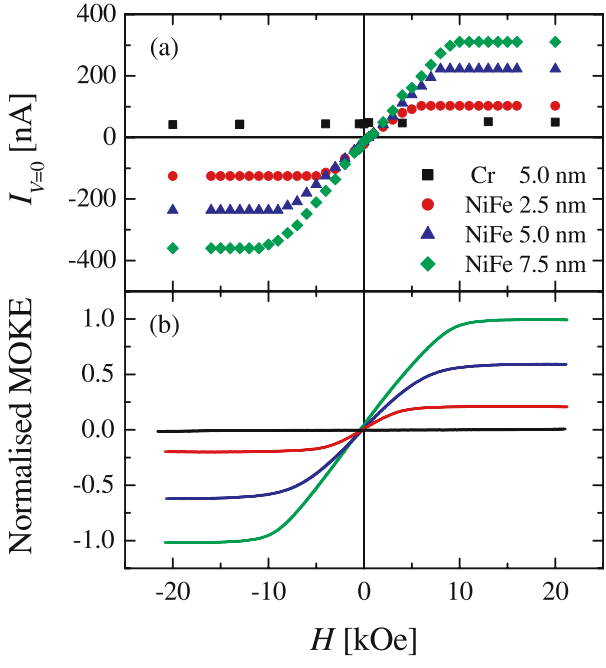

Fig. 4.12. Applied magnetic field dependence of (**a**) the helicity dependent photocurrent at zero bias and (**b**) the normalised polar MOKE signal for the NiFe (2.5, 5.0 and 7.5 nm)/GaAs ($n = 10^{23}$ m^{-3}) and Cr (5.0 nm)/GaAs ($n = 10^{23}$ m^{-3}) samples

In our measurement geometry, the light has to pass the FM layer before entering the GaAs substrate, giving rise to MCD (i.e., the difference in absorption of right and left circularly polarised light in a magnetic material [4.57]). This is illustrated in the inset of Fig. 4.14: the light attenuation coefficients in the FM layer depend on the relative alignment of photon helicity and sample magnetisation. As a consequence, an asymmetry is induced between the light intensities reaching the GaAs for right and left circularly polarised illumination (I^l_+ and I^l_-, respectively). This intensity asymmetry leads to an asymmetry of the photocurrent magnitude (between σ^+ and σ^-) that contributes to the measured helicity dependent photocurrent. Since MCD is proportional to the sample magnetisation, it could obscure or even mimic the true spin filtering signal, complicating the data analysis in earlier studies [4.23, 58]. As can be seen in Fig. 4.12a, I increases with FM layer thickness, indicating that at zero bias there might be a significant contribution due to MCD, since this effect is strongly thickness dependent. In order to study spin dependent electron transport in detail, it is crucial to remove the MCD related background. We demonstrate in the following section how this can be realised.

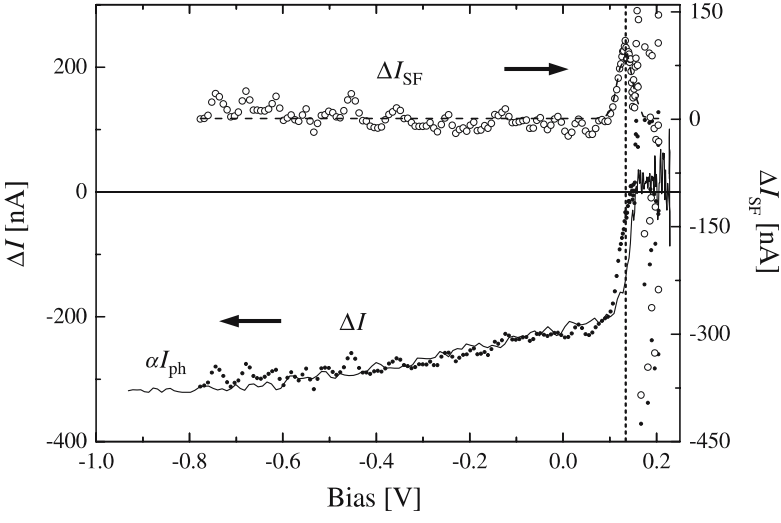

Fig. 4.13. Bias dependence of ΔI (solid circles), αI_{ph} (solid line) and $\Delta I_{\mathrm{SF}} = \Delta I - \alpha I_{\mathrm{ph}}$ (empty circles) at an applied magnetic field of 20 kOe for the NiFe (5.0 nm)/GaAs ($n = 10^{23}$ m^{-3}) sample. The dashed line is a Gaussian fit of the data. The dotted line denotes the center of the ΔI_{SF} peak

4.3.2 Applied Bias Dependence

In order to isolate the true spin filtering effect, we measured the bias dependence of the helicity dependent photocurrent and the unpolarised photocurrent I_{ph} (i.e., the photocurrent for illumination with linearly polarised light) [4.59]. At large reverse bias all photoexcited electrons propagate into the bulk of the GaAs, due to the band bending (Fig. 4.8a). Since no spin dependence can be expected for diffusive hole transport from the SC to the FM (Sect. 4.1.4), it is safe to assume that I arises purely from MCD in this bias regime. From the explanations given in the previous section, it is apparent that the MCD contribution to I is proportional to I_{ph} ($I_{\mathrm{MCD}} = \alpha I_{\mathrm{ph}}$). We can now determine α by comparing the bias dependences of I and I_{ph} at large reverse bias and then extract the spin filtering effect by subtracting αI_{ph} from I. In order to remove the small, field independent offset of I observed in Fig. 4.12a, we introduce the helicity dependent photocurrent magnitude, defined as[5] $\Delta I_H = (I_{-H} - I_{+H})/2$, with the helicity dependent photocurrents I_{-H} and I_{+H} for negative and positive applied field, respectively. Figure 4.13 shows ΔI, αI_{ph} and the spin dependent current across the SC/FM interface $\Delta I_{\mathrm{SF}} = \Delta I - \alpha I_{\mathrm{ph}}$ vs. bias at 20 kOe for the NiFe (5.0 nm)/GaAs ($n = 10^{23}$ m^{-3}) sample. The bias dependence of αI_{ph} matches that of ΔI at reverse bias and consequently $\Delta I_{\mathrm{SF}} = 0$ in this bias range, confirming that the helicity dependent photocurrent is only due to MCD. However, a distinct peak in ΔI_{SF} is observed at forward bias, coinciding with the bias range where I_{ph} and ΔI decrease steeply, i.e., where a significant part of the photoexcited

[5] Note that we use a slightly different notation here to that followed by Hirohata et al. [4.58].

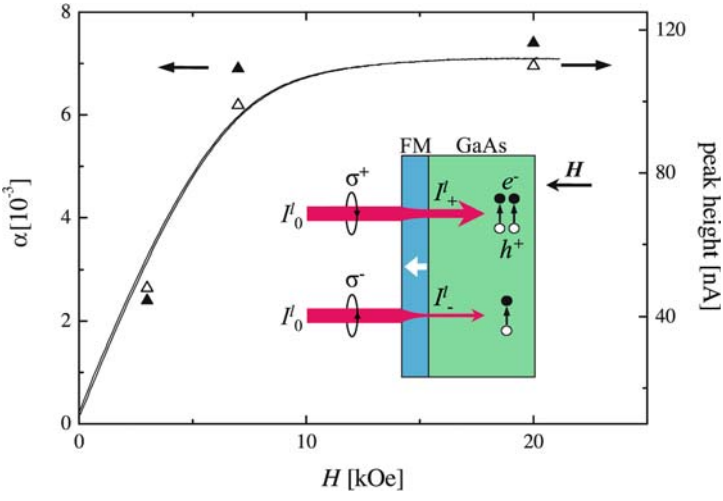

Fig. 4.14. Scaled MOKE signal (solid line), ΔI_{SF} peak height (empty symbols) and MCD parameter α (solid symbols) vs. magnetic field for the NiFe (5.0 nm)/GaAs ($n = 10^{23}$ m^{-3}) sample. In the inset a schematic of the MCD effect in FM/GaAs structures is shown. The light intensities before (I_0^l) and after attenuation in the FM layer (I_+^l and I_-^l, for illumination with right and left circularly polarised light, respectively) are indicated by the thickness of the arrows

electrons propagates into the FM layer. This observation provides clear evidence for the spin filtering of photoexcited spin polarised electrons at the SC/FM interface and adds support to our electron tunnelling picture (Sect. 4.2.1): if electrons propagating over the Schottky barrier were responsible for the measured spin filtering effect, a monotonic increase in ΔI_{SF} with increasing bias would be expected once electrons can overcome the barrier, due to an increase in current from the SC into the FM. However, if only tunnelling electrons are spin filtered at the SC/FM interface, ΔI_{SF} will start decreasing above a certain forward bias (when an increasing amount of electrons travels over the barrier) and become zero when the bands become flat. The ΔI_{SF} peaks are observed for all applied magnetic fields and the peak height scales with the sample magnetisation, as is illustrated in Fig. 4.14.

It is easy to show that α is given by $\alpha = 2(I_+^l - I_-^l)/(I_+^l + I_-^l)$ and therefore a direct measure of the MCD effect. Consequently the magnetic field dependence of α closely follows that of the FM layer magnetisation (Fig. 4.14). The absolute values of α obtained in our measurements are in good agreement with the MCD reported for NiFe [4.60].

4.3.3 GaAs Doping Density Dependence

The depletion layer width (and consequently also the width of the Schottky barrier) strongly depends on the doping density of the GaAs substrate, as is apparent from (4.3). W decreases by a factor of about 3 when N_D is increased by a factor of 10. This

is reflected in the I-V characteristics for differently doped samples: while NiFe/GaAs ($n = 10^{23}$ m^{-3}) only shows a linear ohmic decrease in current in the applied reverse bias range (Fig. 4.11), Fe/GaAs ($n = 10^{24}$ m^{-3}) Schottky diodes were observed to break down at moderate reverse bias, due to electrons tunnelling from the FM into the SC.

Both the 10^{23} m^{-3} and the 10^{24} m^{-3} doped samples show peaks in ΔI_{SF} at forward bias (similar to that shown in Fig. 4.13), providing evidence for spin dependent electron transport from the SC into the FM. For the case of the higher doped structures, these peaks are shifted to lower bias values, as is expected for a tunnelling process: due to the reduced Schottky barrier width, electrons can traverse the SC/FM interface at lower energies. Furthermore the energy range where significant electron tunnelling occurs is increased, resulting in a broadening of the peaks, as is observed in our experiments.

4.3.4 Dependence on the Ferromagnetic Material

According to our model, the spin dependent electron transport process across the SC/FM interface is sensitive to the spin split DOS in the FM (Fig. 4.9) and therefore to the FM material employed. In order to study the dependence of the spin filtering effect on the FM material, different FM (NiFe, Fe and Co)/GaAs Schottky barrier structures were investigated.

Spin dependent electron transport from the SC to the FM occurs at forward bias for NiFe and Fe, whereas at reverse bias only MCD is observed. The sign of the spin filtering effect is the same in both cases, in good qualitative agreement with the form of the spin split DOS in these materials. However, since in single FM layer structures the current component flowing across the SC/FM interface cannot be separated from the net measured photocurrent at forward bias, no exact quantification of the effect can be given. This makes a more detailed comparison between the two materials difficult. Surprisingly, almost no spin filtering was observed for the case of Co (5.0 nm)/GaAs ($n = 10^{24}$ m^{-3}). The bias dependence of I suggests that the MCD effect could dominate in these structures.

4.4 Spin Filtering in Ferromagnet/ Barrier Layer/ Semiconductor Junctions

In Sect. 4.3, we discussed spin dependent electron transport across the direct FM/SC Schottky interface. Our results indicate that the observed spin filtering effect was due to electrons tunnelling through the Schottky barrier from the SC into the FM. In order to verify our model, we examined the importance of electron tunnelling for spin filtering by inserting an additional tunnel barrier at the FM/SC interface. In this section we describe measurements of FM/AlO_x tunnel barrier/SC and FM/AlGaAs tunnel barrier/SC structures in which the electron tunnelling process can be separated from other transport mechanisms, allowing for a detailed study of the spin dependent processes involved in spin filtering.

4.4.1 Role of Barrier Layer in Spin Filtering

The important role of electron tunnelling has been demonstrated by Hanbicki et al. for the case of electrical spin injection into an AlGaAs/GaAs quantum well structure, in which a spin injection efficiency of 32% at 4.5 K was observed [4.61]. A similar enhancement of the spin injection efficiency is also reported by Motsnyi et al. [4.12]. Figure 4.15 schematically illustrates the principal photoexcited carrier transport processes at the interface of a MOS junction. In a Schottky diode, photoexcited electrons flow into the GaAs bulk while holes are collected in the Fe layer at reverse bias as shown in Fig. 4.8, although some photoexcited electrons can tunnel into the FM layer. At a sufficiently large value of forward bias, most of the photoexcited electrons in the SC flow over the Schottky barrier, in which case no spin filtering effect is expected due to the diffusive nature of the transport process, as has been theoretically suggested by Schmidt et al. [4.8]. In the MOS structure, on the contrary, the insertion of an AlO_x barrier layer between the FM and the SC changes the transport mechanism, in particular at forward bias. As we show, the photoexcited electrons are now transmitted through the barrier via a tunnelling process instead of being transported over the barrier, resulting in efficient spin filtering at the interface. This suggests that the presence of an oxide barrier enhances the resultant spin filtering effect due to spin dependent tunnelling at the interface. The introduction of a tunnelling barrier at the FM/SC interface is likely to prove to be a viable approach to enhancing spin filtering.

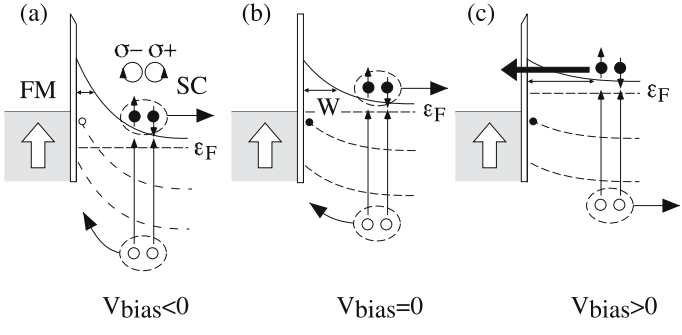

Fig. 4.15. Schematic diagram of the principal photoexcited carrier transport processes at the FM/AlO_x/SC interface at reverse (**a**), zero (**b**) and forward (**c**) bias

4.4.2 Electrical Transport Across the Ferromagnet/Semiconductor Interface

We examine the electrical transport properties of an Fe (3 nm)/GaAs(100) structure (1) and two independent samples of the nominal structure Fe (3 nm)/AlO_x (5 nm)/GaAs(100) (2-a and 2-b) in this section. The *I*-*V* characteristics indicate that the leakage current at reverse bias is pronounced for the epitaxially grown sample (1). This could be caused by the Ga-rich GaAs(100) surface, due to As desorption during

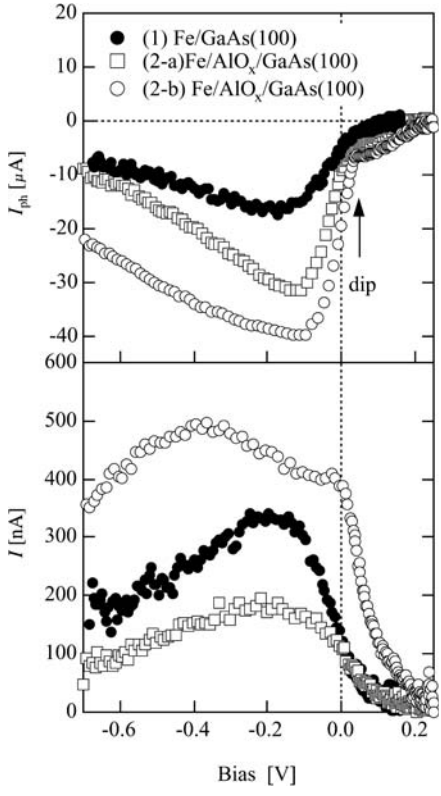

Fig. 4.16. Photocurrent and helicity dependent photocurrent as a function of bias voltage, measured at saturation field of 20 kOe applied perpendicular to the film plane

the annealing process at 500 °C [4.62]. On the other hand, the AlO_x layers prevent desorption in the samples (2-a) and (2-b), giving less leakage current at reverse bias. The difference in the I-V curves between (2-a) and (2-b) is likely to be due to the specific morphology of the AlO_x layer, specifically the flatter AlO_x interface of (2-b) provides the better rectification.

Figure 4.16 (upper panel) shows the measured photocurrent I_{ph} as a function of bias voltage at the interface. A negative photocurrent is observed as seen earlier in NiFe [4.63], Co [4.64] and Fe samples [4.23]. This is consistent with the typical energy band characteristics of the metal-semiconductor diode: the band curvature in the depletion region of the semiconductor causes the photoexcited electrons in the GaAs to flow into the GaAs bulk while simultaneously excited holes are collected in the Fe layer. The photocurrent shows a broad peak at -0.15 V and decreases with increasing reverse bias. This feature can be interpreted as a consequence of the recombination of electrons and holes at the interface: as the reverse bias is increased, the recombination centres with bounding energies just below the Fermi level "start" releasing their bound electrons (see Fig. 4.15). The positively charged recombination

centres then trap electrons from the Fe layer and holes excited by the light irradiation simultaneously. The release and trap processes effectively suppress the photocurrent. These processes occur in both types of structure, with or without the AlO_x layer. Assuming that the recombination centres are associated with the defects created in the annealing process, the capture cross sections for electrons and holes are expected to be larger in sample (1) due to the As desorption. This mechanism explains the I-V characteristics of sample (1) which exhibits a significant leakage current at reverse bias. Of most importance is the observation of a dip in the photocurrent at 0.04 V for samples (2-a) and (2-b). We attribute this feature to the transport of photoexcited electrons through the interface from the GaAs into the Fe, because the hole contribution should not depend on the bias. There are two possible mechanisms for this electron transport process, namely (1) thermally assisted transport over the Schottky barrier and/or the AlO_x insulating barrier and (2) tunnelling through the barriers. The transmission probability of the former mechanism is determined by the height of the barrier, while the latter mechanism depends on a combination of the barrier height and width. As the effective height of the Schottky barrier reduces monotonically with increasing forward bias, the former mechanism cannot explain the dip seen in the photocurrent. The barrier width, on the contrary, increases with increasing forward bias, indicating the existence of an optimum bias for the electrons to tunnel through the barrier. Thus, the tunnelling of the excited electrons through the barrier is most likely to occur at a forward bias value determined by a subtle balance between the barrier height and width. The tunnelling is seen to be optimal in our AlO_x structures at around 0.04 V, giving rise to the dip in photocurrent.

4.4.3 Spin Dependent Transport Across the Ferromagnet/Semiconductor Interface

Figure 4.16 (lower panel) depicts the helicity dependent photocurrent I for an applied magnetic field of 20 kOe, which almost saturates the Fe film perpendicularly to the film plane. For samples (1) and (2-a), I exhibits a single peak at around -0.15 V, similar to the bias dependence of the photocurrent shown in Fig. 4.16 (upper panel). On the other hand, the helicity dependent photocurrent of sample (2-b) has a broad maximum at -0.38 V and a shoulder at zero bias, behaving therefore distinctly differently from the corresponding photocurrent in Fig. 4.16 (upper panel). Since the helicity dependent photocurrent increases proportionally with the number of excited electrons, i.e., the photocurrent, the helicity dependent photocurrent normalised by the corresponding photocurrent $I/2I_{\mathrm{ph}}$ provides a rough measure of the spin filtering of electrons propagating to the FM, allowing for a qualitative comparison between the different samples. Figure 4.17 shows the normalised helicity dependent photocurrent as a function of bias voltage at 20 kOe. The sharp drop of the normalised helicity dependent photocurrent for the sample (1) at $\sim$ 0.12 V is due to the vanishing photocurrent I_{ph} at around V_b. Interestingly, however, a peak in $I/2I_{\mathrm{ph}}$ is seen at 0.04 V for the samples (2-a) and (2-b), which clearly reflects the dip in the photocurrent at 0.04 V, associated with the tunnelling process. The absence of the peak for sample (1) is due to the poor Schottky barrier, causing electrons to pass over the barrier rather

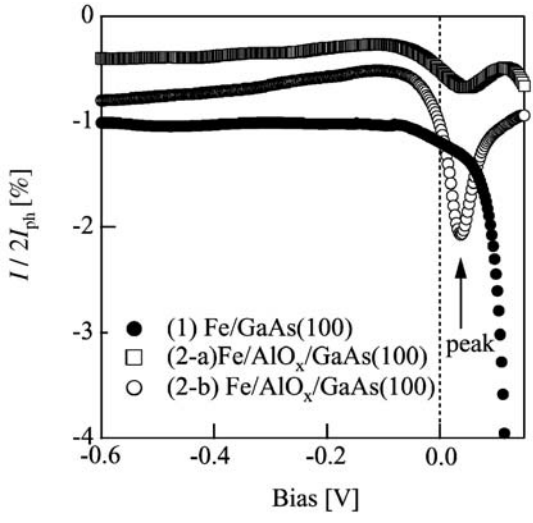

Fig. 4.17. Bias dependence of the normalised helicity dependent photocurrent at 20 kOe for the samples (1), (2-a) and (2-b)

than to tunnel. Therefore, the peak in $I/2I_{ph}$ at 0.04 V is direct evidence that efficient spin filtering occurs due to the tunnelling process at the interface in the presence of a tunnelling barrier.

In our experiment geometry (front illumination) MCD will contribute to the measured signal, as discussed in Sect. 4.3.1. The contribution of MCD was estimated from photoluminescence measurements to be $\sim$ 2.5% for a 20 nm thick Fe film [4.39], which is in good agreement with the calculation for the Fe film [4.23]. A corresponding value of 0.4% is estimated for the MCD contribution in the 3 nm thick Fe films, and an effective value for $I/2I_{ph}$ of 1.7% is estimated for the sample (2-b) at 0.04 V (the total measured value is 2.1%). The effective value is roughly comparable to the spin injection efficiency of 2% reported by Zhu et al. [4.11] Caution is needed here, however, as I_{ph} contains a large spin independent current and so the quantity $I/2I_{ph}$ is not a direct measure of the tunnelling electron polarisation, which will be larger than the value obtained in our measurements. Furthermore, MCD cannot explain the peak in the bias dependence of $I/2I_{ph}$, since the MCD effect is proportional to the unpolarised photocurrent, resulting in a constant value of $I/2I_{ph}$ in the whole applied bias range. Therefore the enhancement in $I/2I_{ph}$ is a clear manifestation of spin filtering at the FM/SC interface.

4.4.4 Spin Filtering in Band Gap Engineered Ferromagnet/AlGaAs Tunnel Barrier/Semiconductor Structures

In order to further investigate the role of electron tunnelling in spin filtering at FM/SC interfaces we used band gap engineered structures of the form Au/NiFe/GaAs/AlGaAs/*n*-GaAs that enabled us to precisely control the bias and temperature range in

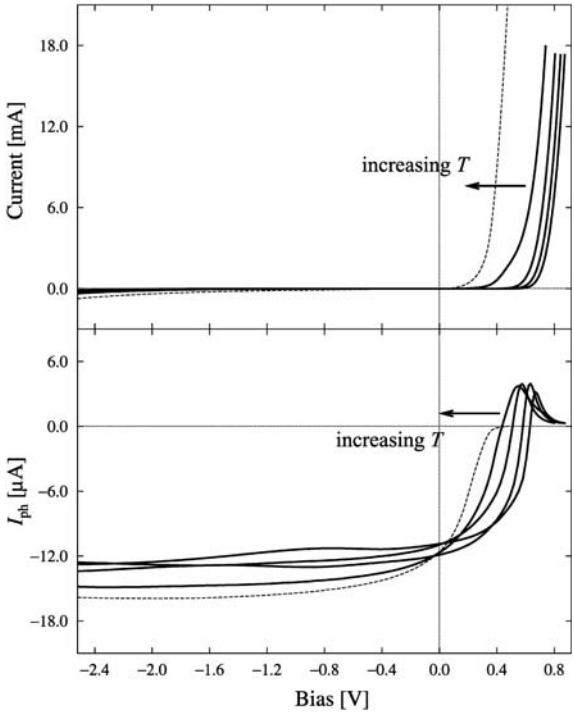

Fig. 4.18. Bias dependence of the current without photoexcitation (top) and the photocurrent induced by photoexcitation (bottom) at different temperatures of 80, 160, 240, 320 and 360 K

which tunnelling processes occur [4.65]. The basic characterisation of the structures was carried out by measuring the I-V and I_{ph}-V characteristics using standard methods described in Sect. 4.2.2. Representative results are shown in Fig. 4.18. A very small current level is seen at reverse bias, while an exponentially increasing current level is observed at forward bias above an onset voltage in the range 0.4–0.6 V. The I_{ph}-V characteristics show a rather stable negative photocurrent level at reverse bias, while a positive photocurrent peak is observed at forward bias above the onset voltage of 0.4–0.6 V. A transition is evident at a temperature of about 300 K, observed as an abrupt decrease in onset voltage and a total suppression of the photocurrent peak. In order to fully understand this behaviour, we consider a simple model of the band bending at different bias conditions as sketched in Fig. 4.19. At zero bias, electron depletion occurs, resulting in the band bending illustrated in Fig. 4.19c. This implies a negative photocurrent originating from electrons diffusing into the SC and holes tunnelling into the FM metal. As illustrated in Fig. 4.19b, a certain value of forward bias voltage V_{flat} will give rise to a flat band configuration with neither electron depletion nor accumulation. The vanishing internal electric field gives rise to a vanishing photocurrent. Fig. 4.19a shows that electron accumulation near the barrier takes over at forward bias above V_{flat}. Electrons tunnelling into the FM metal and holes diffusing

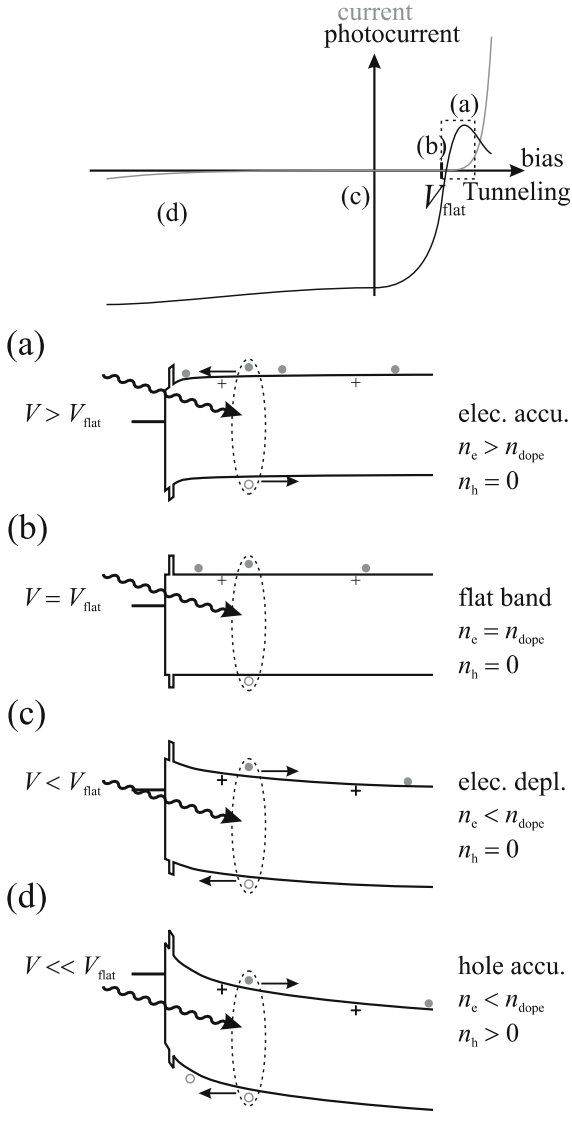

Fig. 4.19. Schematics of the band bending and the corresponding I-V and I_{ph}-V characteristics in the case of (**a**) forward bias electron accumulation, (**b**) forward bias flat band configuration, (**c**) zero bias electron depletion and (**d**) reverse bias hole accumulation

into the SC give rise to a positive photocurrent at forward bias moderately exceeding V_{flat}. As the forward bias is further increased, the electron accumulation region is narrowed, and the photocurrent decreases rapidly. In contrast, hole accumulation occurs over an extensive reverse bias range, as illustrated in Fig. 4.19d, causing less pronounced variations in photocurrent as the bias is changed.

A comparison of the results of the measurements shown in Fig. 4.18 with the model in Fig. 4.19 allows for an identification of the bias regime in which electron tunnelling occurs for both current and photocurrent. This is the case for forward bias values slightly above V_{flat}, as sketched in Fig. 4.19a, which correspond to the photocurrent peaks in Fig. 4.18 at about 0.4–0.8 V. The strong reduction in onset voltage at about 300 K indicates that thermal emission over the AlGaAs barrier becomes significant at this temperature, leaving the Schottky barrier to determine the electron transport process. Thus tunnelling is suppressed at elevated temperatures, which causes the peak in the photocurrent to vanish. The excess energy of the excited carriers has not been taken into account, since the transport processes are governed by the band bending. The excess energy is given by the difference between the excitation energy of 1.58 eV and the band gap energy, which varies with temperature in the range 1.52–1.42 eV [4.66]. The resulting excess energies of 0.06–0.16 eV are under all circumstances insufficient for overcoming the barrier height of about 0.49–0.44 eV.

The dependence of the helicity dependent photocurrent on magnetic field follows the hysteresis loop of the magnetic film with a constant offset as observed in previous studies [4.23, 58]. The offset is only present at non-perpendicular angles of light incidence, and its independence on the magnetic field strength proves that it arises purely from optical effects. In order to remove the contribution from the non-magnetic offset, the magnitude of the helicity dependent photocurrent ΔI at saturation is calculated, as defined in Sect. 4.3.2. Figure 4.20a shows measurements of the bias dependence of the photocurrent and ΔI at different temperatures. The bias dependences of the two currents at reverse bias match each other closely (similar to the case of the FM/GaAs Schottky barrier structures) for all temperatures, as is evident from scaling the helicity dependent photocurrent to the photocurrent (Fig. 4.20a). In contrast to that, a pronounced discrepancy is observed at forward bias, coinciding with the photocurrent peak at 0.4–0.8 V, which was identified above as the bias regime in which electron tunnelling occurs. The well-defined structure of our sample now enables us to determine the importance of the different possible transport mechanisms (hole diffusion into the FM, thermionic emission of electrons over the AlGaAs barrier, electron tunnelling across the AlGaAs barrier) for spin filtering. In order to remove the MCD related background from the measurement and to identify the true spin filtering signal, we apply the method introduced in Sect. 4.3.2. As can be seen in Fig. 4.20b, the spin dependent electron current across the SC/FM interface ΔI_{SF} is non-zero only in the electron tunnelling bias regime. The MCD parameter α is of the order 0.1% at $T = 320$ K, which is in good agreement with the results for the Schottky barrier structures (Sect. 4.3), taking into account the photon energy dependence of MCD [4.60] and the geometry of our experimental set-up (sample magnetisation and photon helicity are not parallel in the in-plane set-up).

The spin filtering efficiency can now be quantified in terms of an effective polarisation P_{eff}, defined as $P_{\text{eff}} = (\Delta I - \alpha I_{\text{ph}})/2I_{\text{ph}}$. P_{eff} is an indirect measure of the polarisation of the tunnelling electrons since the true tunnelling current cannot be separated from I_{ph} and is likely to be much smaller than the total photocurrent. It can, however, be used to determine the relative change in electron polarisation

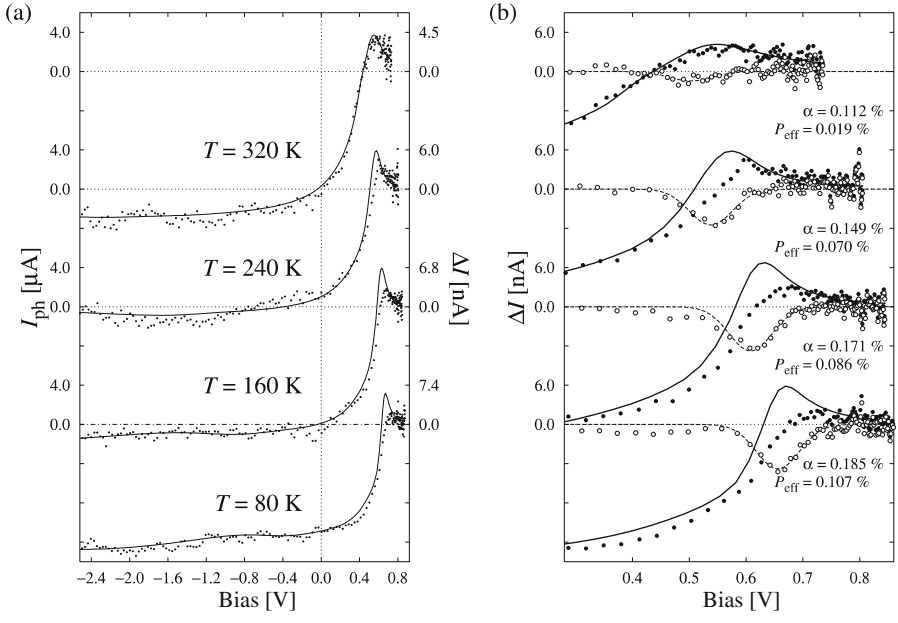

Fig. 4.20. (**a**) Comparative plots of the photocurrent I_{ph} (solid lines) and the magnitude of the helicity dependent photocurrent ΔI (points) versus bias voltage at different temperatures. (**b**) Separation of the total helicity dependent photocurrent ΔI (solid dots) into the magneto-optical contribution αI_{ph} (solid lines) and the contribution due to spin filtering $\Delta I_{SF} = \Delta I - \alpha I_{ph}$ (open circles). Values for the MCD parameter α and the effective polarisation P_{eff} are also shown. The dashed line is a guide to the eye, and the sequence of temperatures is the same as that shown in (**a**)

with temperature. We found that P_{eff} is of the order 0.1% at 80 K and decreases with increasing temperature. At about 320 K, where thermionic emission significantly contributes to the transport process, as pointed out above, P_{eff} approaches zero. As shown in Fig. 4.20b, practically no spin filtering was observed at this temperature. Hence any spin dependent contribution of electrons thermionically emitted over the barrier to the spin filtering process can be ruled out. We can therefore infer from our combined data that only tunnelling electrons show a significant spin dependence, in good agreement with the experiments on FM/GaAs Schottky structures (Sect. 4.3) and MOS structures (Sect. 4.4.3).

4.5 Ballistic Spin Transport in Spin Valve Structures

Successful electron spin detection in single FM layer/GaAs tunnel barrier structures has been demonstrated in Sects. 4.3 and 4.4: in all cases a spin dependent electron current from the SC to the FM was observed at forward bias. However, in these experiments the observed photocurrent modulation with applied field is still relatively

small. One very promising way of achieving a large current modulation is the spin valve transistor [4.67, 68], where hot unpolarised electrons propagate from a Si emitter to a Si collector over a metallic spin valve multilayer. The problem with this approach are the relatively low transfer ratios, i.e., the ratios of the collector-to-emitter current. It has been demonstrated [4.69], however, that the situation can be significantly improved by replacing the Schottky barrier emitter with a conventional tunnel barrier. This allows for a higher energy of the injected electrons, thus considerably increasing the output current [4.70]. These recent studies of spin valve based structures suggest that new spin filtering effects might be expected in a hybrid spin valve/SC structure, where polarised electrons enter the spin valve from the SC. In this section we discuss studies of Au/Co/Cu/NiFe/GaAs spin valve Schottky barrier structures [4.71] that enable us (i) to search for new spin filtering mechanisms and (ii) to study the ballistic electron transport processes in the FM metal. In such a structure the two FM layers can be switched independently, enabling us to distinguish between the spin filtering processes taking place at the SC/FM interface and those within the spin valve. A further advantage is that, in contrast to the case of a single FM layer/SC structure, the spin valve structure allows for a separation of the photocurrent components passing into the SC and into the FM metal multilayer. We are therefore able to quantify the observed spin filtering effect.

4.5.1 Sample Characterisation

Figure 4.21a shows a current in plane (CIP) magnetoresistance (MR) curve for the case of the Au (2 nm)/Co (2 nm)/Cu (3 nm)/NiFe (4 nm)/*n*-GaAs spin valve sample measured using the three-contact geometry shown in Fig. 4.10. The result clearly indicates a large resistance for the antiparallel configuration as is typical for spin valve structures and a minimum resistance for the parallel configuration [4.72]. The parallel to antiparallel configuration switching field is estimated to be 38 Oe, while the field required to align the magnetisations in both the FM1 (Co) and the FM2 (NiFe) layers is approximately 70 Oe as also confirmed by the hysteresis loop obtained by MOKE (Fig. 4.21b). Corresponding I-V curves for both the parallel and the antiparallel configuration are shown in Fig. 4.22a at 1.5 and 300 K. The I-V curves for both configurations (parallel and antiparallel) are almost identical at each temperature and possess large ohmic components below the Schottky barrier height ϕ_b (a leaky Schottky diode). Since this sample shows leaky I-V characteristics, pinholes may play an important role in determining the current distributions within each spin valve layer, causing the in-plane current to short to the adjacent layer through the pinholes. The observed ohmic components might also arise from the contact resistance, since we use a three-contact measurement geometry. Using a surface electrode and a back ohmic contact (across the spin valve structure, see Fig. 4.10), the MR is also measured as shown in Fig. 4.22b. The MR ratio shows a slight increase at negative bias and decreases rapidly above $V \sim \phi_b$. The MR behaviour indicates that the Schottky diode is switched "on" for $V > \phi_b$, causing the MR to vanish due to current shunting. For $V < \phi_b$, the Schottky diode is "off" and spin valve effects are observed.

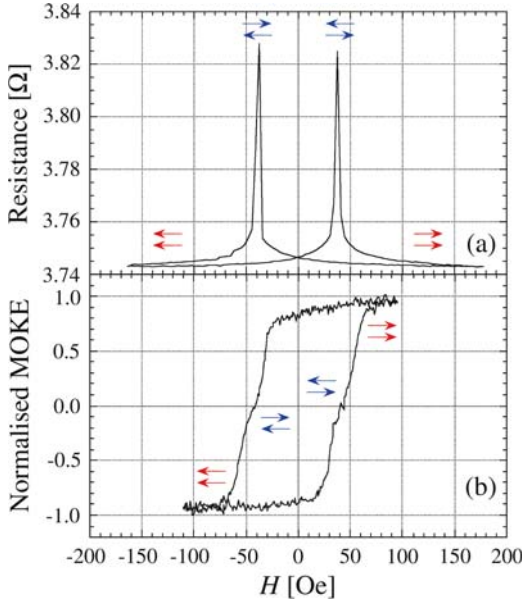

Fig. 4.21. (**a**) CIP-MR curve and (**b**) MOKE loop of the Au (2 nm)/Co (2 nm)/Cu (3 nm)/NiFe (4 nm)/GaAs(100) ($n = 1.5 \times 10^{24}$ m^{-3}) spin valve sample showing both parallel and antiparallel configurations at 300 K

This behaviour suggests that the MR is predominantly due to CIP-MR. The electron transport in our measurement geometry is likely to be a combination of CIP and current perpendicular to the plane (CPP) components; the CPP contribution is largely suppressed due to the relatively large top contact diameter ($\sim$ 0.5 mm), so that the CIP contribution dominates the measurement. The small decrease in the MR ratio at negative bias is related to the density of states in the FM layers [4.51, 52].

4.5.2 Optical Measurements of Spin Valve Structures

Photocurrent and helicity dependent photocurrent across the spin valve/SC structures were measured as described in detail in Sect. 4.2.2. All optical measurements discussed in this section were carried out at zero applied bias. Here we show representative results for the Au (2 nm)/Co (2 nm)/Cu (5 nm)/NiFe (3 nm)/n-GaAs(100) spin valve structure. Qualitatively the same behaviour was found for the Au (2 nm)/Co (2 nm)/Cu (3 nm)/NiFe (4 nm)/n-GaAs(100) sample, however, different absolute values of photocurrent arise due to the modified layer thicknesses, as expected. For illumination with linearly polarised light ($\lambda = 632.8$ nm), Fig. 4.23a, we observed symmetric photocurrent peaks for the two antiparallel states of the spin valve. These peaks arise due to unpolarised photoexcited electrons passing from the SC into the spin valve and are a consequence of the conventional GMR effect only: unpolarised electrons entering the spin valve are scattered according to the relative alignment of

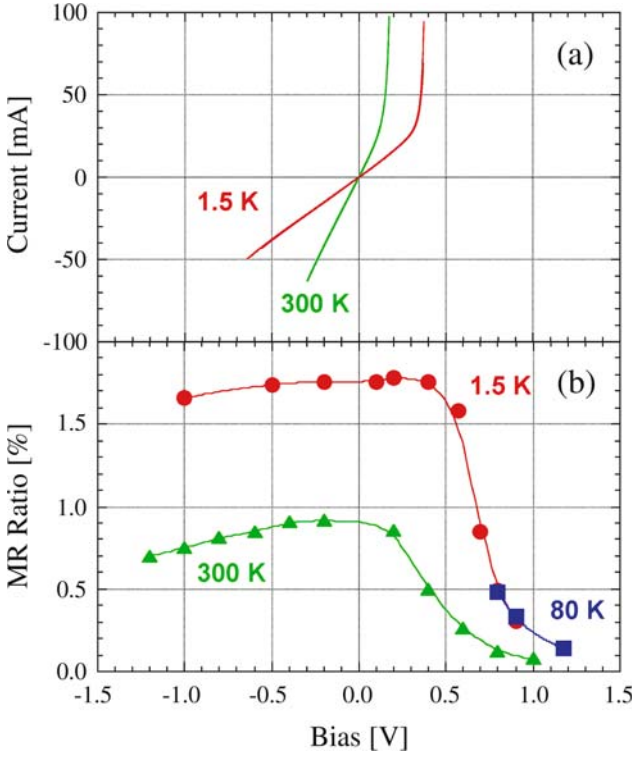

Fig. 4.22. (**a**) *I*-*V* curves in both parallel and antiparallel configurations (overlapping) and (**b**) MR curves of the Au (2 nm)/Co (2 nm)/Cu (3 nm)/NiFe (4 nm)/GaAs(100) (n=1.5×10^{24} m^{-3}) spin valve sample at 1.5, 80 and 300 K

the two FM layers. The finding of peaks instead of dips shows that the net measured photocurrent at zero bias flows into the bulk of the GaAs. In contrast to the case of a single FM layer on GaAs (Sect. 4.3), the use of a spin valve now enables us to separate the contribution of the photocurrent passing from the SC into the spin valve from the net measured photocurrent, allowing for a detailed study of the different transport processes involved in our experiment. Comparing the relative change in photocurrent between the parallel and the antiparallel alignment of the spin valve (Fig. 4.23) with the GMR ratio for CIP transport, we find that only 2.6% of the total photocurrent generated in the SC pass across the FM/SC interface into the spin valve. The finding that only a small fraction of the photoexcited electrons contributes to the spin filtering process at zero bias is not surprising since most of the electrons are expected to be pushed into the bulk of the GaAs due to the potential gradient forming at the FM/SC interface. For illumination with circularly polarised light (Fig. 4.23b), using a $\lambda/4$ plate, we find a significant asymmetry induced in the photocurrent peaks for the two antiparallel spin valve states. Switching the circular light polarisation from left to right reverses the observed asymmetry, showing that the spin filtering

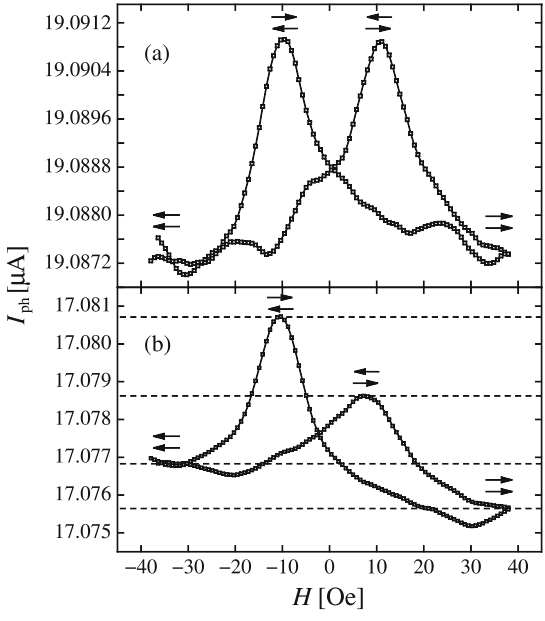

Fig. 4.23. Photocurrent vs. applied magnetic field at zero applied bias and $\lambda = 632.8$ nm for the Au (2 nm)/Co (2 nm)/Cu (5 nm)/NiFe (3 nm)/*n*-GaAs(100) spin valve sample for (**a**) illumination with linearly polarised light and (**b**) illumination with circularly polarised light. The solid line is a guide to the eye. The dashed lines and the arrows denote the parallel and antiparallel states of the spin valve

process in the spin valve structure is dependent on the initial polarisation of the photoexcited electrons. In a very simple qualitative model the existence of an asymmetry might be expected to originate from a simple combination of spin filtering at the SC/FM interface (as observed in single FM layer/SC structures, Sect. 4.3) and GMR (Fig. 4.23a). In this case the photocurrent from the SC into the spin valve would depend on the relative alignment of the photoexcited electron spin with the magnetisation of the first FM layer (NiFe). As a consequence, for a given circular light polarisation, the $\uparrow\uparrow$, $\downarrow\uparrow$ configurations[6] would no longer be equivalent to the $\downarrow\downarrow$, $\uparrow\downarrow$ configurations, respectively, resulting in an asymmetry of the GMR peaks as observed (Fig. 4.23b). However, while these d.c. measurements give the qualitative dependence of the polarised photocurrent on magnetic field, they cannot be used for a quantitative description, due to possible inaccuracies in the alignment of the $\lambda/4$ plate and drift effects at saturation. Moreover we shall now show that a quantitative analysis based on a.c. measurements rules out the validity of this simple model.

In order to circumvent the problems discussed above, we used a photo-elastic modulator to switch between left and right circular polarisation of the light and a lock-in amplifier to detect the signal as described in detail in Sect. 4.2.2. Figure 4.24 shows

[6] Here $\uparrow\uparrow$ and $\downarrow\uparrow$ refer to the negative magnetic field range in Fig. 4.23 and 4.24, respectively.

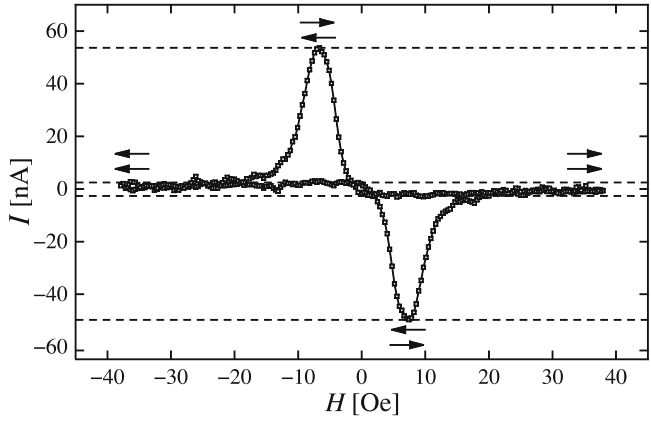

Fig. 4.24. Helicity dependent photocurrent vs. applied magnetic field at zero applied bias and $\lambda = 632.8$ nm for the Au (2 nm)/Co (2 nm)/Cu (5 nm)/NiFe (3 nm)/n-GaAs(100) spin valve sample. The solid line is a guide to the eye. The dashed lines and the arrows denote the parallel and antiparallel states of the spin valve

the measured helicity dependent photocurrent dependence on applied magnetic field at zero bias for $\lambda = 632.8$ nm. We observed a relatively small change in I between the two parallel configurations of the spin valve, but found a much larger change between the two antiparallel states (Fig. 4.24): $I(\downarrow\uparrow) - I(\uparrow\downarrow)$ is about 25 times larger than $I(\uparrow\uparrow) - I(\downarrow\downarrow)$. The height of the peaks seen for the two antiparallel states in Fig. 4.24 corresponds to the asymmetry of the photocurrent peaks (Fig. 4.23b) for illumination with right and left circularly polarised light, respectively. The observation of a $\sim 2400\%$ increase in helicity dependent photocurrent on switching the spin valve from parallel to antiparallel alignment clearly rules out a simple superposition of spin filtering at the SC/FM interface and conventional GMR in the spin valve. In this case changing the alignment of the second magnetic layer (Co) would only weakly modulate the photocurrent (due to GMR), resulting in a relative change of helicity dependent photocurrent between the parallel and the antiparallel configuration of the spin valve of about 8% at most[7] [4.73]. The strong dependence of the helicity dependent photocurrent on the alignment of the Co layer shows that the spin dependent transport process is not purely an interface effect and that spin filtering within the metal structure plays an important role. As pointed out above, the possibility of separating the photocurrent across the spin valve from the net measured signal allows us to quantify the observed spin filtering effect. We are therefore able to give a lower limit for the spin polarisation of the photocurrent passing the spin valve $S(\sigma)$ defined as

$$S(\sigma) = \frac{I^{+}_{\mathrm{SV}}(\sigma) - I^{-}_{\mathrm{SV}}(\sigma)}{I^{+}_{\mathrm{SV}}(\sigma) + I^{-}_{\mathrm{SV}}(\sigma)}, \tag{4.4}$$

[7] We give the value for CPP GMR here as an upper limit.

where I_{SV}^{+} and I_{SV}^{-} are the components of the photocurrent propagating across the SC/FM interface into the spin valve for the case of right and left circularly polarised light illumination, respectively. Here $\sigma = \uparrow\uparrow, \downarrow\downarrow, \downarrow\uparrow, \uparrow\downarrow$ denotes the possible states of the spin valve. We find that $S(\downarrow\uparrow, \uparrow\downarrow) \approx +(-)\ 5.9\%$ for the two antiparallel configurations of the spin valve which is more than 28 times larger than the value for the two parallel states $S(\uparrow\uparrow, \downarrow\downarrow) \approx +(-)\ 0.2\%$. In the case of a simple superposition of spin filtering at the SC/FM interface and conventional GMR in the spin valve, S would *only* be dependent on the alignment of the first magnetic layer (NiFe) with respect to the photon helicity irrespective of the configuration of the spin valve. The strong dependence of S on the relative alignment of the two FM layers suggests that ballistic electrons propagating through the potential energy "landscape" of the spin valve are involved in the spin filtering process. Furthermore the spin polarisation of 5.9% observed in the antiparallel state shows that this transport mechanism is highly spin dependent, since for illumination with He-Ne laser light the spin polarisation of the electrons photoexcited in the GaAs is $\leq 10\%$ [4.16]. Therefore these electrons must be spin filtered in the spin valve structure with a high degree of efficiency. The observed spin filtering effect resembles the reverse effect reported by Rippard and Buhrman [4.74], in which spin filtering of ballistic electrons transmitted through ultrathin Co films is identified from I-V measurements on Co/Cu/Co structures. For very thin (approximately 0.3 nm) Co layers, minority spin polarised electron transport across the Co/Cu interface has been reported below ~ 1.2 eV, while majority spin transport has been observed for both very thin Co layers with energies above ~ 1.4 eV and thicker Co layers (> 0.3 nm). These spin polarised electron transport effects are due to both the spin split density of states in Co and the electron spin attenuation length. Our picture of ballistic electron spin filtering is further supported by the photon energy dependence of the helicity dependent photocurrent. Figure 4.25 shows the variation of I with the applied magnetic field for three different photon energies of (a) 1.96 eV, (b) 1.85 eV and (c) 1.58 eV. In the first two cases the energy of the photoexcited electrons lies above the Schottky barrier height whereas in the latter case it lies below, as depicted in Fig. 4.25 (top). As can be seen, the relative height of the helicity dependent photocurrent peaks at antiparallel alignment decreases with decreasing photon energy (Fig. 4.25a and b) although the spin polarisation of the electrons excited in the GaAs is increased to about 20% [4.16]. For $h\nu = 1.58$ eV (Fig. 4.25c), the peaks disappear, suggesting that either very few electrons travel across the SC/FM interface or that this electron transport process is only weakly sensitive to the relative alignment of the initial spin polarisation in the GaAs and the magnetisation of the Co layer. We conclude that, in contrast to single FM layer/SC structures where electron tunnelling was found to be the dominant spin dependent transport mechanism (Sect. 4.4), ballistic electron spin filtering is responsible for the observed effects in the spin valve/SC structures. In this case spin polarised electrons are excited in the GaAs, enter the spin valve above the Schottky barrier and ballistically propagate through the metal layers.

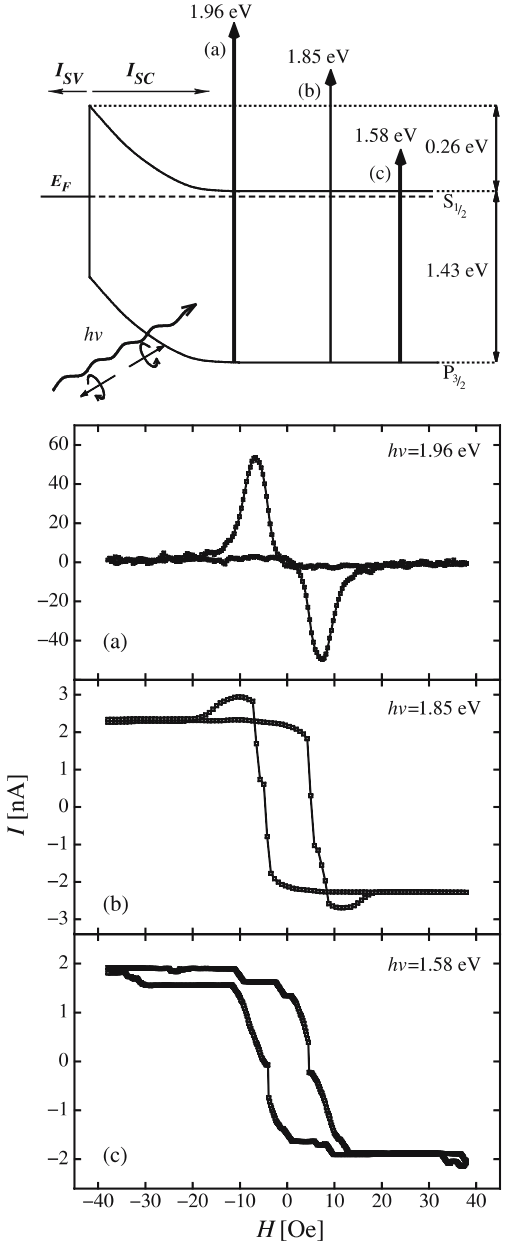

Fig. 4.25. Schematic of electron photoexcitation in the GaAs close to the Schottky barrier for three different photon energies (top). Note that transitions from the split-off spin-orbit band are not shown. Here $S_{1/2}$ and $P_{3/2}$ denote the conduction and light/heavy hole valence bands, respectively. I_{SV} and I_{SC} indicate the current components flowing into the spin valve and into the bulk of the SC, respectively. Helicity dependent photocurrent vs. applied magnetic field for photon energies of (**a**) 1.96 eV, (**b**) 1.85 eV and (**c**) 1.58 eV

4.6 Summary

We have discussed in detail evidence for room temperature spin filtering of spin polarised electrons at the FM/SC interface, in the context of optical studies of spin injection and detection. Hybrid FM/GaAs Schottky barrier structures with different FM layer materials, thicknesses and GaAs doping densities were investigated, as well as an AF Cr sample for reference. The magnetic field dependence of the helicity dependent photocurrent follows that of the polar MOKE signal in all cases, showing that I is determined by the magnetic properties of the FM layer. Any magnetic background from the SC substrate can therefore be ruled out. This is confirmed by the fact that no magnetic field dependent signal was observed for the Cr sample. A comparison of the bias dependence of I with that of the unpolarised photocurrent enabled us to separate MCD from the measured helicity dependent photocurrent and to isolate the true spin filtering signal ΔI_{SF}. We find that at reverse bias, when most of the photoexcited electrons travel into the bulk of the SC, I arises purely due to MCD. However, a peak in ΔI_{SF} is observed at forward bias, providing clear evidence for the spin filtering of spin polarised electrons propagating across the SC/FM interface. The finding of peaks instead of a monotonic increase in ΔI_{SF} with bias suggests that electron tunnelling is the spin dependent transport mechanism. A comparison of ΔI_{SF} for samples with different doping densities shows that peak position and peak width are strongly dependent on the depletion layer width and consequently the Schottky barrier width, as would be expected for a tunnelling process. Significant spin filtering is observed for both NiFe and Fe, whereas magneto-optical effects dominate in Co/GaAs structures.

In order to study the spin filtering mechanism at the FM/SC interface in more detail and to confirm our electron tunnelling model, MOS structures were investigated. The dip in the bias dependent photocurrent observed at forward bias is indicative of the tunnelling of photoexcited electrons from the GaAs into the Fe layer through the AlO_x barrier. Correspondingly, the helicity dependent photocurrent normalised by the photocurrent $I/2I_{\mathrm{ph}}$ clearly shows a peak at the same forward bias value, i.e., the spin filtering effect is enhanced in the structures with the AlO_x barrier due to spin polarised electron tunnelling. Further proof of the importance of electron tunnelling for spin filtering was added by temperature dependent measurements of band gap engineered FM/AlGaAs barrier/SC structures: spin dependent effects were only observed in the bias and temperature range where electron tunnelling occurs. This finding provides clear evidence that significant spin filtering effects can only be expected for tunnelling electrons.

Furthermore we investigated spin dependent electron transport in hybrid spin valve/SC structures. A $\sim$ 2400% increase in helicity dependent photocurrent was observed on switching the spin valve from the parallel to the antiparallel configuration. The strong dependence of the spin filtering effect on the photon energy and the relative alignment of the FM layers shows that electrons ballistically propagating through the metal layer structure are involved in the transport process. The use of a spin valve instead of a single FM layer furthermore enabled us to separate the photocurrent across the FM/SC interface from the net measured signal, allowing for the observed

spin filtering effect to be quantified. For the antiparallel configuration the polarisation of the photocurrent passing the spin valve was found to be close to the expected spin polarisation of the electrons photoexcited in the GaAs. This shows that spin polarised electrons are spin filtered in the spin valve structure with a high degree of efficiency.

In summary these results unambiguously indicate that spin polarised electrons are efficiently transmitted from the SC to the FM. The investigated device structures were not designed to achieve large spin filtering efficiencies, but rather to study the underlying physical principles of spin dependent electron transport. However, the key role of electron tunnelling observed in our experiments suggests that the spin filtering effect could be significantly enhanced by eliminating the shunting current into the SC. Our current understanding of spin transport at the FM/SC interface therefore provides encouraging prospects for achieving efficient spin injection and detection in spin electronic devices using FM injector/detector electrodes at room temperature. The introduction of an insulating barrier at the interface clearly helps to achieve efficient spin injection and detection but a better understanding of the characteristics of the interface and barrier is needed. For spin detection, the spin valve structure may provide a promising basis for designing spin electronic devices, since we observed strongly spin dependent transmission effects associated with ballistic electron transport across the composite spin valve structure. Finally, the authors envisage that band gap engineering and spin engineering together offer a very promising new approach to the control of electron spins in semiconductors which is still very much at a pioneering stage.

Acknowledgement. The authors would like to thank Dr. Y.B. Xu, Dr. C.M. Gürtler, Dr. C.A.F. Vaz, Dr. W.S. Lew, Dr. S.N. Holmes, Dr. M. Tselepi, Mr K. Cooper, Dr. G. Wastlbauer, Mr A. Ionescu and Dr. S.E. Andresen for their help with the sample preparations. Thanks are also due to Dr. W.S. Cho and Prof. G.X. Chen for their assistance with experiments. It is a pleasure to thank Dr. M. Johnson, Dr. B.T. Jonker, Prof. G. Güntherodt, Dr. G. Schmidt and Dr. W.F. Egelhoff, Jr. for enlightening and fruitful discussions. This work was supported by EPSRC (UK), EU (Esprit program), Toshiba Research Europe, ETRI (Korea), and the Japan Society for Promotion of Science (JSPS) Postdoctoral Fellowships Program for Research Abroad 2001.

References

4.1. G. A. Prinz. *Science*, 282:1660, 1998.
4.2. M. Johnson. *IEEE Spectrum*, 37:33, 2000.
4.3. J.M. Kikkawa and D. D. Awschalom. *Nature*, 397:139, 1999.
4.4. H. Ohno. *Mater. Integration*, 13:1, 2000.
4.5. S. Datta and B. Das. *Appl. Phys. Lett.*, 56:665, 1990.
4.6. R. Fiederling, M. Keim, G. Reuscher, W. Ossau, G. Schmidt, A. Waag, and L. W. Molenkamp. *Nature*, 402:787, 1999.
4.7. Y. Ohno, D.K. Young, B. Beschoten, F. Matsukura, H. Ohno, and D. D. Awschalom. *Nature*, 402:790, 1999.
4.8. G. Schmidt, D. Ferrand, L.W. Molenkamp, A.T. Filip, and B.J. van Wees. *Phys. Rev. B*, 62:R4790, 2000.

4.9. E. I. Rashba. *Phys. Rev. B*, 62:R16267, 2000.
4.10. A.T. Hanbicki, B.T. Jonker, G. Itskos, G. Kioseoglou, and A. Petrou. *Appl. Phys. Lett.*, 80:1240, 2002.
4.11. H.J. Zhu, M. Ramsteiner, H. Kostial, M. Wassermeier, H.-P. Schönher, and K. H. Ploog. *Phys. Rev. Lett.*, 87:016601, 2001.
4.12. V.F. Motsnyi, J. De Boeck, J. Das, W. Van Roy, G. Borghs, E. Goovaerts, and V. I. Safarov. *Appl. Phys. Lett.*, 81:265, 2002.
4.13. G. Lampel. *Phys. Rev. Lett.*, 20:491, 1968.
4.14. R. R. Parsons. *Phys. Rev. Lett.*, 23:1152, 1969.
4.15. V.M. Agranovich and A. A. Maradudin. *Modern Problems in Condensed Matter Science, Volume 8*. North-Holland, Amsterdam, fourth edition, 1984.
4.16. D.T. Pierce and F. Meier. *Phys. Rev. B*, 13:5484, 1976.
4.17. I. Malajovich, J.M. Kikkawa, D.D. Awschalom, J.J. Berry, and N. Samarth. *Phys. Rev. Lett.*, 84:1015, 2000.
4.18. S. Adachi. *GaAs and Related Materials*. World Scientific, Singapore, 1994.
4.19. F. Meier and B. P. Zakharchenya. *Optical Orientation*. North-Holland Physics Publishing, Amsterdam, 1984.
4.20. M.W.J. Prins, H. van Kempen, H. van Leuken, R.A. de Groot, W. van Roy, and J. de Boeck. *J. Phys.: Condens. Matter*, 7:9447, 1995.
4.21. K. Nakajima, S.N. Okuno, and K. Inomata. *Jpn. J. Appl. Phys.*, 37:L919, 1998.
4.22. A.F. Isakovic, D.M. Carr, J. Strand, B.D. Schultz, C.J. Palmstrøm, and P. A. Crowell. *Phys. Rev. B*, 64:R161304, 2001.
4.23. A. Hirohata, S.J. Steinmueller, W.S. Cho, Y.B. Xu, C.M. Guertler, G. Wastlbauer, J.A.C. Bland, and S. N. Holmes. *Phys. Rev. B*, 66:035330, 2002.
4.24. K. Sueoka, K. Mukasa, and K. Hayakawa. *Jpn. J. Appl. Phys.*, 32:2989, 1993.
4.25. Y. Suzuki, W. Nabhan, R. Shinohara, K. Yamaguchi, and K. Mukasa. *J. Magn. Magn. Mater.*, 198-199:540, 1999.
4.26. H. Kodama, T. Uzumaki, M. Oshiki, K. Sueoka, and K. Mukasa. *J. Appl. Phys.*, 83:6831, 1998.
4.27. S. M. Sze. *Physics of Semiconductor Devices*. John Wiley and Sons, New York, second edition, 1981.
4.28. O. Pietzsch, A. Kubetzka, M. Bode, and R. Wiesendanger. *Science*, 292:2053, 2001.
4.29. S.N. Okuno, T. Kishi, and K. Tanaka. *Phys. Rev. Lett.*, 88:066803, 2002.
4.30. B.T. Jonker, Y.D. Park, B.R. Bennett, H.D. Cheong, G. Kioseoglou, and A. Petrou. *Phys. Rev. B*, 62:8180, 2000.
4.31. M.E. Flatté and J. M. Byers. *Phys. Rev. Lett.*, 84:4220, 2000.
4.32. M. Oestreich, J. Hübner, D. Hägele, P.J. Klar, W. Heimbrodt, W.W. Rühle, D.E. Ashenford, and B. Lunn. *Appl. Phys. Lett.*, 74:1251, 1999.
4.33. B.T. Jonker, A.T. Hanbicki, Y.D. Park, G. Itskos, M. Furis, G. Kioseoglou, A. Petrou, and X. Wei. *Appl. Phys. Lett.*, 79:3098, 2001.
4.34. Y.D. Park, A.T. Hanbicki, S.C. Erwin, C.S. Hellberg, J.M. Sullivan, J.E. Mattson, T.F. Ambrose, A. Wilson, G. Spanos, and B. T. Jonker. *Science*, 295:651, 2002.
4.35. T. Dietl, H. Ohno, F. Matsukura, J. Cibert, and D. Ferrand. *Science*, 287:1019, 2000.
4.36. G.A. Medvedkin, T. Ishibashi, T. Nishi, K. Hayata, Y. Hasegawa, and K. Sato. *Jpn. J. Appl. Phys.*, 39:L949, 2000.
4.37. H. Ohno. *Science*, 281:951, 1998.
4.38. Th. Gruber, M. Keim, R. Fiederling, G. Ossau, G. Schmidt, and L. W. Molenkamp. *Appl. Phys. Lett.*, 78:1101, 2001.
4.39. T. Manago and H. Akinaga. *Appl. Phys. Lett.*, 81:694, 2002.

4.40. S.F. Alvarado and P. Renaud. *Phys. Rev. Lett.*, 68:1387, 1992.
4.41. H.X. Tang, F.G. Monzon, R. Lifshitz, M.C. Cross, and M. L. Roukes. *Phys. Rev. B*, 61:4437, 2000.
4.42. P. Mavropoulos, O. Wunnicke, and P. Dederichs. *Phys. Rev. B*, 66:024416, 2002.
4.43. Z.G. Yu and M.E. Flatté. *Phys. Rev. B*, 66:021202(R), 2002.
4.44. G.A. de Wijs and R.A. de Groot. *Phys. Rev. B*, 64:020402(R), 2001.
4.45. K.L. Kobayashi, T. Kimura, H. Saweda, K. Terakura, and Y. Tokura. *Nature*, 395:677, 1998.
4.46. Y.S. Dedkov, U. Rüdiger, and G. Güntherodt. *Phys. Rev. B*, 65:064417, 2002.
4.47. K.P. Kämper, W. Schmitt, G. Güntherodt, R.J. Gambino, and R. Ruf. *Phys. Rev. Lett.*, 59:2788, 1987.
4.48. D. Hägele, M. Oestreich, W.W. Rühle, N. Nestle, and K. Eberl. *Appl. Phys. Lett.*, 73:1580, 1998.
4.49. J.M. Kikkawa and D. D. Awschalom. *Phys. Rev. Lett.*, 80:4313, 1998.
4.50. I. I. Mazin. *Phys. Rev. Lett.*, 83:1427, 1999.
4.51. B. Nadgorny, R.J. Soulen, Jr., M.S. Osofsky, I.I. Mazin, G. Laprade, R.J.M. van de Veerdonk, A.A. Smits, S.F. Cheng, E.F. Skelton, and S. B. Qadri. *Phys. Rev. B*, 61:R3788, 2000.
4.52. C. Li, A.J. Freeman, and C. L. Fu. *J. Magn. Magn. Mater.*, 75:53, 1988.
4.53. A. Hirohata, Y.B. Xu, C.M. Guertler, and J. A. C. Bland. *J. Appl. Phys.*, 87:4670, 2000.
4.54. J.A.C. Bland, A. Hirohata, Y.B. Xu, C.M. Guertler, and S. N. Holmes. *IEEE Trans. Magn.*, 36:2827, 2000.
4.55. Y.B. Xu, E.T.M. Kermohan, D.J. Freeland, A. Ercole, M. Tselepi, and J. A. C. Bland. *Phys. Rev. B*, 58:890, 1998.
4.56. T. Taniyama, G.W. Wastlbauer, A. Ionescu, M. Tselepi, and J. A. C. Bland. *Phys. Rev. B*, 68:134430, 2003.
4.57. A.D. Buckingham and P.J. Stephens. *Ann. Rev. Phys. Chem.*, 17:399, 1966.
4.58. A. Hirohata, Y.B. Xu, C.M. Guertler, J.A.C. Bland, and S. N. Holmes. *Phys. Rev. B*, 63:104425, 2001.
4.59. S.J. Steinmuller, C.M. Gürtler, G. Wastlbauer, and J. A. C. Bland. unpublished.
4.60. T. Manago, Y. Suzuki, and E. Tamura. *J. Appl. Phys.*, 91:10130, 2002.
4.61. A.T. Hanbicki, O. M. J. van't Erve, R. Magno, G. Kioseoglou, C.H. Li, B.T. Jonker, G. Itskos, R. Mallory, M. Yasar, and A. Petrou. *Appl. Phys. Lett.*, 82:4092, 2003.
4.62. K.D. Choquette, M. Hong, H.S. Luftman, S.N.G. Chu, J.P. Mannaerts, R.C. Wetzel, and R. S. Freund. *J. Appl. Phys.*, 73:2035, 1993.
4.63. A. Hirohata, Y.B. Xu, C.M. Guertler, and J. A. C. Bland. *J. Appl. Phys.*, 85:5804, 1999.
4.64. A. Hirohata, Y.B. Xu, C.M. Guertler, and J. A. C. Bland. *IEEE Trans. Magn.*, 35:2910, 1999.
4.65. S.E. Andresen, S.J. Steinmuller, A. Ionescu, C.M. Guertler, G. Wastlbauer, and J. A. C. Bland. *Phys. Rev. B*, 68:073303, 2003.
4.66. J. S. Blakemore. *J. Appl. Phys.*, 53:502, 1982.
4.67. D.J. Monsma, J.C. Lodder, Th.J.A. Popma, and B. Dieny. *Phys. Rev. Lett.*, 74:5260, 1995.
4.68. R. Jansen, P.S. Anil Kumar, O. M. J. van't Erve, R. Vlutters, P. de Haan, and J. C. Lodder. *Phys. Rev. Lett.*, 85:3277, 2000.
4.69. R. Sato and K. Mizushima. *Appl. Phys. Lett.*, 79:1157, 2001.
4.70. S. van Dijken, X. Jiang, and S. S. P. Parkin. *Appl. Phys. Lett.*, 83:951, 2003.
4.71. S.J. Steinmuller, T. Trypiniotis, W.S. Cho, W.S. Lew, C.A.F. Vaz, and J. A. C. Bland. *Phys. Rev. B*, 69:153309, 2004.

4.72. U. Hartmann, editor. *Magnetic Multilayers and Giant Magnetoresistence*. Springer, Berlin, 2000.
4.73. Q. Yang, P. Holody, R. Loloee, L.L. Henry, W.P. Pratt, Jr., P.A. Schroeder, and J. Bass. *Phys. Rev. B*, 51:3226, 1995.
4.74. W.H. Rippard and R. A. Buhrman. *Phys. Rev. Lett.*, 84:971, 2000.

5

Introduction to Micromagnetics

A.S. Arrott

This is an introduction to micromagnetics. It is not a review of the achievements and publications of its many practitioners. The modern computational tools of micromagnetics are compared to racing cars. I invite the reader for a spin around the track to feel the response without concern for the history of the automobile. Let us start with the spin of the electron.

5.1 First Spin Around the Track

The electron is a mysterious quantity. Its spin is most unfathomable, but without it, iron would not be the prototype of ferromagnetism. As Dirac showed, the spin and its magnetic moment follow from combining relativity with quantum mechanics. The word spin is often associated with the motion of a top. But an electron is not a top. It does not nutate. So as we start our spin around the track we will experience precession, but there is no inertia associated with the precession of an electron. Its precessional angular frequency ω is proportional to the magnetic field. The energy of a magnetic moment is proportional to the magnetic induction $\boldsymbol{B}$, which by definition determines the force on a moving charge. Line one is that the Zeeman energy is $E_Z = -\boldsymbol{\mu}_B \cdot \boldsymbol{B}$, where $\boldsymbol{\mu}_B$ is the magnetic moment of the electron. The self-energy of the electron charge is an ignorable infinity. The self-energy of the electron magnetic moment is often chosen to be $\mu_0 \mu_B^2/2$. The torque on an electron in a magnetic field is $\boldsymbol{\mu}_B \times \boldsymbol{B}$; or maybe it is $-\boldsymbol{\mu}_B \times \boldsymbol{B}$, I never remember which, for I have never done an experiment where it mattered. Classically this torque changes the angular momentum $\boldsymbol{L}$ of the electron;

$$\frac{\mathrm{d}\boldsymbol{L}}{\mathrm{d}t} = \boldsymbol{\mu}_B \times \boldsymbol{B}. \tag{5.1}$$

There is a theorem by Rabi and Schwinger that says that the classical motion of an electron in a magnetic field can be taken over into quantum mechanics without change,

provided that a quantum interpretation is given in terms of the two components of the spin. The electron always points in some direction, but we can only inquire as to its component along any particular axis at any given time. If we pick the axis correctly and find that the component of the magnetic moment is $\boldsymbol{\mu}_B$, then that is the axis of the moment. The moment is proportional and opposite to the spin angular momentum because the charge is negative. The proportionality constant γ is the gyromagnetic ratio, as in $\gamma\boldsymbol{\mu}_B = \boldsymbol{L}$. In micromagnetics the magnetic induction is replaced by the magnetic field $\boldsymbol{H}$ without changing the torque equation because the difference between $\boldsymbol{B}$ and $\boldsymbol{H}$ is along the direction of the magnetic moment. For negative γ,

$$\frac{\mathrm{d}\boldsymbol{\mu}_B}{\mathrm{d}t} = -\mid\gamma\mid \boldsymbol{\mu}_B \times \boldsymbol{H}. \tag{5.2}$$

Note that the size of the moment is irrelevant. This is a strange expression because it says that there is an instantaneous response to the changes in the magnetic field. The origin of this is in the expression $\gamma\boldsymbol{\mu}_B = \boldsymbol{L}$. Classically, the relation between two vectors, such as $\boldsymbol{\mu}_B$ and $\boldsymbol{L}$ should be expressed using an inertial tensor for γ. The gyromagnetic tensor of an electron has but one component. I don't have a reference for this, other than private communication. At an international conference I once asked the question why there is no nutation for a spin system. At the time I received no answer, but a month later, the *Father of Micromagnetics*, William Fuller Brown, Jr. sent me a letter on the subject.

I point out this problem of the gyromagnetic tensor at the beginning of the spin around the track to warn the reader of a not-uncommon occurrence in physics. The student too often wants to get to the forefront, which might be at line 376, without realizing that the forefront is sometimes at line 1. This strange feature of the electron is carried into the Landau-Lifshitz-Gilbert, LLG, formulation of the equations of motion for a system of coupled magnetic moments. *LLG Micromagnetics Simulator* [5.1] is the name of the racecar that we are taking around the track.

5.2 One Atom of Iron

5.2.1 One Atom of Iron in Space

On the first spin around the track we will look at (5.2) applied to a single atom of iron, with moment $\boldsymbol{\mu}$, first as a free atom then as an atom imbedded in a lattice of non-magnetic atoms. The introduction of the lattice brings with it magnetic anisotropy, which arises from the spin-orbit coupling of the spin of the Fe atom with the electric fields from the neighboring atoms, and damping, which also comes from interaction with the rest of the lattice and may involve spin-orbit coupling. For the free atom there is no damping and no anisotropy; the applied fields appear in (5.2) as the first of the real fields. Damping and anisotropy will appear as effective fields.

Precession. The magnetic moment precesses about the applied field $\boldsymbol{H}$, maintaining a constant component along the field, while its perpendicular components rotate with

an angular velocity ω given by

$$\omega = \gamma H. \tag{5.3}$$

If the direction of the field is maintained but its magnitude changes with time, the path of precession remains the same; only the precessional speed changes, maintaining exact proportionality to H at each instant. The total angle of precession in a given time interval is

$$\Delta\theta = \int \gamma H(t) dt. \tag{5.4}$$

When the direction of the field changes, the axis of precession changes instantly. Note that the equation of motion preserves both the magnitude of the magnetic moment and the energy. The former is because the change in moment is always perpendicular to the moment. The latter is because the change in moment is always perpendicular to the field.

Rotating Fields. Take a look at the motion of the moment $\boldsymbol{\mu}$ in a rotating field $\boldsymbol{H}$. Set the moment and the field along the x direction at the start. Let the field rotate in the (x, y) plane with angular frequency Ω. The motion in the laboratory frame of reference is complex; there are two frequencies in the response. On transformation to a frame of reference that rotates with the field, using $(\partial\boldsymbol{\mu}/\partial t)_{\text{rot}} = (d\boldsymbol{\mu}/dt)_{\text{stat}} - \Omega \times \boldsymbol{\mu}$, it is seen that on inserting (5.2), the two terms combine so that there is only $\omega_p = \sqrt{\Omega^2 + (\gamma H)^2}$ at which the moment precesses about an axis, tilted out of the plane to $\theta = \arctan(-\Omega/\gamma H)$. In the rotating frame it looks as if there is an additional field along the z-axis, $H_f = -\Omega/\gamma$. (Note $-\gamma$ is positive.)

If, for example, we choose to make θ turn out of the plane to 30° by taking $H = -\sqrt{3}\Omega/\gamma$, the precession about that axis is at twice the rate of rotation about the z-axis in the laboratory frame. This provides a simple dynamical check on the performance of an LLG program. In the laboratory frame the time dependence of the components of the moment $\boldsymbol{\mu}$ is given by

$$\mu_z = \sqrt{3}(1 - \cos 2\Omega t)\mu/4, \tag{5.5}$$

$$\mu_y = (3 \sin \Omega t + \sin \Omega t \cos 2\Omega t - 2 \cos \Omega t \sin 2\Omega t)\mu/4, \tag{5.6}$$

and

$$\mu_x = (3 \cos \Omega t + \cos \Omega t \cos 2\Omega t + 2 \sin \Omega t \sin 2\Omega t)\mu/4. \tag{5.7}$$

Note that the magnetic moment appears on both sides of (5.2) so that the units of moment do not matter here. The moment on an atom does not change during the magnetization process. The important property of the moment is its direction. The normalized components $m_x \equiv \mu_x/\mu$, $m_y \equiv \mu_y/\mu$, and $m_z \equiv \mu_z/\mu$ can be considered as components of unit vectors or as the direction cosines α_x, α_y, and α_z.

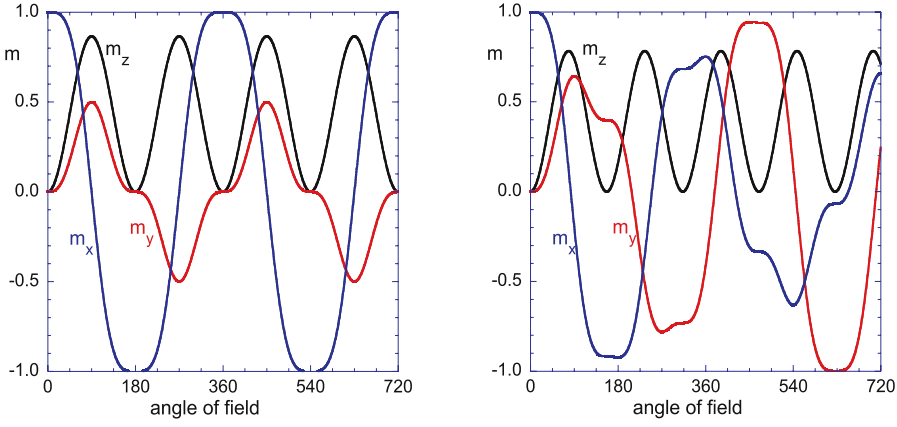

Fig. 5.1. Precession of a moment in a field H rotating at an angular frequency Ω in the (x, y) plane. In (**a**) for $H = -\sqrt{3}\Omega/\gamma$ the moment precesses at $\omega_p = 2\Omega$ about an axis tilted out of the plane by 30°. In (**b**) $\omega_p = 2.3\ \Omega$, but in the rotating frame it is still a simple precession

It is easy to derive the above results and then to plot them. It is quite another thing to look at the results for the precessing moment in Fig. 5.1a and immediately see that this is nothing more than simple precession in the rotating frame. Interpreting results of LLG can be difficult. It is not too difficult for the case shown Fig. 5.1a because the two frequencies differ by a simple factor of two. That factor of two has been changed in Fig. 5.1b to 2.3. This shows how complex a simple precession can look in the laboratory frame.

In general, for a rotating field that starts with the spin along its axis, the change in the component which was along the field at the start (μ_x in the above case) is proportional to t^4, while the component perpendicular to the plane of rotation (μ_z above) increases as t^2 and the component along the direction toward which the field is rotating (μ_y above) increases as t^3. It is necessary for the μ_z component to be finite before the in-plane field can cause rotation in the (x, y) plane. The μ_z component can increase only when there is some field component along y. Once there is some μ_z component, then the field along x gives rise to a rotation toward y. Then, as μ_y increases, μ_x decreases, slowly at first.

In thin film magnetism the fields are generally applied in the (x, y) plane. For rotation to take place there must be μ_z components. These components can serve as speedometers for the in-plane rotations. Usually the μ_z components are small because of magnetostatic self-energy, but they are necessary in the dynamic calculation. For energy minimization calculations they are generally ignorable except for singularities such as vortices; more on vortices later. The differential equations

$$d\mu_x/dt = -\gamma H \mu_z \sin \Omega t, \tag{5.8}$$

$$d\mu_y/dt = \quad \gamma H \mu_z \cos \Omega t, \tag{5.9}$$

and

$$d\mu_z/dt = \quad \gamma H[\mu_x \sin \Omega t - \mu_y cos\Omega t] \tag{5.10}$$

produced the result in Fig. 5.1a for $H = \sqrt{3}\Omega/\gamma$. In solving these differential equations it helps to know that the answer must be a simple precession in the rotating frame. Note that, if μ_z were zero, there would be no rotation in the plane.

5.2.2 One Iron Atom in a Non-magnetic Lattice

Uniaxial Anisotropy. The magnetic anisotropy is included in the equation of motion by generalizing the field H to include effective fields. An effective field H_{eff} is derived by taking the negative gradient of an energy expression with respect to the components of the magnetic moment. For an iron atom imbedded in a lattice with a strong tetragonal distortion in the z direction, the magnetic anisotropy is a uniaxial anisotropy, the energy of which is expressed in terms of the normalized components of the magnetic moment as

$$E_K = E_{K_u}\left(1 - m_z^2\right) = E_{K_u}\left(m_x^2 + m_y^2\right), \tag{5.11}$$

where E_K is the anisotropy energy per atom and E_{K_u} is the second-order uniaxial anisotropy constant per atom. A uniaxial anisotropy acts like a field but there is some arbitrariness because components of the anisotropy field along the magnetization direction produce no torques. Taking the gradient of E_K with respect to the components of the magnetization for the first expression in (5.11) produces

$$H_z = -\frac{\mathrm{d}E_K}{\mathrm{d}\mu_z} = 2E_{K_u}\frac{m_z}{\mu}, \tag{5.12}$$

while the other two components of H vanish. If we use the second expression in (5.11) for the anisotropy energy, we get nothing for H_z, while

$$H_x = -2E_{K_u}m_x/\mu \quad \text{and} \quad H_y = -2E_{K_u}m_y/\mu. \tag{5.13}$$

Either way, the torque equations are the same,

$$\frac{\mathrm{d}m_x}{\mathrm{d}t} = \gamma H_{eff} m_y, \quad \frac{dm_y}{dt} = -\gamma H_{eff} m_x, \quad \text{and} \quad \frac{\mathrm{d}m_z}{\mathrm{d}t} = 0, \tag{5.14}$$

where $H_{eff} = 2E_{K_u}m_z/\mu$, showing that the effective field depends on the z component of the magnetization. Indeed, if the z component of the magnetization is not changing, the anisotropy acts like a field applied in the z direction. This is just the leading term with uniaxial anisotropy. The anisotropy energy can have terms in m_z^4, m_z^6, etc. With only the quadratic term, the minimum energy is in either direction along the principal axis if E_{K_u} is positive or in the equatorial plane if E_{K_u} is negative. With terms in m_z^2 and m_z^4 it is possible to have the minimum energy for a cone of angles, if the second order anisotropy and the fourth order anisotropy have opposite signs.

A particular case of two-fold plus four-fold anisotropy is treated in some detail below because it mimics important features of practical devices.

Cubic Anisotropy. More complexity appears with cubic anisotropy. But here I am cheating a bit because a single Fe atom would not couple to a cubic field. To get cubic anisotropy with Fe, one needs to first couple a group of Fe atoms together. I will ignore that for the moment and pretend that Fe has a spin 2, which would couple to a cubic field. The lowest order term can be written in several ways, just as was the case for uniaxial anisotropy. The fact that the magnetization is a vector of constant magnitude allows this flexibility. I prefer the expression with powers of 4, but it is more usual to find the first order cubic anisotropy written in terms of products of squares of the normalized magnetization components,

$$E_K = E_{K_1}\left(m_x^2 m_y^2 + m_y^2 m_z^2 + m_z^2 m_x^2\right), \tag{5.15}$$

where E_{K_1} is the first order cubic anisotropy constant per atom. The energy is a minimum if two of the components vanish. This gives the same results as writing the energy as

$$E_K = -E_{K_1}\left(m_x^4 + m_y^4 + m_z^4\right)/2, \tag{5.16}$$

which more clearly shows the desirability of pointing along one of the cubic axes if E_{K_1} is positive, as it is for iron, or along the body diagonal if E_{K_1} is negative. Fig. 5.2 shows the contours of constant energy for a first order cubic anisotropy as projected on the (m_y, m_z) plane. In the presence of cubic anisotropy, when there is no damping, the precession follows a contour of constant anisotropy energy. If the moment is close to a $\langle 111\rangle$ direction, it precesses about that axis. The motion is nearly circular close to the axis, but has an increasing three-fold distortion when the moment is further from a $\langle 111\rangle$ direction. If it is close to a $\langle 100\rangle$ direction it precesses about that axis, again with nearly circular motion close to the axis, and with a larger four-fold distortion when the moment is started further from the [100] direction.

When damping is present, one can start the moment near a $\langle 111\rangle$ and it will sweep across all of the contours of constant energy as it approaches a $\langle 100\rangle$. The particular $\langle 100\rangle$ depends on the starting position and the damping coefficient. The contours of Fig. 5.2 include an *LLG Micromagnetics Simulator* calculation for spin precession with cubic anisotropy and with a small amount of damping. The four-fold symmetry about the [100] axis is shown by projecting the magnetic response on the plane perpendicular to the [100] axis in Fig. 5.2a. The three-fold symmetry about the [111] is similarly illustrated in Fig. 5.2b. Here damping is included because it is a necessary ingredient in LLG if we are to move across lines of constant energy to reach equilibrium states. It also affects the mathematical stability of the dynamic calculations. The torques are very small in the region of the [110] saddle points of the energy. If I make the damping small enough, I can come close to following the critical energy contour that connects four of the $\langle 100\rangle$ points in (m_y, m_z) space. Paths in (m_x, m_y) space are used to visualize more complex systems in thin films by replacing the components by their spatially averaged values to create $(\langle m_x\rangle, \langle m_y\rangle)$ space.

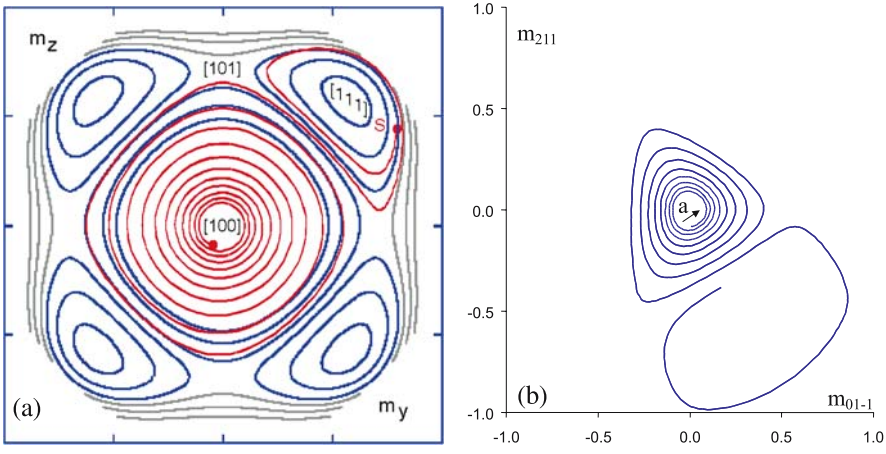

Fig. 5.2. Contours of constant cubic anisotropy energy are shown in blue in (**a**) along with part of the path of a moment precessing in the anisotropy field with enough damping to slowly cross the contours of constant energy. The early part of the precession starts near the [111] as shown in (**b**) projected on the plane perpendicular to the [111]. The later part is shown in red in (**a**), where after passing near the [110] and [101] the moment precesses about the [100]

Damping. The introduction of the lattice surrounding the iron atom is all that is necessary to dissipate energy. The spin of the electrons on the iron atom cause precessions of spins on the neighboring atoms, and these in turn change the spins on their neighbors. Spin diffusion is one mechanism of loss of energy from the iron atom in whatever field it is precessing. The spin-orbit coupling of the precession to the lattice is a direct mechanism for transferring angular momentum and energy away from the precessing spin on the iron atom. The details are not necessary for micromagnetics as long as one has a way of putting an energy dissipation term into the equations of motion. The original Landau-Lifshitz formulation of the problem was completely phenomenological. There had to be a term that produced a torque in the direction of the magnetic field. The way they introduced the torque made it such that the larger the damping term, the faster the magnetization turned into the direction of the field. This is fine for low damping, which is generally the case. But for large damping, their formulation gave the silly result that, for infinite damping, the magnetization came into the field direction in an infinitesimal time. Gilbert corrected this by introducing a damping term proportional to $\mathrm{d}\boldsymbol{m}/\mathrm{d}t$. This leaves the form of the Landau-Lifshitz equations almost unchanged, except that their dm/dt gets multiplied by $1 + \alpha^2$, where α is the damping constant. This leaves the low damping limit unchanged and corrects the high damping limit. All this is shown below in detail in (5.24–5.33). Thus the G in LLG is for Gilbert, who said that there is an effective field acting on the moment that is given by $-G\,\mathrm{d}\boldsymbol{m}/\mathrm{d}t$, where $G = \alpha/(\gamma\mu)$. If the magnetization is precessing in a field, this term creates a torque that turns the moment

into the direction of the field. If the magnetization is turning toward the field, this produces a field that changes the precession.

The way Gilbert put damping into LLG is with us to this day, but the final word on the subject has yet to be heard. There are some problems.

Let us look at two simple examples of precession in external fields with damping as formulated in LLG. Here I can show some completely analytic solutions of the equations of motion that are useful for checking the *LLG Micromagnetics Simulator* code. The first case is for a field in the z direction which is turned on instantly when the magnetization is in the x direction. The second case is for the rotating field as treated above with damping added.

Damping of Precession in a Fixed Field. The equations of motion for precession of a moment in a fixed field with damping are

$$\mu_x = \mu \cos\left(\frac{1}{1+\alpha^2}\gamma H_z t\right) \operatorname{sech}\left(\frac{\alpha}{1+\alpha^2}\gamma H_z t\right) \tag{5.17}$$

$$\mu_y = \mu \sin\left(\frac{1}{1+\alpha^2}\gamma H_z t\right) \operatorname{sech}\left(\frac{\alpha}{1+\alpha^2}\gamma H_z t\right) \tag{5.18}$$

$$\mu_z = \mu \tanh\left(\frac{\alpha}{1+\alpha^2}\gamma H_z t\right) \tag{5.19}$$

The first factor in the expressions for μ_x and μ_y corresponds to the precessional motion. The $(1 + \alpha^2)$ in the denominator shows that the precessional frequency is smaller in the presence of damping. The precession is damped out in time by the hyperbolic secant that goes rapidly to zero for large arguments. In this term the $(1+\alpha^2)$ in the denominator is essential to avoid the effect of large damping making the relaxation faster. The relaxation of μ_z is monotonic following the hyperbolic tangent. These equations are used to show under-damping, $\alpha < 1$, and critical damping, $\alpha = 1$, in Fig. 5.3.

Strangeness of Damping. An immediate result from these equations is the most jarring thing about the Gilbert formulation of damping. The damping is there from the very beginning. When a field is turned on instantly, the magnetization is already at full precessional velocity, and so is the damping. For steady state problems, such as ferromagnetic resonance, for which LLG was developed, this is not a worry. Nor is it a problem for most practical micromagnetic applications, where the rise time is determined by inductances in the current circuits. But it is a conceptual problem. Some time delay should be introduced in the coupling between the first spin and the dissipation of energy in nearby spin systems. But this is a subject for another time and should not concern us on our first spin around the track; see Heinrich's chapter.

The damping determines the deviation from the path of precession around constant energy contours. The path taken by the moment with damping makes an angle with respect to the equatorial plane of precession without damping. The tangent of that angle is α, as can be seen by taking the ratio of μ_z to μ_y for small times when the sin and the tanh are both equal to their arguments. This is a simple check on dynamical calculations.

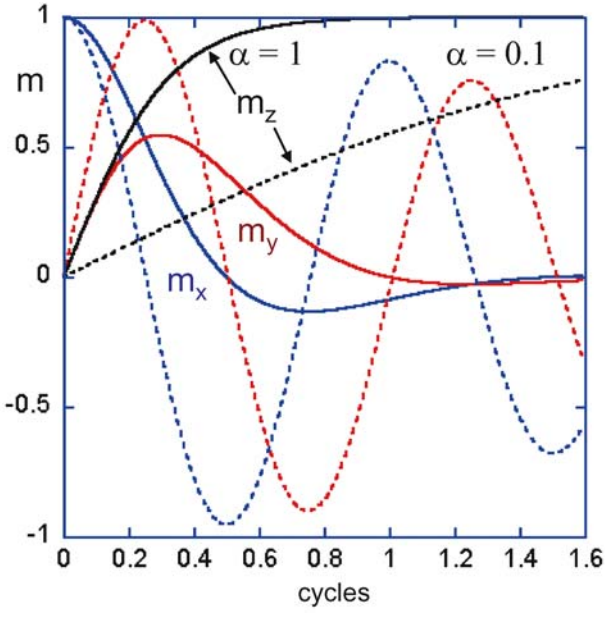

Fig. 5.3. Relaxation of a moment from along the x axis to along the z axis in a field H_z. The time dependence (in cycles of precession) of m_x, m_y and m_z are shown for critical damping, $\alpha = 1$, and for an under-damped response with $\alpha = 0.1$

For emphasis, it should be repeated that the initial motion already takes into account the damping; there is no delay in LLG.

Damping in a Rotating Field. For an Fe moment with damping in a field $\boldsymbol{H}$ rotating in the (x, y) plane with angular velocity Ω, the motion in the plane produces an effective field with a component in the z direction. There is another effective field in the z direction due to the transformation to the rotating frame. In the steady state, these two fields balance one another so that in the rotating frame there is no motion. In the laboratory frame, the magnetization vector is tilted out of the plane to an angle θ and follows the rotating field with a lag angle ψ. To show this from time zero it is necessary to have the initial conditions just right. From arbitrary initial conditions, the steady rotation is reached only after the transients have died out. To see this analytically, assume the steady state solution and then find the θ and ψ that make it self-consistent with $\gamma \boldsymbol{H}$ and Ω. The steady state is described by

$$m_x = \cos\theta \cos(\Omega t - \psi), \quad m_y = \cos\theta \sin(\Omega t - \psi), \text{ and } \quad m_z = \sin\theta. \tag{5.20}$$

The effective field $\boldsymbol{H}_{\text{eff}}$ includes the Gilbert damping; its components are

$$H_x = H\cos\Omega t - \alpha\frac{dm_x}{d\gamma t}, \quad H_y = H\sin\Omega t - \alpha\frac{dm_y}{d\gamma t}, \text{ and } \quad H_z = 0, \tag{5.21}$$

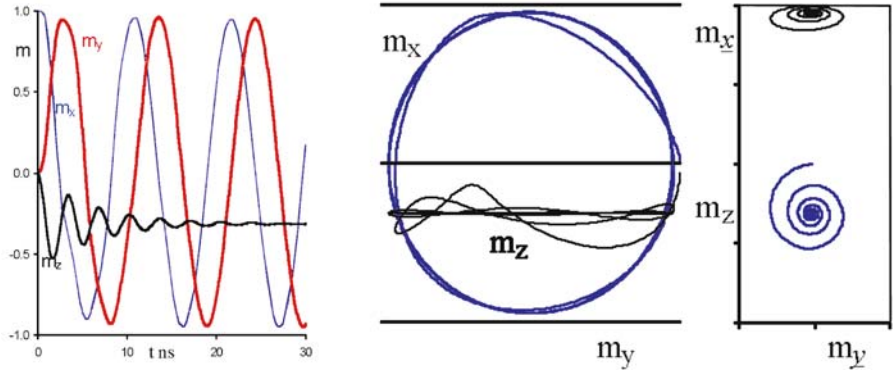

Fig. 5.4. Damped response to a field rotating with angular frequency Ω in the (x, y) plane. In the steady state m_z is constant while m_x and m_y lag behind the field by an angle ψ. The dependence of the steady-state values of $m_z = \sin\theta$ and ψ on the parameters Ω, α and H is given implicitly in (5.22),(5.23) by choosing values of θ. The motion is viewed from the laboratory frame in the central panel and from the rotating frame on the right. The central panel is similar to the response of $\langle m_x \rangle$, $\langle m_y \rangle$, and $\langle m_z \rangle$ in many cases of the switching of thin film memory elements

where the m's are components of a unit vector. For the steady state with a constant m_z, there is no damping term included in H_z. Note that the damping term puts derivatives on the right hand side of the equations of motion. The set of equations are treated by linear algebra to untangle the three derivatives. This is the source of the factor $1 + \alpha^2$. There are two unknowns, ψ, the phase lag of the rotation with respect to the field, and θ, the angle measured from the x-y plane. The dimensionless parameters of the problem are α and $\gamma H/\Omega$. The angle with respect to the plane is found from the condition

$$\gamma H/\Omega = \sqrt{(1 + \alpha^2 \sin^2\theta} \quad \cot\theta, \tag{5.22}$$

which shows that the angle θ is only weakly dependent on the damping. For small fields the steady-state condition is possible only if the magnetization is almost perpendicular to the plane. The phase lag is found from

$$\psi = \arctan(\alpha \sin\theta). \tag{5.23}$$

The greater α, the greater ψ. However, even for $\alpha = 1$, ψ is less than 45°. The transient solutions of this problem are best viewed in the rotating frame. Comparisons with the laboratory frame are shown in Fig. 5.4.

Landau-Lifshitz-Gilbert Equations. Now it seems appropriate to travel the road from (5.2), as modified by Gilbert, to the original Landau-Lifshitz formulation modified by the factor $1 + \alpha^2$. Start with

$$\frac{\mathrm{d}M_x}{\mathrm{d}t} = \gamma(M_y H_z - M_z H_y), \tag{5.24}$$

$$\frac{\mathrm{d}M_y}{\mathrm{d}t} = \gamma(M_z H_x - M_x H_z), \tag{5.25}$$

and

$$\frac{\mathrm{d}M_z}{\mathrm{d}t} = \gamma(M_x H_y - M_y H_x), \tag{5.26}$$

and then add the damping term to the components of the field H_0

$$H_x = H_{x0} - \frac{\alpha}{M_s}\frac{\mathrm{d}M_x}{\mathrm{d}\gamma t}, \tag{5.27}$$

$$H_y = H_{y0} - \frac{\alpha}{M_s}\frac{\mathrm{d}M_y}{\mathrm{d}\gamma t}, \tag{5.28}$$

$$H_z = H_{z0} - \frac{\alpha}{M_s}\frac{\mathrm{d}M_z}{\mathrm{d}\gamma t}, \tag{5.29}$$

where the damping terms have the factor M_s, the magnetic moment per unit volume, to make M_x/M_s, M_y/M_s, and M_z/M_s components of a unit vector. This produces three linear equations for the three first derivatives. These are solved by substitution to give the three Landau-Lifshitz equations with Gilbert's factor $1 + \alpha^2$ multiplying each of the first derivatives;

$$\begin{aligned}\left(1+\alpha^2\right)\frac{dM_x}{d\gamma t} =& (M_y H_{z0} - M_z H_{y0}) \\ &- \alpha\left[\frac{M_x}{M_s}(M_x H_{x0} + M_y H_{y0} + M_z H_{z0}) - M_s H_{x0}\right],\end{aligned} \tag{5.30}$$

$$\begin{aligned}\left(1+\alpha^2\right)\frac{dM_y}{d\gamma t} =& (M_z H_{x0} - M_x H_{z0}) \\ &- \alpha\left[\frac{M_y}{M_s}(M_y H_{y0} + M_z H_{z0} + M_x H_{x0}) - M_s H_{y0}\right],\end{aligned} \tag{5.31}$$

and

$$\begin{aligned}\left(1+\alpha^2\right)\frac{dM_z}{d\gamma t} =& (M_x H_{y0} - M_y H_{x0}) \\ &- \alpha\left[\frac{M_z}{M_s}(M_z H_{z0} + M_x H_{x0} + M_y H_{y0}) - M_s H_{z0}\right].\end{aligned} \tag{5.32}$$

The $1 + \alpha^2$ term slows down the response. As alpha goes to large values, which does not happen in practice, the precession rate goes toward zero. The damping rate depends on how far from equilibrium the moment is at any given time. At equilibrium,

$\boldsymbol{M}$ is along $\boldsymbol{H}$, and the term multiplying α goes to zero. This term is proportional to the difference between $\boldsymbol{H}$ and the component of $\boldsymbol{H}$ along $\boldsymbol{M}$. In vector notation

$$\left(1+\alpha^2\right)\frac{d\boldsymbol{M}}{d\gamma t} = \boldsymbol{M}\times\boldsymbol{H} - \alpha M_s\left[\frac{(\boldsymbol{H}\cdot\boldsymbol{M})}{M_s}\frac{\boldsymbol{M}}{M_s} - \boldsymbol{H}\right], \tag{5.33}$$

where the term in square brackets is also $\boldsymbol{M}\times(\boldsymbol{M}\times\boldsymbol{H})/M_s^2$, portraying the damping as an effective field proportional to $\boldsymbol{M}\times\boldsymbol{H}$.

Two-fold Anisotropy with Damping. The LLG equations do have some analytical solutions. Often it is easier to use a micromagnetic simulator than to use the analytical expressions. One simple example should suffice. Consider the response to a magnetic field H_a applied along the x-direction with the magnetization in the minus x-direction for a two-fold uniaxial anisotropy along the x-axis with damping. There is a single component to the field

$$H_{x0} = H_a + 2K_{u_2}M_x/M_s^2, \quad H_{y0} = 0, \quad \text{and} \quad H_{z0} = 0, \tag{5.34}$$

where K_{u_2}, the two-fold uniaxial anisotropy constant, is an energy density. The equation of motion for M_x,

$$\left(1+\alpha^2\right)\frac{dM_x}{d\gamma t} = \alpha H_{x0}M_s\left[1 - \frac{M_x^2}{M_s^2}\right], \tag{5.35}$$

follows immediately from (5.30). With the notation

$$\tau \equiv \frac{1+\alpha^2}{\alpha\gamma}\frac{M_s}{2K_{u_2}}, \quad m \equiv \frac{M_x}{M_s}, \quad \text{and} \quad h \equiv H_a\frac{M_s}{2K_{u_2}}, \tag{5.36}$$

M_x varies with time according to

$$\begin{aligned}\left(1-h^2\right)\frac{t}{\tau} =& 2\ln\frac{(m+h)}{(m_1+h)} - h\ln\frac{(1+m)(1-m_1)}{(1-m)(1+m_1)} \\ &+ \ln\frac{(1+m)(1-m)}{(1+m_1)(1-m_1)}\end{aligned} \tag{5.37}$$

This explicit equation for t is unravelled graphically by choosing values for h, the reduced field, and m_1, the component m_x at time $t = 0$, and then plotting t as a function of m. (5.37) is used to produce Fig. 5.5 for the time dependence of M_x for a series of fields using $m_1 = -0.98$ for Fig. 5.5a and $m_1 = 0$ for Fig. 5.5b at $t = 0$. The scaled variables of (5.36) make for simplification yet it is hard to see that (5.37) yields Fig. 5.5. The precession of m_y and m_z in the time varying effective field of (5.35) is found using the *LLG Micromagnetics Simulator* and displayed in Fig. 5.6 for $\alpha = 0.1$, $H = 105$ Oe, $K_{u_2} = 60$ kiloerg/cm^3, $M_s = 1714$ Oe, and $\gamma = 17.6$ MHz/Oe, for which $\tau = 8$ ns and $h = 1.5$.

Hysteresis. The single iron atom embedded in a lattice has the qualitative features necessary for a magnetic device. Quantitatively, it is not useful because the magnetic

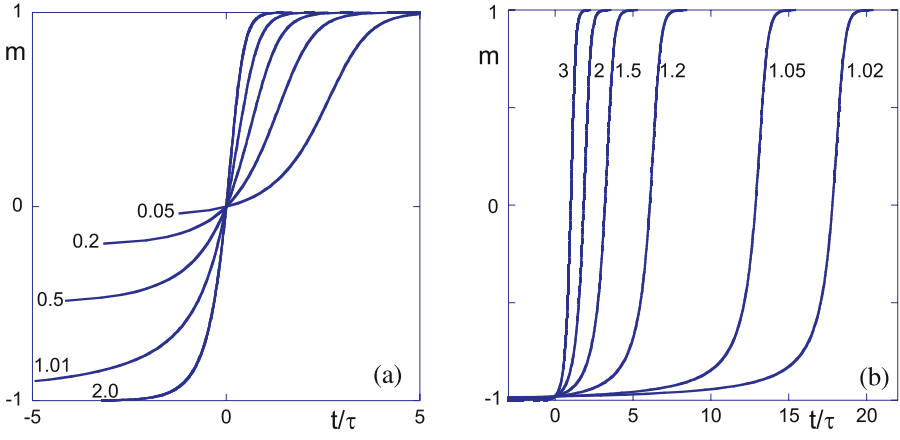

Fig. 5.5. Damped precession with two-fold uniaxial anisotropy. The motion for m_x is determined by m_1, the value of m_x at $t = 0$, and h the applied field marked on the curves in reduced units. In (**a**) $m_1 = 0$. In (**b**) $m_1 = -0.98$

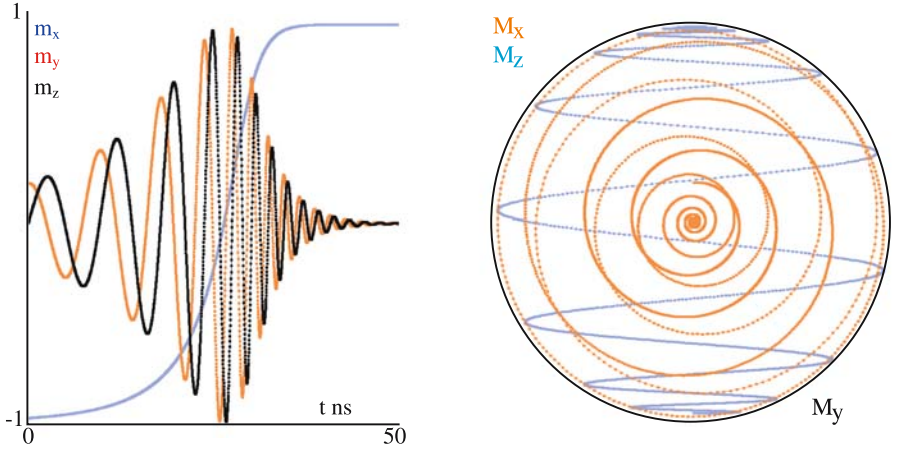

Fig. 5.6. Results for a moment reversing against two-fold uniaxial anisotropy using the *LLG Micromagnetic Simulator*. The motion starts at $m_x = -0.98$, $m_z = 0$ at $t = 0$. With $\alpha = 0.1$, $K_u = 60$ kiloerg/cm^3, $H_x = 105$ Oe, and $M_s = 1714$ Oe, the reduced field is $h = 1.5$ and the time is scaled to $\tau = 8$ ns

energies are much smaller than $k_B T$, unless T is so small that quantum effects would dominate the behavior. Yet the embedded atom does exhibit, in principle, the two essential ingredients for hysteretic behavior, anisotropy and damping. A magnetic moment in an environment with positive uniaxial anisotropy has two states of lowest energy. It can be switched back and forth between the two states by applying a field. If a field is applied along the anisotropy axis in the direction opposite the moment, there is a critical value of the field, $H_K \equiv 2K_{u_2}/M_s$, necessary for switching, but even

then there must be some fluctuation in the direction of the moment for a reversing torque to develop. Thus, switching is assisted by setting the field in directions other than along the anisotropy axis.

For second-order uniaxial anisotropy, the most effective field for switching is one applied at 135° to the direction of the axis from which the moment is to be rotated. At 135°, the critical field for switching is the one that rotates the moment to 45° from the axis. At that point, torque from the anisotropy is a maximum, as is the torque from the applied field, because the moment is perpendicular to the field. Any increase in the applied field will overcome the restoring torque from the anisotropy and the moment will sweep past the field direction into a position close to the anisotropy axis in the reverse direction. The critical field for switching is $H_K/2$. If a field of magnitude greater than H_K is rotated in a plane that contains the anisotropy axis, the moment will follow the field without hysteresis. If a rotating field of magnitude less than $H_K/2$ is applied in the same fashion, there will also be no hysteresis because the moment will oscillate about the original direction. Because it takes torque to rotate the moment away from the anisotropy axis, that axis is called the easy axis. To rotate a moment away from the easy axis and maintain it in a direction perpendicular to that axis takes a field H_K along the perpendicular axis.

It was assumed throughout the above paragraph that the process of magnetization is sufficiently slow that equilibrium is reached at each applied field. The above statements are based on energy analysis, assuming that the damping has had enough time for the minimum energy to be achieved at each field. Note that once the instability discussed for the field at 135° is achieved, the motion of the moment is determined by the dynamical equations of motion for which it is necessary to know the damping parameter. The situation for cubic anisotropy has already been mentioned. The path from near a ⟨111⟩ direction may take the moment to any of the six ⟨100⟩ directions depending on the sequence of fields and the damping parameter.

Thermal Stability. A single magnetic moment is not stable against thermal fluctuations. It is necessary to have a large number of moments coupled together to suppress the effects of temperature. In the world of devices, the important temperature is room temperature. Not all rooms have the same temperature, so there are technical specifications that arbitrarily define room temperature between limits. The most severe technical specifications are military, for which the range of operating temperatures is from −50°C to 125°C, which is from 223 K to 398 K, almost a factor of two in absolute temperature. At 400 K, k_BT is 1/20th picoerg. For typical attempt frequencies, $10^9 s^{-1} \simeq e^{20} s^{-1}$, useful magnetic barriers should be at least as large as a picoerg, which is about an electron-volt or 10^{-19} J.

5.2.3 A Unit with Two Stable States and Two Metastable States

A single Fe atom embedded in a lattice with a particular choice of uniaxial anisotropy serves to illustrate many of the features of magnetic devices. Among these are hysteresis, linear and rotational, the effects of bias fields, response to overdriving, and the role of damping. Much of what I have learned in the past four years of extensive

experimental and theoretical study of patterned magnetic thin films is reflected in my comments about this simple system throughout this section.

The particular anisotropy is two-fold plus four-fold with respect to the preferred axis; see Fig 5.7a. The energy per unit volume, E/V, of the Fe atom in a magnetic field with components H_x and H_y in the presence of this anisotropy is

$$E/V = -H_x M_s \cos\theta - H_y M_s \sin\theta - K_{u_2} \cos^2\theta - K_{u_4} \cos^4\theta, \tag{5.38}$$

or, for H and the angle ψ between $\boldsymbol{H}$ and the x-axis,

$$E/V = -HM_s \cos(\theta - \psi) - K_{u_2} \cos^2\theta - K_{u_4} \cos^4\theta, \tag{5.39}$$

where M_s is the magnetic moment per unit volume, K_{u_2} is the second order anisotropy constant, K_{u_4} is the fourth order anisotropy constant, and θ is the angle between the magnetization and the x-axis. The x-axis is the anisotropy axis; this is an easy axis if $K_{u_2} + 2K_{u_4} > 0$. For Fe at room temperature, the magnetic moment per unit volume is $M_s = 1714$ Oe in Gaussian units, or $\mu_0 M_s = 4\pi 0.1714$ T in SI units. The anisotropy constants are chosen for this illustration to be $K_{u_2} = -60$ kiloerg/cm^3 in Gaussian units, or -6 kJ/m^3 in SI units, and $K_{u_4} = 80$ kiloerg/cm^3 in Gaussian units, or 8 kJ/m^3 in SI units. The anisotropy constants divided by the magnetization have the dimensions of field, with $H = 80000/1714 \cong 50$ Oe, or $\mu_0 H \cong 5$ mT, which are fields of interest for devices.

The calculations, using the anisotropy in Fig. 5.7a and the magnetic moment of Fe, are applicable to a collection of Fe atoms that are tightly coupled to one another and have either cubic or spherical boundaries. If the shape is not cubic or spherical, the magnetostatic self-energy of the collection is anisotropic. If the collection is not rigidly coupled, even the cube has preferred directions for the magnetization. The exchange interaction responsible for ferromagnetism couples the moments tightly over short distances; a collection responds rigidly for dimensions of at most 20 nm.

The main role of micromagnetism is to calculate what happens when the atoms can no longer be treated as rigidly coupled and the magnetostatic interactions give rise to non-collinear magnetization patterns. Much of what is seen there relates to the behavior of tightly coupled systems. The anisotropy energy in Fig. 5.7a mimics the response of non-collinear systems with particular shapes that produce a similar dependence of the internal energy on the average values $\langle M_x \rangle$, $\langle M_y \rangle$, and $\langle M_z \rangle$. The internal energy is magnetostatic self-energy plus anisotropy energy plus exchange energy.

Hysteresis Loops. Equilibrium states of this system, with the anisotropy energy density of Fig. 5.7a, are found by equating to zero the derivative of the energy with respect to θ, which is still the angle between the magnetization and the x-axis. The stability of each state is found by checking the sign of the second derivative. The critical fields are when both derivatives vanish, yielding two equations for H_x and H_y, or H and ψ, in terms of the value θ at the critical field and angle. From the vanishing of the first derivative:

$$H_x = \left[\frac{H_y}{\sin\theta} - \frac{2K_{u_2}}{M_s} - \frac{4K_{u_4}}{M_s} \cos^2\theta \right] \cos\theta. \tag{5.40}$$

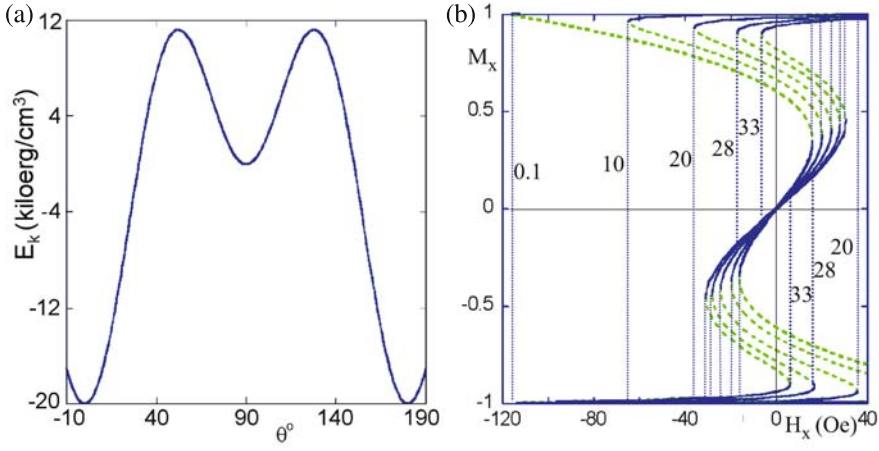

Fig. 5.7. (**a**) *An anisotropy energy density*. As the magnetic moment rotates from 0° to 360° there are two deep minima and two shallow minima. The energy density has been chosen to make the fields for reversal comparable to those used in practice. (**b**) *Hysteresis loops*. M_x/M_s, for a magnetic moment per unit volume of an Fe atom and the anisotropy energy density given in (**a**), subjected to switching fields H_x in the presence of bias fields $H_y = 0.1$, 10, 20, 28 and 33 Oe. The blue lines follow the magnetization. The dashed green lines show the equilibrium states that are not stable, but mathematically related to the stable states by a continuous curve. The jumps in M_x are shown as dotted vertical lines

Equation (5.40) gives the independent variable H_x in terms of the dependent variable θ and the parameter H_y. This describes $\boldsymbol{M}$ switching from along x in one direction to the opposite direction. During switching, H_y is a bias field that promotes switching in the (x, y) plane, which is what happens if H_x is slowly varied. The ratio K_{u2}/K_{u4} is chosen to make this interesting by producing a second minimum in the anisotropy energy density as shown in Fig. 5.7a.

For low bias fields, H_y, the switching field H_x is sufficiently high that the second minimum plays no essential role in the process. But for higher bias fields it does. One uses bias fields for selectivity in magnetic devices, where one bit is to be chosen from an array. The selected bit should switch in a field considerably lower than that required to switch an unbiased bit. The switching of the Fe atom, with the anisotropy as given above with $K_{u2} < 0$ and $K_{u4} = -4K_{u2}/3$, is shown in Fig. 5.7b for the case where H_y is held fixed at a series of values while H_x is varied. Equation (5.40) gives H_x, while the other parametric equation needed to produce Fig. 5.7b is $M_x = M_s \cos\theta$. One can also ask what happens when H_x is held fixed and H_y is changed, by solving (5.40) for H_y. Also one can plot $M_y = M_s \sin\theta$ as a function of H_x or H_y.

The second quadrant of a plot of M_x versus H_x is generally the most interesting. Here switching is initiated in a device; see Fig. 5.7b. (Actually it is a plot of M_x/M_s, but the convention of normalizing magnetic quantities to unity is used here and throughout this chapter.) The presence of a bias field H_y lowers the remanent magnetization and promotes rotation away from the preferred axis in the (x, y) plane.

The presence of a 20 Oe bias field allows switching in a single step to occur at 40 Oe rather than at 120 Oe, as in the case of a very small bias field. Increasing the bias field further eventually becomes self-defeating. The magnetization gets trapped in the second minimum; see Fig. 5.7b where, for $H_y = 28$ Oe or higher, the switching is in 2 steps. The higher the bias field, the harder it is to get out of the trap. The bias field helps at the start of switching but, when the bias field is too high, is a hindrance to complete switching. The bias field adds to the stability of the second minimum in this case.

Figure 5.7b illustrates (5.40), showing the equilibrium energy states with distinction between the stable and the unstable states by changing the color along the path so that negative dM_x/dH_x appears as a dotted green line. The central blue lines describe the magnetization moving back and forth in the secondary minimum. At the origin $\boldsymbol{M}$ is aligned in the y direction for $H_x = 0$. Increasing H_y increases the range of stability of this state.

Figure 5.7a does not address what happens if the magnetization rotates out of the (x, y) plane. For purely uniaxial anisotropy, all directions in the (y, z) plane are equivalent. A field anywhere in that plane just rotates the perpendicular component of the magnetization to its direction. If additional anisotropy were present that more or less confined the magnetization to the (x, y) plane, it would make sense to talk about the effect of a negative H_y bias field. Then an H_y can make the state with $M_y = 1$ become unstable against rotation into $M_x = \pm 1$. The magnetostatic self-energy of a thin film has shape anisotropy that tends to confine the magnetization to the (x, y) plane. This is a dominant feature of thin film devices.

An example of the dependence of M_y on H_x is shown in Fig. 5.8a for $H_y = 28$ Oe. The lower portions in blue, are near saturation in the $+x$ or $-x$ directions. In the upper portions in blue, corresponding to large M_y, the magnetization is perpendicular to the anisotropy axis. The dotted lines are the unstable portions of (5.40). The same information is displayed in Fig. 5.8b, showing the dependence of θ on H_x. The student should try to find as many ways as possible to look at even the simplest phenomena.

A different view of (5.40) is found by plotting the inverse transverse susceptibility $M_s H_y/M_y \equiv H_y/\sin\theta$ versus H_x for various H_y as shown in Fig. 5.9. It should be noted that the slope of the inverse transverse susceptibility versus H_x for small H_y at *small* H_x is sufficient to predict the large switching field H_x for vanishing H_y. It is often the case even in complex systems that the barrier to be overcome is predictable from measurements in small fields. The reason is quite similar to that in the present case. There is a quadratic dependence of energy on the angle of rotation from the anisotropy axis. The curvature is reduced linearly with H_x applied in the reverse direction, so the behavior in small fields predicts when the curvature will change sign. The inverse transverse susceptibility measures that curvature. In many systems, once this happens, the reversal goes all the way to completion without trouble from intermediate states that are stabilized by larger bias fields.

Switching Diagrams. Critical fields for irreversible changes are found by solving two equations in two unknowns for H_x and H_y in terms of θ. Then θ can be used as a parameter to generate a diagram known as the switching astroid. For the case of

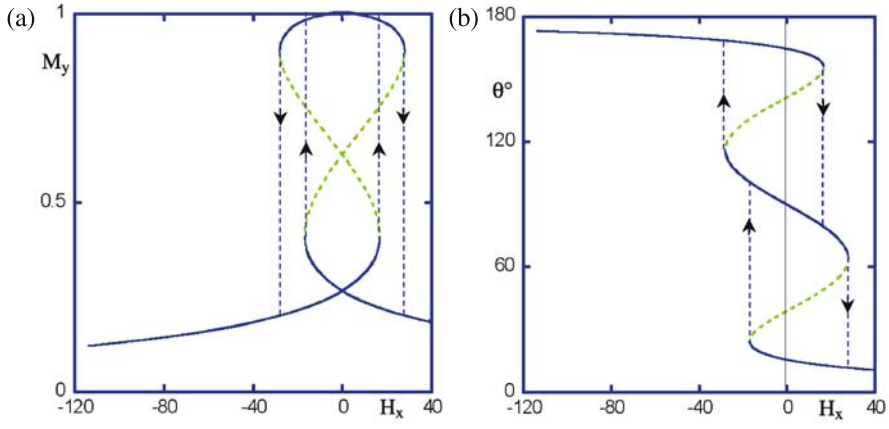

Fig. 5.8. Two alternative views of the hysteresis shown in Fig. 5.7b for $H_y = 28$ Oe. (**a**) Dependence of M_y on H_x. Note that M_y goes to one before dropping back to the upper curve. (**b**) The dependence on H_x of the angle θ between $\boldsymbol{M}$ and H_x. The blue sections are stable and reversible. The green sections are unstable

uniaxial anisotropy with second and fourth order terms, the equations of the switching diagram are

$$M_s H_x = -\left(2K_{u_2} + 12K_{u_4}\left[\cos^2\theta - 2/3\right]\right)\cos^3\theta \tag{5.41}$$

$$M_s H_y = \left(2K_{u_2} + 12K_{u_4}\cos^2\theta\right)\sin^3\theta. \tag{5.42}$$

To help interpret these equations, I digress to the case where there is only second-order uniaxial anisotropy. For that case, the relation between H_x and H_y is the mathematically defined astroid

$$H_x^{2/3} + H_x^{2/3} = H_k^{2/3} \tag{5.43}$$

where $H_k = 2K_{u_2}/M_s$. This is the real mathematical astroid, a four-cusped hypercycloid; see Fig. 5.10a. In magnetism the term astroid is carried over to switching diagrams that are not the mathematically defined astroid. Regions of (H_x, H_y) space inside the astroid can be traversed without switching from one state to another.

For a given H_x and H_y there can be two stable states in two-fold uniaxial anisotropy. The realm of fields in which this is the case is inside the astroid. Outside there is only one stable state for each point in (H_x,H_y) space. Crossing the boundary to the outside region results in switching, or not, depending on the starting condition. If the starting state is magnetized to the right, then passing over the red line will result in switching to the left by rotating counterclockwise. The red instability line is for states with a magnetization component to the right. The green instability line is for states with a component to the left.

Perhaps an excursion clockwise from the point $(H_x, H_y) = (0, 0)$ will illustrate the use of the astroid diagram. The magnetization direction rotates counterclockwise

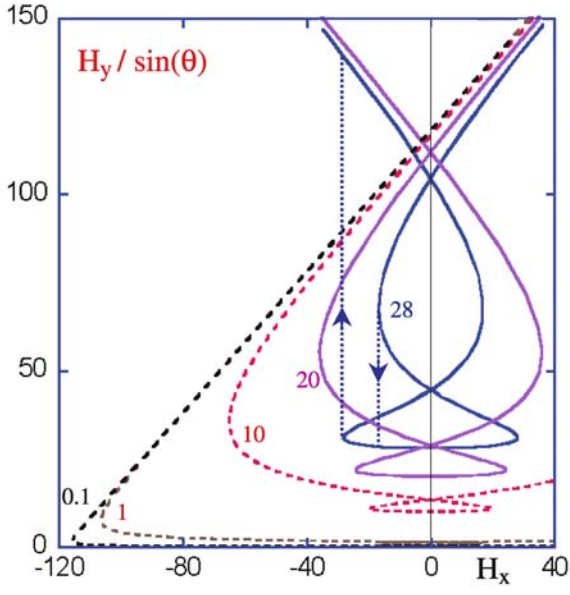

Fig. 5.9. Dependence of H_y/M_y on H_x for $H_y = 0.1$, 10, 20 and 28 Oe. The dotted black line, corresponding to $H_y = 0.1$ Oe, predicts switching at $H_x = -116.4$ Oe from the slope at $H_x = 0$. H_y/M_y measures the curvature at the origin, which decreases linearly with H_x until the system becomes unstable

until crossing the instability (red) line where it is tangent to the line. It then flips to the left. For the rest of this path in (H_x, H_y) space the magnetization rotates clockwise continuously until, on returning to the starting point, the moment is back in its original direction. If the same path is traversed counterclockwise, the magnetization turns continuously through 180°, not changing direction on crossing the red line. The arrows are drawn using a construction by Slonczewski described in Hubert and Schäfer's Magnetic Domains [5.3].

Now return to the case being treated here, the anisotropy energy density of Fig. 5.7a. This case gives a more complex switching diagram; see Fig. 5.10b. The extra branches correspond to being in the secondary minima of Fig. 5.7a. In the center of the switching diagram, there are four states for each value of (H_x, H_y). In each of the eight points of the switching diagram there are two states. In the eight triangles, between the inside and the points, there are three states for each region. Outside the astroid there is only one state. The red line in Fig. 5.10b corresponds to the instabilities along the descent from saturation in the upper portion of Fig. 5.7b, where the switching is a rotation away from $M_x = 1$. The blue line corresponds to the instabilities on the left end of the central region of Fig. 5.7b, where the switching is a rotation away from $M_y = 1$. The path from a to b corresponds to turning on the bias field H_y. The path from b to c describes the switching process. First the red line is crossed with the magnetization switching from the deep minimum about the

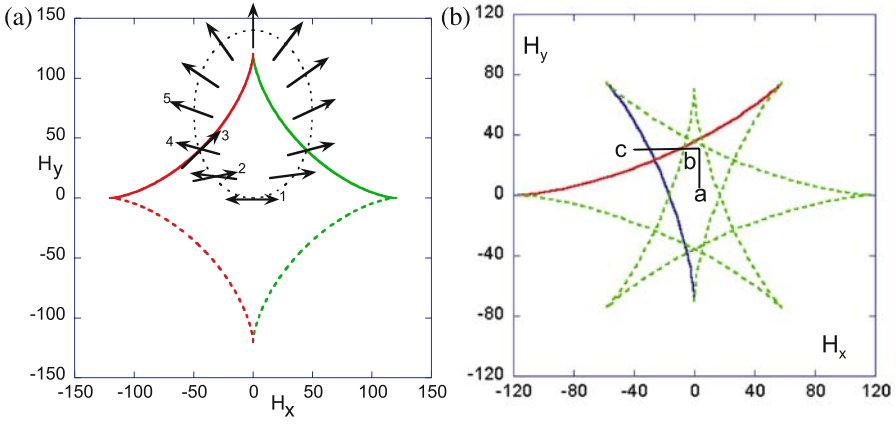

Fig. 5.10. Switching diagrams. (**a**) The switching astroid for a simple uniaxial anisotropy. If there is a magnetization component to the right, crossing a red line from the right causes switching. Crossing a green line from the left causes switching if the magnetization has a component to the left. An excursion around the elliptical path in (H_x, H_y) space, starting from the origin with the magnetization to the right, produces different results depending on the direction around the path. On the clockwise path there is a jump on crossing the red line but not on crossing the green line. On the counterclockwise path there are no jumps but the moment reverses smoothly. (**b**) The switching diagram for the anisotropy of Fig. 5.7a as described by (5.40). The meaning of the red and blue lines and the behavior along the path a, b, c is discussed in the text

anisotropy axis to the shallow minimum perpendicular to the anisotropy axis. Then the blue line is crossed with the magnetization switching to the deep minimum in the opposite direction from the start. For the direct path from a to c, the switching is directly from one deep minimum to the opposite deep minimum, because the blue line is applicable only when the magnetization is already in the shallow minimum. The negative H_y region of the diagram is inaccessible unless there is an additional anisotropy restricting the magnetic reversal to the (x, y) plane. The switching diagram in Fig. 5.10b, if it only had the red curve and not the blue, would be most favorable for devices. The switching field H_x decreases more sharply with bias field H_y in Fig. 5.10b than it does in Fig. 5.10a. But this advantage is balanced by the disadvantage of the possibility of getting trapped in the secondary minima.

Rotational Hysteresis. There is still another way to think about a device that has an anisotropy as shown in Fig. 5.7a. This is to hold the magnitude of the field constant and change its direction. The starting point for this is the energy written as it is in (5.39). The derivative of this energy with respect to θ is equated to zero and solved for ψ, the angle between the field and the anisotropy axis. The relation between θ and ψ for fixed magnitude of H depends on that value of H,

$$\psi = \theta + \arcsin\left(\sin 2\theta \left[K_{u_2} + 2K_{u_4}\cos^2\theta\right]/HM_s\right). \tag{5.44}$$

If H is below a threshold, θ just oscillates about its original position. (To see this from (5.44) one must plot $\arcsin x$, $-\arcsin x + \pi$, etc.) If H is sufficiently large and above another threshold, θ smoothly follows the magnetization, sometimes lagging and sometimes leading. In the limit of high H, $\theta = \psi$. Between the two thresholds, there is a region of H where the magnetization follows the field with irreversible jumps. This is the region of rotational hysteresis as depicted in Fig. 5.11a for $H = 33$ Oe.

A comparison of this analytical solution to the numerical solution using the *LLG Micromagnetics Simulator* is made in Fig. 5.11b. The disagreement comes because, for the dynamical calculation, the angle ψ is changed in discrete steps of 5°. The points shown in Fig. 5.11b are periodic samplings of the iterations of the dynamical calculation during each step in angle. Note that the simulation and the analytic expressions agree at the end of each step, as they should, which shows that, most likely, the algebra is correct and the micromagnetic code has no apparent bugs. But the simulation does not catch the onset of instability because it occurs in the interval between field steps. The vertical rise is assigned to the angle of the field in which it occurred. The separation of the points, taken with equal time steps, shows that the

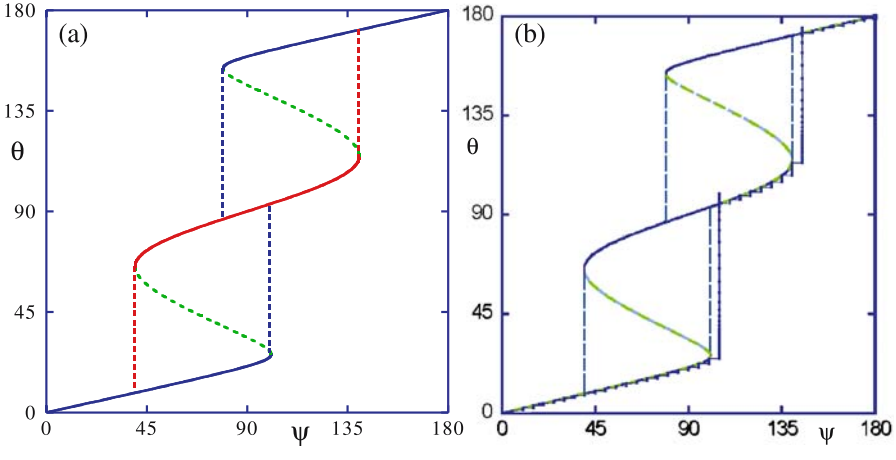

Fig. 5.11. Rotational hysteresis for Fe with anisotropy as shown in Fig. 5.7a. The applied field is 33 Oe. The curve repeats every 180°. Again the dotted green lines are regions of unstable equilibrium. The sections with positive slope are regions of reversible stability. The line through the origin corresponds to the deeper potential wells about 0° and 180°. The magnetization remains in one of these wells for more than 180° of rotation. The shorter curved section in the middle of the diagram corresponds to the shallower potential wells about 90° and 270°. There the range of stability is slightly more than 90°. (**b**) A comparison of the analytical solution (smooth curve), from (**a**) to the numerical solution using the *LLG Micromagnetics Simulator* (stepped curve). In a micromagnetic calculation it is usual to take steps in angle (or in field), letting the dynamics of the equations with damping approach the equilibrium for each angle. The points are periodic samplings of the iterations of the dynamical calculation, during each step of 5° in angle. See text

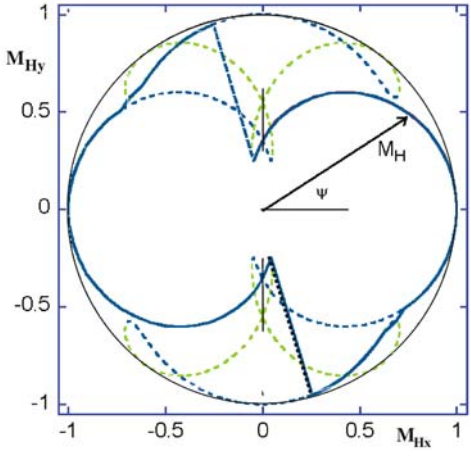

Fig. 5.12. A polar plot of M_H, the component of the magnetization along the applied field, as a function of ψ, the angle of the field, for the anisotropy as shown in Fig. 5.7a. This is the case $H = 33$ Oe. The solid blue lines are the result of a calculation using finite steps in angle with the *LLG Micromagnetics Simulator*. These cover much of the dashed blue lines plotted from the analytical expression (5.44). All of the dashed blue lines can be reached by reversing the direction of rotation of the field. The dashed green lines are again the unstable equilibrium configurations

calculation proceeds very slowly at first, then speeds up, and finally slows down as it overshoots the final value and settles back with critical damping. Trying to find the critical angle by this method is prohibitive in calculation time, because the closer the angle is to the critical angle the longer the calculation takes because the torques vanish at the critical angle. This is called critical slowing down. Fortunately, the points taken at the step beyond criticality, where the torques are large enough for rapid calculation, are sufficient to calculate with all necessary precision just where the irreversible rise would have occurred. Just how this is done will be discussed in Sect. 5.3.5, where it is demonstrated for non-uniform magnetization.

Rotational hysteresis is often shown on a diagram giving the component of the magnetization along the direction of the field M_H as a function of ψ. This can be a polar plot, as shown in Fig. 5.12 for $H = 33$ Oe, which is just above the threshold for rotational hysteresis at $H = 31.925$ Oe. To make Fig. 5.12, (5.44) is used to get ψ from θ and then $M_{H_y} = \cos(\theta - \psi)\sin\theta$ is plotted against $M_{H_x} = \cos(\theta - \psi)\cos\theta$.

The solid lines in Fig. 5.12 show the actual path as calculated using the *LLG Micromagnetics Simulator*, while the dashed curves are the analytic expression obtained using (5.44). The small jump back from the outer arc to the inner arc occurs within one step in the *LLG* calculation, so that it appears continuous, but inspection of the analytic curves show that this is not the case. Again the jumps are back and forth between the deeper minima (the inner arcs) and the shallower minima (the outer arcs). For H above the highest field for which there is hysteresis, the path is almost

a circle of radius one. For small H, well below the lowest field for which there is hysteresis, the path approaches a circle with radius 0.5 centered at $M_{H_x} = 0.5$ and $\psi = 0$.

Time Dependent Fields. All of the above relates to equilibrium states reached by waiting long enough at each field for the magnetization to settle down. Next consider the response to fields changing in time. The uniaxial anisotropy with two sets of minima (Fig. 5.7a) serves to illustrate the problem of not fully switching. It mimics the behavior of memory elements. To obtain selectivity from an array of elements, the H_x switching field is applied using a current carrier called the word-line. Every element along the word line is subjected to the same H_x. The H_y bias field is applied using a current carrier called the digital line, which is orthogonal to the word line. Every bit along the digital line is subjected to the same H_y, but only the bit at the intersection of the two lines experiences both fields. Because one must anticipate that not all elements will have identical characteristics, it is necessary to have a comfortable working margin. In the most efficient switching operation, the net field from the two lines would be at 135° to the easy axis; for the switching astroid shown in Fig. 5.10a, this is $H_x = -70$ Oe and $H_y = 70$ Oe. Both of these values are well below the 120 Oe field given by the tips of the astroid. The situation is better for the switching diagram in Fig. 5.10b; for example, $H_x = -50$ Oe and $H_y = -30$ Oe. Neither of these fields alone has much chance of putting an element in a wrong state. But the bit being switched might get trapped in a secondary minimum. One approach to this problem is to investigate varying the time of the application of the two fields. The H_y field is useful to get the process started, but is a hindrance to finishing the process. Clearly one should consider turning the H_y field off partway through the switching process. The dynamics of this has a few surprises. In the quasi-static case, the magnetization stays close to the (x, y) plane. When the fields are applied suddenly, the magnetization makes excursions out of the plane. Once there is an m_z, the H_y field serves to drive the magnetization into the $-m_x$ direction, which aids the switching process. For switching an element with uniaxial anisotropy with full symmetry about the x-axis, it does not pay to turn off the H_y field. All this changes if one constrains the magnetization to the (x, y) plane, as is the case for thin films, where the magnetostatic interaction operates to discourage excursions out of the plane. There it really does pay to turn off the H_y field during the reversal. It is necessary to have the m_z component to produce the magnetostatic field that keeps the m_z component from becoming large. That same magnetostatic field serves to increase the precession rate of the magnetization in the plane. The switching takes place more rapidly for the constrained motion than for the free motion. It would even pay to have the H_y field reversed during the switching process, except for technical reasons, involving circuitry, that makes this prohibitive for memory arrays.

Adding In-plane Anisotropy. For illustrating the foregoing remarks, I move beyond the single Fe atom and consider a thin plate (thin in z) in the form of a square or a circle in the (x, y) plane. The magnetostatic energy is isotropic in the plane but highly anisotropic with respect to magnetization pointing out of the plane. Modifying the anisotropy energy of (5.38) to include a magnetostatic term corresponding to a flat

plate mimics this;

$$E/V = -H_x M_s \cos\theta - H_y M_s \sin\theta\cos\phi - K_{u_2}\cos^2\theta - K_{u_4}\cos^4\theta + S\sin^2\theta\sin^2\phi, \tag{5.45}$$

where ϕ is the angle out of the plane and $S = 0.0185$ picoerg/nm^3 or 1.85 MJ/m^3. If the magnetization is tightly coupled, the magnetostatic energy is independent of the direction of the magnetization in the plane for the square or the circle. To the extent that the magnetic moments are not perfectly coupled, the magnetization configuration changes with the direction of magnetization and so does the magnetostatic energy. To first and second order this contributes to the two-fold and four-fold in-plane anisotropies.

The response with the constraint of (5.45) is shown in Fig. 5.13a for two slightly different time sequences of magnetic fields. The calculation is carried out with critical damping; $\alpha = 1$, a larger damping than one finds experimentally.

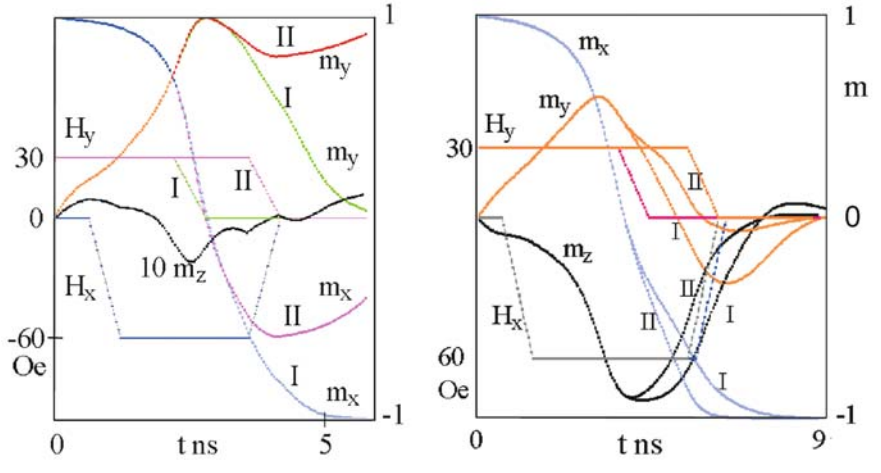

Fig. 5.13. The response of an Fe atom to pulsed magnetic fields for the anisotropy energy density of Fig. 5.7a with (**a**) and without (**b**) the magnetostatic energy density as added in (5.45) to make it hard for the magnetization to turn out of the x,y plane. First H_y is turned on and then H_x. In (I) H_y is turned off in the middle of the switching process. In (II) H_y is turned off at the end of the switching process. For (**a**) the switching process goes to completion in (I), but in (II) the magnetization is trapped in a secondary minimum. Throughout both processes m_z is small, but it produces the torque that drives the reversal. It is shown magnified by 10 for the process (II) where the magnetization becomes trapped. In (**b**) the effective field has little z component. Maintaining H_y during the second half of the switching aids in the reversal because the magnetization develops a large m_z that responds to H_y by driving the magnetization in the $-x$ direction to complete the reversal

The same calculation carried out for the anisotropy as given in (5.38), without the constraint of (5.45), is used to produce Fig. 5.13b. When the constraining magneto-

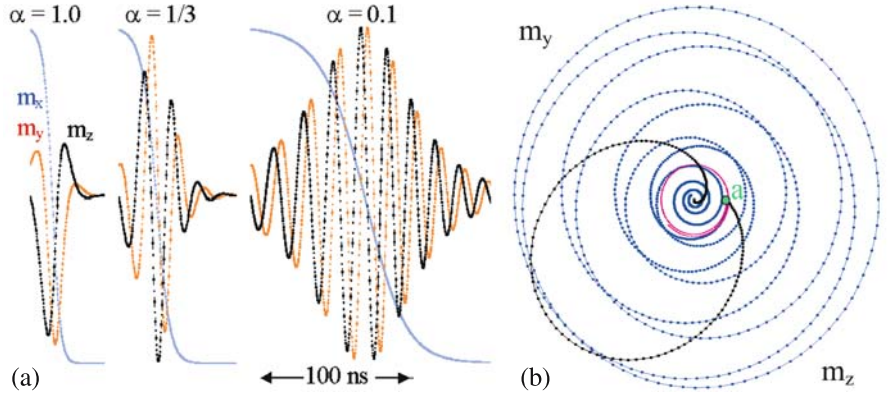

Fig. 5.14. (**a**) The effect of damping on the magnetization reversal, in $H_x = 20$ Oe, for a tightly coupled permalloy sphere or cube starting from $m_x = 0.98$, $m_y = 0.2$, $m_z = 0$. To reach steady state, the number of cycles on reversal is approximately $1/\alpha$. The damping of m_x may be obtained analytically from (5.37) as well as by LLG as done here. The results for $\alpha = 0.01$ are not shown because it is on a long time scale and the cycles are close together. (**b**). The paths in (m_y, m_z) space are shown in black for $\alpha = 1.0$, blue for $\alpha = 0.1$, and slightly more than one cycle is shown in red for $\alpha = 0.01$, all starting at the point labelled "a" near the center

static energy is absent, the excursion in the z direction lengthens the time of response, but the presence of a large m_z makes H_y effective in completing the reversal in contrast to the behavior in Fig. 5.13a.

5.2.4 Effect of Planar Geometry on Dynamical Response

Look more closely at the difference between a spherical or cubic system and a circular or square thin film. Consider permalloy with M_s = 800 emu, which has a very small anisotropy, 1000 erg/cm^3, switching in a field of 20 Oe. The apparent value of the damping constant for bulk Permalloy is $\alpha = 0.007$. Here α will be treated as a variable to illustrate the role of damping and the effect of shape on the reversal process. Let the dimensions be small enough for the magnetization to be so strongly coupled that it acts as a single atom, but subjected to the demagnetizing effects of the thin film. The size would be too small to be of practical interest because of thermal instability, but it serves as a guide to what happens in less tightly coupled systems.

The case of a spherically symmetric or cubic system was treated above. An analytic expression is given in (5.37). The role of α is illustrated in Fig. 5.14. The reversal processes are compared for α = 0.1, 1/3 and 1.0 for the sphere or cube. The curves for all the components, shown in Fig. 5.14, were produced using the *LLG Micromagnetics Simulator*.

For a tightly coupled system, if, at any point in the motion, the precession is almost in a fixed plane, there are two important relations for the ellipticity of the orbit and the frequency of precession. If a precessing moment experiences an effective field

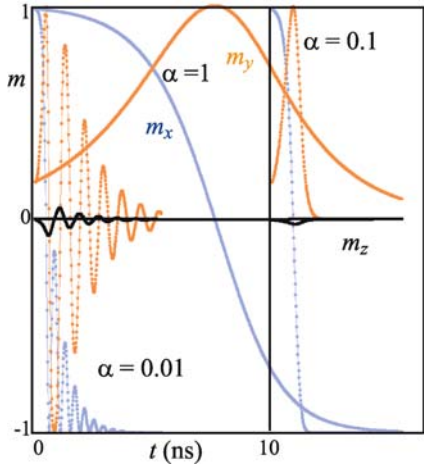

Fig. 5.15. The dynamical response to a reversing field for a tightly coupled magnetic system in the form of a thin film square plate or circle for damping parameter $\alpha = 1.0$, $\alpha = 0.1$ and $\alpha = 0.01$. For clarity, the zero of time is shifted for plotting the results for $\alpha = 0.1$. The large magnetostatic energy, generated when the magnetization tries to precess into the z direction, perpendicular to the thin film, results in a very elliptical orbit with m_z much less than m_y. For low damping, in each cycle there is a well-defined precessional frequency that varies only slightly throughout the full reversal

H_1 at the maximum of the orbit and an effective field H_2 at the minimum, the major and minor axes are in the ratio $a/b = (H_2/H_1)^{1/2}$ and the angular frequency of the precession is given by $\omega = \gamma(H_1 H_2)^{1/2}$. This qualitatively accounts for the elliptical orbit for the constrained motion of Fig. 5.15, the dynamical response to a reversing field for a tightly coupled magnetic system in the form of a thin film square plate or circle for damping parameter $\alpha = 0.01$, $\alpha = 0.1$ and $\alpha = 1$. The extra magnetostatic field acts when the magnetization is out of the plane. This increases H_2, making the orbit elliptical and also increases the rate of precession; even for the case where the motion is hardly constrained to the (x, y) plane as the reversal takes place in one cycle.

Experimenters report values of α near 0.01. In thin films this leads to oscillations after switching and long times for the oscillations to die out. Things go better for device purposes with $\alpha = 0.1$, which can be achieved by alloying. The speed of precession is twice that of critical damping and the oscillations fall off rapidly in time; see Fig. 5.15.

The dynamic response is important to consider even when carrying out calculations to find the equilibrium states, because it determines the time necessary for the calculation. Close to equilibrium, the time scale becomes very long. This makes it important to use analytical techniques to determine equilibrium behavior from calculations well away from equilibrium.

5.3 Non-uniform Magnetization

All of the above discussion of anisotropy and damping for the single iron atom extends to larger aggregates of Fe as long as the exchange interaction responsible for ferromagnetism is able to couple the magnetic moments together so that the collection acts like a big atom. The crystalline anisotropy serves also to keep the moments well aligned. If the magnetization deviates from uniform magnetization, it can do so either by bending, twisting or splaying the array of magnetization vectors on adjacent atoms. Bends and twists are represented by functions that have a curl and no divergence. Splays are functions that have a divergence but no curl. Together these functions form the basis set for vector harmonics. The divergence of the magnetization is a source term for the magnetic field $\boldsymbol{H}$. As $\nabla \cdot \boldsymbol{B} = 0$, it follows that $\nabla \cdot \boldsymbol{H} = -4\pi\nabla \cdot \boldsymbol{M} = 4\pi\rho_m$, where the magnetic charge density ρ_m increases the energy, serving as the source of $\boldsymbol{H}$, which in turn acts on all the charge density resulting from $\nabla \cdot \boldsymbol{M}$. This self-magnetostatic energy also acts to suppress $\nabla \cdot \boldsymbol{M}$. There is no magnetostatic penalty for curling, which includes scalar twists, $\boldsymbol{m} \cdot \nabla \times \boldsymbol{m}$, and vector bends, $\boldsymbol{m} \times \nabla \times \boldsymbol{m}$.

There are two ways to obtain non-uniform magnetization. One is to have spatially varying anisotropy that has different preferred directions from place to place. The other comes from magnetic charges that appear on the surface of an object that is uniformly magnetized. The surface charge tends to rotate the magnetization into the surface. This acts like a surface anisotropy. Competing anisotropies are satisfied by distorting the magnetization pattern, which leads to a decrease in the extent to which the exchange energy is able to keep the magnetization uniform. This decrease in the degree of alignment is an increase in the negative exchange energy. The exchange energy term in micromagnetics is the positive change in exchange energy due to divergences and curls.

5.3.1 Exchange Energy

Changes in the exchange energy depend on the nine derivatives of the three magnetization vectors with respect to the three directions. To the lowest order, the combination of derivatives should be sums of products of the first derivatives such that the inversion symmetry of the quantum mechanical effect called the exchange interaction is preserved. The exchange energy density, depends on spatial derivatives of the magnetization;

$$\begin{aligned} E_{ex}/V = A\big[&(\mathrm{d}m_x/\mathrm{d}x)^2 + (\mathrm{d}m_x/\mathrm{d}y)^2 + (\mathrm{d}m_x/\mathrm{d}z)^2 \\ &+ (\mathrm{d}m_y/\mathrm{d}x)^2 + (\mathrm{d}m_y/\mathrm{d}y)^2 + (\mathrm{d}m_y/\mathrm{d}z)^2 \\ &+ (\mathrm{d}m_z/\mathrm{d}x)^2 + (\mathrm{d}m_z/\mathrm{d}y)^2 + (\mathrm{d}m_z/\mathrm{d}z)^2\big], \end{aligned} \tag{5.46}$$

where the m's are the components of the unit vector in the direction of the magnetization. This is summarized using the gradient operator

$$E_{ex}/V = A\left[(\nabla M_x)^2 + (\nabla M_y)^2 + (\nabla M_z)^2\right]/M_s^2 \tag{5.47}$$

The exchange energy enters micromagnetism as an effective field

$$\begin{aligned}\boldsymbol{H}_{ex} =& 2A\left[(\partial^2 m_x/\partial x^2 + \partial^2 m_x/\partial y^2 + \partial^2 m_x/\partial z^2)\hat{\boldsymbol{x}}\right.\\ &+ (\partial^2 m_y/\partial x^2 + \partial^2 m_y/\partial y^2 + \partial^2 m_y/\partial z^2)\hat{\boldsymbol{y}}\\ &+ \left.(\partial^2 m_z/\partial x^2 + \partial^2 m_z/\partial y^2 + \partial^2 m_z/\partial z^2)\hat{\boldsymbol{z}}\right]/M_s, \end{aligned} \tag{5.48}$$

which is written in the deceptively simple form, using the Laplacian operator,

$$M_s \boldsymbol{H}_{ex} = 2A\triangle \boldsymbol{m}, \tag{5.49}$$

which is an elegant way to hide nine second derivatives. The exchange energy could have been written as

$$E_{ex}/V = -A\boldsymbol{m}\cdot\triangle\boldsymbol{m}. \tag{5.50}$$

The exchange constant A is, typically, 0.2 picoerg/nm. The exchange field adds spatial derivatives to the dynamical equations, leading to severe restrictions on the time steps for which the calculations are mathematically stable. These fields tend to fight against curvatures in the vector magnetization whether they are twists, bends or splays. This generally is achieved by making the angles between moments as small as possible over the distance that spans the regions where anisotropy would have the moments in different directions.

The simplest example is where the magnetization is pinned on one plane to be in one direction in the plane and on a parallel plane to be in another direction in the plane. The exchange energy is minimized by a uniform variation in angle from one plane to the other, in the plane as in a Bloch wall. The exchange field vanishes because there is no curvature in the magnetization pattern. For such a wall between two planes of area $100\times 4\,\text{nm}^2$ separated by 100 nm, the exchange energy is about 4 picoerg for permalloy. If the wall width were increased to 1 μm, the exchange energy would decrease by a factor of 10. Such a wall would have a large magnetic surface charge density.

5.3.2 Magnetic Surface Charge Density

Defects in crystal structure cause variations in anisotropy direction. If the variation is gradual in space, the magnetization follows the preferred direction with little increase in exchange energy. To the extent that the magnetization deviates from the preferred direction, there is an increase in the anisotropy energy. Also, to the extent that there is curvature in the magnetization pattern, there is an increase in the exchange energy. It is the surface of the material that is the biggest of all defects. If the magnetization points out of a surface, there is a discontinuity in the magnetization. This produces surface magnetic charge density σ_m,

$$\sigma_m = \boldsymbol{n}\cdot\boldsymbol{M}, \tag{5.51}$$

which is the main source of fields that point in different directions in different parts of a ferromagnetic body, causing the magnetization to vary in direction, thus increasing the exchange energy.

When a finite body is uniformly magnetized, the magnetic surface charge density is the source of fields in the opposite direction to the magnetization. For a slab, infinite in x and y, magnetized in the z direction, the field from charges on the two surfaces would be opposite to M_z and precisely cancel the contribution of M_z to the magnetic induction B; that is, $H_d = -4\pi M_z$ which is 22 kOe for iron. The field H_d from the surface charge is called the demagnetizing field. For this case there is no field outside the slab. Inside the slab, each surface contributes $-2\pi M_z$ to H. When a slab is magnetized perpendicular to the surface, the magnetostatic self-energy is a maximum, given by $2\pi M_z^2 V$, where V is the volume of the slab. This is possible when there is an H_z for which the energy of M_z in that field is at least twice as negative as the maximum in the magnetostatic self-energy is positive. The factor of two arises because the magnetostatic self-energy goes as M_z^2 and the field energy goes as $-M_z$ for the field in the z direction. For a square slab $100 \times 100 \times 4\ \text{nm}^3$ with the magnetization in the plane, the magnetostatic energy from the surface charges is 8 picoerg for permalloy. If magnetized out of the plane, it is 144 picoerg.

The way to avoid the large surface charge density is to have the magnetization always lie in the surface. Thus every surface is a source of anisotropy; the magnetization has a preferred plane at the surface. (There are additional contributions to the anisotropy from the atomic structure at the surface.) If the magnetization everywhere lies in the surface, there must be changes in the direction of magnetization that increase the exchange energy, increase the anisotropy energy and lead to divergences in $\boldsymbol{M}$ in the interior, all of which increase the energy. For a small body, this is prohibitive. To have the magnetization lie everywhere in the surface of a larger body requires a doubly connected surface such as a toroid. For a simple surface there are always two points where the magnetization must point into or out of the surface.

5.3.3 A Vortex in a Circular Ultrathin Film

The simplest example of a non-uniform magnetization pattern is a circular thin film with a single vortex. The magnetization is tangent to the edge around the circumference and circulates in the plane of the circle. The two points where the magnetization must point into or out of the surface are in the centers of the two flat faces. This configuration has cylindrical symmetry, rotational invariance and negligible dependence on z for sufficiently thin films. In fact, the lack of z dependence is the definition of an ultrathin magnetic film.

It is convenient to express the exchange energy density in cylindrical coordinates, (ρ, ϕ, z) for the case where there is only dependence on ρ.

$$\frac{E_{ex}}{V} = A\left[\left(\frac{\partial m_\rho}{\partial \rho}\right)^2 + \left(\frac{\partial m_\phi}{\partial \rho}\right)^2 + \left(\frac{\partial m_z}{\partial \rho}\right)^2 + \frac{m_\rho^2 + m_\phi^2}{\rho^2}\right]. \tag{5.52}$$

The configuration of a vortex in an ultrathin film of radius R and thickness t, with components M_ϕ and M_z, has M_ϕ going to zero as ρ goes to zero and M_z going to

M_s at the center. The hyperbolic functions $\mathrm{sech}(x)$ and $\tanh(x)$ are useful in thinking about unit vector fields, because $\mathrm{sech}^2(x) + \tanh^2(x) = 1$. It seems that nature knows this, for this is the basis for the vortex configuration. The two components are very close to

$$M_z = M_s \quad \mathrm{sech}(\rho/\lambda) \quad \text{and} \quad M_\phi = M_s \quad \tanh(\rho/\lambda). \tag{5.53}$$

There is a simpler configuration where $\boldsymbol{M} = M_\phi \hat{\boldsymbol{\phi}}$, but then the exchange energy density is just the last term in (5.52), which produces an infinite energy density at the origin and a logarithmic singularity in the total energy. This curling pattern eliminates all the magnetostatic energy, but not without a severe complaint from the exchange energy. The configuration of (5.53) avoids the logarithmic singularity, but at the price of magnetostatic surface charges developing on the top and bottom surfaces,

$$\sigma_{\pm t/2} = \hat{\boldsymbol{n}} \cdot \boldsymbol{M} = \pm M_s \ \ \mathrm{sech}(\rho/\lambda,) \tag{5.54}$$

and bulk magnetic charge density throughout the volume given by

$$\rho_m = -\nabla \boldsymbol{M} = -M_s \left[\mathrm{sech}^2(\rho/\lambda)/\lambda + \tanh(\rho/\lambda)/\rho\right]. \tag{5.55}$$

The magnetostatic energy includes the self energies of the charges on the three surfaces, the self-energy of the bulk charges, and the interaction of each of these with each other. This is might be approached analytically, but not by me. The magnetostatic energies are the great challenge in micromagnetics. I rely on the *LLG Micromagnetics Simulator.*

Magnetostatic energy. To illustrate what is involved in calculating the magnetostatic energy of a vortex, consider a simpler case, the magnetostatic energy of a slab with dimensions a, b, c with the magnetization along a. This is found by two four-fold integrations. The first is over an end surface of area bc. The second is over the two ends separated by the distance a. The result has 11 terms, including 6 complicated logarithms, an arctan, and four rational functions; for example, see (5.57). If you want to see all the terms, the reference is Aharoni [5.4]. The slab results provide a check on two of the integrations that go into a micromagnetics calculation.

To sense the complexity of magnetostatic interactions, consider just the integration over one end, which is a rectangle of uniform charge density M_s and area bc. The form of the interaction of the charge density with itself in a square of area s^2 is that of two equal charges $Q_1 = Q_2 = M_s s^2$, separated by a distance given by the inverse of $\langle 1/r \rangle$, the average inverse of the separation of all elements of the charge distribution. This energy is

$$E_m = Q_1 Q_2 \langle 1/r \rangle / 2 = M_s^2 s^4 \beta / s, \tag{5.56}$$

where the factor 1/2 comes from this being a self-energy, or from correcting for counting each pair of charges in the distribution twice, and the factor $\beta = 1.4866$ comes from the integration of

$$
\begin{aligned}
E_m =& \frac{M_s^2}{2} \int_{-c/2}^{c/2} \int_{-c/2}^{c/2} \int_{-b/2}^{b/2} \int_{-b/2}^{b/2} \frac{\mathrm{d}y\,\mathrm{d}y'\,\mathrm{d}z\,\mathrm{d}z'}{\sqrt{(y-y')^2+(z-z')^2}} \\
=& \frac{M_s^2}{2} \left[bc^2 \ln \frac{\sqrt{b^2+c^2}+b}{\sqrt{b^2+c^2}-b} + b^2 c \ln \frac{\sqrt{b^2+c^2}+c}{\sqrt{b^2+c^2}-c} \right. \\
& \left. + \frac{2}{3} \left(b^3 + c^3 - \left[b^2 + c^2 \right]^{3/2} \right) \right] \qquad (5.57)
\end{aligned}
$$

for b = c = s.

In micromagnetic calculations using finite grids, preferably cubic, the charges all lie on the faces of the cubes, because $\boldsymbol{M}$ is assumed to be constant within each cube. The magnetostatic energy is the self-energy of each surface plus the interaction energies between the charges on one face of one cube with the charges on the other faces of that cube and all the faces of all the other cubes. This depends on the position and orientation of the faces with respect to one another. All the integrals can be done. After being told by Aharoni that they could be done, it took me a month to do one and I still got a sign wrong. I use programs developed by others with skill and persistence.

In finite element calculations, the fields are obtained from the magnetic potential found from solving Laplace's equation using the magnetic volume charge density and the magnetic surface charge density [5.6]. This has been explained to me several times, and I have followed some calculations using finite elements, but I am not competent enough to explain its many complexities.

In answer to the question of whether one should choose to learn finite element or finite grid techniques, I can only say that "it depends". The taste, talents and ambition of the chooser are part of the answer. Finite element may be more powerful if pursued sufficiently, but there are reasons why finite grid programs for micromagnetics are available to the general public while finite element programs are not.

Exchange Energy of a Vortex. For a vortex in an ultrathin film, the exchange energy density follows directly from (5.52) on substituting the components from (5.53).

$$
E_{ex}/V = A \left(\operatorname{sech}^2 (\rho/\lambda) / \lambda^2 + \tanh^2 (\rho/\lambda) / \rho^2 \right). \qquad (5.58)
$$

The integral of the first term is straight forward; that of the second is not. Fortunately, I have a very good approximation to the $\tanh^2(\rho/\lambda)/\rho$ function, one that can be integrated. That approximation produces the result that the total exchange energy out to the radius R in a slab of thickness t is

$$
\begin{aligned}
E =& 2\pi t A \ (R/\lambda) \tanh(R/\lambda) \\
& + \ln [\operatorname{sech}(R/\lambda)] + \ln [(\beta R/\lambda)/\tanh(\beta R/\lambda)] \qquad (5.59)
\end{aligned}
$$

with $\beta = 1.2393$ as a good (0.01 out of 100) empirical fit of the approximation to a numerical integration of $\tanh^2(x)/x$. This result should be useful for checking computer codes. A Permalloy disk with 21.3 nm radius and 4.3 nm thickness is sufficiently large for a vortex to be stable against displacement.

A Full LLG Calculation for a Vortex. Finally, on our spin around the track we have reached a full LLG calculation. The material is Permalloy with $M_s = 800$ Oe, $K_{u_2} = 1000$ ergs/cm^3 along the x axis, $A = 1.05$ μergs/cm^3, $\gamma = 17.6$ MHz/Oe and $\alpha = 1$. The grid is $60 \times 60 \times 6$ with cubic cells 0.7165 nm on a side. The computed circular disk is contained within the thickness of 4.299 nm and a circle of diameter 42.6 nm. The adjacent cells on both sides of the boundary are used to correct for the coarseness of the cubic elements. Each cell is uniformly magnetized, so that all the volume charges as well as the surface charges are on the boundaries of the cells. The calculation is carried out with rotational matrices with second-order corrections for the finite time steps, here 1/60 ps. The magnetostatic interactions are evaluated using fast Fourier transforms for all but the near neighbors, which are calculated by brute force to minimize the serious problems that arise from the boundary elements [5.5]. The magnetostatic interactions are re-evaluated every 64th time step. The vortex is created in the input file with its center displaced from the center of the disk, so, when the pattern becomes symmetrical, it is from the equations of motion and not because the original configuration was trapped by artifacts from the grid. The calculation was carried out for 500,000 iterations covering 8 ns of relaxation with a time constant of 1.4 ns over a real time period of 9 hours on a 2-GHz dual-processor workstation.

The final configuration is excellently described by (5.53); see Fig. 5.16a. Fitting the magnetization to (5.53) yields the parameter $\lambda = 4.848$ nm. The dimensions of the disk are just sufficient for vortex stability. The diameter is big enough that the vortex does not have a large m_z at the boundary, but not so big that m_z has room to change sign under the influence of the field from the vortex core. The variation of the magnetization from the bottom to the top layer is a maximum at the circumference, but this does not have significant effects unless the thickness approaches 30 nm. This configuration is useful for checking micromagnetic codes, because, not only are the magnetization components known analytically with λ as a fitting parameter, so also the exchange energy is known analytically. As the energy expression contains the parameter λ these should be self-consistent.

Magnetostatic-exchange Length of a Vortex. An estimate of λ is found starting with the exchange energy, $2\pi tA \ln(R/\lambda)$. If the magnetic surface charge is treated as a capacitor of thickness t, area $\pi\lambda^2$ and charge density M_s, the magnetostatic energy is $\pi t\lambda^2(2\pi M_s^2)$, where the choice of 1 λ for the radius of the vortex is arbitrary. Minimizing the two energies with respect to λ yields the classic magnetostatic exchange length $\lambda_0 = [A/(2\pi M_s^2)]^{1/2}$. For Permalloy $\lambda = 5$ nm. From the *LLG Micromagnetics Simulator* calculation, the parameter $\lambda = 4.85$ nm. The closeness of λ obtained by the dimensional argument and λ found from fitting the magnetization is the result of choosing the effective radius for the magnetostatic approximation as 1 λ.

The exchange energy calculated by LLG is 6.7508 picoerg. One can find the value of λ in (5.59) that produces this energy. The difference in the λ from fitting the magnetization pattern and the λ from fitting the energy is less than 0.5 %. The value from fitting the magnetization gives a slightly higher energy. This may be fortuitous but it is in the direction consistent with minimizing the energy by functional variation. The computer should be able to use a million degrees of freedom to improve on

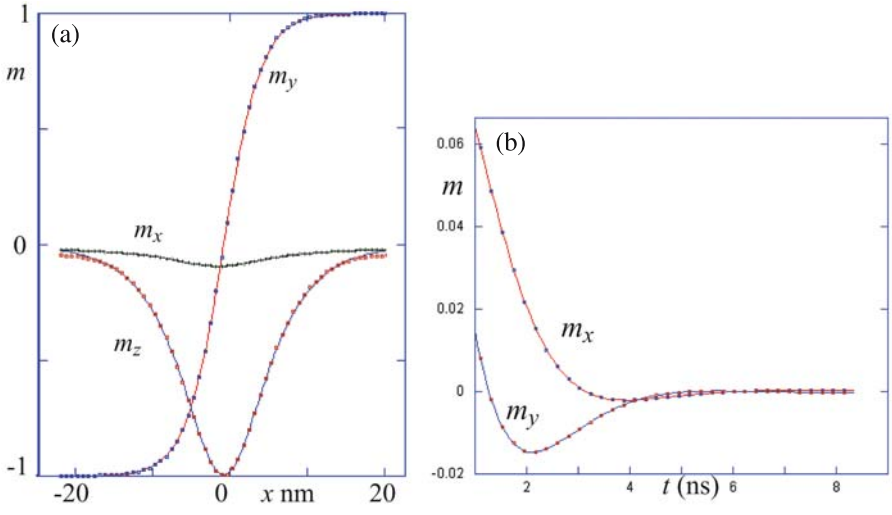

Fig. 5.16. (**a**) The components of the magnetization for a vortex along a line through the center of the vortex in a circular permalloy disk of radius 21.3 nm and thickness 4.299 nm. The solid lines are the fits to (5.53). Note the small deviations near the edge of the circular disk for the m_z component. The m_x component appears because the grid has an even number of points. There is no slice through the origin, only along the rows adjacent to the midline, one of which is shown here. This is taken into account in the curve fitting. (**b**) The relaxation of the vortex to the center of the circle after removing the field used to displace it. The magnetization components, m_x and m_y, relax as a slightly under-damped oscillator coming to equilibrium. The curves through the points are 5 parameter fits using $m_f + m_1 \exp(-t/t_1)\cos(\omega t + \psi)$ with error on the order of the round-off errors in the calculation

a calculation with but one degree of freedom. Indeed it does, for one can see that near the circumference, M_z no longer decreases as rapidly as the $sech(\rho/\lambda)$ function. The further from the center of the vortex, the more important are the magnetostatic terms, which set the conditions on the boundaries in the first place.

While such correspondence may seem fortuitous, it is not, because the other important length in the problem is the thickness t, which here was chosen close to the exchange length as this is the thickness needed to sustain a vortex. It is much smaller than the thickness, approximately 30 nm, needed to have a vortex form spontaneously from the reduction of an applied field.

Extrapolation. The vortex calculation above was carried out to complete relaxation, but if it had been stopped earlier all the results could have been found by extrapolation. The approach to the equilibrium values of the variables is either an exponential, a critically damped oscillation with a single sign change, or a slightly underdamped oscillation, depending on which variable is being extrapolated. The derivative of the total energy cannot change sign. Any of the energy terms making up the total energy or the magnetization components can have a reversal of its derivative with respect to time. The approach to equilibrium is shown in Fig. 5.16b for the magnetization

components. For each of the energy terms, the approach is a simple exponential with all points fit to the precision of the computer. This is a special feature of the vortex relaxation, for in many other systems the magnetostatic energy and the exchange energy both come in as under-damped oscillators. The simple exponential fits are so good that the asymptotic result is found to full accuracy when the data are restricted to two time constants. Using the data for one-fifth of a time constant, the extrapolation to the final value is off by 3 units compared to the 140 units to extrapolate to the final value.

In micromagnetic calculations it is necessary to have a criterion for stopping the calculation. Often the limit is set by prejudging the number of iterations or the change per iteration. A more powerful criterion is to set a limit from changes of the extrapolated values. If the extrapolated values are not changing, one already has the answer. If they are changing drastically, most likely there is an instability developing, because the magnetization pattern is either about to switch or to become mathematically unstable. Then the calculation should be restarted with changed conditions.

Vortex Motion. For the above example of a vortex state, the vortex state is far from the lowest energy state. An almost uniform magnetization pattern is more stable. The vortex state is easily converted to the uniform state by the application of a field. When the vortex moves in an applied field, its internal energy E_{int} (exchange plus anisotropy plus magnetostatic) rises until the derivative of E_{int}, with respect to the component of the magnetization along the field, is equal to the applied field. As the field is increased the vortex moves further from the center. Above a critical field, the vortex moves out through the edge of the circle if that field is maintained. If the field is lowered just after the vortex starts to accelerate, it moves back towards the center. The further the vortex moves out, the smaller the field necessary to keep it moving, until it reaches the point where $\partial E_{\text{int}}/\partial M_\rho = 0$. Beyond that point, if the field is removed the vortex keeps moving. This implies that knowledge of the position of the vortex, or of M_ρ, is sufficient to describe the system; the system acts as if either of these quantities is a state variable. For the vortex in a circle, this is approximately the case. For other magnetic configurations in various geometries, it may be a better or worse approximation. So in some cases it is more useful than in other cases to think of the path in $(\langle mx\rangle, \langle my\rangle)$ space and E_{int} along that path.

5.3.4 Non-uniform states

A circular disk, such as the one used above to discuss the vortex, has lower energy states than the vortex state if the diameter is less than 50 nm. These states are almost uniformly magnetized, but the magnetostatic energy from charges on the vertical periphery tends to rotate the moments toward the tangent to the circle. There are two directions for the moment to point along a tangent. If the direction taken is always in the same sense around the periphery, there must be at least one vortex in the material. To avoid a vortex it is necessary to have at least two reversals of the magnetization direction on going around the periphery. If there are two reversals, there are two types of patterns in addition to the possibility of having a vortex.

S-states and C-states. If there is no vortex and both reversals are directly opposite each other, inversion symmetry can be maintained. This is called an S-state. If the two reversals are not directly opposite from each other, the inversion symmetry is broken. This is called a C-state. Even in a circular disk without crystalline anisotropy, these two states will find directions that are preferred, because the circle is composed of cubic cells. There are methods of correcting for the jagged surfaces that result, but they are approximate corrections leaving some residual preference for the orientation of the patterns.

The Anti-vortex. If there are four reversals on going around the periphery, there must be at least one anti-vortex. The winding number for the vortex is $+1$; for the anti-vortex, it is -1. The winding number is the number of rotations of the magnetization on going around the periphery. The S- and C-states have zero winding number. The -1 for the anti-vortex is because the magnetization rotates in the opposite sense to the clockwise or counter-clockwise direction chosen to go around the periphery.

The Super-octagon. The poet and inventor Piet Hein generalized the ellipse to a super-oval, for which the formula is

$$|x/x_0|^{2n} + |y/y_0|^{2n} = 1. \tag{5.60}$$

For the ellipse $n = 1$, for a diamond $n = 1/2$, and for a rectangle $n = \infty$. n can be used to describe patterned bits; see Fig. 5.17. For $n = 3/2$ it is easily to distinguish positions of maximum curvature that can be called corners. For an S-state with $n = 3/2$, the two reversals of sense of magnetization with respect to the surface tangent occur at opposite corners (x_1, y_1) and $(-x_1, -y_1)$, rather than at $(x_0, 0)$ and $(-x_0, 0)$, which is the fully symmetric S-state found for n=1. In the C-state with $n = 3/2$, the two reversals occur on the same side of the pattern at (x_1, y_1) and $(-x_1, y_1)$. A fully symmetric state is achieved at high fields. What happens as the field is lowered depends on the index n.

The super-oval is incorporated in the super-octagon for generating a variety of shapes; see Fig. 5.17. The trapezoidal distortion serves to stabilize the C-state and the parallelogram distortion leads to airplane propeller response to alternating fields. The super-octagon adds up to 12 parameters to the standard length, width and thickness.

The Hysteron. All bit patterns discussed to this point have been convex. The simplest surface with some concavity is called the dog's-bone. The dog's-bone can be generalized by connecting two super-octagons. The dog's-bone pattern in its simplest form is two circles connected by a bridge of smooth curvature. This configuration has such remarkable features that I have named it the "hysteron"; see Fig. 5.18. It switches by vortex motion, without losing the vortex. The vortex is analogous to the domain walls in soft magnetic materials that, by never going away, keep the soft magnetic material soft. The hysteron behaves like two interacting dipoles. The lowest energy is when the two dipoles are aligned along the axis joining them. This is the origin of the force that drives the vortex upward when the magnetization is to the right and down when the magnetization is to the left. The strength of the dipole on the vortex

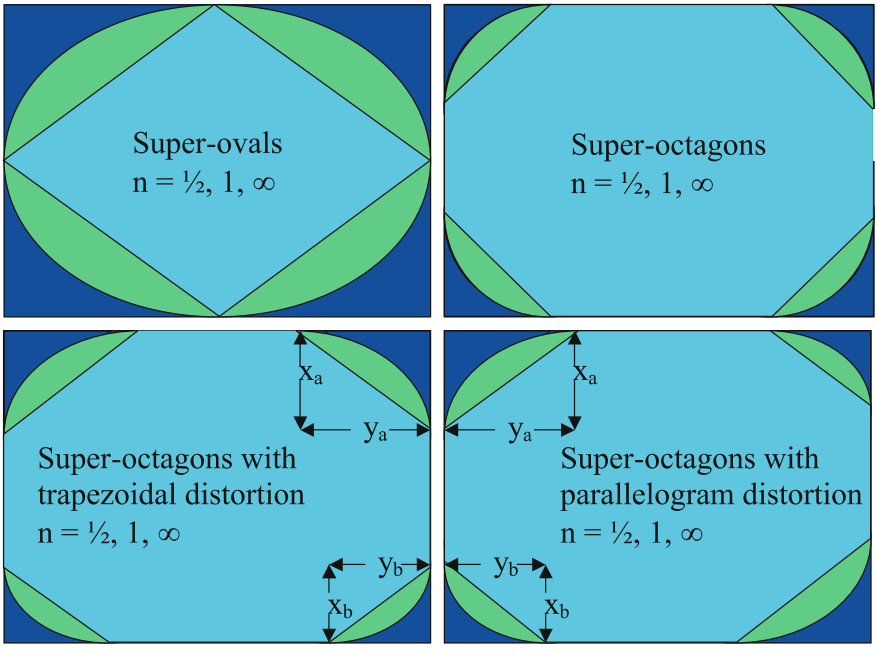

Fig. 5.17. The super-octagon for generating convex shapes with seven or more parameters using (5.60) for the super-oval in each corner. The shapes in each corner are determined by the index n. The outside shapes are all rectangles generated in the limit $n = \infty$. In the super-octagon the index n varies the shapes of the quarter sections of super-ovals in the corners. For trapezoidal distortions, the coordinates of the corners on the right and left are the same, but those on the top and bottom are not. The corners match diagonally for parallelogram shapes

side varies with position of the vortex. The system reverses by turning off the dipole when the vortex is in the center of its circle.

Distinction Between C and S States. The distinction between C and S states is important in switching patterned elements for memory applications; see Fig. 5.19. To switch a fully symmetric state with maximum curvature at $x_1 = x_0$ and $y_1 = 0$ it is necessary first to break the symmetry. This is done by applying a bias field or naturally by thermal fluctuations. If $y_1 \neq 0$, the S-state is already biased. To switch the C-state easily, it is necessary first to convert it to an S-state. Without bias the C-state will form a 360° wall in large $-H_x$. This wall eventually becomes unstable with respect to displacement at higher fields. In even higher fields, $\sim$ 2 kOe, the C-state can reverse by the motion of its virtual vortex, centered outside the element, moving through the surface at $(0, -y_0)$. The fully symmetric S-state in the absence of a bias field can behave like the C-state or like the biased S-state depending on thermal fluctuations.

For memory devices, it is better to start with the C-state rather than the S-state [5.7]. The S-state is already biased for switching. The C-state is biased against

switching. It will not switch by simple rotation unless a sufficient bias field is applied. It is stable against thermal fluctuations. A robust memory would have the elements always starting from the C-state. A trapezoidal distortion of the super-octagon can make the C-state (with two senses) the state to which it always returns in the absence of external fields; see Fig. 5.19d.

Anisotropy-exchange Length. If there is no lattice, as in an amorphous material, there are still the local crystalline electric fields, which, through spin-orbit coupling, give preferred directions to each moment. These very strong local anisotropies are yet weak compared to the exchange interactions that closely align neighboring moments. In this case, the randomly directed anisotropies with varying strength are subject to averaging over distances set by the anisotropy exchange length, $\lambda_K = (A/\langle K \rangle)^{1/2}$, where $\langle K \rangle$ is some measure of the strength of the local anisotropies to be averaged over. The smaller $\langle K \rangle$, the larger the range of averaging. The larger the range, the better the averaging approaches zero.

Magnetoelasticity. For amorphous materials, the anisotropy is not a determining factor in the magnetic response. Its place is taken by magnetoelastic effects. Strain gradients change the direction of the magnetization and changes in magnetization direction cause strain gradients. Magnetoelastic effects call into play another set of non-linear higher-order differential equations, both for the elastic effects and for

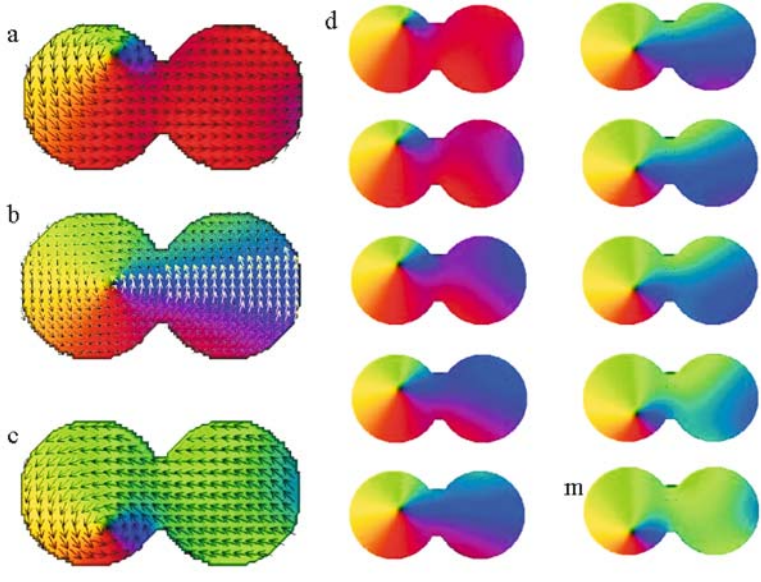

Fig. 5.18. The hysteron with dimensions $200 \times 100 \times 4\,\text{nm}^3$ has two stable states (**a**) and (**c**) and one metastable state (**b**) in zero field. It is shown switching by wall motion (**d** to **m**) in $H_x = -50$ Oe with bias $H_y = 50$ Oe. In zero field the wall is the small blue section in (**a**) and (**c**)

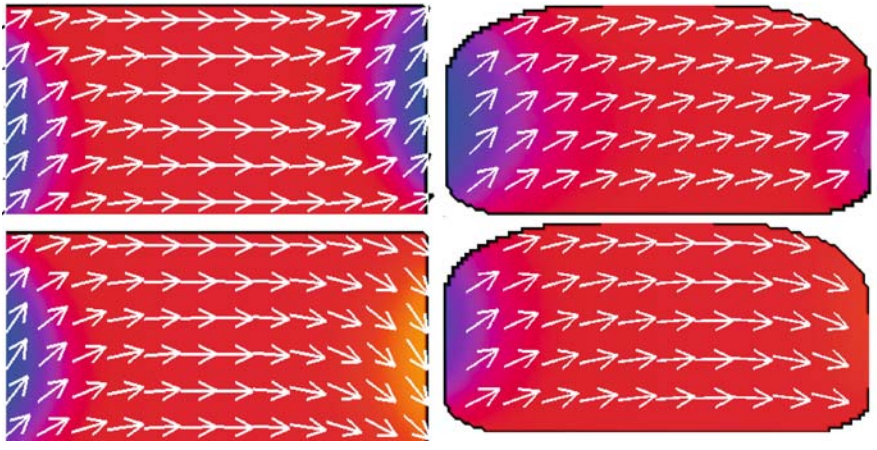

Fig. 5.19. S-state and C-state for a rectangle (**a**) and (**b**) and S-state and C-state for a trapezoidal superoctagon (**c**) and (**d**). The dimensions are $200 \times 100 \times 2$ nm^3. The C-state is locked against switching because it forms a 360° wall if $-H_x$ is applied without bias. An $H_y = 50$ Oe bias field converts the C-states to S-states to facilitate switching in $H_x = -50$ Oe. The trapezoidal superoctagon always returns to the C-state in absence of fields. The rectangle gets to the C-state under thermal fluctuations or gradient fields, neither of which are technically useful

how they interact with the magnetism. Elastic effects are described by a fourth order Laplacian. These are extremely long ranged in their effects; pressure in a pipe uniformly expands the whole pipe, no matter how thick the wall. Only the magnitude of the uniform expansion is changed by the thickness. Magnetoelastic interactions are not included in this spin around the track.

5.3.5 A Non-uniform System with Two-fold Plus Four-fold Anisotropy

To demonstrate the role of exchange and magnetostatic self-energy in micromagnetics in non-uniformly magnetized systems, I follow the example given for the single atom with a combination of second and fourth order uniaxial anisotropy. The results for a single atom were treated extensively above; see Sect. 5.2.3. The next step is to show that, in a small circle with dimensions such as the one used for the vortex, the behavior is almost the same as for the single atom. The $\boldsymbol{M}$ is no longer completely uniform and its response to $\boldsymbol{H}_{\text{eff}}$ is not the same at the edges as it is near the center because of the tendency of the magnetostatic-self energy to reduce the magnetic charge on the surfaces.

From one Atom to Many. For a well-coupled system, LLG reproduces something that approximates the earlier calculations for a single iron atom. This is shown for a series of disks of increasing radii. The method of calculation uses 2D real FFT's with rotation matrices. The calculations are carried out with edge corrections. The thickness is kept at 4 nm, as this is about the magnetostatic-exchange length

and is also a thickness of technological interest. The diameters chosen are 12, 24, 48, and 96 nm. The parameters are: $M_s = 1714$ emu/cm^3, $K_{u_2} = -60$ kiloerg/cm^3, $K_{u_4} = 80$ kiloerg/cm^3, $\alpha = 1$ and $\gamma = 17.6$ MHz/Oe, just as in the case studied in Sect. 5.2.3. From the finite size, the new parameter is the exchange constant, which should have been $A = 0.21$ picoerg/nm, but, much to my chagrin, I have discovered at a late date toward publication that I inadvertently used the value for permalloy $A = 0.105$ picoerg/nm for the remainder of this chapter.

12 nm Disk. The 12 nm diameter disk is small enough that there is close agreement with the calculation carried out for the single iron atom. The hysteresis loops for the 12 nm diameter disk are compared in Fig. 5.20a with the analytical expression of (5.40) and the LLG calculation for the atom. The energy is shown in Fig. 5.20b as a function of M_x for a series of fields around the critical value for completion of the hysteresis loop. These energies are calculated assuming that, to a good approximation, E_{int}, M_x, and M_y behave as state functions independent of applied fields. Knowledge of any two of them determines the other. For this 12 nm diameter disk the change in E_{int} with M_x is almost entirely the change in the anisotropy energy. What variations there are in the magnetostatic energy are partially compensated by opposite variations in the exchange energy; see X and M in Fig. 5.21a. All of these variations in energy are small compared with 300 k_B.

24 nm Disk. The 24 nm diameter disk shows some deviation from rigid response. The exchange energy, X in Fig. 5.21b, and the magnetostatic self-energy, M in Fig. 5.21b, have noticeable variation with M_x. The variation in X is of opposite sign and close to half of the variation in M. The variation of these with M_x is now sufficient to make a difference in the hysteresis loop; see Fig. 5.22a. The width of the hysteresis loop decreases and the slope of the central section increases, both in the direction of the response being more magnetically soft. The effect of the competition between X and M is to create patterns that are non-collinear. This decreases the net effect of the anisotropy to some extent, but the main effect of the non-collinearity is that it varies as θ_m changes with respect to the anisotropy axis, reducing the effect of the anisotropy further. The mean angle $\theta_m = \arctan(\langle M_y \rangle / \langle M_x \rangle)$ is just as useful as m_x or m_y for analyzing the changes in energy.

48 nm Disk. The behavior for the 48 nm diameter disk, shown in Fig. 5.22a, differs from the rigidly responding 12 nm disk. The hysteresis is almost gone and the slope of the central section is three times that of the smallest disk. The small loops about ± 12 Oe provide an illustration of the power of using E_{int}, M_x and M_y as state functions independent of field. The time for the LLG dynamical equations to reach equilibrium would make it not worth the effort to find the details of the small loop. The loop can be easily calculated by reading from the graph of energy as a function of M_x for a series of H_x values in the $H_y = 28$ Oe bias field as shown in Fig. 5.22b. This can be done automatically with a computer program that fits the nonequilibrium E_{int}, and $\langle M_y \rangle$ to functions of $\langle M_x \rangle$ in the region of the instability.

For the 48 nm diameter disk, the deviation of $\langle M \rangle$ from M_s becomes noticeable but it is almost independent of θ_m; the path in $(\langle m_x \rangle, \langle m_y \rangle)$ space is close to a circle

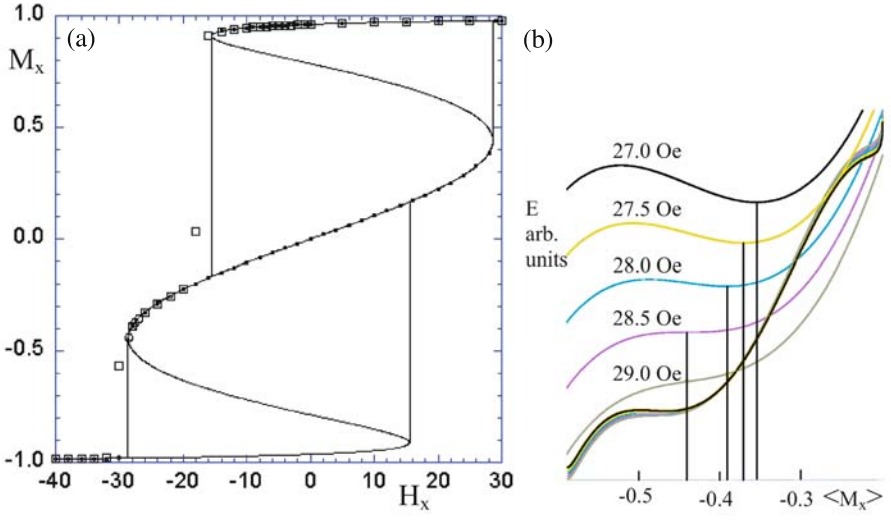

Fig. 5.20. (**a**) The analytic (from (5.40), solid line) and *LLG Micromagnetics Simulator* (square symbols) calculations for a 4 nm thick, 12 nm diameter, disk of iron with the artificial anisotropy of Fig. 5.7a in a bias field $H_y = 28$ Oe. The square symbols that are off the curve are the result of using a predetermined number of iterations for the calculations. It would take days of computing for M_x at $H_x = -16$ Oe to come to equilibrium because the torques are vanishingly small at the critical fields; here it is still near the start. Even the points at $H_x = -18$ Oe and $H_x = -30$ Oe have not converged. The dots along the line are calculations using LLG for a single atom. A precise description of the switching is obtained by the analysis shown in (**b**). M_y and E_{int}, the internal energy, equal to exchange energy plus anisotropy energy plus the self-magnetostatic energy, are first found as a function of M_x, along the calculated path. The total energy E is then recalculated for different applied fields, assuming that M_y and E_{int} are only functions of M_x. (Here this is a very good approximation). The value of M_x for which E is a minimum at each field is determined graphically as shown here. Three points read from this curve are shown as circles on the curve between -27 and -28 Oe. The unlabeled curves in the background of (**b**) are E's is for the entire range of M_x and energy

with slightly smaller radius than M_s; see Fig. 5.23a. The non-collinear structure changes only slightly with angle, but it is enough to wash out the second minimum in the anisotropy; see T in Fig. 5.21c. The variation in the magnetostatic self-energy M with M_x, is still opposite to the variation in the exchange energy X, but now three times as much.

So far I have kept the bias field at 28 Oe. Now that the magnetization is less uniform, it should be informative to change that bias. By reducing H_y to 21 Oe, see Fig. 5.23b, it is clear that the bias field plays the same role as the second minimum in the anisotropy energy in favoring the intermediate state with large M_y. This can be seen by comparing Fig. 5.23b with Fig. 5.22a for $H_y = 28$ Oe.

96 nm Disk The 96 nm disk is already big enough that there is more than one stable configuration, even if there is no anisotropy. In addition to the S-state, which has

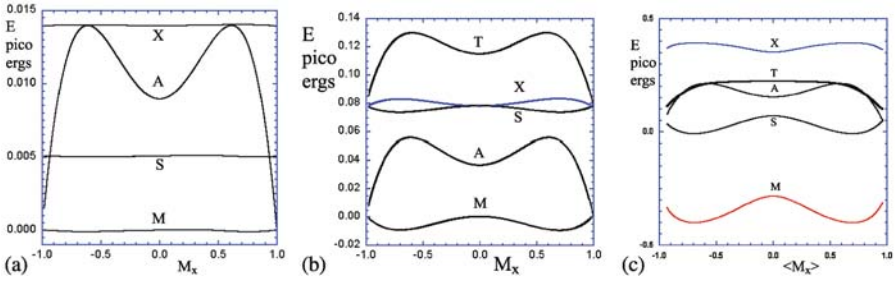

Fig. 5.21. The dependence on M_x of the anisotropy energy A, the exchange energy X, the magnetostatic self-energy M, and E_{int} labelled T, along with S = M + X. Arbitrary constants have been subtracted from M and S to emphasize the dependence on M_x. The energies are correct for A and X. The panels are for the 12 nm (**a**), 24 nm (**b**) and 48 nm (**c**) diameter disks. The exchange energy and the changes in magnetostatic self-energy tend to cancel one another. For the 48 nm diameter disk, E_{int} no longer reflects the second minimum in the anisotropy

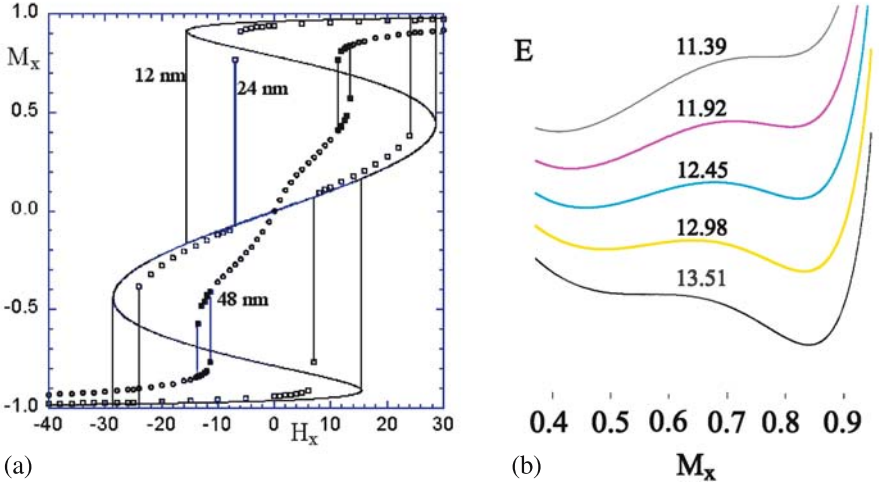

Fig. 5.22. (**a**) Comparison of hysteresis loops for 4 nm thick disks of diameters 12, 24 and 48 nm in a bias field $H_y = 28$ Oe. The open squares are computed directly by the *LLG Micromagnetics Simulator*. The transitions for the 48 nm disk, found by analyzing the LLG energies in (**b**), are shown in (**a**) as darkened squares. The analysis of (**b**) extracts the entire minor loop from the response to a single change in field as discussed in the caption of Fig. 5.20b

almost uniform magnetization, large magnetostatic self-energy and small exchange energy, and the vortex state, which has small magnetostatic self-energy and large exchange energy, there is a third state, which is a strong C-state, approaching what David Mermin whimsically called the boojum. This C-state has intermediate magnetostatic and exchange energies. This disk is not big enough to sustain an anti-vortex.

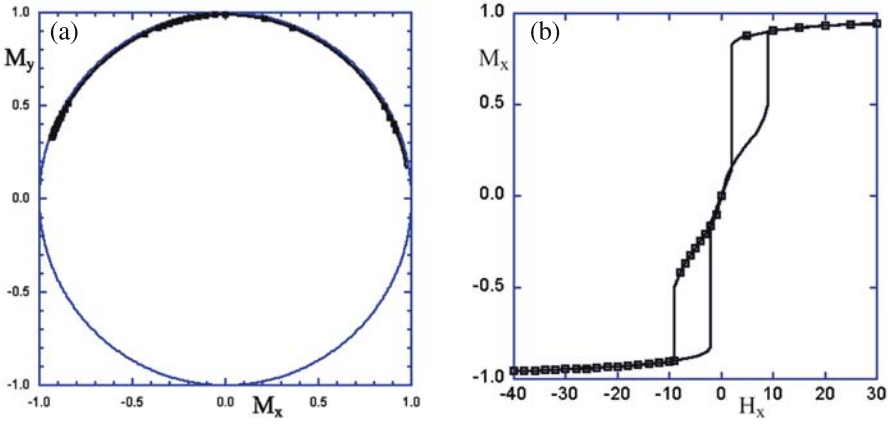

Fig. 5.23. (**a**) The path in $(\langle m_x \rangle, \langle m_y \rangle)$ space for the 48 nm diameter disk with $H_y = 28$ Oe. The outer circle is of unit radius for comparison. (**b**) The effect of reducing the bias field to $H_y = 21$ Oe for the disk with diameter 48 nm. The magnetization process is still one of almost uniform rotation. The square symbols are the equilibrium values of M_x for various H_x. The lines are calculated from E_{int} and M_y as functions of M_x along the non-equilibrium path between the points

The S-state, the strong C-state, the vortex and the anti-vortex are compared for a disk with 4 nm thickness and a 96 nm diameter using the magnetization of Fe, but without anisotropy; see Fig. 5.24. The energies for these configurations are given in Table 5.1.

Table 5.1. Comparison of energies for different configurations in a 4 nm thick circle of diameter 96 nm with the magnetization of Fe, but without anisotropy, with no applied fields

Configuration	$\langle \boldsymbol{M} \rangle$		Energies in picoerg		
	$\lvert M \rvert$	direction	magnetic	exchange	internal
uniform (100)	1.0000	(1,0,0)	28.5420	0.0000	28.5420
uniform (110)	1.0000	(1,1,0)	28.5423	0.0000	28.5423
S-state (100)	0.9704	(1,0,0)	23.8911	1.0525	24.9436
S-state (110)	0.9699	(1,1,0)	23.7486	1.0446	24.7933
C-state	0.6768	(0,1,0)	20.1462	4.0467	24.1930
vortex	0.0058	(0,0,1)	1.4189	10.2897	11.7086
anti-vortex	0.0070	(0,0,1)	38.7789	10.8994	49.6783

The S-state is metastable in zero field when aligned in the (1, 1, 0) direction. When it is started in the (1, 0, 0) direction, it is not stable, but it takes a very long time to turn into the strong C-state. This comes from way the cubic grid approximates

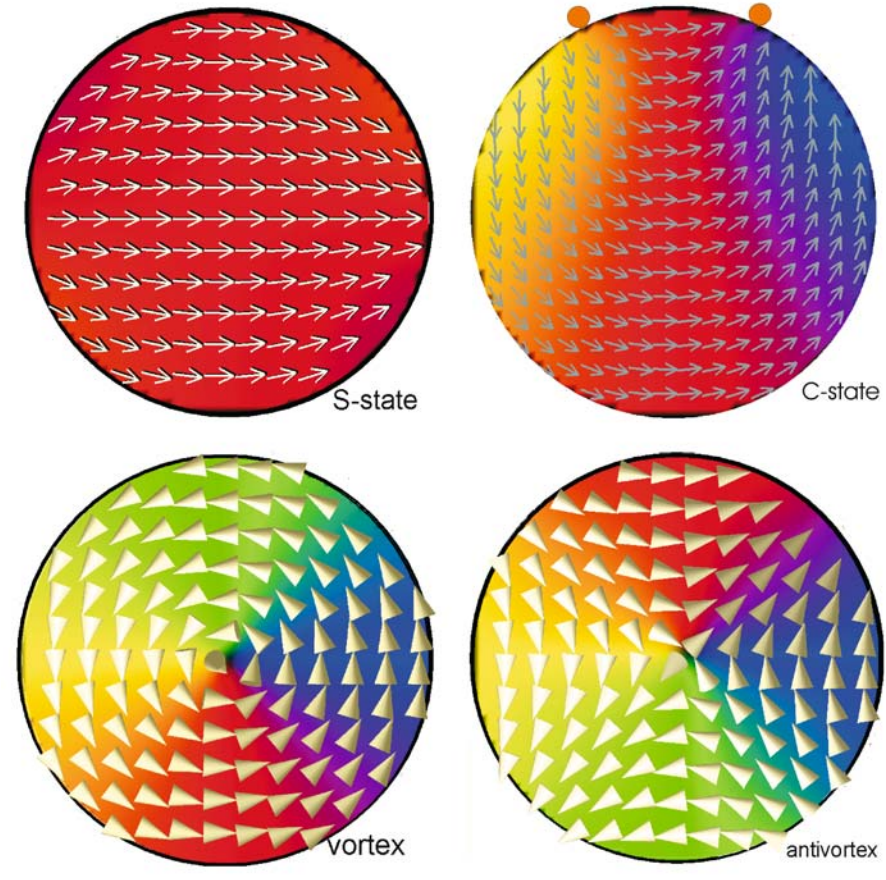

Fig. 5.24. Four configurations for a 96 nm diameter disk, 4 nm thick with the magnetization of Fe, but no anisotropy. The color code is that blue is up, red is to the right, yellow is down, and green is to the left. The S-state is not stable without some anisotropy or field to keep it from converting to the C-state. The vortex is the most stable state. The anti-vortex is not stable for these dimensions and parameters. The orange moons correspond to the reversals of the direction of the magnetization at the edges with respect to the tangent to the circle. The arrows and cones represent 1/9 of the cubes, 2 nm on a side, used in the calculations

the circular boundary with flats in $\langle 1, 0, 0\rangle$ directions and staircases in the $\langle 1, 1, 0\rangle$ directions.

The C-state and S-state configurations respond to magnetic fields as almost rigid entities. The magnetic flexibility of the 96 cm diameter disk is apparent during transitions between the various states.

The region of the vortex near its center responds rigidly to magnetic fields.

The anti-vortex, when created artificially, reaches equilibrium with itself before drifting out to the edge of the circle and vanishing.

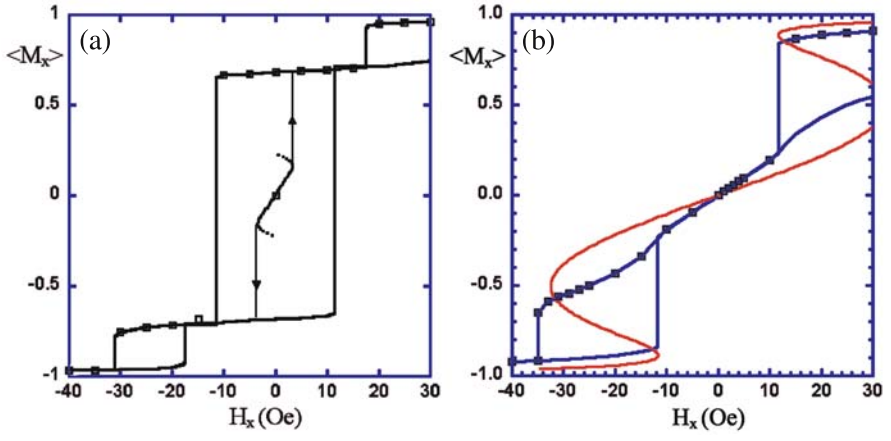

Fig. 5.25. Hysteresis for a 96 nm disk in bias fields $H_y = 2$ Oe and $H_y = 28$ Oe. At high H_x the configuration is close to an S-state. As the field is lowered it switches to the strong C-state with its smaller net moment perpendicular to its symmetry axis; see Fig. 5.24. (**a**) For $H_y = 2$ Oe the strong C-state rotates sharply at ± 11.8 Oe and returns to the S-state at ± 31 Oe. (**b**) For $H_y = 28$ Oe the strong C-state rotates continuously with H_x until it returns to the S-state at $H_x = \pm 35$ Oe. The configurations along the loop are illustrated in Figs. 5.27, 5.28 a–h. The red line in (**b**) is (5.40) with K_{u_4} lowered from 80 to 60 kiloerg/cm^3 to make the anisotropy more like $\cos^4\theta$. For the red line the moment is constant throughout the hysteresis loop

The hysteresis loop for the 96 nm disk in a bias field $H_y = 2$ Oe is shown in Fig. 5.25a. The parameters are the same as used for all the other hysteresis loops in this section. The major loop has transitions from an almost uniformly magnetized state to the strong C-state and back.

The strong C-state as shown in Fig. 5.24 has its symmetry axis in the y direction and its net magnetization in the x direction. In this orientation there is little torque from the H_x field, resulting in only a slight slope as the major loop goes through $M_x = 0$ in Fig 25a. When it does switch, the pattern rotates by almost 180°. During switching at -11 Oe, the magnetization pattern does not stop as it rotates through the position where $\langle M_x \rangle = 0$, because at that point the net magnetization is in the y direction, where the switching field can exert maximum torque. There is a small range of H_x fields for which the magnetization is stable when pointing in the y direction. This is indicated by the curve in the middle of the hysteresis diagram of Fig. 5.25a, which was calculated from the internal energy after showing that the energy and $\langle M_y \rangle$ are fit well by the first four terms of an even power series in $\langle M_x \rangle$. The calculation yields the stable and unstable equilibrium values of $\langle M_x \rangle$ for each H_x, which accounts for the backward curvature.

For bias fields greater than 5 Oe, the stable states in low H_x fields have the symmetry axis of the strong C-state along x and the net magnetization along y. Our standard bias, $H_y = 28$ Oe, is shown in Fig. 5.25b. It resembles the curves in Fig. 5.7b that were calculated using (5.40). The red curve in Fig. 5.25b uses (5.40) for

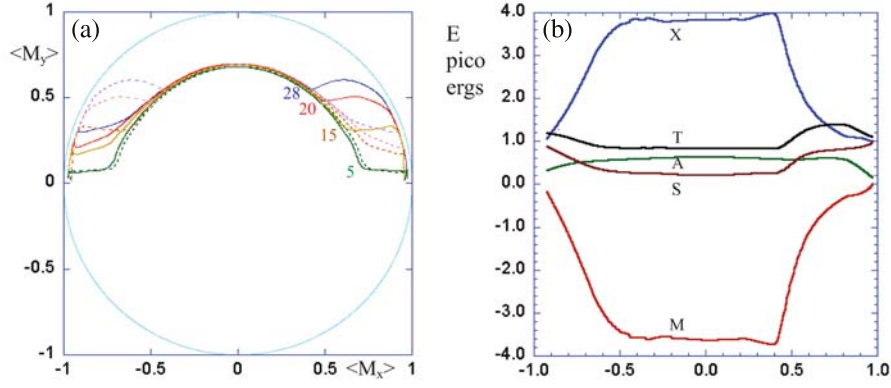

Fig. 5.26. (**a**) Paths in $(\langle M_x\rangle, \langle M_y\rangle)$ space for the 96 nm disk for bias fields H_y = 5, 15, 20 and 28 Oe. The outer circle of unit radius is just for reference. The arcs close to the reference circle are mild C-states. The arcs of radius 0.65 are strong C-states. The transitions between the two arcs are nonequilibrium states. The dotted curves are for fields increasing from negative values. In (**b**) the energies are analyzed as in Fig. 5.21 for the hysteresis loop of Fig. 5.25b with $h_y = 28$ Oe. The energies have small variation with rotation of the strong C-state for which M_x goes between ± 0.5

a fixed moment with $H_y = 28$ while modifying the fourth-order anisotropy constant from 80 to 60 kiloerg/cm^3, making the anisotropy look more like $\cos^4\theta$. But the physics is different, because here the size of the moment that rotates changes as the magnetization configuration switches from the mild C-state at high fields to the strong C-state in lower fields. Configurations encountered along the hysteresis loop are shown in Figs. 27 and 28. The two points, where the magnetization at the edge reverses its direction with respect to the tangent to the circle, move as solitons, with one of them making an excursion halfway around the circumference of the circle.

The magnetization pattern of the strong C-state acts as a unit, once it is formed. Converting it to and from the mild C-state depends on the bias field and the switching field, but the strong C-state changes very little with field. The conversion between the two states is shown in Fig. 5.26a for the bias fields H_y = 5, 15, 20 and 28 Oe. Over this range of fields, there is very little effect of the field on the magnetization pattern during the rotation of either the mild or strong C-states. The way that one pattern evolves into the other pattern is also almost independent of the field in which it happens.

Yet, the pattern does change enough with field that both the exchange energy and the magnetostatic self-energy change more than the anisotropy energy on rotation. It is a general rule in micromagnetism that the changes in pattern affect both the exchange energy and the magnetostatic self-energy in opposite ways, with the result that the changes in energy tend to cancel each other. This is illustrated here by Fig. 5.26b. The changes in the two major energies are large compared with 300 k_B, but the net energy differences are well within the realm of thermal activation, particularly in the region where $\langle M_x\rangle$ lies between -0.5 and 0.5. As a result, the soliton motions, which

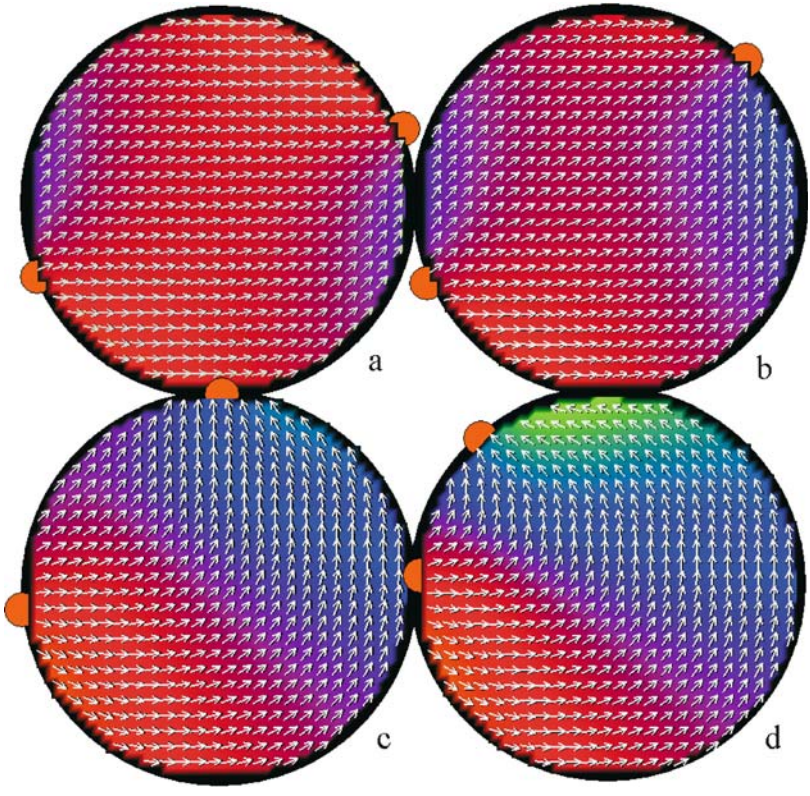

Fig. 5.27. Transformation from the S-state to the strong C-state with decreasing fields, 30, 15, 11.8 (middle of transformation), and 10 Oe for the 96 nm disk with $H_y = 28$ Oe as in Fig. 5.25b. The orange moons denote the edge reversals, which move around the circumference

accompany the rotation of the magnetization, will be thermally active. Again analysis of the changes in E_{int} during the magnetization process is useful.

The high and low field regions of the magnetization curve can be modelled independently, as there are two distinct phenomena. Each can be treated with a single moment rotating against an effective anisotropy, given by fitting E_{int} and $\langle M_y \rangle$ as functions of $\langle M_x \rangle$ using

$$\langle M_x \rangle \equiv M_1 \cos\theta_m, \tag{5.61}$$

$$\langle M_y \rangle \equiv M_1 \sin\theta_m, \tag{5.62}$$

and

$$E_{int} = E_0 - K_{u_2} \cos^2\theta_m - K_{u_4} \cos^4\theta_m. \tag{5.63}$$

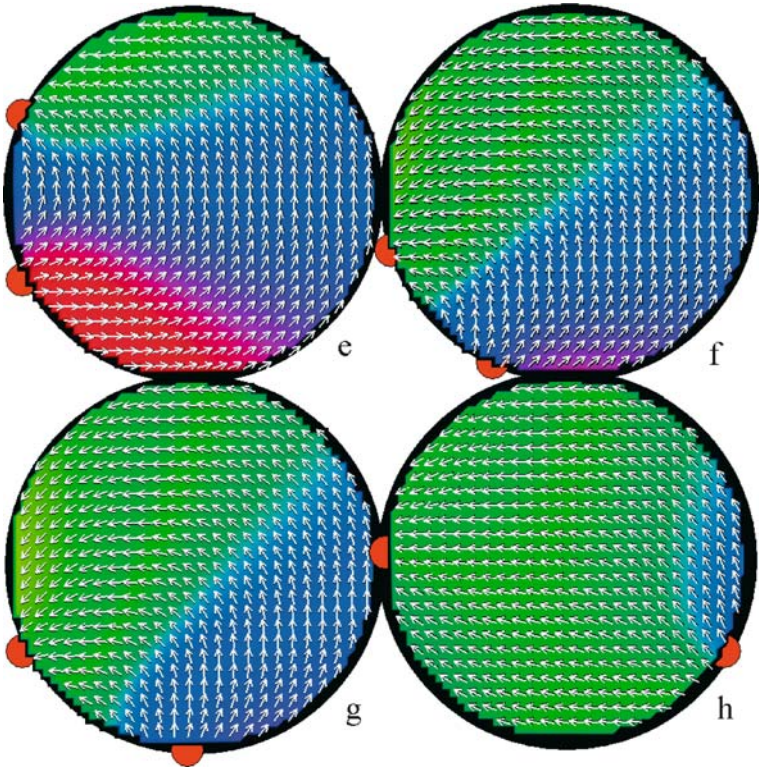

Fig. 5.28. Continuation of Fig. 5.27 for $H_x = 0, -20, -35$ (at beginning of transformation), and -40 Oe. Configurations c-g are strong C-states. Configurations (**a**), (**b**), and (**h**) are mild C-states

With three parameters for each of the two regions, it is not difficult to fit most results, theoretical or experimental.

The late Professor Eugene Wigner is famous for, among many other things, saying that "given three parameters, I can fit an elephant; give me a fourth, I can wiggle his nose." The elephant's nose is not being wiggled when the micromagnetic calculation for the reversal of a circle with two-fold plus four-fold anisotropy is fit with two sets of three parameters in (5.61)–(5.63) with one set for the strong C-state and one for the S-state. At this diameter and thickness, the iron disk looks like two elephants. As the diameter increases so does the population of the jungle.

Acknowledgement. Two major works have appeared in recent years devoted to the study of magnetism on the microscopic level. Amikam Aharoni published his text *Introduction to the Theory of Ferromagnetism* [5.2] and Alex Hubert with Rudolf Schäfer published their treatise on *Magnetic Domains* [5.3]. As good as these volumes are, the work of William Fuller Brown, Jr in the early 1960's on *Magnetostatic Principles in Ferromagnetism* [5.8] and *Micromagnetics* [5.9] remain the fundamental starting points for the study of micromagnetism. I did not use

the current literature in writing this chapter, but I did open these volumes from time to time as well as my forty-year-old copy of the *Physics of Magnetism* by Chikazumi and Charap [5.10]. It is to all of these men that I dedicate this work.

The dearth of references other than these is intentional. Hubert and Schäfer have more than 1500 references. They also show over 1000 photographs, most of which stand as challenges to our understanding of the complexity of ferromagnetism. A starting graduate student could spend a year studying just the five books mentioned above. Or he could get a copy of the *LLG Micromagnetics Simulator* and start having fun. In my first ten minutes of playing with the *LLG Micromagnetics Simulator*, I already discovered something that got me an invited talk at the annual magnetism conference later that year. That certainly beats having to read five books and going through some 1500 references. Ever since that first encounter with the *LLG Micromagnetics Simulator*, I have enjoyed my time on the frontier exploring ways to use micromagnetics to make a successful magnetic random access memory. MRAM may never materialize. Like the beautiful technology of bubble memories, it may become only a memory. But no one can take away the fun of discovery that I have had for the past four years.

For all this I want to thank Professor Jing Shi who introduced me to modern micromagnetics and MRAM, Dr. Michael R. Scheinfein who created the *LLG Micromagnetics Simulator* and continues to improve it over the years, and Dr. Theodore Zhu who gave me the opportunity to measure some 100,000 hysteresis loops and to use LLG every day for two years in attempts to explain them. Currently I work at the Center for Interactive Micromagnetics under the direction of Professor Carey Stronach at Virginia State University. The center is supported by the Air Force Office of Scientific Research. I am much indebted to Dr. Harold Weinstock for this support. I am also a Guest Scientist at the National Institute for Science and Technology in Dr. Robert D. Shull's Magnetic Materials Group in Gaithersburg, where I have benefited from my many colleagues working in micromagnetics [5.11]. In the corrections to and presentation of this article I have been aided by the help of Dr.T.L. Templeton, Dr. George Woltersdorf and Alexander Krichevsky. None of this would have happened and this chapter surely would not have been written if it were not for the more than thirty years of collaboration and friendship with Dr. Bretislav Heinrich at Simon Fraser University. If I were to have but one reference for this work, it would be B. Heinrich, private communication.

References

5.1. M.R. Scheinfein, *Landau-Lifshitz-Gilbert Micromagnetics Simulator*, http://llgmicro.home.mindspring.com.
5.2. A. Aharoni, *Introduction to the Theory of Ferromagnetism, 2nd Edition*, Oxford University Press, Oxford, 2000.
5.3. A. Hubert and R. Schäfer, *Magnetic Domains, the analysis of magnetic microstructure*, Springer, Berlin, 1998.
5.4. A. Aharoni, J. Appl. Phys. **83**, 3432 (1998).
5.5. C.J. Garcia-Cervera, Z. Gimbutas and Weinan E, J. Comp. Phys. **184**, 37 (2003).
5.6. R. Hertel, Z. Metallkd **93**, 957 (2002)).
5.7. A.S. Arrott, Z. Metallkd **93**, 963 (2002)).
5.8. W.F. Brown, Jr., *Magnetostatic Principles in Ferromagnetism*, Interscience, New York, 1962.
5.9. W.F. Brown, Jr., *Micromagnetism*, Interscience, New York, 1963.
5.10. S. Chikazumi with S.H. Charap, *Physics of Magnetism*, Wiley, New York, 1964.
5.11. www.metallurgy.nist.gov/magnet.

6

Spin Valve Giant Magnetoresistive Sensor Materials for Hard Disk Drives

B.A. Gurney, M. Carey, C. Tsang, M. Williams, S.S.P. Parkin, R.E. Fontana, Jr.,

E. Grochowski, M. Pinarbasi, T. Lin, and D. Mauri

Today virtually all recording heads in hard disk drives (HDD) use spin valve structures that employ giant magnetoresistance (GMR) to read back the magnetic information recorded in magnetic transitions on the hard disk. Introduced into products in 1997, remarkably soon after the discovery of the effect in 1988, they are produced economically by the hundreds of millions annually, and were a key factor in making possible the rapid storage areal density increase in HDD of the last 5 years. Spin valve structures are layered structures with layers only a few nanometers thick, and consist of a free magnetic layer, a conducting spacer layer, and a second magnetic layer whose magnetization is pinned by an antiferromagnet. Relative resistance changes in excess of 10% or larger are typical for spin valves used in devices. The fundamental physics of spin valves, structural details, operation and a variety of variants are discussed [6.1].

6.1 Introduction

Hard disk drive recording heads that separate the reading and writing processes into an inductive write element and a magnetoresistive read sensor have been described since 1975 and have been available for disk drives since 1991. The separation of the read and write elements permitted separate optimisation of each part of the recording process and fuelled a rapid rate of growth of more than a 60% annual increase in areal density for much of the 90s that has helped make possible personal computers with unprecedented storage and power, and helped create the Internet through server products capable of storing and manipulating enormous amounts of data with fast access times.

Even as the first MR head products were being introduced, however, it was clear that they would be of use only for a limited time. The reason is apparent in Fig. 6.1, which shows how the anisotropic magnetoresistive (AMR) effect used in

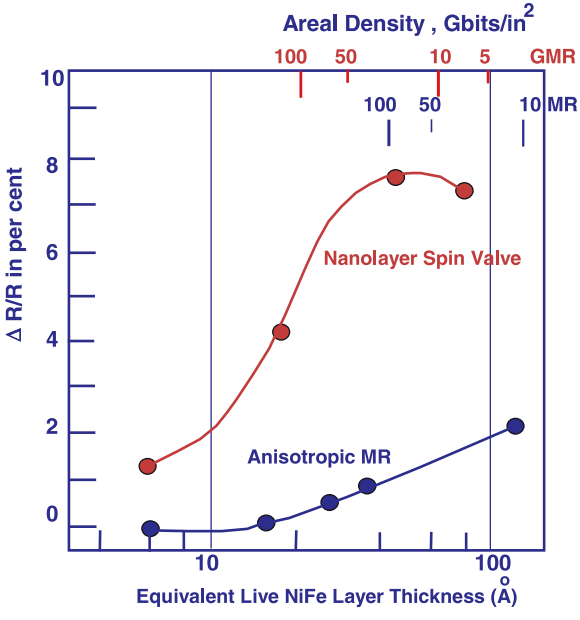

Fig. 6.1. Typical AMR and GMR amplitudes as a function of sense layer thickness. Also shown is the approximate areal density corresponding to each thickness. Present disk drives are delivering between 5 and 10 Gbit/in^2

those devices decreases with decreasing thickness of the ferromagnetic layer in the sensor used to detect the magnetic flux coming from written bits on the disk. In order to increase the areal density, A, (in Gbits/in^2) of data written on the disk it is necessary to decrease the thickness, t, of the sensing ferromagnetic layer so as to maintain a match between the flux arising from the disk and the moment of sense layer, so:

$$M_s t \approx M_r d \ , \tag{6.1}$$

where M_s and t are the magnetisation and thickness of the sense layer and M_r and d are the magnetisation and thickness of the media. Choosing this thickness allows the magnetisation of the sense layer to rotate a substantial angle, resulting in a large fraction of the available magnetoresistive change to occur. In AMR, the resistance changes as:

$$(\Delta R/R) = (\Delta R/R)_{\mathrm{AMR}} \cos^2(\theta_{\mathrm{sense}} - \theta_{\mathrm{current}}) \ , \tag{6.2}$$

where θ_{sense} is the direction of the magnetization of the sense layer and $\theta_{\mathrm{current}}$ is the direction of current flow. Thus an angular change of θ_{sense} of ± 45 degrees would cause the largest change in electrical resistance to be sensed. To increase areal density it is necessary to decrease $M_r d$ in order to squeeze magnetic transitions closer to each other. Fig. 6.1 shows that the AMR amplitude actually decreases with smaller

thickness so that the amplitudes from the AMR sensor would be decreasing. This is the result of boundary scattering of electrons from the top and bottom surfaces of the AMR layer. In order to reach further increases in areal density, the MR amplitude cannot remain constant but must increase. This is due in part to the increase in data rate coming from the increased linear density of bits, so a corresponding increase in detector bandwidth is required which also increases the noise. With more noise present, the signal must also rise in order to maintain a high signal to noise ratio. The need for higher MR amplitude is also driven by the power dissipation of current flowing though the smaller structure. The sensor will not operate reliably above a certain temperature (after all, if it gets too hot it will melt!) and so a maximum power density per unit area is allowed. Thus as the sensor size is reduced, the current that can be passed through it decreases and therefore the signal drops. To compensate, the AMR signal must be increased. Table 6.1 indicates how the magnetoresistive amplitude must increase with increasing areal density to maintain a required readback signal of 630 microvolts. The AMR effect, however, is limited to only a few percent and would be unable to deliver the required signal even at 10 Gbit/in^2.

It could have been projected that this thickness dependence of AMR foretold a slowing in the increase trend in areal density for magnetic recording, and this might have been the case except for the discovery of a new magnetoresistive effect, giant magnetoresistance (GMR), in Germany and France in 1988 [6.2]. The first GMR structures consisted of thin alternating layers of Fe and Cr grown using molecular beam epitaxy. In a magnetic field of several kiloOersteds (about 100 times larger than the field from the media at the sensor in a disk drive) and at liquid helium temperatures, a resistance change of 50% was observed. The high magnetic field was required to overcome the naturally occurring antiparallel coupling of the layers first observed in these films [6.3]. Even though these test conditions were very different from those in hard disk drives, the magnitude of the effect caught the attention of

Table 6.1. The future of GMR head technology

Areal density (Gbits/in^2)	10	20	40*	80*	100*
Total Read Gap (nm)	160	113	80	57	40
Sensor/Shield spacing (nm)	80	57	40	28	20
Read trackwidth (μm)	0.50	0.35	0.25	0.18	0.13
Sensing film (Å)	65	46	33	23	16
Sensor height (μm)	0.40	0.28	0.20	0.14	0.10
Flying height (μin)	1.0	0.71	0.50	0.35	0.25
TAA†(signal amp.) (μV/μm)	1400	1782	2520	3564	5040
Amplitude sensitivity (μV)	630	630	630	630	630

* Projected. † Track Averaged Amplitude.

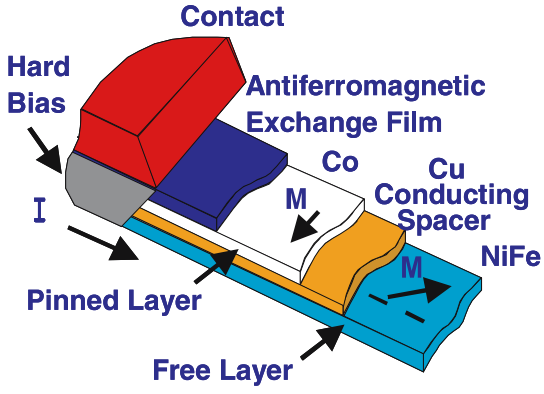

Fig. 6.2. A simple spin valve structure. The free layer is free to respond to weak magnetic fields, while the reference layer is pinned with the antiferromagnet

many scientists and engineers interested in a possible application of GMR to magnetic recording.

Researchers at the IBM Almaden Research Center and elsewhere undertook to investigate the origin of GMR and demonstrated that it arises from spin dependent scattering at the interfaces [6.4, 5] and within the bulk [6.6] of the ferromagnetic layers. Using their understanding of the effect, the IBM team found materials other than Fe and Cr for the layers that could be easily fabricated by sputtering, and developed a structure that showed a magnetoresistive effect $> 6\%$ in only a few Oersteds of magnetic field at disk drive operating temperatures (around 50–100 °C). These structures [6.7] did not use the strong natural antiparallel coupling of Fe/Cr and some other multilayers but fixed the magnetisation direction of one of the ferromagnetic layers (called the pinned layer or reference layer) using its interaction with an antiferromagnet layer placed in direct contact. A second ferromagnetic layer (called the free layer) was separated from this pinned layer by a thin spacer layer of highly conducting nonmagnetic metal, such as Cu. The weak interaction of the pinned and free layer through the spacer allowed the free layer to rotate easily in response to external fields while the pinned layer magnetisation remained fixed. The change in relative angle of the free and pinned layer resulted in a GMR signal, see Fig. 6.2. This structure was dubbed a "spin valve" in part due to its similarity to a theoretically predicted effect in tunnelling between ferromagnet layers called a "magnetic VALVE" [6.8] and in part due to the modulation of SPIN dependent current that leads to GMR, as described below.

The spin valve structure is quite flexible in the choice of layer materials, in the number of layers and other details, and there is therefore an entire class of GMR structures that use pinned and free layers. Fig. 6.1 shows that the GMR effect grows with decreasing thickness just at the point where AMR drops off, and that the GMR amplitude is many times that of AMR. In addition, the spin valve structure was purposefully designed to bear some similarity to the soft-adjacent layer (SAL) implementation of the AMR sensor, making it straightforward to implement. It is

understandable that the hard disk drive industry is moving quickly to use spin valves, as illustrated in Table 6.1. Spin valve materials are also finding applications as magnetic field sensors and are proposed for magnetic random access memories.

6.2 The GMR Effect

The GMR effect can be understood by considering the electrons that flow back and forth between the layers of a GMR multilayer or spin valve stack. Electrons are propagating in all directions within the structure, forming the Fermi sphere. The application of an electric field in the plane of the layers accelerates all the electrons uniformly and thus shifts this Fermi sphere slightly, but electrons continue to flow in all directions. Occasionally an electron undergoes a scattering event, and loses its momentum to the lattice through interactions with phonons or magnons. Then that electron begins to be accelerated by the electric field again, and is said to begin its next scattering lifetime. The distance, on average, that an electron travels before scattering again is called the mean free path, λ, and it is a well known result that the electrical conductivity is proportional to λ and the number density of electrons in the material.

All materials consist of atoms whose nuclei are surrounded by electrons that fill quantum orbitals with space for one spin up and one spin down in each orbital. In magnetic materials the number of spin up and spin down electrons is not equal because it is energetically favourable to promote an electron to a higher energy orbital with the same spin. This compares with having electrons sharing the same orbital with opposite spins where the Coulomb energy is high. Electron spin generates a magnetic dipole, in analogy to the magnetic dipole generated by a loop of wire with current flowing. So a spin imbalance within a material also causes a net magnetic moment; this is what makes magnetic materials magnetic. The difference between spin up and spin down electrons in magnetic materials is even more profound: in the early part of the century as quantum mechanics was being developed, it was proposed that the mean free paths of spin up and spin down electrons in magnetic metals are different. Recently spin valve structures have confirmed this particular hypothesis [6.6]. In addition, work over the past 30 years has shown that electron scattering from some kinds of impurities in magnetic metals is also spin dependent, leading to different spin up and spin down mean free paths [6.9] and can generate GMR [6.10].

With the understanding that the mean free paths of electrons can be spin dependent in magnetic metals, we can understand GMR. We consider the spin up and spin down current independently and add them in parallel, ignoring spin flip scattering which is typically small because disk drive temperatures are well below the Curie temperature of typical magnetic materials. It is easy to see that only electrons that start their lifetime in one ferromagnetic layer and end their lifetime in another can have mean free paths that are affected by the relative orientations of the magnetisations of adjacent layers in a GMR structure. Shown in Fig. 6.3 are representative trajectories of just such spin up and spin down electrons when the magnetisations of two layers in a spin valve are parallel and antiparallel. Here we choose the electrons with spin

antiparallel to the magnetisation, so called majority spins (+), to have a longer mean free path than the minority electrons (−), with spin parallel to the magnetisation. When the magnetisations are parallel, the spin up electron can travel far into the layer it penetrates (λ^+ on average), and can start its lifetime deep in the layer it comes from (as far as λ^+ on average). The spin down electrons cannot penetrate far and only those near the layer surface can enter the spacer before being scattered. When the magnetisation of the free layer is reversed so that the magnetisations are antiparallel, the distance that the spin up electron can penetrate is reduced to λ^- . Recalling that the product of electron density and mean free path is proportional to conductivity, we can obtain a factor in the change of conductivity between parallel and antiparallel magnetisation. When parallel, the average distance of penetration by spin up electrons is λ^+ and the number of spin up electrons emanating from the initial layer is also proportional to λ^+ on average, so the spin up conductivity is proportional to $(\lambda^+)^2$. When the magnetisations are antiparallel, the number of spin up electrons available from the initial layer is the same, λ^+, but the distance they penetrate is only λ^- , and the conductivity of spin up electrons is proportional to $\lambda^+\lambda^-$. So the difference in conductivity between parallel and antiparallel magnetisations is proportional to $\Delta C_{\text{up}} \propto (\lambda^+)^2 - (\lambda^+\lambda^-)$. Similarly $\Delta C_{\text{down}} \propto (\lambda^-)^2 - (\lambda^+\lambda^-)$. Adding these to obtain the overall difference in conductivity, we obtain:

$$\Delta C_{\text{total}} = \Delta C_{\text{up}} + \Delta C_{\text{down}} \propto (\lambda^+)^2 + (\lambda^-)^2 - 2(\lambda^+\lambda^-) = (\lambda^+ - \lambda^-)^2 \qquad (6.3)$$

showing that the key ingredient in GMR is the difference in spin dependent scattering for spin up and spin down electrons. Using spin valves, measurements of $a = \lambda^+/\lambda^-$ for Co (≈ 6), NiFe permalloy (≈ 8) and Fe (≈ 2) have been obtained [6.5]. These values suggest that large GMR values should be possible, and Co/Cu multilayers have shown GMR amplitudes greater than 80%. Various factors reduce the GMR in typical spin valve structures, including shunting of current through parts of the structure not participating in GMR, interdiffusion at the interfaces that leads to spin independent scattering, and spin flip scattering. GMR values from typical spin valves are presently about 10%, although laboratory experiments demonstrating structures with GMR in excess of 20% have been reported. It is worth noting that impurities embedded in the ferromagnetic layers may have strong spin dependent scattering asymmetries leading to GMR, including impurities arising from intermixing of the layers. This is the cause of GMR in Fe/Cr multilayers where embedded Cr atoms have a scattering asymmetry > 5 leading to large GMR values, whereas Fe has a modest asymmetry of about 2, which would lead to a small GMR on its own.

6.3 A Simple But Powerful Model

There are a number of sophisticated theories of GMR but most include some form of the above result. Some of these theories include the electronic potential mismatch in the band structure of the layers [6.11] and others include the possibility of specular scattering of the electron from the interfaces and boundaries. It is possible, however, to

obtain a reasonably good estimate of current flow in spin valves by simply solving the Boltzmann transport equation for the relaxation time approximation in 1 dimension. Only the major points of the solution using the path integral method will be sketched here (see the Appendix for the detailed calculations). Consider electrons flowing into and out of a point within the spin valve structure (see Fig. 6.4). In the absence of scattering, all electrons with trajectories that include the point would travel through that point. Those electrons that are scattered away from such trajectories reduce the conductivity. This is usually written in terms of the distribution function $f^s(x,k) = f_0^s + g^s$ where s is the spin index and g^s is the deviation from equilibrium due to the applied electric field, E. The current density of spin s with positive velocity at position x, $j^s(x)$, can then be written (assuming no interface scattering):

$$j^s(x) \sim -e\int \mathrm{d}k\; v(k)g^s(x,k) = E\frac{ne^2}{v_\mathrm{F}m}\int \mathrm{d}\rho \exp\left\{\sum\int \mathrm{d}l/\lambda^s\right\} \tag{6.4}$$

where v_F is the Fermi velocity, n the electron density, m the electron mass and where we have defined λ^s as the local mean free path for spin s, and the sum is taken of all the layers that electrons traverse on their trajectory from the film boundary to point x. The equation is best understood by example. Consider calculating the current arriving from all the electrons in layer -2 at a point in layer 0 a distance x from the layer 0 /layer -1 boundary. The term $\Lambda^s_{-2} = \lambda^s_{-2}[1 - \exp\{-L_{-2}/\lambda^s_{-2}\}]$ is the contribution of spin s to current density from L_{-2} arriving at the L_{-2}/L_{-1} interface; it is then

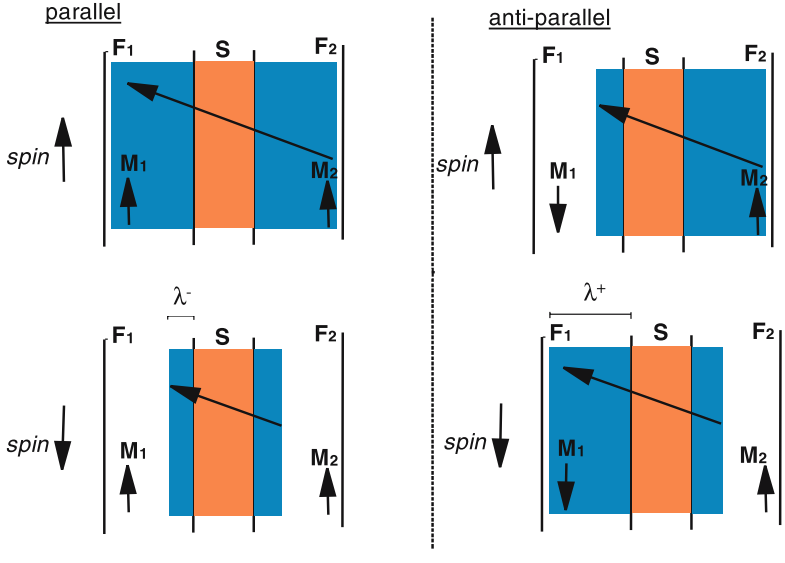

Fig. 6.3. A simple picture of electrons shared between the free and pinned layers of a spin valve illustrates the GMR effect. Electrons emanating from one ferromagnetic layer pass through the spacer and are scattered in the other ferromagnetic layer. The distance they penetrate depends on the projection of their spin onto the magnetisation direction of the layer penetrated

reduced by the factor $e^s_{-1} = \exp\{-L_{-1}/\lambda^s_{-1}\}$ as it passes through layer L_{-1} and by $\exp\{-x/\lambda^s_0\}$ as it passes a distance x into L_0. The total current density can be obtained by adding the terms from each layer to obtain:

$$j^s(x) \sim \lambda_0 \left(1 - e^{-x/\lambda^s_0}\right) + e^{-x/\lambda^s_0}\left[\Lambda^s_{-1} + e^s_{-1}\Lambda^s_{-2} + e^s_{-1}e^s_{-2}\Lambda^s_{-3} + ...\right]$$
$$+\lambda^s_0 \left(1 - e^{-(L_0-x)/\lambda^s_0}\right) + e^{-(L_0-x)/\lambda^s_0}\left[\Lambda^s_1 + e^s_1\Lambda^s_2 + e^s_1e^s_2\Lambda^s_3 + ...\right] . \quad (6.5)$$

Although this equation has many terms, it is relatively easy to implement on a personal computer. The contribution to the conductance from layer "0" is just the integral over x of the current density and can be written for an arbitrary layer i as:

$$G^s_i \sim 2\lambda^s_i[L_i - \Lambda^s_i] + \Lambda^s_i \left\{ \Lambda^s_{i-1} \sum_{j=1} \Lambda^s_{i-j-1} \prod_{k=1}^{j} e^s_{i-k} \right.$$
$$\left. +\Lambda^s_{i+1} + \sum_{j=1} \Lambda^s_{i+j+1} \prod_{k=1}^{j} e^s_{i+k} \right\} , \quad (6.6)$$

where the indices k and j ensure that contributions from all layers are included.

To obtain the magnetoresistance it is necessary to calculate the conductance, and at first it appears that this is all such a complicated expression might be useful for. However, when one calculates the difference in conductance between parallel and antiparallel alignment, almost all of the terms disappear, and one is left with the simple and powerful expression (for a simple spin-valve structure):

$$\Delta G = G^{\uparrow\uparrow} - G^{\uparrow\downarrow} \sim 2e^{-t_{\text{spacer}}/\lambda_{\text{spacer}}} e^{-2t_{\text{mix}}/\lambda_{\text{mix}}} \left[\Lambda^+_{F1} - \Lambda^-_{F1}\right]\left[\Lambda^+_{F2} - \Lambda^-_{F2}\right] \quad (6.7)$$

where we have explicitly identified the two ferromagnetic layers $F1$ and $F2$ and the spacer layer as well as the intermixed layers at the ferromagnetic/spacer interface (where we have taken the scattering to be spin independent). This result confirms the explanation described above that the change in conductance is given by the product of the number of electrons emanating from one layer multiplied by the distance travelled in the second, and introduces new terms that contain reductions in GMR due to scattering in the spacer and in intermixed interfaces. Because $\Delta R/R \approx \Delta G/G$ it is clear that to obtain larger GMR values, materials with large spin dependent scattering asymmetries are required. Asymmetries of NiFe and Co have been measured to

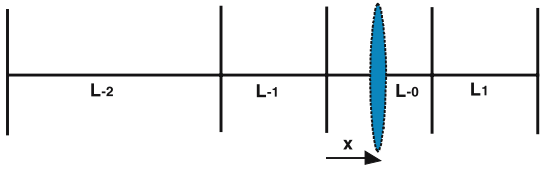

Fig. 6.4. Illustration of the 1-dimensional model showing the contribution to current density from layer −2 to a point in layer 0 a distance from the interface

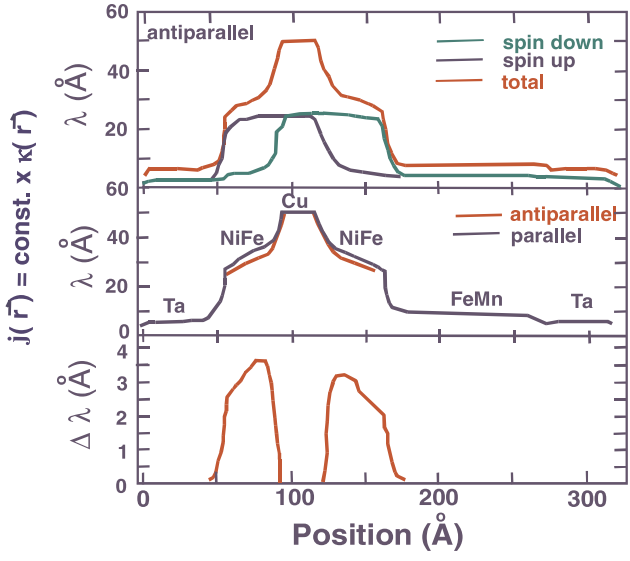

Fig. 6.5. Current density (expressed as a local mean free path) for a typical spin valve structure. Note that the local mean free path in the copper is much less than for bulk copper because so many electrons arriving in that layer have come from lower mean free path layers, and electrons emanating from the copper quickly enter adjacent layers with lower mean free paths

exceed 5, but Heusler alloys and other half metallic ferromagnets are expected to have even larger asymmetries and are under investigation by a number of researchers. With increasing thickness of the ferromagnetic layers, the value of ΔG increases and finally saturates, but the value of G continues to increase. Thus the total conductance G is a key determinant in the overall GMR, and overly thick layers and highly conducting layers can reduce GMR considerably. Along with all models of GMR, our results show that layer thicknesses chosen around the mean free path of electrons will yield the largest GMR values, so layers of a few tens of Angstroms thick are used. We note that spin dependent impurity scattering can be included by adding layers with appropriate impurities to enhance the difference in scattering for spin up and spin down electrons.

Considering the simplicity of the 1D model, it provides a remarkably good estimate of the GMR amplitude and thickness dependence of simple spin valve structures where the values of the mean free paths and thickness of the intermixed layers have been measured. The 1D model of GMR also provides a guide to how and where current is flowing in the structure. Solution of the Boltzmann transport equation for a layered geometry in 3D provides nearly the form as the 1D case. Other more advanced models provide somewhat superior results, but the current density shown in Fig. 6.5 is typical and will be used in the next section.

6.4 Biasing and Device Physics

Having developed a picture of GMR and current flowing within a layered structure, we now consider how to implement a spin valve in a recording head. Details have been described elsewhere [6.12–14]. The spin valve sense layer is formed into a stripe at the air bearing surface (ABS) of the head and electrical leads are attached to permit current flow. In order for the magnetisation of the free layer to swing the largest amount before saturating, and thus obtain the highest symmetrical signal, the free layer should be parallel to the ABS in the absence of a signal from the disk. In this configuration the sensor is said to be properly biased. In order to obtain this condition the forces acting on the free layer must be considered and are shown Fig. 6.6. The magnetostatic field from the pinned layer, which is oriented at 90° with respect to the ABS to obtain a high linear signal from the sensor, is given approximately by:

$$H_{\text{magneto}} \approx \pi^2 M_s t_{\text{pinned}}/h \tag{6.8}$$

in a recording head with two shields where h is the stripe height and is typically 10 to 30 Oe, depending upon a number of parameters including the shield to shield spacing of the read element. An interlayer coupling between the free and pinned layers due to pin holes, orange peel (sometimes called Néel coupling), and electronic effects can result in an effective field between 0 and 20 Oe or more in the direction of the pinned layer. Finally, the current flowing through the structure creates a magnetic field. The current density calculation above allows one to predict this field by knowing how much of the current flows in each side of the free layer (generating field of opposite sign) and how much the current in the free layer itself contributes. The effect of the current can be expressed as a fraction Q of the field that would be present if all the current were flowing on one side of the free layer. Generally values for Q are between 0.5 and 0.6. We will see below that there are a variety of spin valve structures with differing numbers of ferromagnetic layers, etc., and so a general expression for proper biasing of the free layer is:

$$H_{\text{i}} + \sum H_{\text{magneto}} + 2\pi Q i/h = 0\,, \tag{6.9}$$

where the sum is over the ferromagnetic layers other than the free layer (H_{i} is the interlayer exchange coupling and i is the electric current in mA, h the stripe height in μm). This expression is accurate for very long stripes with very large stripe heights, but significant deviations appear when micrometer dimensions are approached. Significant deviations occur for the submicrometer dimensions now used and micromagnetic calculations are required. These calculations show that as the stripe height is lowered, demagnetising effects, which are strongest at the top and bottom of the stripe, cause a rotation of the magnetisation of the pinned layers toward the ABS direction that is spacially dependent with the largest rotation at the stripe top and bottom. Similar spacially dependent demagnetising effects limit the amount the free layer can rotate at the top and bottom of the stripe. Overall this reduces the GMR signal and can also cause non linearities in the response. These calculations also show that as we approach stripe widths less than 0.5 μm, the effect of the edge

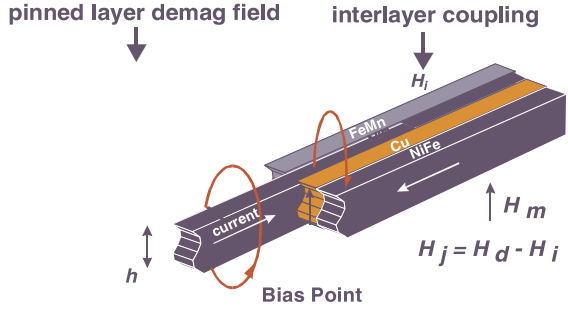

Fig. 6.6. The forces acting on the free layer that determine proper biasing

of the stripe may also cause stiffening of the free layer, further reducing the GMR signal. Schemes such as *lead overlay*, where the stripe remains long but the electrical leads are brought close together on top of the sensor to define a narrow electrical track width, are being investigated as a possible method to regain some of the signal lost as very small stripe dimensions are reached [6.15].

6.5 Antiferromagnets in Spin Valves

Most spin valves rely on exchange anisotropy, the interaction between a ferromagnet and an adjacent antiferromagnet (AF), to pin the spins in the pinned layer. The phenomenon is well known but still poorly understood, and the need for a strong, reliable and stable pinning effect has led to a resurgence of research in this area. A number of promising antiferromagnets exhibiting this phenomenon have been described, including NiMn [6.16], IrMn, NiO [6.17], PtMn, PdPtMn, RhMn, and α-Fe_2O_3, as shown in Table 6.2. The requirements for useful application of an AF material are that the exchange field associated with the effect be large (>500 Oe), that the temperature above which the effect disappears (so called blocking temperature T_b) be high (> 200 °C), and that the effect remain strong over long times (>10 years). The latter requirement is particularly interesting because it has not been thoroughly investigated, and many questions remain unanswered [6.18]. As an example of exchange anisotropy in spin valves, Fig. 6.7 shows how the exchange field in exchange coupled IrMn (100 Å)/CoFe pinned layers decays in spin valves at elevated temperatures when the pinned layer is subjected to a field opposite to the exchange field direction, much as the situation near the top and bottom of submicrometer stripes used in sensors. The initial decay rates are significant, even at moderate temperatures like 100 °C. The decay rate increases with temperature, demonstrating that the decay is thermally activated. The decay is initially log-linear, and one might predict a loss of about 15% in exchange field over 10 years at 125 °C. However, the rates increase over time, making it difficult to predict long-term behaviour without modelling. Investigations in many research groups continue in an effort to find an optimal antiferromagnet for spin valve applications, see Table 6.2. Such an antiferromagnet would be thin

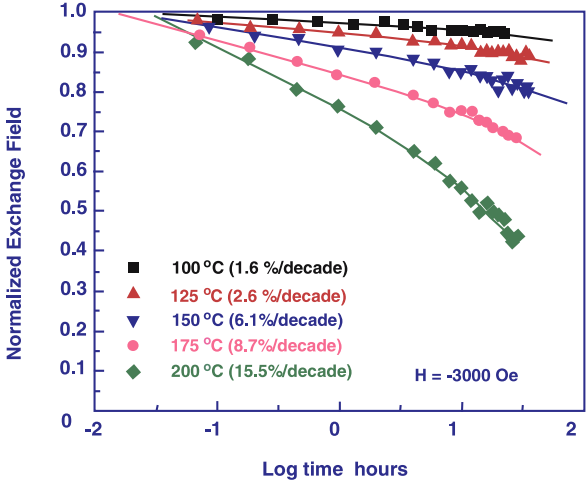

Fig. 6.7. Log time plots of several antiferromagnets showing different decay rates

Table 6.2. Comparison of antiferromagnets for spin valves (J is the exchange coupling energy)

Antiferromagnet	Blocking temperature (°C)	J (erg/cm^2)	Critical thickness (Å)
$Ni_{45}Mn_{55}$	375	0.24	300
$Pt_{49}Mn_{51}$	340	0.2	300
α-Fe_2O_3	320	0.1	<500
$Pt_{20}Pd_{30}Mn_{50}$	300	0.12	250
$Cr_{45}Mn_{45}Pt_{10}$	280	0.09	300
$Ir_{20}Mn_{80}$	280	0.15	80
$Ru_{12}Rh_8Mn_{80}$	225	0.17	100
$Ni_{50}O_{50}$	210	0.12	400
$Fe_{50}Mn_{50}$	180	0.11	110

(< 200 Å), have a high blocking temperature (> 250 °C) and show good exchange (> 400 Oe) at an operating temperature of 125 °C. It is not necessary to obtain a high exchange field to obtain extraordinary stability, though, if one uses the antiparallel pinned layer design described below.

6.6 Menagerie of Spin Valve Structures

As described above, spin valves are the class of GMR layered structures having pinned ferromagnetic layers whose magnetisation is rigid in moderate magnetic fields and having free layers whose magnetisation rotates easily in response to relatively small external magnetic fields. The GMR effect is observed when the relative angle of the free and pinned layers changes as electrons are shared back and forth across the spacer layers. A wide variety of such structures can be envisioned, and some of them with potential application in hard disk drives are described below.

6.6.1 The Simple Spin Valve

This is the basic structure described above (Fig. 6.2), with a single free layer and a pinned layer exchange coupled to an antiferromagnet [6.19]. Although easy to visualise, the proper deposition of this structure requires skill in the art of thin film deposition. Underlayers are required that create a template for the proper arrangement of atoms deposited in subsequent layers. For example Ta, Cu, and NiFe alloys promote fcc (111) growth in subsequent cubic lattices of ferromagnets and antiferromagnets that together exhibit high exchange anisotropy. In the absence of proper growth the exchange field can be weak or nonexistent. Structures with the pinned layer located either near the top are called top spin valves while the reverse are referred to as bottom spin valves. Even when the same ferromagnetic, antiferromagnetic, and spacer layers are used, top and bottom spin valves may have different underlayers to obtain optimal properties.

6.6.2 The Nanolayered Spin Valve

As models of GMR suggest, the modification of spin dependent scattering at the interface between the spacer and free and pinned layers can greatly increase the GMR amplitude. By adding as little as one monolayer of Co or CoFe alloy at the NiFe/Cu interface, the GMR amplitude increases and with thicker layers a 50% improvement can be achieved [6.20], see Fig. 6.8. Although not completely understood, this appears to be a combination of spin dependent scattering at the interface [6.21] and the return of magnetic moment to Ni and Fe atoms [6.22, 23] that lost exchange contact to the NiFe layer when they intermixed with the Cu as is typical in sputtering processes. This latter effect is likely due to the strong exchange and high Curie temperature of Co, and can be measured as the reduction or elimination of a ‘dead layer’ at the interface when Co is deposited, thereby reducing spin independent interface scattering that reduces GMR. The nanolayer can be added to the free layer, the pinned layer or both. Today, many spin valve heads use nanolayering to achieve high GMR amplitudes.

6.6.3 The Spin Filter (or Backed) Spin Valve

This structure was developed after an increased GMR was predicted from the considerations that led to (6.6) and (6.7) above. It consists of the addition of a nonmagnetic

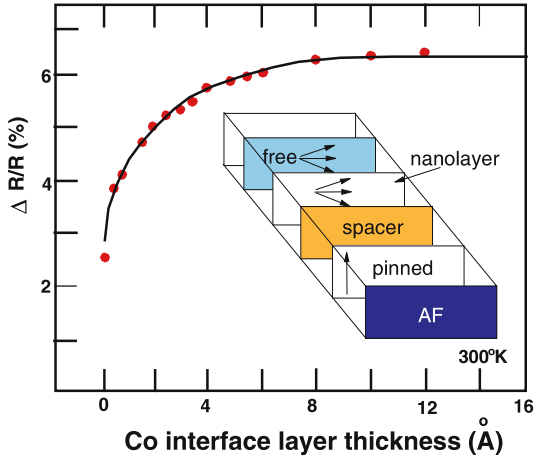

Fig. 6.8. Structure of a nanolayered spin valve (inset) and increase in magnetoresistance with increasing Co thickness at the NiFe/Cu interface of a typical simple spin valve

conducting layer next to the free layer on the side away from the spacer [6.24]. At first one would expect little beneficial effect from the addition of a conducting layer located away from the ferro/spacer/ferro interfaces, and shunting will reduce GMR if the layer is too thick, but as a look at the total conductance from such a structure shows:

$$\Delta G = \Delta G_{\text{simple}} + \Delta G_{\text{filter}} \left(1 - e^{-\beta t_{\text{filter}}/\lambda_{\text{filter}}}\right) , \tag{6.10}$$

where ΔG_{simple} is the change in conductance from the structure without the filter layer, ΔG_{filter} the increase due to the filter and λ_{filter} is the mean free path of electrons in the filter layer (sometimes called a back layer). (β is a factor that accounts for the average distance that carriers traversing the filter layer travel, since their trajectories are inclined with respect to the multilayer interface normal.) This result can be interpreted as showing that the additional distance the majority carrier can travel through the filter layer increases its average mean free path, whereas the minority carrier is easily scattered in the free layer and its mean free path remains unchanged. So the difference $\lambda^+ - \lambda^-$ increases and by (6.3) the GMR should increase. Experimental results with Cu or AuCu alloy as the back layer [6.5] show an increase in ΔG with increasing layer thickness that follows (6.10), with the largest observed ΔG from a spin valve (0.009/ohm) resulting from the addition of the non-magnetic metal Cu! The shunting does increase with increasing Cu thickness so the $\Delta R/R \approx \Delta G/G$ increases only at first and then decreases, see Fig. 6.9. The difference in GMR between structures with and without spin filters is largest when the free layer is thin and the filter substantially increases the majority carrier mean free path back toward the bulk value. Thus this structure will be most useful in obtaining higher GMR values at higher areal densities (when the free layer must be thin).

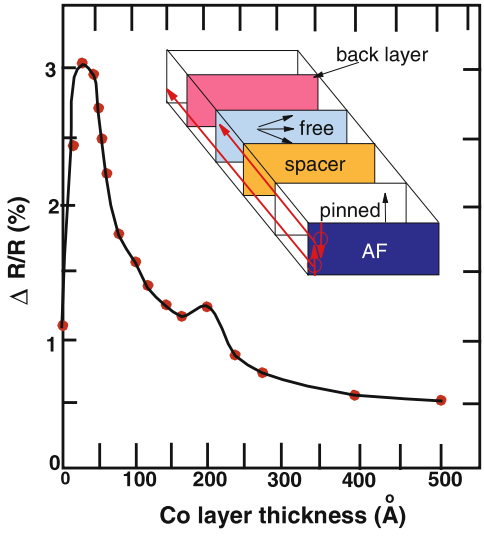

Fig. 6.9. Structure of a spin filter spin valve showing the addition of a non-magnetic layer adjacent to the free layer (inset) and GMR as a function of back layer thickness for a spin filter spin valve with a thin free layer of only 15 Å of NiFe alloy. The decrease in GMR over a similar structure without a spin filter is threefold

6.6.4 Dual Spin Valve

In the structures discussed so far, electrons shared between the free and pinned layers have been described as emanating from one of the layers and travelling toward the other. But of course there are many other electrons emanating from the other side of the free and pinned layers that are travelling in the opposite direction that do not participate in the GMR of these structures. The dual spin valve structure [6.25] is a combination of the simple bottom and top structures that allows all the electrons emanating from the free layer to potentially reach a pinned layer, see Fig. 6.10. The increase in GMR is easily estimated by considering that in the simple structure there are two layers with half of their electrons flowing in directions that contribute to GMR, so the GMR is something like half of what it could be if all electrons were contributing. In the dual spin valve there are three layers with two layers contributing half of their electrons and one layer contributing all of its electrons, so we expect about $4/6$ of the maximum. So the enhancement in GMR from the dual structure is about $(2/3)/(1/2) = 4/3$ or about a 33% increase. A useful feature of this structure is that with equal current flowing on both sides of the free layer, the field from the current is cancelled and $Q = 0$ in (6.9). This has tremendous practical consequences in the implementation of the spin valve in a recording head: if properly designed this means that the head will be properly biased independent of the current applied. On the other hand, the inability to use current to adjust for variations in the strip height and interlayer coupling places greater constraints on the control of film deposition and processing. In addition, because additional layers appear in the structure the

overall sheet resistance is lower than in typical simple spin valves, so that the overall signal (the product of GMR amplitude and resistance) can actually be lower than the constituent top or bottom structures.

6.6.5 Antiparallel Pinned Spin Valves

The discovery of the GMR effect was actually one of two discoveries made on the same Fe/Cr multilayer samples. The other discovery was natural antiparallel coupling, which appears in some multilayers. Substantial theoretical and experimental effort went into understanding the origin of this antiparallel coupling. Its cause lies in the electronic structure of the spacer material. The oscillation in its strength observed with spacer layer thickness [6.3] is a clue to its origin: oscillations in the magnetic polarisation of certain electronic wave functions with thickness similar to Kondo oscillations in isolated impurities. This coupling is much stronger than the magnetic coupling previously observed in ferromagnet/non-magnet multilayers and sandwiches which is caused either by Néel coupling (which comes from magnetic poles set up on the protrusions of rough films) [6.26] or is caused by direct magnetic exchange between the layers from small regions of magnetic material that bridge across pinholes in the spacer. Antiparallel coupling, Néel coupling, and pinhole coupling are all present in spin valves, and the layers and film growth conditions are chosen so that the net coupling is a few tens of Oersteds or less. The net coupling that is achieved is the interlayer coupling H_i referred to in (6.9) in the section above on proper biasing.

Because antiparallel coupling can be made large, it is possible to use this interaction to help stabilise the pinned layer in what is called an anti-parallel pinned (AP-p) configuration, as shown in Fig. 6.11. The pinned layer now consists of two ferromagnetic layers separated by an AP-spacer. Typically Ru or Rh are chosen for the AP-spacer as these provide the strongest antiparallel coupling. The AP-p sublayer closest to the free layer is active in GMR, acting much as the pinned layer in a simple

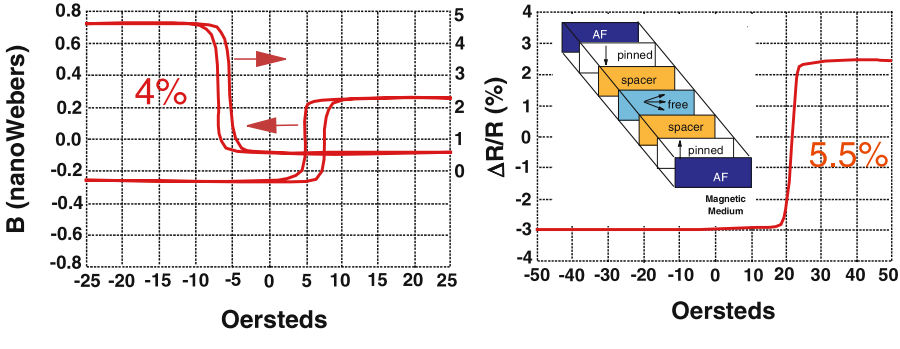

Fig. 6.10. Left: normalized resistance vs. applied field (MR transfer curve) and magnetic moment vs. applied field (field reversed for clarity) for a typical simple spin valve and (right) the corresponding MR transfer curve for dual spin valve showing a 33% enhancement of GMR

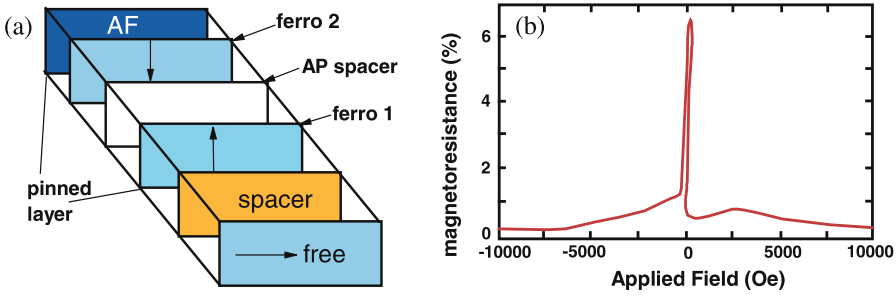

Fig. 6.11. (**a**) Antiparallel pinned (AP-p) spin valve structure. (**b**) resistance vs applied field for an AP-p spin valve. The resulting curve is much more complicated than the simple spin valve due to rotation and reorientation of the AP-p structure at very high fields. In particular the resistance drop around −5000 Oe is due to rotation of the two AP sublayers to parallel orientation showing the relatively small reduction in GMR by having the sublayers antiparallel at smaller fields

structure. The effect of the other ferromagnet sublayer on GMR is much reduced due to spin independent scattering in the dead layers around the AP-spacer and in the AP-spacer itself, but is still observed as the small decrease in resistance at high fields when the two sublayers rotate to parallel alignment, see Fig. 6.11b. The additional layers used in this structure result in some additional shunting of current away from the layers active in GMR and there is a corresponding small loss in GMR amplitude.

The source of increased stabilisation for an AP-p spin valve is twofold. First, the exchange field due to interaction with the antiferromagnet is enhanced because the net moment of the overall pinned layer is reduced. The exchange anisotropy interaction is described by a surface energy J so that the exchange field for a single pinned layer (simple spin valve) is given by:

$$H_{ex} = \frac{J}{\text{net moment}} = \frac{J}{M_s t} \,. \tag{6.11}$$

While for the AP-p structure:

$$H_{ex} = \frac{J}{\text{net moment}} = \frac{J}{M_{s1}t_1 - M_{s2}t_2} \,. \tag{6.12}$$

By moving to an AP-p structure where the sublayers have nearly the same moment the enhancement in exchange field is:

$$f_{AP} = (M_{s1}t_1 + M_{s2}t_2)/(M_{s1}t_1 - M_{s2}t_2) \tag{6.13}$$

and can be a factor of five or more larger than for a single pinned layer. This permits many antiferromagnets to be used in spin valve structures that otherwise do not produce a sufficiently high exchange field, such as NiO, PdPtMn and RhMn, but have other desirable properties such as being insulating or having high blocking temperatures. The second improvement in stabilisation of the pinned layer achieved

by moving to an AP-p structure is a second consequence of the reduced net moment of the pinned layer: the demagnetising field of the pinned layer has also been reduced by the factor f_{AP}. Thus any rotation of the pinned layer near the ABS and top of the stripe of an AP-p structure has been reduced by the factor $(f_{AP})^2$, enhancing the stability of the pinned layer by 25 to 100 times. The AP-p structure was used in the first spin valve recording head product. As stripe heights narrow with increasing areal density, the AP-p structure is expected to become even more popular.

The AP structure can be used to fix the spins in the pinned layer without the use of an antiferromagnet [6.27]. This synthetic ferrimagnet spin valve structure (Fig. 6.12) relies on the amplification of the magnetic anisotropy field by the factor f, which can result in anisotropy fields of several kiloOersteds when the right ferromagnet and film texture are chosen. This structure has the advantage of not containing an antiferromagnet with its associated thermal decay and alignment issues, but the pinned layer is generally less stable than the AP-p structure because the energy stored in the antiferromagnet anisotropy is not present.

6.6.6 AP-free Layer Spin Valve

Some of the same advantages that antiparallel pinning brings to the AP-p structure can also be applied to the free layer, see Fig. 6.13 [6.28]. Here the free layer consists of two magnetically soft ferromagnetic sublayers with an antiparallel spacer inducing antiparallel coupling. The coupling is sufficiently strong that at small and moderate fields the AP structure behaves as a single rigid magnetic moment that rotates in the direction of the applied field. Because the sublayers are soft the rotation happens easily, unlike the synthetic ferrimagnet structure. The resistance versus applied field displayed in Fig. 6.13 shows a recognisable spin valve response but with a reversed GMR (higher resistance at moderate fields) because the sublayer closest to the Cu spacer has a lower moment than the other sublayer. In this case the free layer net moment follows the applied field but the sublayer next to the Cu is directly opposite and is parallel to the pinned layer at small fields and antiparallel at moderate fields.

A key feature of the AP-free structure is its potential use at ultrahigh densities. Just as the AMR amplitude dropped with thickness below 300 Å, so the GMR effect drops below 50 Å when the free layer gets too thin, see Fig. 6.1. This is because the GMR amplitude begins to lower as free and pinned layer thickness falls below the mean free path of majority carriers (about 5 nm) and drops significantly for thickness below 3 nm. But as areal densities increase, the free layer moment must continue to decrease and simple spin valve amplitudes drop as indicated in Fig. 6.14. The AP-free structure allows one to independently control free layer thickness and net moment, so the layer thickness can be maintained at high GMR levels while the net moment can be reduced arbitrarily, also shown in Fig. 6.14. The result is a spin valve structure that is sensitive to the extremely small fluxes expected from disks required for areal densities of hundreds of Gbit/in^2.

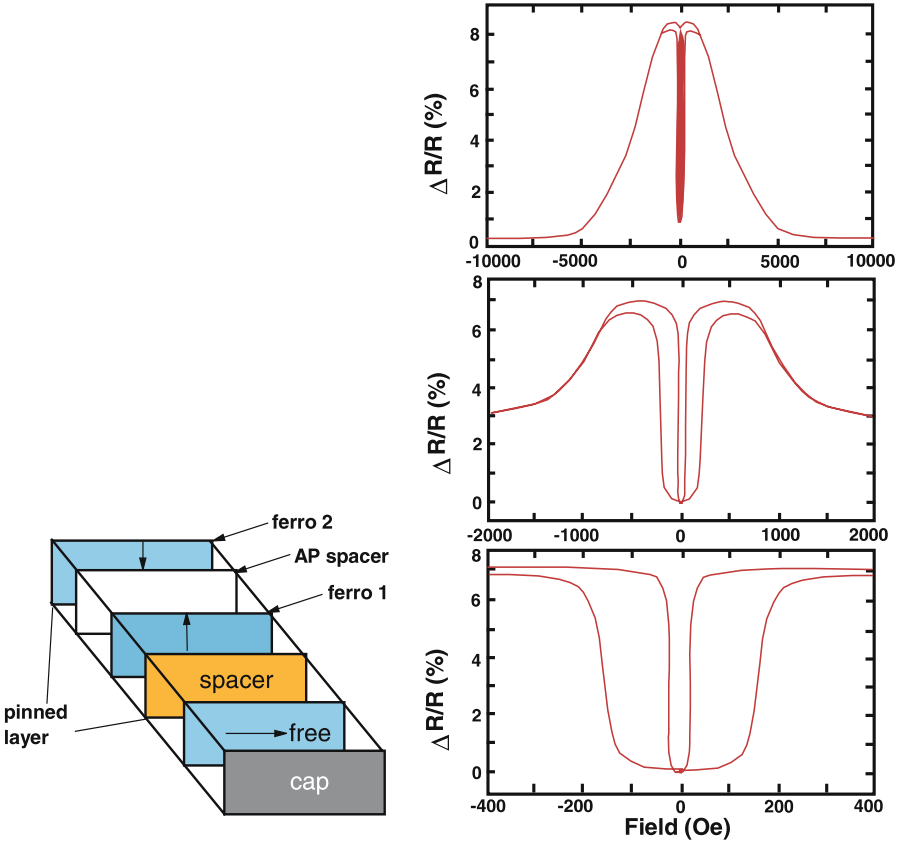

Fig. 6.12. Left: synthetic ferrimagnet spin valve structure. Right: typical transfer curves for this spin valve show a sharp resistance change at small fields as are present in disk drives, but with increasing field the presence of the AP sublayers is revealed by the complicated resistance changes due to the reorientation and reversal of the AP sublayers

6.7 Future Directions

Figure 6.15 shows the recent trend in products and demonstrations of recording technology. One is first struck by how the trend before 1997 showed products evolving at a faster rate than demonstrations, with a collision apparently due to occur in the year 2000. This disaster was averted in part due to the introduction of spin valves, which have been a key component of these demonstrations starting in 1997. Spin valves have permitted both demonstrations and products to maintain a roughly 100% annual compound growth since their introduction. Various combinations of the spin valve structures described above have been investigated and can offer features of the advantages of the individual structures. Dual AP-p structures, for example, offer the advantages of bias point insensitivity to current and enhanced pinned layer stability. Nanolayered spin filter spin valves offer very high amplitude. Spin valve structures in

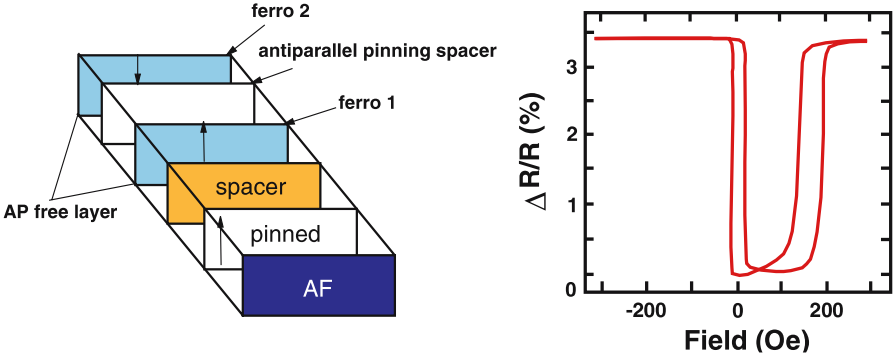

Fig. 6.13. Left: antiparallel pinned free (AP-free) layer spin valve structure. Right: the resistance versus applied field shows a reversed GMR.

one form or another will be incorporated into most of the recording heads shipped for hard disk drive applications in year 2000 and the proportion is expected to increase for many years. Spin valve structures we now have available are likely to take us to areal densities of at least 100 Gbit/in^2. The spin valve story does not end with the structures described above. Exciting new spin valve structures continue to be developed and investigated. Recent innovations include that of a nano-oxide layer introduced into the pinned layer that enhances GMR amplitude, and research is ongoing to uncover the mechanism of this enhancement. The use of oxide antiferromagnets such as α-Fe_2O_3 have yielded spin valves with GMR amplitudes in excess of 25%, demonstrating that spin valves have the signal required to take magnetic recording well into the many hundreds of Gbit/in^2.

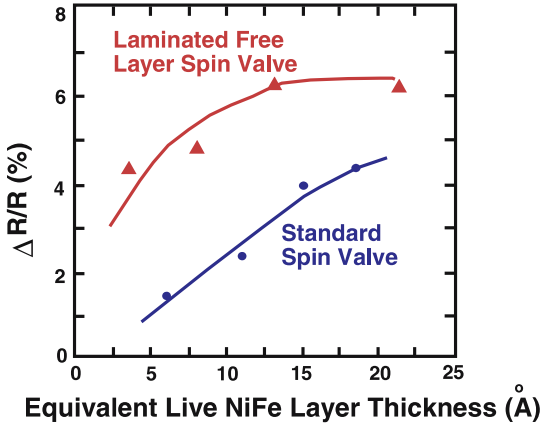

Fig. 6.14. Comparison of the dependence of GMR on the net moment of the free layer of a standard spin valve structure and one with an AP-free layer

As magnetic recorded tracks shrink below 0.1 micrometer wide and data rates approach a Gigahertz spin valve structures may be unable to provide a sufficiently high signal to noise ratio, hitting a sensitivity wall similar to the one encountered by AMR structures a decade earlier. As a result there has been renewed interest in magnetic to electrical transducers with very high sensitivity, and some research on potential future recording heads. Current perpendicular to the plane (CPP) GMR structures, where the different direction of current flow perpendicular to the layers offers some increase in GMR [6.29] are impractical at today's dimensions because their overall resistance is too low giving a low sensitivity. At higher areal densities they may play an important role if their magnetoresistance is improved. Magnetic tunnel junctions, which are typically spin-valve like structures where the spacer has been replaced with a thin tunneling barrier and where current flows as in the CPP-GMR structure, exhibit attractive MR values of >20% [6.30] . However, they have an additional noise source, shot noise, that partially devalues the increase. This is especially problematic at small trackwidths where large head resistances occur because it has proved difficult to make the tunnel barrier highly conducting while maintaining large magnetoresistance. Nevertheless tunnel heads have been demonstrated [6.31] that show promise.

A variety of even more exotic sensors have been envisioned and some are now being investigated, many using three electrical leads in analogy with the transistor.

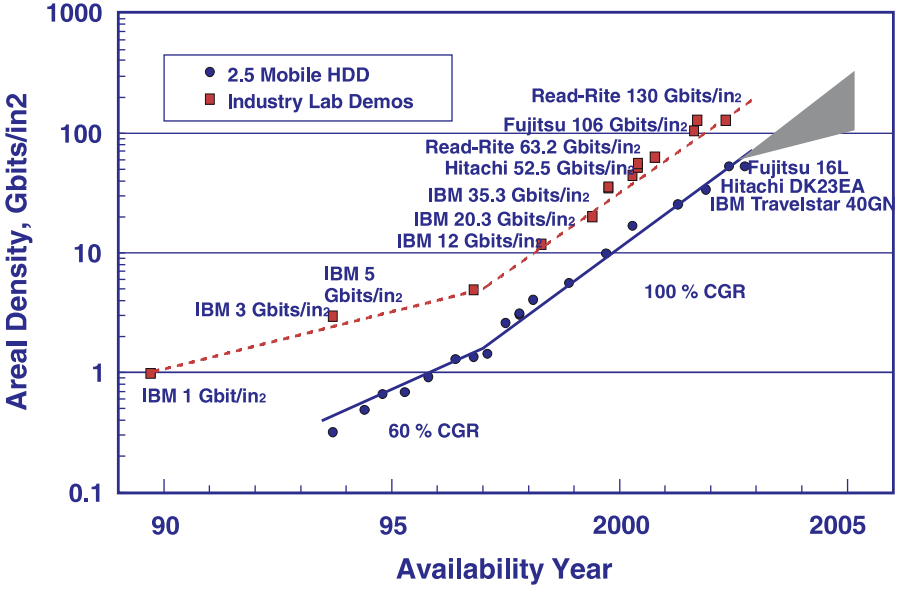

Fig. 6.15. Areal densities of hard disk drive recording demonstrations and products vs time shows how spin valves have helped permit the redirection of demonstrations to a feverish 100% annual compound growth rate, and maintain the high growth in areal density for HDD products

One such device is the spin valve transistor [6.32] where spin accumulation is used to achieve a potential difference between the spacer and ferromagnetic layers of a spin valve operated in CPP mode. Other devices are taking advantage of discoveries related to spin transport and spin injection into semiconductors. An example is the magnetic tunnel transistor, where spin is injected from a ferromagnetic layer either across a tunnel barrier or Schottky barrier, traverses the semiconductor, and must overcome a second tunnel barrier or Schottky barrier to be accumulated in the collector [6.33].Other versions inject unpolarised electrons from a doped semiconductor across the layers of a spin valve where they are filtered for spin, and then collected in a second semiconductor [6.34]. Although magnetoresistance values $>50\%$ have been obtained with these devices the current flowing in the collector in this case is typically nanoamps to microamps. These values are very small compared with the current flowing in the base, typically by a factor of 10^{-3}, resulting in very low signal to noise.

Magnetic field sensors continue to evolve and develop as researchers and engineers find ingenious ways to combine materials and exploit the rich physics of the nanometer scale. Those devices that can be made increasingly sensitive to magnetic fields while shrinking in size may be candidates for future recording heads.

Appendix: Semiclassical Theory of GMR

Consider a multilayer system with interfaces in the y-z plane subjected to an electric field along the y direction (this corresponds to the current in-plane, CIP, geometry). In order to calculate the total current density, we need to calculate the electron distribution function of the system, which is perturbed from the equilibrium by the presence of the electric field. The perturbed electron density function obeys the Boltzmann transport equation, which reads, for each individual layer in the relaxation time approximation:

$$\frac{\partial f}{\partial t} + \frac{\partial f}{\partial \boldsymbol{r}} \cdot \boldsymbol{v}(\boldsymbol{k}) + \frac{\partial f}{\partial \boldsymbol{k}} \cdot (-e/\hbar)\boldsymbol{E} = -\frac{f - f_0}{\tau^s} \tag{6.14}$$

where f_0 is the equilibrium Fermi distribution function and τ^s is the mean scattering time for electrons of spin $s = \pm 1/2$. Writing

$$g_{\boldsymbol{k}}(x) = f_{\boldsymbol{k}} - f_0 \tag{6.15}$$

we can re-write (6.14), in the steady state and neglecting terms in $o(E)$, as the one dimensional equation for $g_{\boldsymbol{k}}(x)$:

$$\frac{\partial g_{\boldsymbol{k}}}{\partial x} + \frac{1}{v_x \tau^s} g_{\boldsymbol{k}} = \frac{eE}{\hbar v_x} \frac{\partial f_0}{\partial k_y} \,, \tag{6.16}$$

which has the general solution

$$g^s_{\boldsymbol{k}}(x) = \frac{eE\tau^s}{\hbar v_x} \frac{\partial f_0}{\partial v_y} \left(1 - \phi_{\pm} \exp\{\mp x/|v_x|\tau^s\}\right) \,, \tag{6.17}$$

where $\phi_{\pm}$, an arbitrary function of $\boldsymbol{k}$, applies for electrons with positive (negative) velocities and where we made use of the free electron gas energy dispersion relation $\boldsymbol{v} = \hbar^{-1}\nabla_{\boldsymbol{k}}E(\boldsymbol{k}) = (\hbar/m)\boldsymbol{k}$ to rewrite the derivative. The $\phi_{\pm}$ are determined by the boundary conditions pertinent to the problem under study. At a given boundary x_0,

$$g^s_+(x_0^+) = Tg^s_+(x_0^-) + Rg^s_-(x_0^+) \tag{6.18}$$

$$g^s_-(x_0^-) = Tg^s_-(x_0^+) + Rg^s_+(x_0^-) \tag{6.19}$$

where T and R are the probabilities of specular transmission and reflection respectively, which in general can be spin dependent. The remainder, $D = 1 - T - R$, gives the probability of diffuse scattering (which means that the distribution function of the electrons leaving the interface must be independent of the direction of the velocity).

The current density for each electron spin current is given by

$$j^s_y(x) = -\frac{e}{8\pi^3}(m/\hbar)^3 \int v_y g^s(\boldsymbol{v}, x)\,\mathrm{d}\boldsymbol{v} \tag{6.20}$$

where the integration extends through the first Brillouin zone. Inserting (6.17) in this equation and recalling that $f_0 = f_0(|\boldsymbol{v}|)$, we obtain, in spherical coordinates:

$$\begin{aligned} j^s_{y\pm}(x) = -\frac{e^2 E\tau^s}{4\pi^2 m}(m/\hbar)^3 \int_0^{\infty}\mathrm{d}v \int_0^{\pi/2}\mathrm{d}\theta\, v^3 \sin\theta\cos^2\theta \frac{\partial f_0}{\partial v} \\ \times \left(1 - \phi_{\pm}\exp\{\mp x/v|\cos\theta|\tau^s\}\right) \end{aligned} \tag{6.21}$$

The integration can be performed by noting that, at $T = 0$ K, $\partial f_0/\partial v$ becomes $\delta(v - v_{\mathrm{F}})$:

$$-\int_0^{\infty}\phi(v)\frac{f_0}{\partial v}\,\mathrm{d}v = \psi(v_{\mathrm{F}}) \text{ at } T = 0\ . \tag{6.22}$$

Therefore:

$$j^s_{y\pm}(x) = \frac{3e^2 En}{4m}\tau^s \int_0^1 (1-\mu^2)(1 - \phi^s_{\pm}\exp\{\mp x/|\mu|\tau^s v_{\mathrm{F}}\})\,\mathrm{d}\mu \tag{6.23}$$

where $n = (mv_{\mathrm{F}}/\hbar)^3/3\pi^2$ is the number of electrons per unit volume. In order to obtain an analytical expression for the current density, we approximate the integral by using the mean value theorem of the integral calculus, resulting in

$$j^s_{\pm}(x) = \frac{e^2 En}{2m v_{\mathrm{F}}}\lambda^s(1 - \phi_{\pm}\exp\{\mp x/\mu_1\lambda^s\}) \tag{6.24}$$

where $\lambda^s = \tau^s v_{\mathrm{F}}$ is the electron mean free path and μ_1 is an unknown value between 0 and 1. The quantity $\mu_1\lambda^s$ can be interpreted as the average mean free path seen by the electrons in the x-direction and the experimental data suggest $\mu_1 \approx 0.5$ [6.35] (in the main text we used $\mu_1 = 1$ for simplicity).

Multilayer System with No Interface Scattering

We consider now the particular case where the electrons are not scattered as they cross the layer interfaces (i.e., $T = 1$, $R = 0$). In this situation, the only source of scattering is bulk scattering in the interior of each layer. The boundary conditions (6.18)–(6.19) then reduce to

$$g_+^s(x_0^+) = g_+^s(x_0^-) \tag{6.25}$$

$$g_-^s(x_0^-) = g_-^s(x_0^+) \tag{6.26}$$

while at the outer boundaries, say $x = 0$ and $x = t$,

$$g_+^s(0^+) = 0\,; \quad g_-^s(t^-) = 0\,, \tag{6.27}$$

meaning that no electron current flows into the system from outside the multilayer structure. The parameters $\phi_\pm^s$ can then be calculated from the above conditions; we consider here the case for electrons with positive velocity (in the x-direction). The first of the conditions in (6.27) gives:

$$\phi_+^s = 1 \tag{6.28}$$

irrespective of the electron spin. Therefore, for the first layer

$$g_+^{s(1)}(x) = \frac{eE\tau_1^s}{\hbar v_x}\frac{\partial f_0}{\partial v_y}\left(1 - e^{-x/v_x\tau_1^s}\right)\,, \tag{6.29}$$

For the second interface, at $x = x_1$, from the boundary condition (6.25) and from (6.29),

$$\tau_1^s\left(1 - e^{-x_1/v_x\tau_1^s}\right) = \tau_2^s\left(1 - \phi_+^{s(2)}e^{-x_1/v_x\tau_2^s}\right) \tag{6.30}$$

and therefore,

$$\phi_+^{s(2)} = e^{x_1/v_x\tau_2^s}[\tau_2^s - \tau_1^s(1 - e^{-L_1/v_x\tau_1^s})]/\tau_2^s \tag{6.31}$$

where L_i is the thickness of layer i, and from this we obtain

$$g_+^{s(2)}(x) = \frac{eE}{\hbar v_x}\frac{\partial f_0}{\partial v_y}\left\{\tau_2^s - \left[\tau_2^s - \tau_1^s\left(1 - e^{-L_1/v_x\tau_1^s}\right)\right]e^{-(x-x_1)/v_x\tau_2^s}\right\} \tag{6.32}$$

and so on. The local current density is then given by:

$$j_{y,+}^{s(1)}(x) = \frac{e^2En}{2mv_\mathrm{F}}\lambda_1^s(1 - \exp\{-x/\mu_1\lambda_1^s\}) \tag{6.33}$$

$$j_{y,+}^{s(2)}(x) = \frac{e^2En}{2mv_\mathrm{F}}\left\{\lambda_2^s - \left(\lambda_2^s - \Lambda_1^s\right)\exp\left\{-(x - x_1)/\mu_1\lambda_2^s\right\}\right\} \tag{6.34}$$

$$\cdots$$

$$j_{y,+}^{s(n)}(x) = \frac{e^2En}{2mv_\mathrm{F}}\left\{\lambda_n^s - (\lambda_n^s - \Lambda_{n-1}^s - \Lambda_{n-2}^s\mathrm{e}_{n-1}^s - \Lambda_{n-3}^s\mathrm{e}_{n-2}^s\mathrm{e}_{n-1}^s - \ldots - \Lambda_1^s\mathrm{e}_2^s\mathrm{e}_3^s\ldots\mathrm{e}_{n-1}^s)\exp\left\{-(x - x_{n-1})/\mu_1\lambda_n^s\right\}\right\} \tag{6.35}$$

and similarly for electrons with negative velocity (along the x direction), where

$$\Lambda_i^s = \lambda_i^s \left(1 - e^{-L_i/\mu_1 \lambda_i^s}\right); \;\; \mathrm{e}_i^s = e^{-L_i/\mu_1 \lambda_i^s} \; . \tag{6.36}$$

The total current density is obtained by integrating the current density for the whole thickness, and summing over the two velocity components, i.e.,

$$j_y^s = \sum_{n=1}^{N} \int_{y_{n-1}}^{y_n} \left[j_{y,+}^{s(n)}(x) + j_{y,-}^{s(n)}(x) \right] \mathrm{d}x \tag{6.37}$$

(where N is the total number of layers) which is given by

$$j_y^s = \frac{e^2 E n}{2 m v_\mathrm{F}} \sum_{n=1}^{N} \left\{ 2\lambda_n^s \left(L_n - \mu_1 \Lambda_n^s\right) + \mu_1 \Lambda_n^s \left(\Lambda_{n-1}^s + \sum_{k=2}^{n-2} \Lambda_k^s \prod_{i=k+1}^{n-1} \mathrm{e}_i^s \right.\right.$$
$$\left.\left. + \; \Lambda_{n+1}^s + \sum_{k=n+2}^{N} \Lambda_k^s \prod_{i=k-1}^{n-1} \mathrm{e}_i^s \right) \right\} \; , \tag{6.38}$$

which is identical to (6.6) of the main text.

Case of a Simple Trilayer Spin-valve

From the previous expression it is now possible to calculate the GMR effect by calculating the difference in conductivity between the parallel and antiparallel configurations of the magnetic layers. For each magnetic configuration the spin index has to be summed over and as a consequence only the spin-dependent cross terms give rise to differences in conductivity between the parallel and anti-parallel configurations (in particular, the first terms under the summation in (6.38) cancel out). However, the expression in the general case becomes rather involved. For the case of a simple trilayer system, however, the GMR expression has a simple form and can be easily calculated. Writing explicitly the terms of the second part of the sum in (6.38) for this particular case, we obtain

$$j_y^s = \frac{e^2 E n \mu_1}{2 m v_\mathrm{F}} \left[\Lambda_1^s \left(\Lambda_2 + \Lambda_3^s \mathrm{e}_2 \right) + \Lambda_2 \left(\Lambda_1^s + \Lambda_3^s \right) + \Lambda_3^s \left(\Lambda_1^s \mathrm{e}_2 + \Lambda_2 \right) \right] \tag{6.39}$$

and again, since only spin-dependent cross terms contribute to the GMR,

$$(j_y^s)^{\mathrm{GMR}} = \frac{e^2 E n \mu_1}{m v_\mathrm{F}} \mathrm{e}_2 \Lambda_1^s \Lambda_3^s \tag{6.40}$$

and therefore, summing in s and subtracting between the parallel and anti-parallel configurations, we arrive at:

$$(\Delta\sigma)^{\mathrm{GMR}} = \frac{e^2 n \mu_1}{m v_\mathrm{F}} \mathrm{e}_2 \left(\Lambda_1^{\uparrow} - \Lambda_1^{\downarrow} \right) \left(\Lambda_3^{\uparrow} - \Lambda_3^{\downarrow} \right) \; . \tag{6.41}$$

If we consider two intermixed layers at the interface between the ferromagnetic layers and the spacer layer, the above expression is only slightly modified by the factor $\mathrm{e}_{\mathrm{mix}1}\mathrm{e}_{\mathrm{mix}2}$.

References

6.1. This chapter is based on an earlier article that appeared in DataTech Magazine (Issue 4, 2000) and is used with permission of Henley Publishing Group, Ltd, UK.
6.2. M.N. Baibich, J.M. Broto, A. Fert, F. Nguyen Van Dau, F. Petroff, P. Etienne, G. Creuzet, A. Friederich, and J. Chazelas. *Phys. Rev. Lett.*, 61:2472, 1988.
6.3. S.S.P. Parkin, N. More, and K. P. Roche. *Phys. Rev. Lett.*, 64:2304, 1990.
6.4. B.A. Gurney, D.R. Wilhoit, V.S. Speriosu, and I. L. Sanders. *IEEE Trans. Magn.*, MAG-26:2747, 1990.
6.5. S. S. P. Parkin. *J. Appl. Phys.*, 79:6078, 1996.
6.6. B.A. Gurney, V.S. Speriosu, J.-P. Nozieres, H. Lefakis, D.R. Wilhoit, and O. U. Need. *Phys. Rev. Lett.*, 71:4023, 1993.
6.7. B. Dieny, V.S. Speriosu, S.S.P. Parkin, B.A. Gurney, D.R. Wilhoit, and D. Mauri. *Phys. Rev. B*, 43:1297, 1991.
6.8. J. C. Slonczewski. *Phys. Rev. B*, 39:6995, 1989.
6.9. I.A. Campbell and A. Fert. Transport properties of ferromagnets. In E.P. Wohlfarth, editor, *Ferromagnetic materials*, volume 3, page 747. North-Holland Publishing Company, 1982.
6.10. P. Baumgart, B.A. Gurney, D.R. Wilhoit, T. Nguyen, B. Dieny, and V. S. Speriosu. *J. Appl. Phys.*, 69:4792, 1991.
6.11. W.H. Butler, X.-G. Zhang, T.C. Schulthess, , D.M.C. Nicholson, J.M. MacLaren, V.S. Speriosu, and B. A. Gurney. *Phys. Rev. B*, 56:14574, 1997.
6.12. D.E. Heim, R.E. Fontana, V.S. Speriosu, B.A. Gurney, and M. L. Williams. *IEEE Trans. Magn.*, MAG-30:316, 1994.
6.13. B.A. Gurney, V.S. Speriosu, D.R. Wilhoit, H. Lefakis, R.E. Fontana, Jr., D.E. Heim, and M. Dovek. *J. Appl. Phys.*, 81:3998, 1997.
6.14. C.H. Tsang, R.E. Fontana, Jr., T. Lin, D.E. Heim, B.A. Gurney, and M. L. Williams. *IBM J. of Research and Development*, 42:103, 1998.
6.15. Y. Ohsawa et al. *J. Magn. Soc. Japan*, 21:355, 1994.
6.16. T. Lin, D. Mauri, N. Staud, C. Hwang, J.K. Howard, and G. L. Gorman. *Appl. Phys. Lett.*, 65:1183, 1994.
6.17. T. Lin and D. Mauri. *IEEE Trans. Magn.*, 35:2607, 1999.
6.18. V.S. Speriosu, Jr.D.A. Herman, I.L. Sanders, and T. Yogi. *IBM J. of Research and Development*, 34:884, 1990.
6.19. B. Dieny, V.S. Speriosu, S. Metin, S.S.P. Parkin, B.A. Gurney, P. Baumgart, and D. R. Wilhoit. *J. Appl. Phys.*, 69:4774, 1991.
6.20. U.S. Patent 5,341,261.
6.21. W.P. Pratt, Jr., Q. Yang, L.L. Henry, P. Holody, W.-C. Chiang, P.A. Schroeder, and J. Bass. *J. Appl. Phys.*, 79:5811, 1996.
6.22. J.P. Nonzières, V.S. Speriosu, B.A. Gurney, B. Dieny, H. Lefakis, and T. C. Huang. *J. Magn. Magn. Mater.*, 121:386, 1993.
6.23. D.M.C. Nicholson, W.H. Butler, X.-G. Zhang, J.M. MacLaren, B.A. Gurney, and V. S. Speriosu. *J. Appl. Phys.*, 76:6805, 1994.
6.24. U.S. Patent 5,422,571.
6.25. U.S. Patent 5,287,238.
6.26. J.C.S. Kools, W. Kula, D. Mauri, and T. Lin. *J. Appl. Phys.*, 85:4466, 1999.
6.27. U.S. Patent 5,583,725.
6.28. U.S. Patent 5,408,377.
6.29. M. Takagishi, K. Koi, M. Yoshikawa, T. Funayama, H. Iwasaki, and M. Sahashi. *IEEE Trans. Mag.*, 38:2277, 2002.

6.30. J.R. Childress, M.M. Schwickert, R.E. Fontana, M.K. Ho, P.M. Rice, and B. A. Gurney. *J. Appl. Phys.*, 89:7353, 2001.
6.31. T. Kuwashima, K. Fukuda, H. Kiyono, K. Sato, T. Kagami, S. Saruki, T. Uesugi, N. Kasahara, N. Ohta, K. Nagai, N. Hachisuka, N. Takahashi, M. Naoe, S. Miura, K. Barada, T. Kanaya, K. Inage, and A. Kobayashi. *IEEE Trans. Mag.*, 40:176, 2004.
6.32. M. Johnson. *J. Magn. Magn. Mat.*, 156:321, 1996.
6.33. S. van Dijken, X. Jiang, and S. S. P. Parkin. *Appl. Phys. Lett.*, 80:3364, 2002.
6.34. R. Jansen. *J. Phys. D*, 36:R289, 2003.
6.35. G.J. Strijkers, M.M.H. Willekens, H.J.M. Swagten, and W.J.M. de Jonge. *Phys. Rev. B*, 54:9365, 1996.

7

Magnetic Switching in High-Density MRAM

J. Shi

The anticipated commercialization of magnetoresistive random access memory (MRAM) chips spurs a great deal of interest in the magnetism community. Since non-volatile information is stored on increasingly shrinking magnetic elements in high-density MRAM, magnetic switching of patterned nanostructure elements plays a key role in memory functioning. In this chapter, we will first briefly review the existing mainstream semiconductor memories, followed by a review of different modes of MRAM. Then we will concentrate on magnetic switching and the effect of switching on selectivity for reading and writing in structures ranging from ideal single domains to patterned thin film elements whose dimensions are much greater than single domain. Lastly, we will discuss some specific issues related to magnetic switching in increasingly high-density MRAM.

7.1 Random Access Memories (RAMs)

Built in the 1950s, the earliest memory storage device for commercial computers was the "ferrite-core memory", which consists of wire wound doughnut-shaped coils [7.1, 2]. Since it was slow ($\sim$1 ms access time), bulky ($\sim$1 mm per bit) and expensive ($\sim$1 cent per bit), it was rendered obsolete by semiconductor memories in the 1970's. RAMs are referred to as solid state memory devices that do not use any moving parts. Due to the great advances in semiconductor technology in the last three decades, today's RAMs are being built with ever-increasing memory performance while dramatically reducing cost [7.3]. The basic unit of a RAM device is the memory cell. Multiple rows and columns of cells are arranged to form a large two-dimensional (2D) array that can be accessed quickly and directly, which is different from serial access memory devices such as shift registers or recording tapes. According to the memory cell functions, there are several different types of semiconductor RAMs [7.4], ranging from the most commonly used ones such as static-RAM (SRAM), dynamic-RAM (DRAM), and Flash (a type of electrically erasable programmable read only

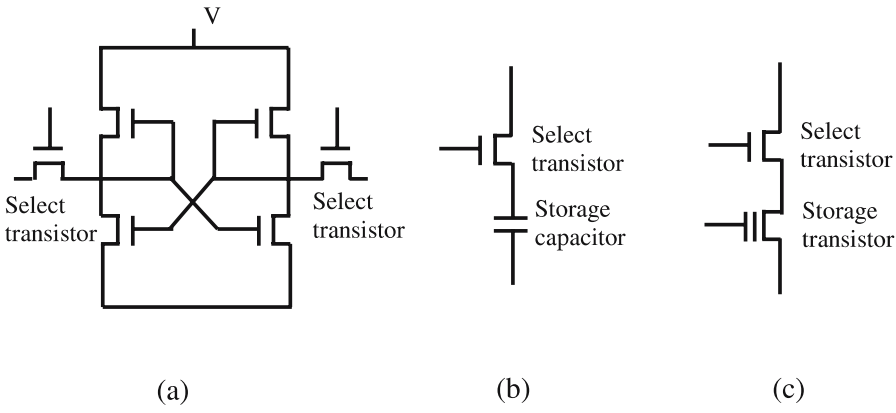

Fig. 7.1. Memory cell architecture for three types of RAMs. (**a**) SRAM. (**b**) DRAM. (**c**) EPROM/EEPROM (EPROM stands for erasable programmable read only memory)

memory or EEPROM), to ferroelectric-RAMs (FeRAM or FRAM). In this section, we briefly review those commercially available RAMs.

SRAM is generally used for cache memory in computers. Its cell consists of a basic flip-flop circuit that needs a DC current to retain its memory [7.3, 4]. Each cell contains four transistors plus two additional transistors (shown in Fig. 7.1a) or two load resistors as pull-up devices. Either diagonal transistor pair can be simultaneously on or off, representing two stable memory states. The gate electrodes of the horizontal memory cells are linked to form rows and the sources or drains of the vertical cells are linked to form columns. When a particular cell in the 2D array is selected for writing, a voltage pulse applied to one select transistor of the cell allows the cell to store a "0", or the other select transistor to store a "1". For reading, the asymmetry of the current flow in the select transistors distinguishes the state "0" from the state "1". SRAM is a very fast memory, but it requires a relatively large cell area and it is relatively more expensive to build. The memory state disappears when power is turned off; therefore, it is a volatile memory.

A DRAM cell consists of one select transistor and a storage capacitor (Fig. 7.1b) [7.3, 4]. Hence, DRAM is simpler and denser than SRAM. A charged capacitor represents a "1"; a discharged capacitor represents a "0". When a cell is selected for reading, the electrons stored in the capacitor flow to the column wire, changing the memory state to a "0" and the resulting current pulse is picked up by a sense amplifier. This pulse is interpreted as a "1", but meanwhile, the original "1" state is destroyed. This reading process is called destructive readout (DRO). Each time such a cell is read, the "1" needs to be rewritten. In addition, the charge stored in the storage capacitor cannot be held there indefinitely due to leakage; therefore, the DRAM cells need to be refreshed every millisecond or so. As a result, DRAM is not as fast as SRAM, and it is also a volatile memory.

The one transistor plus one ferroelectric capacitor (1T/1C) FRAM cell architecture [7.5] is similar to that of the DRAM cell, except that the capacitor is replaced

by a ferroelectric capacitor which can permanently hold the charge. Furthermore, the polarity of the capacitor can be switched by a voltage; therefore, the two polarization states serve naturally as two stable memory states. $PbZr_{1-x}Ti_xO_3$ (PZT) is an example of the ferroelectric material used for these capacitors. FRAM is a non-volatile memory, but it has limited read/write endurance ($< 10^{13}$ cycles).

Figure 7.1c shows an EPROM/EEPROM cell [7.3, 4]. The storage transistor has two gates: a control gate and a floating gate separated from the control gate by a layer of silicon dioxide. The floating gate is used for storing charges, which represent the memory states. When a cell is selected for writing, a high applied drain voltage causes electrons to transfer to the floating gate. The electrons pass through the oxide layer to the floating gate by "hot" injection or avalanche injection in the case of EPROM, and by Fowler-Nordheim tunneling mechanism in EEPROM. The tunneling requires a thin oxide layer (< 10 nm in thickness). Another difference between the EPROM and EEPROM is in the erasure. In EPROM, cells are erased by shining ultraviolet light on the whole memory chip. Electrons at the floating gate gain enough energy to jump the energy barrier of the oxide. In EEPROM, electrons can leave the floating gate by Fowler-Nordheim tunneling in a reversed voltage. In state "1", electrons at the floating gate shift the threshold of the transistor; therefore, it can be read out from the current. Flash memory is one type of EEPROM. It is a high-density and non-volatile memory. However, it has limited write endurance (10^5–10^6 cycles). It requires high voltage (5–12 V) and has slow programming (ms) and erase (sec) times.

7.2 Magnetoresistive Random Access Memory (MRAM)

In spite of tremendous advances made in the solid state RAMs in the past three decades, there has been no single commercially available solid state memory that possess all the desirable attributes: non-volatile, fast, dense, low power consumption, unlimited read/write endurance, yet economical. MRAM is a newly developed memory that possibly offers such potential [7.6]. Prototypes of MRAM have already been demonstrated by Motorola (Fig. 7.2), [7.7] IBM, and Honeywell after only a few years of active research and development. Commercial MRAM chips of at least 1 megabit (1 Mb) are anticipated in year 2003-2004 [7.8].

The modern MRAM concept resembles the early magnetic ferrite-core memory. They both utilize bi-stable remanent magnetization states to store information; therefore, they are intrinsically non-volatile. Memory cells are row and column addressable and are written by the magnetic fields generated by two sets of current lines. The write access time is determined by the magnetic switching speed of the materials, which is inherently fast (~ 1 ns or less). The two memories differ in the way the memory bits are read. The ferrite-core memory uses an inductive method to sense the magnetization direction stored in the rings. When a particular cell is selected for reading, the orthogonal fields generated by the two lines interrogate the memory element. The inductive signal level depends on the original magnetization state with respect to the resultant field direction. In magnetoresistive RAMs, the magnetoresistance (MR) of a cell is used to directly discern the memory states. In general, the higher the MR

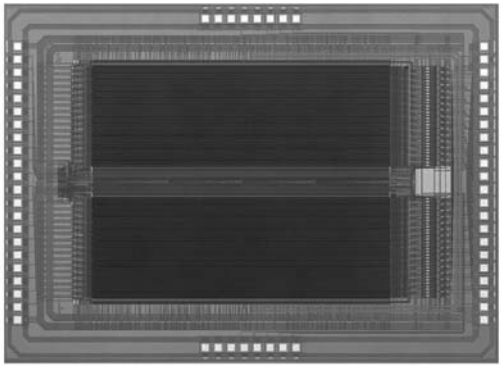

Fig. 7.2. 1 Mb MRAM chip demonstrated by Motorola in 2002. (Courtesy of Motorola Labs)

ratio the cell material has, the shorter the read access time. Recent breakthroughs in thin film magnetism marked by the discoveries of giant magnetoresistance (GMR) and tunneling magnetoresistance (TMR) provided an enormous impetus to MRAM research. There are several different types of MRAM designs according to the MR mechanism. In the following subsections, we will review a few variations of MRAM.

7.2.1 Anisotropic Magnetoresistance-based MRAM

Many ferromagnetic metals and alloys exhibit sizeable anisotropic magnetoresistance (AMR) [7.10]. The resistance of the materials not only changes with applied magnetic field strength, but also depends on the direction of the applied field, which determines the magnetization orientation. When the field is applied along the electrical current such that the magnetization is parallel to the current flow, the resistance is greater than when the field or the magnetization is perpendicular to the current flow. The AMR effect was explained by Kondo [7.11] in terms of the scattering of s-electrons by a small unquenched orbital moment induced by 3*d* spin moment. This effect can be as large as 4%.

Memory states: An AMR based-RAM cell is a narrow stripe consisting of two magnetic layers separated by a non-magnetic conducting layer, such as a three-layer stack of permalloy ($Ni_{81}Fe_{19}$)/ tantalum nitride (TaN)/ permalloy [7.12]. The permalloy films have an induced anisotropy during film deposition with the anisotropy axis set along the width of the etched stripe. When the isolated cells are electrically linked to form a column (or row), the line carries a "sense" current that is used to sense the memory state of a cell when it is selected. The sense current also generates a "sense field" that acts on the two magnetic layers in opposite directions according to the right-hand rule. Orthogonal isolated current lines, called "word lines", generate magnetic fields perpendicular to the anisotropy axis. The remanent magnetization state of the two permalloy layers can have either clockwise or counterclockwise configurations around the sense current, which serve as two stable memory states. In the absence of any magnetic field, these two states give rise to the exact same

Table 7.1. A summary of the main features of MRAM in comparison with other mainstream RAMs (Courtesy of the MRAM Development Alliance of IBM and Infineon Technologies) [7.9]

	SRAM	DRAM	NAND Flash	NOR Flash	1T1 MTJ MRAM	XPC MRAM
	Existing Products				Technology Products	
Cell size in F^2	100	8	5	6	> 8 [published 20–40]	> 4
Supply Voltage	2.5 V	2.5 V	1.8 V	3.3 V	1.8 V [pusblished 2.5–3.3 V]	1.8 V
Retention Power	1 μW –375 mW	10 mW	0	0	0	0
Retention Time	∝ [with power]	64 ms	10 yrs	10 yrs	10 yrs	10 yrs
Random Read Access	2–100 ns	60 ns	10 μs	90 ns	10–50 ns [published 3–50 ns]	50 ns–11 μs
Random Write	2–100 ns	60 ns	100 μs [erase 100 ms]	10 μs [erase 100 ms]	10–40 ns [published 3–50 ns]	20–40 ns
Endurance	$> 10^{15}$	$> 10^{15}$	$> 10^{15}$ read 10^{15} write	$> 10^{15}$ read 10^{15} write	10^{15} [expected]	10^{15} [expected]

resistance, because the layer magnetization in both states is perpendicular to the sense current direction.

Reading: Let's consider state "0" and state "1" as shown in Fig. 7.3. When a pair of sense and word currents is simultaneously turned on, only the memory cell at the crossing of the current lines experiences two magnetic fields. Memory states "0" and "1" respond to the fields differently, resulting in different MR. This produces different signal levels in the sense line. Fig. 7.4 is a top view of the two layer magnetization configurations for both memory states when a sense and word field is applied for reading. The sense current flowing through the memory cell creates a clockwise or counterclockwise field. The word current creates a word field along the length of the memory cell. For a fixed sense current direction as shown in Fig. 7.3, the combination of the sense and word currents turns the layer magnetization in state "0" towards the direction of the sense current flow, therefore increasing the resistance of the cell due to AMR. However, the same combination of the sense and word fields has a much smaller effect on the magnetization in state "1". Therefore, compared with the resistance in the remanent state, the resistance rise of state "1" is much smaller

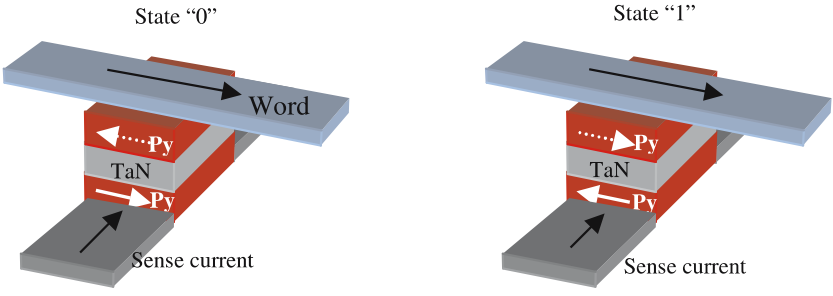

Fig. 7.3. Two memory states in an AMR-based memory cell. The easy axs direction of the two permalloy (Py) layers is set along the width of the etched stripe. The word line is electrically isolated with the memory cell

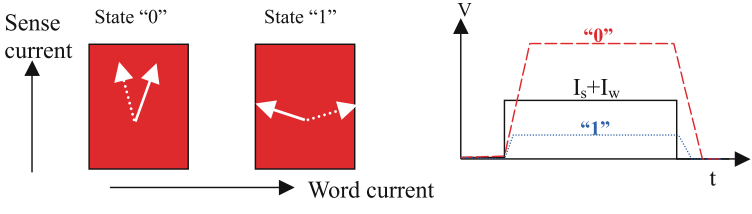

Fig. 7.4. Read operation in AMR memory cells. Magnetization configurations for two memory states during reading. The *dashed line* represents the top layer magnetization and the *solid line* the bottom layer magnetization (left). The sense signal form state "0" and state "1" for a current pulse $I_s + I_w$ (right)

than that of state "0". In the reading operation, the resultant field from the sense and word currents must be kept below the switching threshold so that the magnetization rotation is reversible. Hence, the original state is preserved after the reading is done. This is the non-destructive readout (NDRO) scheme.

It should be pointed out that when a pair of sense and word currents is turned on, the other memory cells along either the sense or word line also experience a field. These cells are called "half-selected" cells. For the half-selected cells along the sense line, the magnetization does not change regardless of their memory state. For the half-selected cells along the word line, the magnetization does rotate away from the easy-axis direction, but because they are not on the sense line, their resistance change does not contribute to the sense signal. After the word current is turned off, these cells restore to their remanent states. In real AMR-based RAM devices, because of edge effects, the maximum differential resistance of a cell between a "1" and a "0" is only about 1/4 of the total AMR, or about 0.5%. The sense signal is very small; therefore, the read access speed is slow. In 16 Kb integrated MRAM chips, the read access time is about 250 ns [7.13].

Writing: State "0" can be written into state "1" and vice versa by increasing the current flow in both the sense and word lines. When the resultant field strength

exceeds the switching threshold, states "0" and "1" can be switched to each other. The magnitude of either current is chosen such that a single field is not strong enough to switch the magnetization. In all MRAM devices, the cell selection for writing is accomplished by this half-select scheme, which will be discussed in more detail in following sections.

AMR-based RAMs for the first time demonstrated the possibility of solid state memory devices using MR for readout. But it has a relatively long read access time. The memory mode described here apparently stops working for submicron and smaller memory cells because the shape anisotropy dominates thus the memory states are different. To improve the read access time, a large signal, i.e. a large MR is required.

7.2.2 Spin-Valve MRAM

The discovery of the giant magnetoresistance (GMR) effect [7.14, 15] was a turning point in MRAM research and development. GMR originates from the spin-dependent scattering in alternating ferromagnetic/non-magnetic multilayers. The multilayer resistance depends on the relative orientation of magnetization in adjacent layers. In low field applications such as read heads, the original antiferromagnetically coupled multilayers are not used, primarily due to the strong interlayer exchange coupling ($\sim$1 kOe). A simpler and more practical structure is the spin-valve (SV). A SV structure consists of only two magnetic layers separated by a thin conducting spacer layer (e.g. 3 nm thick Cu layer). One of the two magnetic layers is magnetically pinned by an antiferromagnetic material (e.g. FeMn or IrMn) due to exchange anisotropy, and the other layer is free to rotate under a relatively small magnetic field. If the applied magnetic field strength is greater than the coercive field of the unpinned magnetic layer (or free layer) but smaller than the exchange pinning field, the free layer magnetization is switched parallel or anti-parallel to the pinned layer magnetization. In consequence, a large change in resistance (GMR) is realized between the two states. The change in resistance is typically about 5%, but in optimized films it can be as high as 17% [7.16].

Memory states: The memory states of a SV MRAM cell are the two remanent magnetization states of the free layer (Fig. 7.5). The pinned layer magnetization does not change; therefore, it only serves as a reference for the free layer.

Reading: In a one-transistor-per-cell architecture [7.17], the transistor is used for selecting the cell as well as sensing the in-plane resistance of the cell when selected. The cell selection for reading is achieved by turning on a select transistor whose gate and source (or drain) are connected to a row (bit line) and a column (word line) respectively. When a pair of row and column lines is chosen, the cell at the crossing is selected, and the remanent state resistance of the cell is read and compared with a reference cell. The memory state is determined by the sense voltage signal. Since the magnetization state is not disturbed during reading, the reading operation is non-destructive.

Writing: The one-transistor-per-cell design requires another set of lines called digit lines parallel to the word lines for writing operation. The digit line provides an

orthogonal field to the field generated by the sense current. A pair of sense and digit current lines is simultaneously turned on to select the cell at the crossing for writing, similar to the half-select scheme in AMR-based RAM.

7.2.3 Pseudo-Spin-Valve (PSV) MRAM

A second type of GMR-based memory is PSV MRAM. PSV memory cells are similar to SV cells, except that both layers of a PSV cell are switchable but they switch at different fields. The two magnetic layers can be made of different materials or the same material with different film thickness. In the latter case, the coercive field becomes dependent upon the film thickness when the lateral dimensions are below 1 µm [7.18]. Here we focus on the latter PSV cells.

Memory states: When a PSV film is patterned to submicron stripes, the magnetization of each layer is along the cell length at the remanent state due to shape anisotropy. There are in principle four possible memory states in a PSV memory cell, e.g. two parallel and two anti-parallel states. In actual PSV MRAM, only two magnetization states of the thicker layer are used to store information [7.19, 20], as shown in Fig. 7.6. Similar to the two states in an AMR cell, memory states in a PSV cell have the same remanent resistance; therefore, they cannot be distinguished by simply sensing their static resistance.

Reading: The thin magnetic layer in a PSV cell is used for reading. When a sense line is turned on, the sense current flows through all the cells along the line. However, if a perpendicular word line is turned on, only the cell at the crossing is selected. To read the selected cell, the resultant field from both the sense and word lines has to be strong enough to switch the thin layer magnetization, i.e. greater than H_{c1}, but less than the switching field of the thick layer, H_{c2}. In addition, the fields from either line must be small enough such that the thin layer magnetization of the half-selected cells along either line is not switched. The reading operation is executed in the following steps. First, a negative word field is applied so that the resultant field on the selected cell is between $-H_{c1}$ and $-H_{c2}$, which initializes the state of the

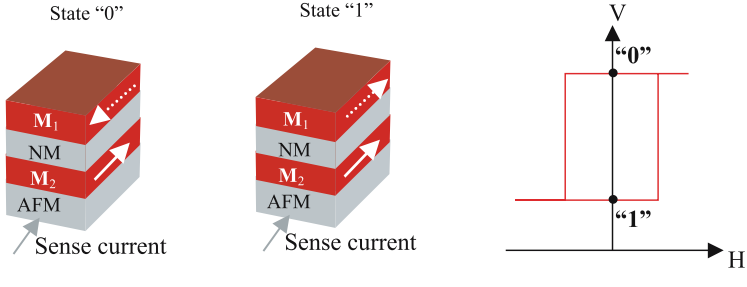

Fig. 7.5. Memory states "0" and "1" in a SV MRAM cell. The bottom layer magnetization is pinned and the magnetization direction of the top layer represents the memory state (left). The voltage is high or low depending on the memory state (right)

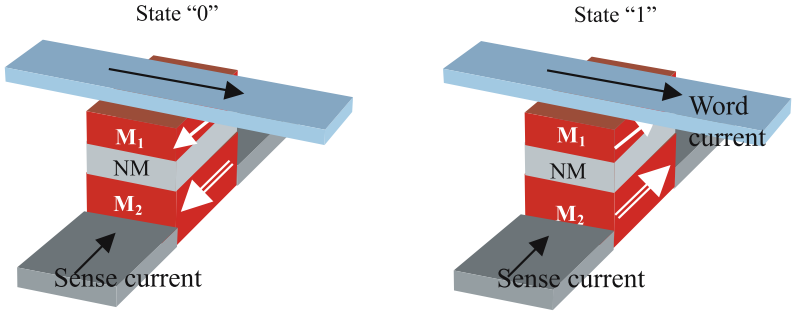

Fig. 7.6. Memory states in a PSV cell. A certain length-to-width aspect ratio is needed for obtaining large signal. The overall magnetization direction of both layers can be either parallel or anti-parallel to each other along the cell length. The etched PSV cells are electrically connected to form a sense line (vertical scale is out of proportion). The word lines are electrically isloated from the cell

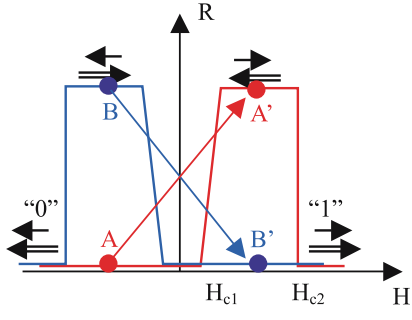

Fig. 7.7. Reading operation in PSV MRAM. The thin layer is interrogated by two sequential word pulses: a negative one to initialize the cell and followed by a positive one to check the voltage change. The combined field strength is set between H_{c1} and H_{c2}

thin layer. In doing so, state "0" is set to point A on the red curve, and state "1" to point B on the blue curve. Next the sense amplifier is auto-zeroed, and the word current pulse ramps to a positive field so that the resultant field is between $+H_{c1}$ and $+H_{c2}$. Hence, state "0" goes from A to A' and state "1" goes from B to B'. The cell voltage signal with respect to zero is negative for state "1" and positive for state "0". The difference in resistance swing between the two states is twice as much as the full MR of the materials. This is also called dynamic read-out scheme. To the half-selected cells along the sense line, the magnetization of both layers rotates away from the equilibrium position but neither would switch. As the sense field is set back to zero, the respective original states are restored. To the half-selected cells under the word current, the magnetization of neither layer changes; therefore, these cells are not disturbed.

Writing: To change from one memory state to the other, a higher field ($>H_{c2}$) is needed to switch the thick layer magnetization. In actual MRAM chips, the writing

may need another set of current lines called digit lines parallel to the sense lines to aid to the sense field. In addition, "wrap-around" word current lines are used to generate a higher and more uniform field [7.19].

In PSV MRAM, all the cells along a sense line share one transistor. It is a denser design than one-transistor-per-cell architecture in SV MRAM. Furthermore, the effective signal is doubled using dynamic read-out scheme; therefore, it is advantageous in terms of the read access speed. Nevertheless, there are serious drawbacks. First, in order to ensure a reasonable separation between H_{c1} and H_{c2}, a thick film is usually used for a high H_{c2}. Hence, writing demands a large current, which means large transistors. Second, similar to SV MRAM, PSV cells often need large aspect ratio to gain higher signal and faster read access speed. Large aspect-ratio cells occupy more area and also require higher switching fields, which compromises memory density as well as power consumption.

7.2.4 Magnetic Tunnel Junction (MTJ) MRAM

Clearly, a key to high-speed, high-density, and low power MRAM is the high signal level ΔV or large magnetoresistance ΔR, not necessarily the high MR ratio $\Delta R/R$. In all-metal GMR structures, the speed, density, and power consumption are often incompatible with each other. The magnetic tunnel junction (MTJ) material having large tunnel magnetoresistance (TMR) provides real potential for high performance MRAM [7.21]. So far it is the most attractive MRAM, and many companies are vigorously pursuing it. In fact, MTJ MRAM cells and prototype chips have demonstrated outstanding performance in terms of the access times, cell size, and power consumption. In this chapter, we will not go to details about the TMR effect and MTJ materials, which are reviewed by Moodera in separated chapters of volume III.

MTJ cell resistance and signal: MTJ materials consist of two ferromagnetic layers separated by a thin insulating layer (1–2 nm thick) such as Al_2O_3 [7.22–25]. Since the resistance of a MTJ junction is inversely proportional to the area of the junction cross-section, an appropriate quantity to describe the specific resistance is the product of the resistance and the area of the junction, or the *RA* product. The tunneling current flowing through the insulating layer depends exponentially on its layer thickness [7.26]. Hence, by controlling the thickness of the oxide layer the RA product can be tuned over many orders of magnitude. In general, it is relatively easy to control the oxide layer thickness when the layer is thick, but it is rather challenging to produce a very thin oxide layer for low RA product MTJ films.

The magnetoresistance ratio $\Delta R/R$ is on the other hand determined by the spin-polarization of the magnetic layers on both sides of the tunnel barrier [7.27]. Nowadays very large TMR ($\sim$ 50%) can be routinely achieved in sputtered MTJ films in several laboratories. Although the TMR ratio decreases with the increase of the voltage bias, the usable TMR at a reasonable bias ($\sim$ 200 mV) can be still significantly large compared with that of PSV materials ($>$ 20%) [7.28].

With the high resistance and TMR ratio, the signal level of a MTJ cell (ΔR or ΔV between the two memory states) is very favorable, which is essential to fast read access in MRAM. This also brings additional benefits such as high-density and low

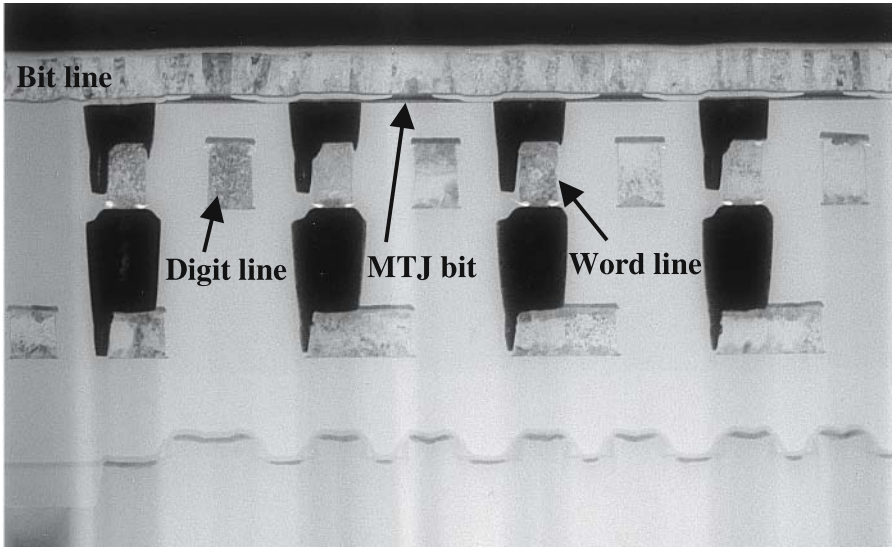

Fig. 7.8. Cross-section transmission electron micrograph of integrated MTJ MRAM (Courtesy of IBM Research)

read and write power consumption, due to the small aspect ratio cells and low sense current.

Although the large resistance and magnetoresistance are responsible for the above advantages over other MRAMs, if the cell resistance is too high, it will have an adverse effect on the read access speed. First, a high cell resistance requires a small current, as the maximum voltage drop across the cell must be less than the voltage supplied by the batteries. Hence, it requires a very quiet current source or a long average time for reading. Second, since the MTJ cell has capacitance, a high cell resistance means a long RC time constant. Obviously the cell resistance has to be optimized in actual design. In general, low RA product materials are needed for high-density MTJ MRAM.

Reading and writing: The reading and writing operations in 1MTJ/1T architecture are very similar to those in SV MRAM. As shown in Fig. 7.8, the word line connects the transistor in the cell to the MTJ element. Therefore, when a transistor is turned on, a sense current will flow from the bit line to the word line through the MTJ. Thus the resistance of the selected cell is sensed to read the memory state. Reading operation consumes only a small amount of power. For writing, the select transistor is not used. Currents flowing in the digit and bit lines generate a magnetic field required to switch the selected bit at the crossing of the lines. Since the MTJ cells do not need a large length-to-width aspect ratio for high signal, the required switching field is lower than in that SV or PSV MRAMs, which leads to relatively low power consumption in writing as well.

Challenges: No doubt MTJ MRAM offers attractive advantages over other MRAMs as just discussed; however, there are also unique challenges to overcome.

First of all, the tunnel resistance is very sensitive to both the insulating layer thickness and tunnel barrier height. Controlling the resistance uniformity over the whole wafer (which can be as large as 6 or 8 inches) is obviously a daunting task. The memory state of a cell is distinguished by the resistance level of the cell. Hence, to determine the memory state correctly, the cell resistance variation has to be much smaller than the difference in the resistance between the two memory states; i.e. the percentage variation of the resistance must be much smaller than the TMR of the MTJ material. Either the oxide barrier thickness or the barrier height can vary to cause a huge resistance variation; therefore, the Al-layer deposition and oxidation must be controlled extremely well. To achieve the high degree of the resistance uniformity, it first requires a very smooth substrate that the MTJ film is deposited on. Actual MRAM cells are built on wafers containing required CMOS circuitry; therefore the MRAM back end process must start with careful planarization to produce smooth surface. In addition, a reference cell has to be built next to the MTJ cell. When the active cell resistance is read out, it will be compared with the resistance of the reference cell, and then its memory state can be unambiguously determined. Very tight local resistance variation can be achieved [7.7] so that a meaningful comparison between the active and reference cells can be made. Another practical challenge unique to MTJ materials is the device yield. Electrical shorts across the very thin insulating layer can easily develop along the peripheral of a patterned MTJ element. This requires a very careful etching process in the patterning.

7.2.5 Other MRAM Concepts

Another type of MRAM that utilizes GMR materials in current-perpendicular-to-plane (CPP) geometry was proposed [7.29]. The memory cell of this vertical MRAM or VMRAM is a multilayered "doughnut-shaped" ring. The memory states are the clockwise and counterclockwise magnetization states. A dynamic read-out scheme similar to that used in PSV MRAM was proposed for reading. The magnetic switching mechanism is considerably different from that in other MRAM cells. In order to read and write the VMRAM cells, a tangential field is required. A double word and digit line design was proposed for generating the tangential field. Due to the inherently low signal level in all-metal GMR materials, the read access speed of the VMRAM will suffer until a very small cell size is reached. Another drawback is that the magnetic element alone (not the entire cell) would occupy at least $9F^2$ (F: minimum dimension in lithography), compared with $\sim 2F^2$ for a rectangular element.

Another proposed non-volatile RAM utilizes a single magnetic layer for storage and the Hall effect for reading [7.30]. The stray field of a single magnetic layer element is sensed by the Hall voltage of a two-dimensional electron or hole gas sheet underneath. Although the reading scheme is drastically different from the MR reading, the writing operation is essentially the same as other types of MRAM.

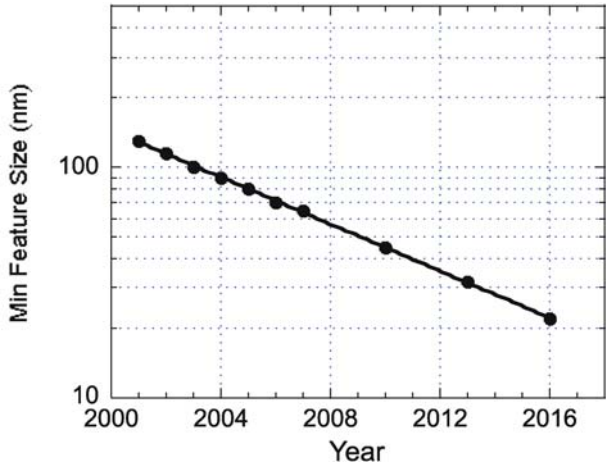

Fig. 7.9. Minimum feature size determined by semiconductor lithography vs. year for DRAM production (Data from ITRS 2001 report)

7.3 MRAM Cell Scaling

There are no adverse effects on the cell signal level as the MRAM cell size (not the length-to-width aspect-ratio) shrinks. However, the reduction in cell size drastically affects magnetic switching of the layer magnetization; therefore, it definitely affects the writing process. Although the reading operation does not involve any change to the magnetization state in the static read-out scheme, it does depend on magnetization rotation or switching in the dynamic read-out scheme. In addition, all the writing and reading operations using dynamic read-out rely on the half-select mechanism. It is very important to understand the magnetization reversal of the ever-shrinking MRAM elements under one or two orthogonal fields [7.31].

First of all, let us look at the general trend in DRAM cell scaling. If MRAM is to compete with DRAM, MRAM cell size has to be compared with the DRAM counterpart. Fig. 7.9 was plotted according to the latest data in the "The International Technology Roadmap for Semiconductors" or ITRS 2001 report for DRAM products [7.32]. The minimum feature size F refers to the "half-pitch" size in DRAM. This size is projected to pass the 100 nm mark in 2003 and continue to shrink steadily. The DRAM trend serves as a benchmark for future MRAM products, which means that the magnetic element has to shrink accordingly in future MRAM product generations.

In addition to the minimum feature size reduction that relies on the future advances in lithography technology, another quantity affecting the ultimate memory density is the "cell area factor". The absolute DRAM cell size ($C.S.$) is defined as $C.S. = a \cdot F^2$. The cell area factor, a, also decreases as F decreases according to the projected curve. This makes the packing density of the memory bits increase even more rapidly. For example, the area factor is eight in current product generation, but it will decrease to four when F reaches 32 nm. If MRAM is to follow the same trend, MRAM elements have to be packed more closely.

Let us not be concerned about technological challenges in making sub-100 nm magnetic elements in the next several product generations, but rather about possible fundamental limitations to MRAM scaling. In the 1970's and early 1980's, magnetic bubble memory, a type of non-volatile storage device, exceeded 1 Mb storage capacity, but it failed to compete with solid state memory devices or hard disks. The operation of the bubble memory devices was based on the formation and transport of bubble domains [7.33] in soft magnetic films such as epitaxial garnet films. The smallest bubble diameter in these films is about 0.3 μm. Clearly, the ultimate density is limited by the bubble domain size. As will be discussed in the following sections, as the magnetic element shrinks in future generations, it approaches the ideal single-domain. Fundamentally speaking, the higher-density MRAM elements are expected to perform much better in terms of magnetic switching and bit selection. No doubt, there are still challenging issues associated with very small memory devices, one of which is the superparamagnetic limit. In the next section, we focus on the switching characteristics of ideal single domains before reviewing experimental results on small patterned structures.

7.4 Coherent Rotation of Single-Domain Elements

7.4.1 Single-domain Size and Exchange Lengths

Magnetic domains exist in both hard and soft magnetic materials due to the magnetostatic (dipolar) interaction [7.34, 35]. In patterned magnetic elements, domain formation becomes less energetically favorable as the element size decreases because of the increasing cost in exchange energy. Eventually, below a certain size, called the single-domain size l_{SD}, the magnetic structures prefer to be single-domains. In general, l_{SD} depends on the physical shape and material parameters such as the exchange stiffness constant A, the saturation magnetization M_s, and the anisotropy constant K. The single-domain size and detailed "phase diagrams" have been numerically calculated with a broad range of anisotropy and various shapes [7.35].

The occurrence of magnetic domains depends on the element size compared with two fundamental length scales, both called exchange lengths, $l = \sqrt{A/K}$ and $l_D = \sqrt{A/2\pi M_s^2}$. The first exchange length represents typical domain-wall width in an unpatterned film; the second exchange length represents typical size of a magnetization vortex core. In polycrystalline soft magnetic materials such as NiFe or NiFeCo, which are often used in MRAM, the anisotropy K is the induced uniaxial anisotropy that is set by an aligning field during film deposition. According to experimental data, this uniaxial anisotropy constant is about 10^3 erg/cm^3, equivalent to an anisotropy field of a couple of Oersteds. The energy scale associated with the demagnetizing field, $2\pi M_s^2$, is about $5 \cdot 10^6$ erg/cm^3 in NiFe. If we take A=1 $\cdot$ 10^{-6} erg/cm, then the first exchange length l is approximately 300 nm and the second exchange lengthl_D is only about 4 nm. In structures whose lateral dimensions are much greater than l, the domains can be treated as different areas within which magnetization is uniform but between which the magnetization forms thin and abrupt boundaries, similar to

the crystallographic picture of a polycrystalline solid. Clearly, the patterned elements of interest are smaller than this length scale. This means that the magnetization continuously varies in a submicron element, just as within classical domain walls. In patterned soft magnetic materials, a more important length scale that determines domain formation is the second exchange length l_D. If the size of a magnetic element is below l_D, it will be in the single-domain state. The actual boundary between the single – and multi-domain or single-domain and vortex state may be several times large than l_D. Quantitative phase diagrams for patterned thin-film structures require detailed micromagnetic calculations.

In MRAM devices of many generations to come, the lateral dimensions are still much greater than the exchange length l_D, although the film thickness is comparable with the l_D. Although submicron and sub-100 nm MRAM elements are not truly single domains, we expect smaller devices to behave more like single domains. Next, we will consider the switching behaviors of single-domain elements.

7.4.2 Coherent Rotation of Single-domains with Uniaxial Anisotropy

Let us assume the magnetization in a small magnetic element to be uniform. In general, an ellipsoidal shape is considered so that both the magnetization and the demagnetizing field inside the body are uniform. For a sufficiently small element, the actual shape of the element is not important. For simplicity, we assume that the energy density has a well-defined second-order uniaxial symmetry. The uniaxial anisotropy can be a crystalline field anisotropy, induced anisotropy, magnetostriction, shape anisotropy or a combination of two or more anisotropy contributions. For a planar single-domain element of interest, we only need one parameter to represent the magnetization. The model based on this coherent or uniform magnetization rotation is called the Stoner-Wohlfarth (SW) model [7.36]. The free energy density is simply a sum of the uniaxial anisotropy and the Zeeman energy density due to the external field,

$$F_T = K \sin^2 \alpha - HM \cos \phi \ .$$

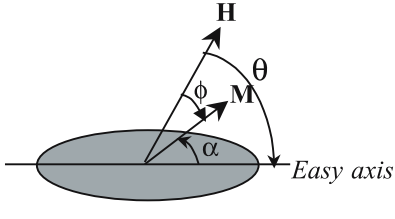

Easy-axis loop ($\theta = 0$, and $\phi = \alpha$). When the field is applied along the easy-axis direction, the total free energy density can be written as

$$F_T = K \sin^2 \phi - HM \cos \phi \,,$$

where the angles θ and ϕ are shown in the figure. For a given field H, a stable equilibrium direction of the magnetization can be found by minimizing F_T. First we have

$$\frac{\mathrm{d}F_T}{\mathrm{d}\phi} = 2K \sin \phi \cos \phi + HM \sin \phi = 0 \,. \tag{7.1}$$

Denote $h \equiv \frac{H}{\left(\frac{2K}{M}\right)} = \frac{HM}{2K}$. Equation (7.1) has two solutions: $\sin \phi = 0$ and $\cos \phi = -h$. Then we can find which one is the stable solution, i.e. the minimum of the free energy density by examining the second order derivative,

$$\frac{\mathrm{d}^2 F_T}{\mathrm{d}\phi^2} = 2K \cos 2\phi + HM \cos \phi \,. \tag{7.2}$$

For the first solution $\sin \phi = 0$, $\mathrm{d}^2 F_T / \mathrm{d}\phi^2 = 2K(1 \pm h)$; the positive and negative signs correspond to $\phi = 0$ and $\phi = \pi$, respectively. $\phi = 0$ is metastable (i.e. $\mathrm{d}^2 F_T / \mathrm{d}\phi^2 > 0$) until h approaches -1 from the positive side. Likewise, $\phi = \pi$ is metastable until h approaches $+1$ from the negative side. When one angle becomes unstable, it jumps to the other. This jumping represents a magnetic switching event, and the corresponding reduced magnetic field is called switching field or critical field, h_c. Here we have, $h_c = \pm 1$.

For the second solution $\cos \phi = -h$, we have $\mathrm{d}^2 F_T / \mathrm{d}\phi^2 = 2K(h^2 - 1) \leq 0$. It represents an energy maximum, or an energy barrier separating the two minima. The energy barrier height is the difference between the maximum energy and the energy at the metastable state, and can be expressed by $\Delta = K(1 - |h|)^2$. Note that the energy barrier height is K in the absence of any easy-axis field, and it decreases quadratically as an easy-axis field is applied.

Now we can construct the easy-axis hysteresis loop. Fig. 7.10 shows the easy-axis normalized magnetization $\cos \phi$ vs. the reduced field h.

Hard-axis loop ($\theta = \pi/2$, $\alpha = \phi - \pi/2$). When an external field is applied perpendicular to the easy-axis, the total free energy density is, $F_T = K \cos^2 \phi - HM \cos \phi$. Let the first-order derivative be zero to determine the equilibrium angle,

$$\frac{\mathrm{d}F_T}{\mathrm{d}\phi} = -2K \sin \phi \cos \phi + HM \sin \phi = 0 \,, \tag{7.3}$$

There are again two solutions: $\sin \phi = 0$ and $\cos \phi = h$. Then we examine the second-order derivative. For the first solution $\sin \phi = 0$, $\mathrm{d}^2 F_T / \mathrm{d}\phi^2 = -2K \cos 2\phi + HM \cos \phi$ is $2K(h - 1)$ when $\phi = 0$, and $-2K(h + 1)$ when $\phi = \pi$. It means that $\phi = 0$ is not stable until $h > 1$ and $\phi = \pi$ is not stable until $h < -1$. Both cases state one fact: the magnetization will be aligned along the field direction when the reduced field strength is greater than one.

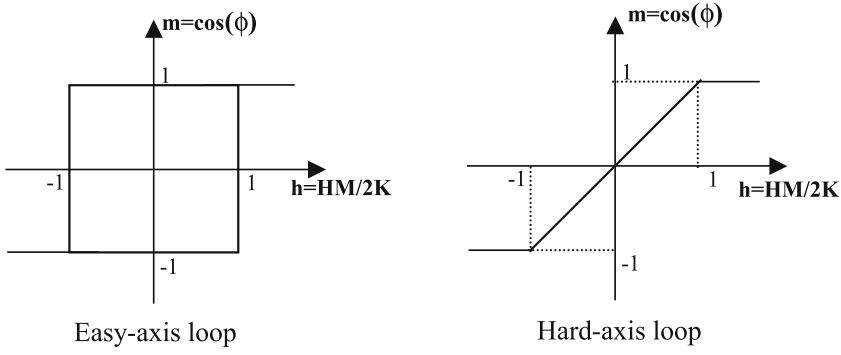

Fig. 7.10. Easy- and hard-axis hysteresis loop for planar single-domain elements with a unaxial anisotropy

For the second solution $\cos\phi = h$, we have $\mathrm{d}^2F_T/\mathrm{d}\phi^2 = -2K\cos 2\phi + HM\cos\phi = 2K(1+h^2) > 0$. Note that$|h| = |\cos\phi| \leq 1$; therefore, this solution is always stable when $|h| \leq 1$.

When a hard-axis field is applied, the hard-axis magnetization component increases linearly with the field strength until it saturates at $h_c = 1$, which is equal to the easy-axis critical field. A hard-axis hysteresis loop is also shown in Fig. 7.10.

Single-domain switching field with an arbitrary field angle. Above are two special cases when an external field is applied along the easy- or hard-axis. For an arbitary field direction, a numerical calculation is needed to construct the hysteresis loop. The critical field or switching field h_c can be solved by finding the instability point [7.36], i.e. by letting both first- and second-order energy derivatives vanish. The reduced switching field is expressed by,

$$h_c = \left(1 - w^2 + w^4\right)^{1/2} / \left(1 + w^2\right), \quad \text{with} \quad w = \tan^{1/3}\theta\,. \tag{7.4}$$

The switching field has a four-fold symmetry when the applied field direction is varied with respect to the anisotropy axis (Fig. 7.11). When $\theta = \pi/4$, it reaches the minimum at $h_c = 1/2$. In small magnetic elements, this perfect four-fold symmetry is rarely observed due to various reasons [7.37, 38].

In the SW model, switching of magnetization occurs at $h_c = 1$, or $H_c = 2K/M$. The absolute easy-axis switching field H_c is uniquely determined by the uniaxial anisotropy constant and the saturation magnetization. In small patterned magnetic elements, the predominant anisotropy is the shape anisotropy due to the strong demagnetizing effect. When the aspect-ratio is greater than one, the shape anisotropy can often be approximated by uniaxial anisotropy. Note that this approximation only applies to small elements in which nearly uniform magnetization prevails. Otherwise, the non-uniform magnetization tends to reduce the magnetostatic energy; therefore, the shape anisotropy is not a meaningful quantity. Let us consider a thin-film element with principal axes along x, y and z directions, the shape anisotropy energy density

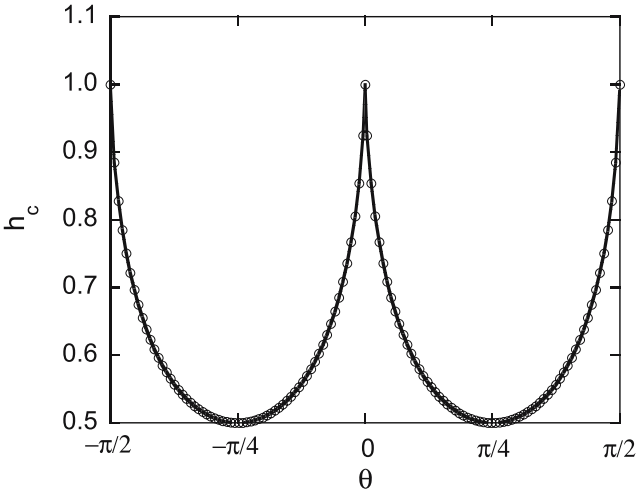

Fig. 7.11. Critical field as a function of the field angle for unaxial planar single-domain elements

can be written [7.39],

$$F_D = \frac{1}{2}N_x M_x^2 + \frac{1}{2}N_y M_y^2 + \frac{1}{2}N_z M_z^2 \ , \tag{7.5}$$

where N_x, N_y, and N_z are three demagnetizing factors, and in CGS, $N_x + N_y + N_z = 4\pi$. If the long axis is along x-axis, and the film thickness is along z-axis, then we have $N_x < N_y < N_z$. If the field is in the x-y plane, the magnetization rotates in the x-y plane. Then we have,

$$F_D = \frac{1}{2}N_x M^2 + \frac{1}{2}(N_y - N_x)M_y^2 = \text{const} + \frac{1}{2}(N_y - N_x)M^2 \sin^2\alpha \ . \tag{7.6}$$

If we ignore the unimportant constant term in the demagnetizing energy density, we can identify the uniaxial anisotropy constant, $K = \frac{1}{2}(N_y - N_x)M^2$. For an ellipsoid with semi-axes a, b, and c along x, y and z directions respectively, the demagnetizing factors can be found for various cases. For $a \geq b \gg c$, i.e. a very flat ellipsoid [7.40], the demagnetizing factors contain elliptic integrals, but N_x and N_y depend on the ratio c/a, and parameter $e = (1 - b^2/a^2)^{1/2}$. For a small patterned thin film element with length L, width W, and film thickness t, the switching field H_c can be approximately written as,

$$H_c = \frac{t}{W} f\left(\frac{L}{W}\right) \ . \tag{7.7}$$

7.4.3 Switching Astroid

In a 2D array of MRAM cells, switching of a selected cell is always done by two fields. Let us first understand how single domains switch under a pair of orthogonal fields.

We choose the easy- and hard-axes of a uniaxial planar single-domain element as the x- and y-axes. If two independent fields, H_x and H_y, are simultaneously applied, the total free energy density is,

$$F_T = K \sin^2 \alpha - H_x M \cos \alpha - H_y M \sin \alpha \ . \tag{7.8}$$

Again we will determine the switching field by setting both the first- and second-order derivatives to zero,

$$\frac{\mathrm{d}F_T}{\mathrm{d}\alpha} = 2K \sin \alpha \cos \alpha + H_x M \sin \alpha - H_y M \cos \alpha = 0 \ , \tag{7.9}$$

$$\frac{\mathrm{d}^2 F_T}{\mathrm{d}\alpha^2} = 2K \cos 2\alpha + H_x M \cos \alpha + H_y M \sin \alpha = 0 \ . \tag{7.10}$$

We again define the reduced fields, $h_x = H_x M/2K$ and $h_y = H_y M/2K$. From the above two equations, we obtain the following reduced switching fields:

$$h_{xc} = -\cos^3 \alpha, \quad h_{yc} = \sin^3 \alpha, \quad \text{or} \quad h_{xc}^{2/3} + h_{yc}^{2/3} = 1 \ . \tag{7.11}$$

Equation (7.11) represents the well-known Stoner-Wohlfarth switching astroid (SW astroid) [7.36]. If there is only an easy-axis field, the critical field is one. The easy-axis switching field decreases from one, as an orthogonal field component is present. The same message is contained in the previous h_c vs. θ curve. The SW astroid not only determines whether switching occurs in the presence of a pair of orthogonal fields, but also graphically shows the metastable magnetization directions [7.41] (Fig. 7.12). If you draw a tangent to the astroid from a tangential point to the endpoint of the field vector $\boldsymbol{h} = (h_x, h_y)$ for any given point inside the astroid (i.e. below the switching threshold), then the direction of the vector is the equilibrium magnetization direction, represented by angle the α. The hysteresis loops can be constructed by finding the α value graphically, or by solving (7.9) numerically. A series of hysteresis loops is shown in Fig. 7.13.

The switching astroid is a wonderful benefit for selectivity. If the switching threshold did not depend on the applied field direction, the half-select scheme would still work. Each line would then need to supply 71% (or $1/\sqrt{2}$) of the required switching field to switch the selected cell and a single line would not affect the half-selected cells. Since the switching threshold varies with the field orientation according to the SW astroid, the minimum field strength needed is $h_c = \sqrt{h_{xc}^2 + h_{yc}^2} = 1/2$ instead of one, and we have $h_{xc} = h_{yc} = 2^{-3/2} = 0.35$. In other words, each line needs only 35% (or $(1/\sqrt{2})^3$) of the full switching field to switch the selected cell! Therefore, the half-selected cells have a much smaller probability to be switched since they only see 35% of the required full switching field. If there is additional anisotropy present, then the switching astriod can be more complex. In general patterned MRAM elements do not follow the SW astroid.

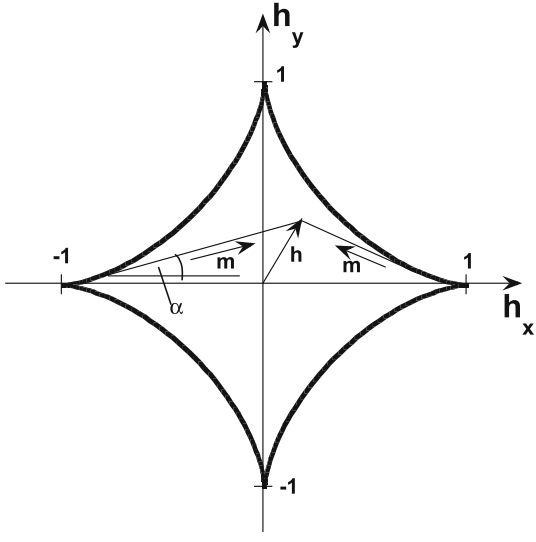

Fig. 7.12. SW switching astroid for single-domain elements. For any field ***h***, the vector linking the tangential point on the SW curve to the endpoint of ***h*** vector represents the metastable magnetization direction. There are two metastable magnetization directions, but the actual magnetization direction depends on the initial magnetization state

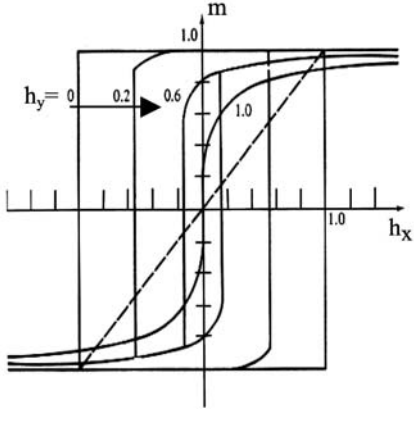

Fig. 7.13. Easy axis hysteresis loops with various hard-axis field values for unaxial single-domain elements

7.5 Switching of Submicron MRAM Devices

7.5.1 Single-domain-like Switching Characteristics

Submicron and sub-100 nm MRAM devices are still greater than the single-domain size; therefore, in many product generations to come, we do not expect the coherent switching to occur as described by the SW model. On the other hand, we also know that

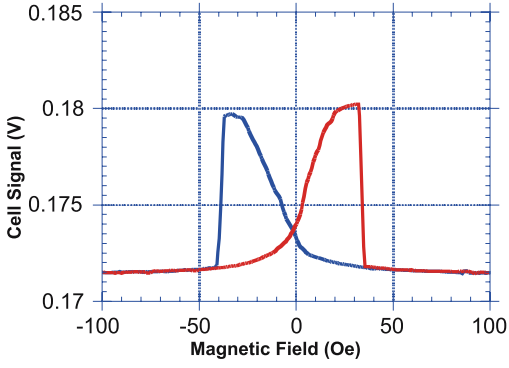

Fig. 7.14a. Magnetoresistance of a 1 μm×10 μm PSV MRAM device. At high field strength, magnetzation of both layers are aligned by the external field. Because of the differential coercive fields (for 4 and 6 nm thick NiFeCo respectively), as the field reverses the direction, the thin layer magnetization, creating an anti-parallel configuration. In this device, the anti-parallel state is not fully reached

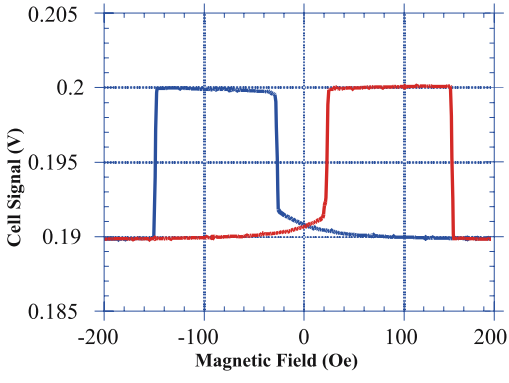

Fig. 7.14b. Magnetoresistance of a 0.25 μm×2.5 μm PSV MRAM device patterned from the same PSV film as used in Fig. 7.14aa. Complete parallel and anti-parallel alignments are realized as indicated b the resistance plateaus

the device lateral dimensions are comparable with or smaller than the first exchange length, i.e. the length scale characterizing the width of a domain-wall in unpatterned soft magnetic films. In general, the switching characteristics of submicron devices are expected to be much simpler than those of the large structures whose switching is dictated by the motion of domain walls. This point is nicely illustrated by two PSV MRAM devices [7.20] (Fig. 7.14a). The two constituent magnetic layers of a PSV film differ only in the thickness. The coercive field of an unpatterned film is not sensitive to its thickness; consequently, the unpatterned PSV films do not show any GMR because no anti-parallel magnetization alignment can be realized by an applied field. When patterned to 1 μm × 10 μm stripes, the PSV layers start to show different coercive fields, with the thick film switching at a higher field. There are two peaks

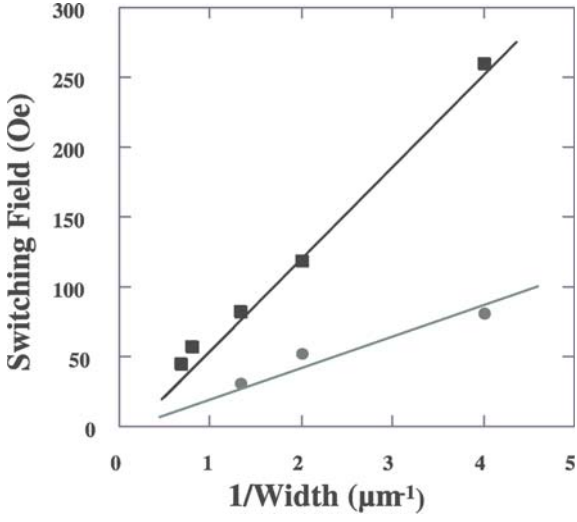

Fig. 7.15. Switching fields of two layers in PSV MRAM devices. Similar inverse relationships have been observed in submicron SV MRAM devices and single-layer elements

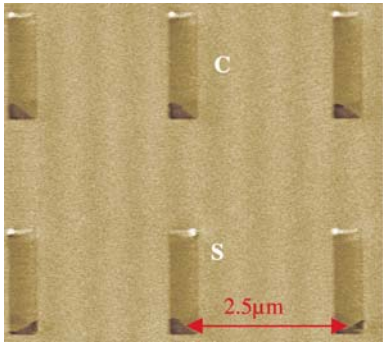

Fig. 7.16. Magnetic force microscopy (MFM) image of patterned submicron NiFe elements. The end-domain state can be either "C" or "S"

in MR traces, caused by some degree of anti-parallel alignment (Fig. 7.14a). When the device width reaches 0.7 μm or so, the switching characteristics are qualitatively different. The MR vs. field traces become very squared. In a 0.25 μm × 2.5 μm device (Fig. 7.14b), both the thick and thin layers switch abruptly, and moreover, they switch between two well-defined magnetization states as suggested by the plateaus. This is indicative of the easy-axis single-domain-like switching characteristics. In addition, the switching field of both films is found to be inversely proportional to the element width for a fixed length-to-width aspect-ratio (Fig. 7.15), which is consistent with the SW coherent switching model (7.7).

On a submicron scale, patterned MRAM devices clearly possess well-defined shape anisotropy and stable single-domain-like remanent states. Systematic stud-

ies have also shown that when the film thickness is small compared with l_D, the switching field of submicron single-layer elements follows the above inverse relationship well [7.42]. As the thickness increases, more deviation from the inverse relationship is developed. It is attributed to the increased magnetostatic energy in thick film elements, which is usually the driving force for domain formation. The remanent state of submicron elements, especially those with large aspect ratio, is generally characterized by uniform magnetization except at the element ends. These end domains (we reserve the terminology "edge domains" for domains in edge-pinned states) can have "S" and "C" configurations (Fig. 7.16), which refer to the parallel and anti-parallel transverse magnetization at two ends respectively. In long aspect-ratio elements, the partial flux-closure end domains do not affect the shape anisotropy as much as in small aspect-ratio elements for quite obvious reasons. In small aspect-ratio elements, the end domains cause the anisotropy to deviate from the uniaxial symmetry; consequently, they have greater impact on the magnetization-reversal [7.42].

7.5.2 Switching Irreproducibility

Submicron MRAM devices appear to work like single-domain objects. According to the SW model, the easy-axis switching field depends only on the device geometry and the magnetization. However, the switching field of submicron devices is not always reproducible and the irreproducibility is often found in thick PSV devices. In PSV films, the thin layer is typically 3–4 nm thick and the thick layer 6–9 nm thick. Even for identical field sweeps (field range, sweeping rate, etc.), the switching of the thick layer occurs unpredictably from sweep-to-sweep, but it often shows a discrete distribution (Fig. 7.17a). The distribution varies from device-to-device on the same wafer even though they are made identical. This kind of switching anomaly is inconsistent with the single-domain picture.

An interesting fact about this anomaly is that those seemingly "ill-behaved" devices work perfectly if the range of field sweeps is expanded (Fig. 7.17b). But when going back to the narrow range is restored, the same anomaly reappears. By "overdriving" the devices, good switching reproducibility can be readily achieved. It is worth noting that this approach would not work for MRAM devices, because the overdriving field would switch all half-selected devices so that the selectivity is completely lost.

This type of anomaly actually provides us some insights about the micromagnetic "defects" developed in those seemingly single-domain structures. First, the "defects" cause the switching to vary. Second, they appear in a rather unpredictable way. In addition, the remnants of the "defects" can be swept out by increasing the magnetic field strength. Similar anomalous behavior also exists in small aspect-ratio MTJ MRAM devices when the free layer is made of thick films (Fig. 7.18).

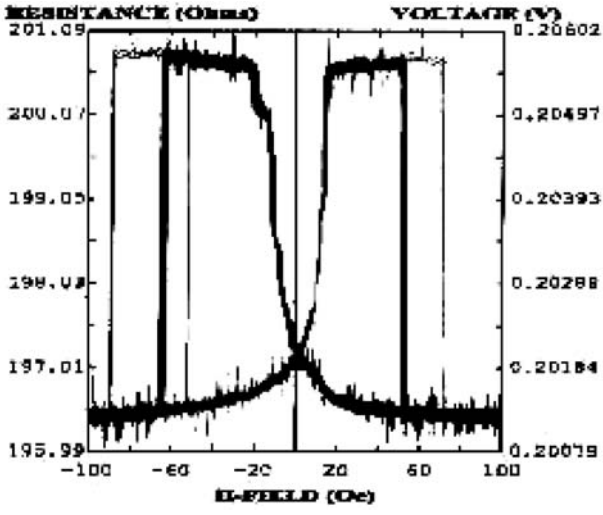

Fig. 7.17a. Magnetoresistance of a 0.5 μm×5 μm PSV MRAM device (overlay of 40 identical continuous field sweeps). The switching field of the thick layer can vary by a factor of two in many similar devices

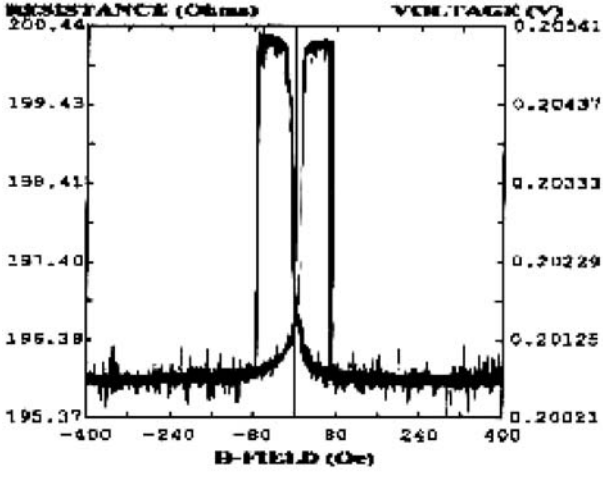

Fig. 7.17b. Magnetoresistance of the same device shown in Fig. 7.17a (also 40 sweeps). The range of the field sweeps is increased by a factor of four. The switching of the thick layer magnetization is perfectly reproducible

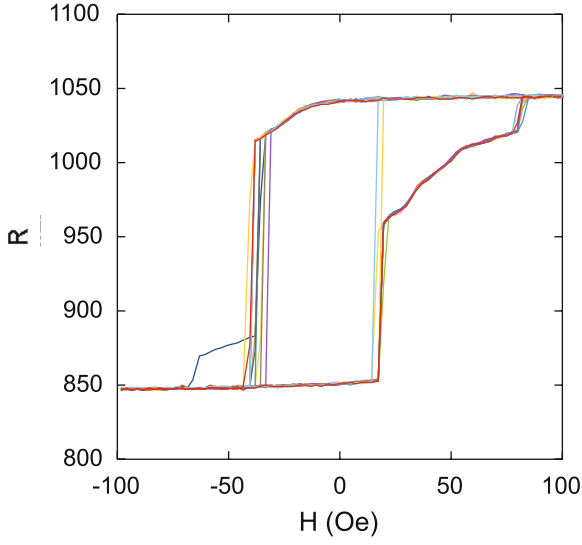

Fig. 7.18. TMR of a 0.9 µm×1.5 µm MTJ MRAM device (12 sweeps). The free layer is about 6 nm thick

7.5.3 Hard Axis-loops

The hard-axis loops of submicron elements appear somewhat like the SW model predictions, but differ in detail. First, if the hard-axis loop is compared with the easy-axis loop, the saturation field in the hard-axis direction is often greater or much greater than the easy-axis switching field. This is the case in a variety of submicron and deep submicron patterned elements [7.43] (e.g. in Fig. 7.19. According to the SW model, the critical field has a four-fold symmetry in the field angle; therefore, the easy- and hard-axis critical field should be equal for uniaxial single-domains. This discrepancy is often ascribed to the non-coherent mechanism in magnetization reversal. In the hard-axis direction, the saturation field is a measure of the anisotropy. When an easy-axis field is applied, local nucleation always takes place instead of coherent rotation so that the switching process does not have to go over the anisotropy barrier. This argument is essentially the same as the one used for the case of Brown's paradox [7.44, 45].

Second, there is always a small amount of hysteresis in the hard-axis loop. In short aspect-ratio elements, the hard-axis loop can be very significant. The finite hard-axis loop also contradicts the uniaxialsingle-domain model. In nearly single-domains, the hard-axis remanence is due to end-domains whose magnetization is transverse to the easy direction. At the end of each hard-axis field sweep, the end-domain magnetization is left in that field direction. From one end-domain state to the other equivalent state, there is a barrier to overcome, which consequently produces a hard-axis loop. Different end-domain states can result in different switching behaviors in easy-axis field sweeps. Hence, the hard-axis remanence is undesirable but unavoidable in submicron MRAM devices.

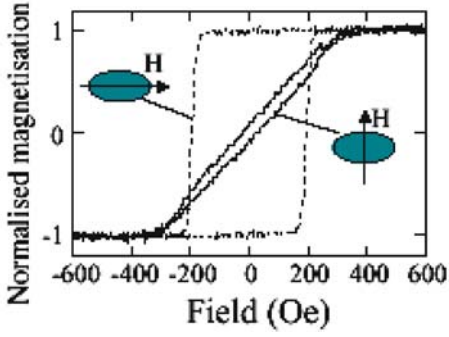

Fig. 7.19. Easy- and hard-axis hysteresis loops of an array of elliptical supermalloy elements. The major- and minor-axis lengths are 250 nm and 125 nm respectively, and the film thickness is 10 nm (Data from [7.43])

7.5.4 Deviation from the SW Astroid

The easy- and hard-axis behavior already implies that the submicron MRAM devices do not follow the ideal SW astroid. Along the hard-axis direction the observed astroid is usually elongated. The degree of this elongation is lessened in small elements. The experimental astroid of a PSV MRAM device shown below (Fig. 7.20a) displays a significant deviation from the standard SW astroid, which would result in an inefficient bit selection. In devices that show anomalous switching as discussed previously, the astroid would have multiple branches along the easy-axis. However, the general trend is that the astroid curves approach the SW curves as the size of the element shrinks (Fig. 7.20b). This is good news in terms of switching selectivity. It should be pointed out that having nice and reproducible easy-axis switching characteristics is necessary but not sufficient for bit selection.

Hard-axis field sensitivity is generally poorer for small aspect-ratio rectangular elements [7.46]. An example is given for a single-layer NiFe rectangular element array (Fig. 7.21). The easy-axis switching field shifts only about 1 Oe for every 10 Oe hard-axis field increment. The square element case is a disastrous extreme. Because of the four-fold symmetry in square elements, the usual half-select scheme stops working even if they are perfect single-domains. In general, the h_y vs. h_x "astroid" is much more complex than the SW astroid if the anisotropy is not purely uniaxial.

7.6 Micromagnetic Properties of Submicron MRAM Devices

Switching anomalies discussed in the last section are clearly related to non-uniform magnetization in submicron elements. Non-uniform magnetization states are developed because the magnetostatic energy is lower than that of the uniform state. If the magnetization varies locally, the magnetostatic energy does not depend solely on the shape of the elements, but on the actual configuration or spatial variation of the

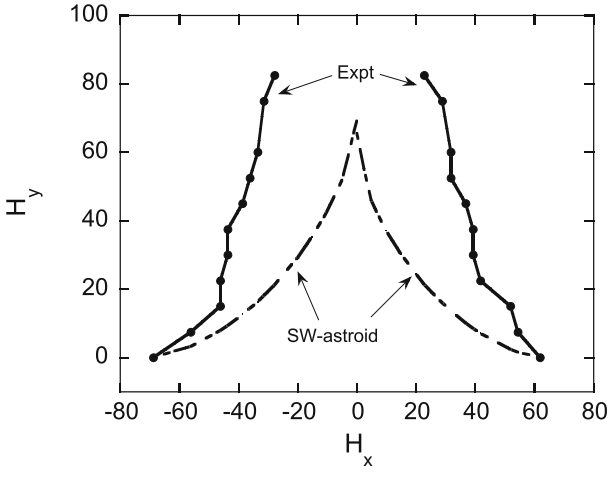

Fig. 7.20a. A half switching astroid for a 0.6 μm×6 μm PSV device. The experimental curves are severely stretched vertically. To reduce the switching field of the selected bits in an array, a very high hard-axis field is needed.

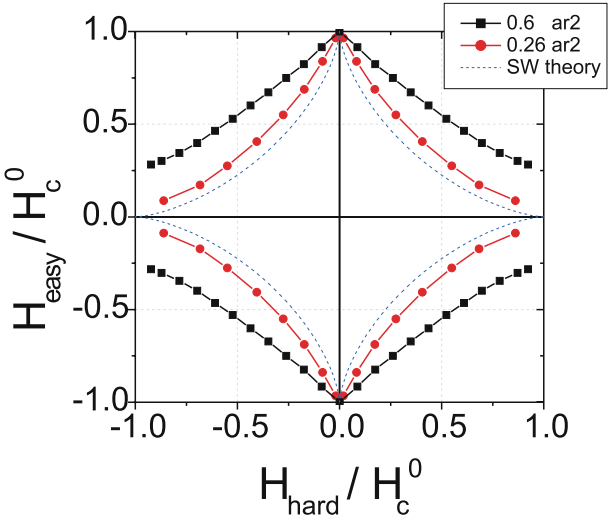

Fig. 7.20b. Simulated SW astroids for 0.6 μm and 0.26 g μm wide elements (aspect ratio = 2). The behavior of the 0.26 μm element is closer to the SW theory prediction. The simulation was done by solving Landau-Lifshitz-Gilbert equation. Note that the easy- and hard-axes are switched (Courtesy of Motorola Labs)

magnetization. The equilibrium magnetization configuration will be settled in a minimum energy state. Unlike single-domains, there can exist multiple minimum energy states. The final state depends on the actual path that the magnetization takes (related to field history) and the thermal fluctuations near the critical field. Computing static

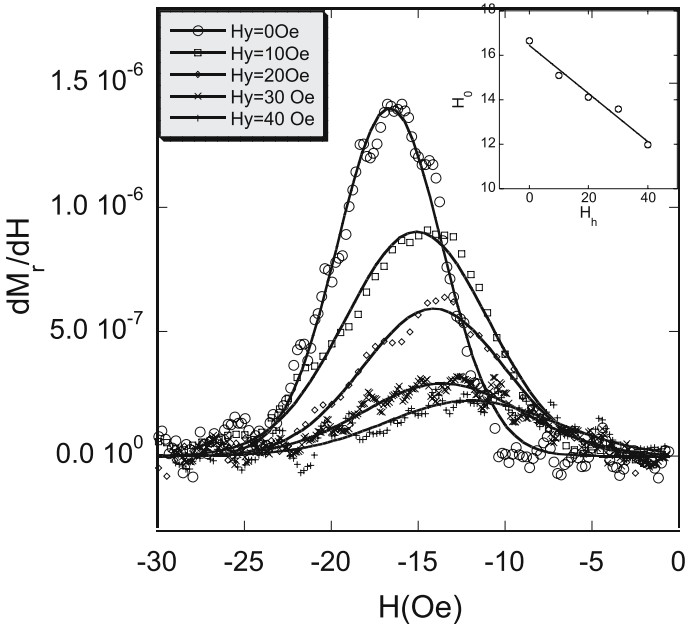

Fig. 7.21. $dM_r\,dH$ vs. H for an array of 0.9 μm×1.2 μm NiFe elements with different hard-axis fields. M_r is the magnetization remanence measured as a function of reversal field. The solid lines are Gaussian fits. The Gaussian center moves to lower fields as the hard-axis field increases, while the standard deviation of the Gaussian distribution increases slightly. The inset shows the Gaussian center as a function of the hard-axis field

and dynamic magnetization configurations as well as magnetic hysteresis loops is an objective of "micromagnetics", which is reviewed by Arrott in a separate chapter. The subject of micromagnetics has been a rapidly developing field in the past several years due to the growing interest in MRAM. In this section, we will discuss the micromagnetic properties of patterned elements related to the switching anomalies described earlier.

7.6.1 Trapped Magnetization Vortices

A common form of micromagnetic "defects" in nearly single-domain structures is magnetization vortices. Since all three dimensions of a submicron MRAM element are greater than or comparable with the exchange length l_D, i.e. the vortex core size, the vortex plays an important role [7.47] in submicron and sub-100 nm MRAM devices. Magnetization vortices can be locally trapped in an element at remanent states. In large aspect-ratio elements where the uniaxial anisotropy dominates, the remanent state even with trapped vortices still has well-defined overall magnetization. Since a trapped vortex causes only a local disturbance to the nearly uniform magnetization, the deviation from the full saturation magnetization is often hidden in the tail of the hysteresis loop. Magnetization remanence measurements can reveal the trapped

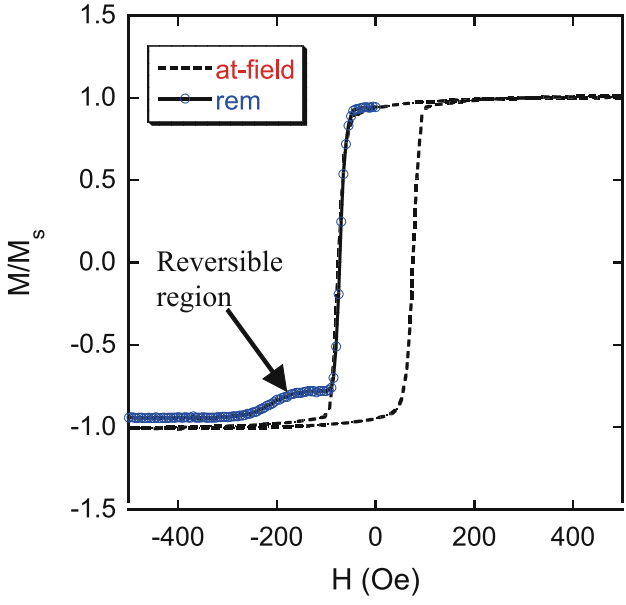

Fig. 7.22. Normal hysteresis loop vs. magnetization remanence curve of 30 nm thick 0.9 μm×4.5 μm NiFe patterned array. In the plateau region, the magnetization is reversible. "At-field" curve is the regular hysteresis loop, and "rem" is the remanence curve

vortices, for there is always a reversible component in the magnetization when a vortex is pushed away from the equilibrium position (Fig. 7.22). On the remanence curve, the magnetization has a plateau before the vortices are driven out of the elements [7.48].

Although the remanent states with trapped vortices in large aspect-ratio elements can still serve as memory states, the trapped vortices greatly affect the magnetization reversal [7.49, 50]. Two strikingly different hysteresis loops from the same array of patterned elements are shown in Fig. 7.23. One loop is taken between two end fields where magnetization is fully saturated; the other is between two end fields that would correspond to the plateau region on the remanence curve, i.e. trapped vortex region. When a hysteresis loop starts from the plateau region, it exhibits two-step switching, denoted by the respective fields, H_{c1} and H_{c2}. In fact, H_{c2} is the same as the switching field of the major loop, but H_{c1} is much smaller. Since this is a measurement over a collection of nominally identical patterned elements, the two-step switching points to two possibilities: either each element switches in two steps, or the element array divides into two separate groups having different switching fields.

Magnetic force microscopy (MFM) imaging clearly supports the latter case (Fig. 7.24). Zero-field MFM reveals two types of magnetization configurations: with and without trapped vortices. The relative ratio between the two types varies with the initial condition or the field that prepares the initial state. MFM tracking of a same group of elements under a varying field has confirmed that the elements with trapped vortices switch at a lower field [7.50]. We also found after each sweep that the

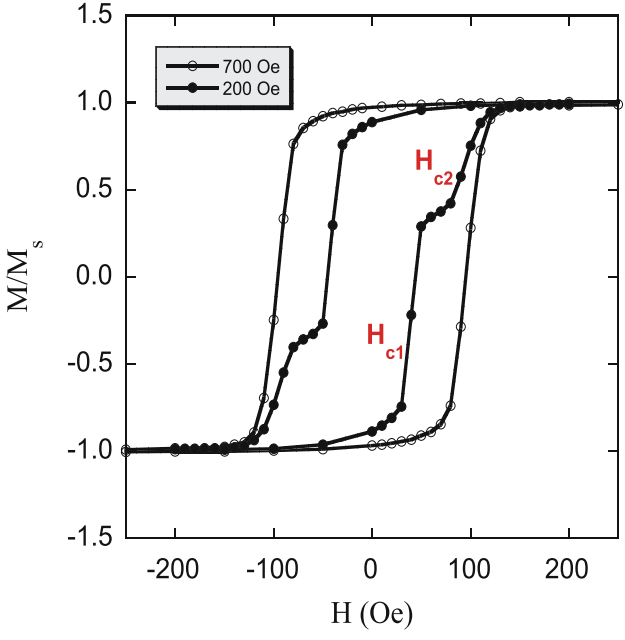

Fig. 7.23. Two representative hysteresis loops of 20 nm-thick 1 μm×5 μm NiFeCo patterned array. When the two end-fields are below 300 Oe, the hysteresis loops has two steps. This is true for element widths down to 0.2 μm

presence of the trapped vortices in the same element group is probabilistic, but the percentage of elements with trapped vortices varies with the end-field of the previous field sweep. As the end-field increases, the vortex population decreases progressively until all elements are free of trapped vortices (Fig. 7.25). To eliminate the "nuclei" of reversal domains, a high field is required to ensure reproducible switching. This is reminiscent of the switching anomaly in single PSV devices.

The microscopic process associated with the anomalous switching is further corroborated by Landau-Lifshitz-Gilbert (LLG) micromagnetic simulation [7.50]. In Fig. 7.26, the simulation was carried out for an element with the same geometry as that in Fig. 7.24. State "a" is the remanent state from a high field; state "b" is the remanent state from an intermediate field where the full saturation has not been reached. State "b" corresponds to the tail region on the remanence curve. Although the remanent state still retains almost full magnetization, it contains two trapped vortices. Starting from these two states, the subsequent switching takes place at two different fields (Fig. 7.27).

The anomalous switching in PSV MRAM devices has also been simulated using LLG micromagnetics. Trapped magnetization vortices in the thick layer can indeed cause switching field to vary from sweep-to-sweep (Fig. 7.28). The micromagnetic simulation results qualitatively agree with the experimental data in PSV devices.

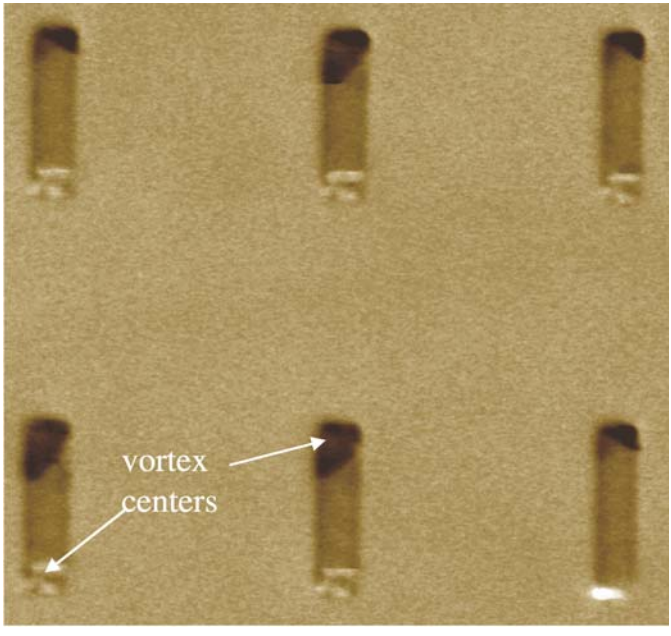

Fig. 7.24. MFM image of the patterned elements used for Fig. 7.23. It is an image of a remanent state from an intermediate field (about 150 Oe). Although the magnetization of all elements has reversed from their initial direction, most elements have one or two trapped vortices

Vortices in small aspect-ratio MRAM devices can not only cause switching field variation as shown in Fig. 7.18, but also a complete loss of memory states if the vortices are trapped. For MRAM devices, magnetization vortices seem to always adversely affect magnetization switching and should be avoided at all cost. Recently, "doughnut" or ring geometry, similar to the ferrite-core, has been proposed to utilize the two senses of a magnetization vortex as two memory states in VMRAM. Then, the goal in VMRAM is just the opposite: a stable vortex state must always be maintained.

Magnetization vortices in both large and small aspect-ratio patterned elements have recently been studied by many researchers [7.47, 51–55] (e.g. Fig. 7.29). In general, the thicker the film (compared with l_D) is, and the smaller aspect-ratio the patterned device has, the more energetically favorable trapped vortices become. A magnetization vortex "phase diagram" [7.52] such as Fig. 7.30 can be used as a guide to prevent trapped vortices in various structures.

7.6.2 Edge-Pinning

The edge-pinned state is another non-uniform magnetization configuration often found in submicron devices. In particular, when a hard-axis field promotes the center of the element to rotate first, the long edges resist rotating in unison with the center to avoid high "pole" density. As a consequence, the edge-pinned state or edge-domain

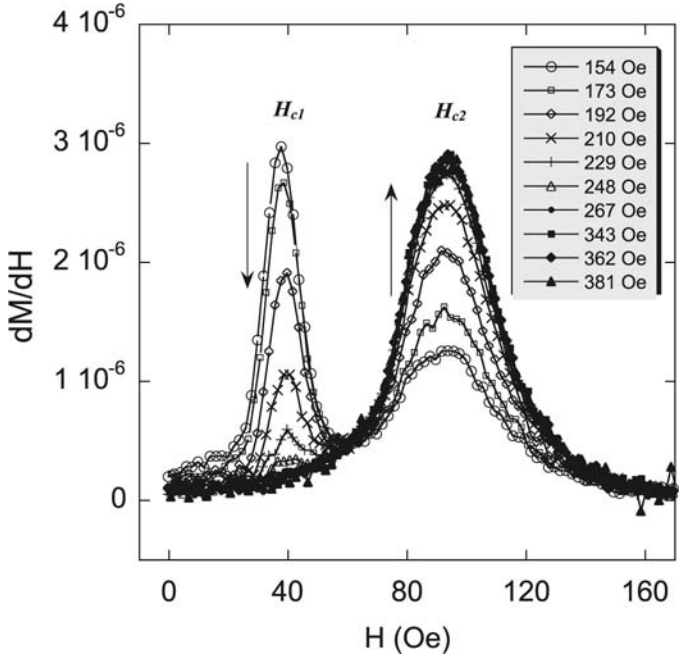

Fig. 7.25. dM/dH data from a series of hysteresis loops for NiFe elements used in Figs. 7.23 and 7.24. The initial state was a demagnetized state. Then regular hysteresis loops are taken with an increasing range of field sweep (shown in legend). As the field range expands, the low-field portion progressively decreases until all elements switch at H_{c2} as the field reaches about 300 Oe.

state is preferred (Fig. 7.31, simulated using LLG Micromagnetics Simulator [7.56]). Although the center magnetization is reversed, the edge-pinned state may not be a fully reversed state [7.46, 57]. Full switching of the memory state depends on the switching of the pinned edges, which starts at corner spins. Once the corner spins are depinned, it triggers an avalanche of the edge spin reversal. This edge wall propagation, similar to the motion of a soliton, takes place rather effortlessly shown by micromagnetic simulations.

7.6.3 360 °C Domain Wall

For long-aspect ratio elements relevant to PSV MRAM devices, the "C" state reversal can result in trapped 360 °C domain walls [7.58], according to micromagnetic simulations. This metastable state also causes the switching field to vary. Since the 360 °C wall formation is caused by "C" end domain initial state, it can in principle be eliminated by a hard-axis field which always forces the end domains to be biased toward an "S" state. In small aspect-ratio elements relevant to MTJ MRAM, the 360 °C domain wall is less likely.

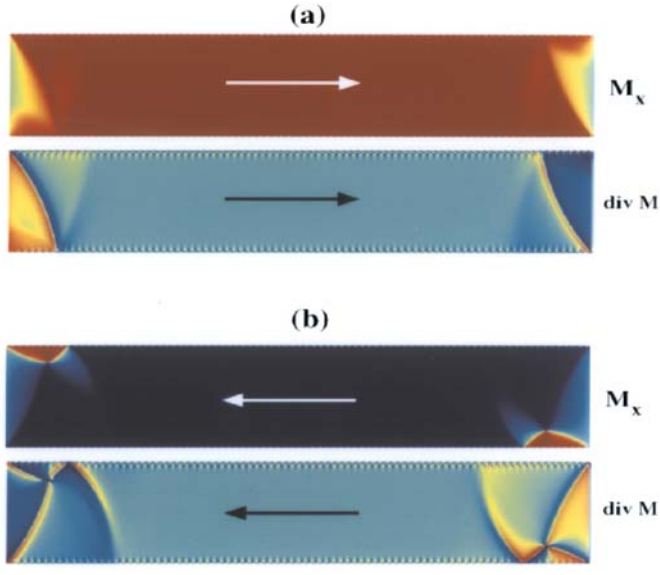

Fig. 7.26. Easy-axis magnetization component (M_x) and magnetization (div**M**) divergence from micromagnetic simulation. The div**M** patterns can be directly compared with the MFM images. The element is 20 nm thick 1 μm×5 μm NiFeCo. States "a" and "b" are two remanent states in the hysteresis loop shown in Fig. 7.27

7.6.4 Effect of Element Shape

In small devices, the local charge density $\sigma = \boldsymbol{M} \cdot \widehat{\boldsymbol{n}}$; therefore, the magnetostatic energy becomes increasingly dependent upon the element shape. This shape sensitivity actually offers some degree of flexibility to tailor desired magnetization configuration and switching characteristics. This "shape engineering" or "micromagnetic engineering" has been investigated by many researchers [7.43, 51, 58, 59]. One direct consequence of shape variation is the effect on the demagnetizing field, and therefore on the switching field (Fig. 7.32). The switching field can be drastically increased if a sharp end is introduced. Another consequence is the influence on the switching modes of the elements. For example, an asymmetric shape can be used to bias the magnetization toward the "C" state; therefore, the element will not switch unless a hard-axis field is simultaneously present. In other words, a steep switching astroid can be engineered to achieve perfect selectivity [7.60]. However, the second aspect of shape control will become less effective when the dimensions of the element approach single-domain size.

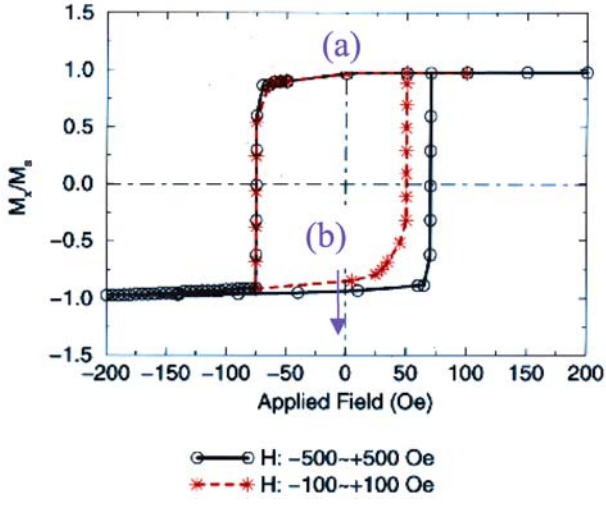

Fig. 7.27. Simulated hysteresis loops with different field sweep ranges. One loop (open circles) starts from 500 Oe, to −500 Oe, and then returns to 500 Oe. After the first sweep ends at 500 Oe, the field is set to 100 Oe. The second loop (crosses) starts from 100 Oe, to −100 and then returns to 100 Oe. The magnetization configurations at states (**a**) and (**b**) are shown in Fig. 7.26

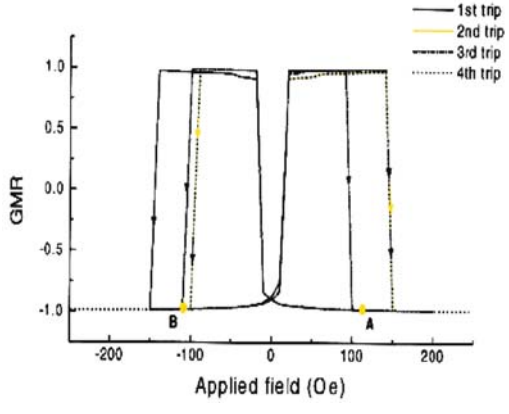

Fig. 7.28. Micromagnetic simulation for a PSV MRAM device. Trapped vortices can produce switching field variations (Courtesy of J.-G. Zhu).

7.7 Issues Related to Magnetic Switching in Future High-Density MRAM

7.7.1 Interlayer Magnetostatic Coupling Due to End Charges

To achieve high density, the cell aspect ratio needs to be small. Unlike PSV materials, MTJ materials do not need large aspect-ratio to boost signal level. Hence, the aspect-ratio requirement has no fundamental effect on reading. However, a small aspect-ratio

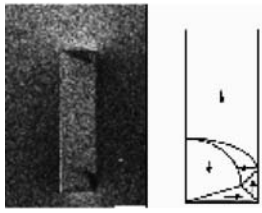

Fig. 7.29. Lorentz microscopy image of a patterned NiFe element. A trapped vortex is present at one end of the submicron element (Data from [7.51])

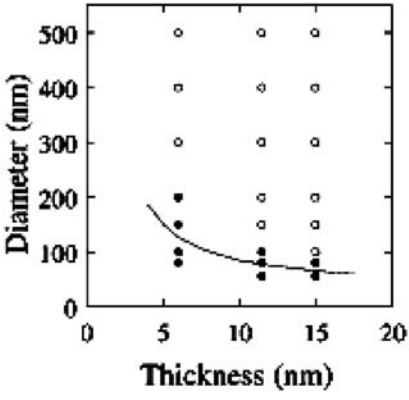

Fig. 7.30. Vortex phase diagram for patterned Supermalloy disks. Solid dots represent the vortex-free state and open circles the vortex state (Data from [7.52])

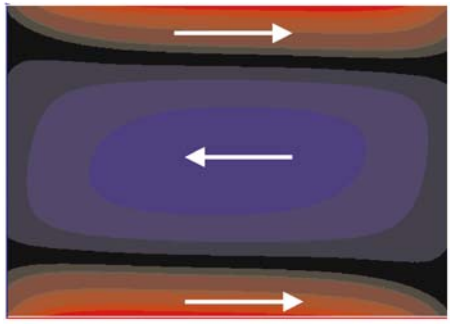

Fig. 7.31. Simulated edge-pinned state in a 5 nm thick 0.9 µm×1.2 µm NiFe element.

element produces a stronger longitudinal demagnetizing field, $\boldsymbol{H}_{\mathrm{d}}$. By definition, this demagnetizing field is anti-parallel to the magnetization inside the element. Immediately above and below the element, the tangential component of the field must be continuous; therefore, it is also anti-parallel to the layer magnetization and its strength increases in small aspect-ratio elements. In a sandwich structure used in MRAM, this demagnetizing field acting on the other layer can be so strong

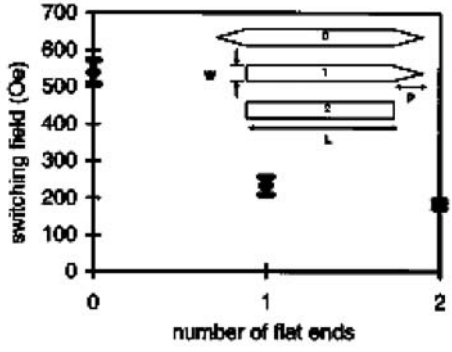

Fig. 7.32. Effect of sharp features on switching field. The width of all elements is 200 nm (Data from [7.51]).

that it always keeps the magnetization of the other layer anti-parallel to its own magnetization. Likewise, the other layer's demagnetizing field also reinforces this anti-parallel coupling. Hence the stable remanent configuration of small aspect-ratio elements tends to be the anti-parallel state (Figs. 7.33 and 7.34) [7.61]. This puts a shift in the free-layer hysteresis loop. If the demagnetizing field is larger than the coercive field of the thin layer, the free-layer loop is completely off center, causing a loss of the other memory state. In PSV devices where both magnetic layers are required to switch, the magnetostatic coupling further increases the switching field of the thick layer. This demagnetizing field varies approximately with $1/(\text{length})^2$ for a fixed element width [7.61]. To minimize this magnetostatic bias on the free layer, a pair of antiferromagnetically coupled layers such as Co/Ru/Co can be used. In the Co/Ru/Co sandwich, flux is almost closed between the two Co-layers; therefore, the bias on the free layer can be effectively reduced.

7.7.2 Interlayer Néel Coupling Due to Interfacial Charges

In increasingly small MTJ MRAM devices, a thinner oxide layer has to be used to reduce the tunneling resistance (for small RC constant). Due to the unavoidable interfacial roughness, the Néel coupling or orange-peel coupling between the two magnetic layers increases drastically. This coupling favors a parallel alignment between the two layers as schematically shown below. In a simple analysis [7.62], the coupling strength, H_{cpl}, is related to the amplitude and wavelength of the interfacial roughness (7.1). This analysis can be extended to a more complex situation involving many layers in MTJ stacks [7.63]. For a thin free-layer with a thin oxide layer, this coupling can also put the hysteresis loop completely off center.

$$H_{\text{cpl}} = \left(\frac{\pi^2 h^2 M_P}{\sqrt{2}\lambda \cdot t_F}\right) \cdot \exp\left(-2\pi\sqrt{2} \cdot t_s/\lambda\right) \tag{7.12}$$

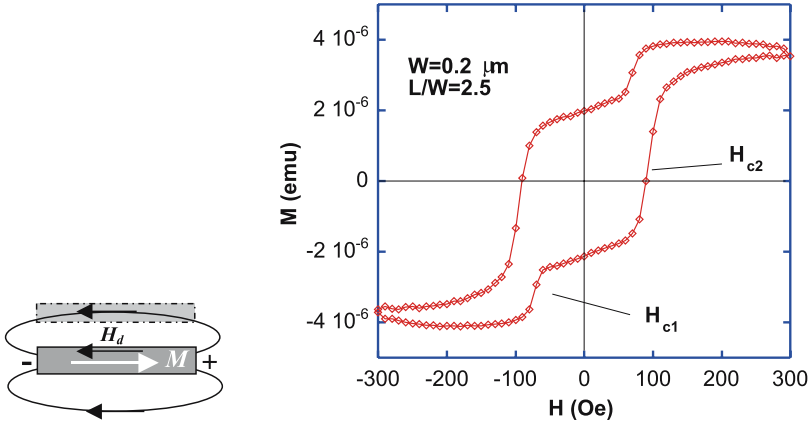

Fig. 7.33. Hysteresis loop of a patterned PSV element array (4 nm NiFeCo/4 nm Cu/6 nm NiFeCo). The remanent state is an anti-parallel state. When the field sweeps to the positive direction, the thin layer switches at a negative field

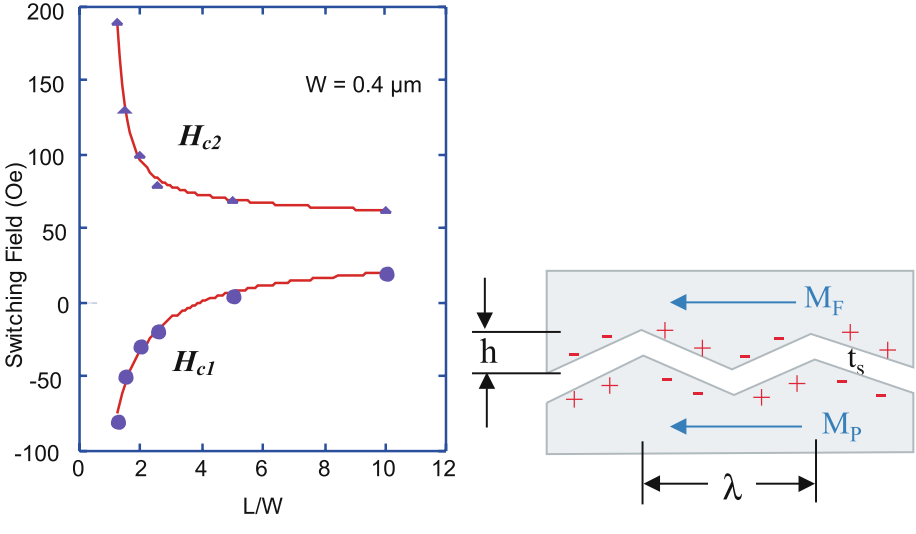

Fig. 7.34. Switching fields of two layers in 0.4 μm wide elements as a function of element aspect ratio. The thin layer switching field, H_{c1}, crosses zero at about $L/W = 4$

7.7.3 Inter-element Magnetostatic Interaction

At current DRAM density, each cell occupies $8F^2$, which means that the center-to-center separation is less than $3F$, and the nearest edge-to-edge separation is less than $2F$. As discussed in Sec. 7.3, the DRAM cell area factor also decreases in addition to the decrease in F itself. High-density MRAM demands a smaller cell size in future generations. This means that the inter-element distance will scale more rapidly

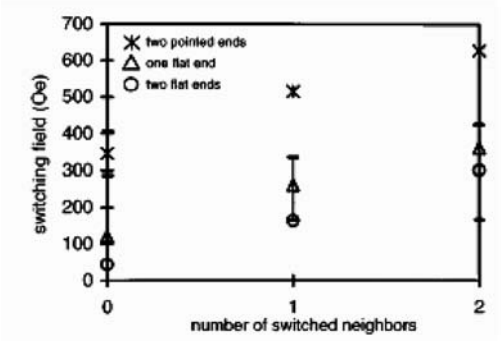

Fig. 7.35. Effect of switched neighbors on switching field of a chosen element in a linear chain of 26 nm thick, 200 nm wide and 3.5 μm long Co elements placed 50 nm (edge-to-edge) apart from each other. Different symbols represent different element shapes. As the neighboring elements switch, the demagnetizing field acting on the element pushes its switching field higher. This coupling field is quite strong (∼150 Oe) in this geometry (Data from [7.45])

than $2F$. A rough point-dipole estimation for a constant cell area factor suggests a $\mu/r^3 \propto F^2/F^3 = 1/F$ dependence of the inter-element coupling field strength. But the switching field itself also approximately follows $1/F$ (7.7). Therefore, the shrink in minimum feature size does not imply an increase in the inter-element coupling relative to the switching field. In practice, the inter-element coupling field also depends on the detailed shape and geometry of the elements as well as the inter-element spacing [7.51, 53, 64, 65]. However, more detailed micromagnetic analyses as well as systematic experiments are needed to further understand the effect of the coupling on both the switching field and switching mode in high-density MRAM.

7.7.4 Switching Field Distribution

Let us assume the distribution of the switching field in a 2D MRAM array is a Gaussian around the center $\langle H_c \rangle$ with a standard distribution σ. Upon the application of a half-select hard-axis field, $\langle H_c \rangle / 2^{1.5}$, the Gaussian center shifts approximately to $\langle H_c \rangle / 2^{1.5}$ according to the SW theory, if the starting distribution is narrow. (If the initial distribution is broad, the distribution is no longer a Gaussian when a hard-axis field is applied because of the non-linear nature of the SW astroid). In the meantime, the standard deviation is decreased by a factor of $2^{0.25}$. We can ignore this change in width. The two Gaussians must be separated from each other with a large enough distance to ensure that the bits are selectable. For example, if 6σ of the Gaussian distribution is selectable (10^{-6} error rate), the distribution should be so narrow that $6\sigma\langle(1-2^{-1.5})\rangle\langle H_c\rangle$, i.e. $2\sigma/\langle H_c\rangle < 0.2$. In submicron element arrays such as the one in Fig. 7.21, the switching astroid is far less steep than what the SW-model predicts, so the criterion for the switching distribution width must be more stringent.

In small magnetic elements approaching single-domain size, the magnetostatic energy is determined by the surface charges, $\sigma = \boldsymbol{M} \cdot \widehat{\boldsymbol{n}}$, which varies with the surface

roughness. The shape variation can be a source of broad switching field distribution among 10^6–10^9 elements. In addition, inter-element magnetostatic coupling can be another important source of broad distribution in high density MRAM.

7.7.5 Thermal Stability

The anisotropy barrier, $K_u V$, decreases sharply due to the rapid shrink in minimum feature size. For recording media [7.66], a 10 year data retention time requires $K_u V/k_B T \sim 40$. This ratio is found to be about 100 for 10 nm-thick 200 nm × 1000 nm NiFe elements [7.67], and between 100 to 200 for 7.9 nm-thick 1 μm-wide NiFe elements [7.68]. In smaller and thinner elements, this ratio will further decrease. Moreover, in half-selected bits, according to the SW-model, the energy barrier decreases as $(H_c - H)^2$. At $H = H_c/2^{1.5}$, the energy barrier is decreased to $(1 - 2^{-1.5})^2 = 0.4$ of the original value. At any given time of writing, for a MRAM chip with total number of memory bits of N, $1/\sqrt{N}$ of the total memory bits are under this half-select condition. In addition, the thermally activated magnetization reversal is closely related to the dynamic switching with ultra-fast pulses [7.69]. This issue also needs further systematic investigation.

In summary, high-density MRAM offers a very attractive potential for high-performance memory devices. Further advances in MRAM development call for better understanding of magnetization reversal of patterned magnetic nanostructures. In general, as the size of the MRAM elements approaches the single-domain size, the switching mechanism appears to be simpler. However, in many product generations to come, micromagnetics will still play a role in magnetic switching of MRAM devices. In addition, even for single-domain devices, there are many challenging issues ahead that demand a further understanding of nanomagnetism.

Acknowledgement. The author would like to thank S. Tehrani, W.J. Gallagher, J.M. Daughton, T. Zhu, J.-G. Zhu, J.N. Chapman, R.P. Cowburn, J.M. Slaughter, M. DeHerrea, W.C. Uhlig, and A. Arrott for their tremendous help in preparing this chapter.

References

7.1. B.D. Cullity, *Introduction to Magnetic Materials*, Addison-Wesley, 1972.
7.2. W. Renwick and A.J. Cole, *Digital Storage Systems*, Chapman & Hall Ltd, 1971.
7.3. B. Prince and G. Due-Gundersen, *Semiconductor Memories*, John Wiley & Sons Ltd. 1983.
7.4. B. Price, *Semiconductor Memories: A Handbook of Design, Manufacture, and Application* , Jonn Wiley & Sons Ltd., 1996.
7.5. J.F. Scott, *Ferroelectric Memories*, Springer-Verlag, 2000.
7.6. R.R. Katti and T. Zhu, *Attractive Magnetic Memories*, IEEE Circuits & Devices Magazine, **17**, 26 (2001).
7.7. S. Tehrani, Tunneling *Magnetoresistive Random Access Memory*, to appear in VLSI Symposium (June 2002).

7.8. S.A. Wolf, D.D. Awschalom, R.A. Buhrman, J.M. Daughton, S. von Molnár, M.L. Roukes, A.Y. Chtchelkanova, and D.M. Treger, *Spintronics: A Spin-Based Electronics Vision for the Future*, Science, **294**, 1488 (2001).
7.9. W. Reohr, H. Hönigschmid, R. Robertazzi, D. Gogl, F. Pesavento, S. Lammers, K. Lewis, C. Arndt, Y. Lu, H. Viehmann, R. Scheuerlein, L.-K. Wang, P. Trouilloud, S. Parkin, W. Gallagher, and G. Müller, *MTJ MRAM, A Magnetically Attractive RAM*, IEEE Circuits and Devices Magazine, July 2002 (to be published).
7.10. S. Chikazumi, *Physics of Ferromagnetism*, Clarendon Press (1997).
7.11. J. Kondo, *Anomalous Hall Effect and Magnetoresistance of Ferromagnetic Metals,* Progr. Theor. Phys. **27**, 772 (1962).
7.12. J.M. Daughton, *Magnetoresistive Memory Technology,* Thin Solid Films, **216**, 162 (1992).
7.13. A. Pohm, C. Comstock, and A. Hurst, *Quadrupled Non-Destructive Output from Memory Cells Using Reversed Word Fields*, J. Appl. Phys. **67**, 4881 (1990).
7.14. M.N. Baibich, J.M. Broto, A. Fert, F. Nguyen Van Dau, F. Petroff, P. Eitenne, G. Creuzet, A. Friederich, and J. Chazelas, *Giant Magnetoresistance of (100)Fe/(001)Cr Magnetic Superlattices*, Phys. Rev. Lett. **61**, 2472 (1988).
7.15. S.S.P. Parkin, Chapter 2.4, page 148, *Ultrathin Magnetic structures II*, ed. by B. Heinrich and J.A.C. Bland.
7.16. W.F. Egelhoff, Jr., P.J. Chen, C.J. Powell, M.D. Stiles, R.D. McMichael, C.-L. Lin, J.M. Siertsen, J.H. Judy, K. Takano, A.E. Berkowitz, T.C. Anthony, and J.A. Brug, *Optimizing the Giant Magnetoresistance of Symmetric and Bottom Spin-Valves*, J. Appl. Phys. **79**, 5277 (1996).
7.17. D.D. Tang, P.K. Wang, V.S. Speriosu, S. Le, R.E. Fontana, and S. Rishton, *An IC Process Compatible Nonvolatile Magnetic RAM*, IEDM Tech. Digest. New York: IEEE, 1995, pp. 997–1000.
7.18. S. Tehrani, E. Chen, M. Durlam, T. Zhu, and H. Goronkin, *High Density Nonvolatile Magnetoresistive RAM*, IEDM Tech. Digest, 193 (1996).
7.19. S. Tehrani, J.M. Slaughter, E. Chen, M. Durlam, J. Shi, and M. DeHerrera, *Progress and Outlook for MRAM Technology*, IEEE Trans. Magn. **35**, 2814 (1999).
7.20. S. Tehrani, E. Chen, M. Durlam, M. DeHerrera, J.M. Slaughter, J. Shi, and G. Kerszykowski, *High Density Submicron Magnetoresistive Random Access Memory*, J. Appl. Phys. **85**, 5822 (1999).
7.21. J.M. Daughton, *Magnetic Tunneling Applied to Memory*, J. Appl. Phys. **81**, 3758 (1997).
7.22. T. Miyazaki and N. Tezuka, *Giant Magnetic Tunneling Effect in Fe/Al_2O_3/Fe Junction*, J. Magn. Magn. Mater. **139**, L231 (1995).
7.23. R.C. Sousa, J.J. Sun, V. Soares, P.P. Frestaa, A. Kling, M.F. da Silva, and J.C. Soares, *Large Tunneling Magnetoresistance Enhancement by Thermal Annel*, Appl. Rev. Lett. **73**, 3288 (1998).
7.24. J.S. Moodera, L.R. Kinder, T.M. Wong, and R. Meservey, *Large Magnetoresistance at Room Temperature in Ferromagnetic Thin Film Tunnel Junctions*, Phys. Rev. Lett. **74**, 3272 (1995).
7.25. W.J. Gallagher, S.S.P. Parkin, Y. Lu, X.P. Bian, A. Marley, R.A. Altman, S.A. Rishton, K.P. Roche, C. Jahnes, T.M. Shaw, and G. Xiao, *Microstructured Magnetic Tunnel Junctions*, J. Appl. Phys. **81**, 3741 (1997).
7.26. J.G. Simmons, *Generalized Formula for the Electric Tunnel Effect between Similar Electrodes Separated by a Thin Insulating Film,* J. Appl. Phys. **34**, 1793 (1963).
7.27. M. Julliere, *Tunneling between Ferromagnetic Films*, Phys. Lett. **54A**, 225 (1975).

7.28. S. Tehrani, B. Engel, J.M. Slaughter, E. Chen, M. DeHerrera, M. Durlam, P. Naji, R. Whig, J. Janesky, and J. Calder, *Recent Development in Magnetic Tunnel Junction MRAM*, IEEE Trans. Magn. **36**, 2752 (2000).
7.29. J.-G. Zhu, Y.F. Zheng, and G.A. Prinz, *Ultrahigh Density Vertical Magnetoresistive Random Access Memory*, J. Appl. Phys. **87**, 6668 (2000).
7.30. M. Johnson, B. Bennett, and M. Yang, *Hybrid Ferromagnetic Semiconductor Nonvolatile Memory*, IEEE Trans. Magn. **34**, 1054 (1998).
7.31. B. Heinrich, *Magnetic Nanostructures: from Physical Principles to Spintronics*, Canadian J. Phys. **78**, 161 (2000).
7.32. Available on ITRS website: http://public.itrs.net/Files/2001ITRS/Home.htm.
7.33. A.H. Eschenfelder, *Magnetic Bubble Technology*, Springer-Verlag, 1981.
7.34. C. Kittel, *Physical Theory of Ferromagnetic Domains,* Rev. Mod. Phys. **21**, 541 (1949).
7.35. A. Hubert and R. Schäfer, *Magnetic Domains,* Springer-Verlag, 2000.
7.36. E.C. Stoner and E.P. Wohlfarth, *A Mechanism of Magnetic Hysteresis in Heterogeneous Alloys*, Phil. Trans. Roy. Soc. A**240**, 599 (1948).
7.37. M. Lederman, S. Schultz, and M. Ozaki, *Measurement of the Dynamics of the Magnetization Reversal in Individual Single-Domain Ferromagnetic Particles*, Phys. Rev. Lett. **73**, 1986 (1994).
7.38. W. Wernsdofer, B. Doudin, D. Mailly, K. Hasselbach, A. Benoit, J. Meier, J.-Ph. Ansermet, and B. Barbara, *Nucleation of Magnetization Reversal in Individual Nanosized Nickel Wires*, Phys. Rev. Lett. **77**, 1873 (1996).
7.39. For example, A.H. Morrish, *The Physical Principles of Magnetism, IEEE Press, 2001.*
7.40. J.A. Osborn, *Demagnetizing Factors of the General Ellipsoid*, Phys. Rev. **67**, 351 (1945).
7.41. J.C. Slonczewski, *Theory of Magnetic Hysteresis in Films and Its Application to Computers,* Research Report RM 003.111.224 (IBM Corp., 1956).
7.42. J. Shi, T. Zhu, M. Durlam, E. Chen, S. Tehrani, Y.F. Zheng, and J.-G. Zhu, *End Domain States and Magnetization Reversal in Submicron Magnetic Structures*, IEEE Trans. Magn. 34, 997 (1998).
7.43. R.P. Cowburn, *Property Variation with Shape in Magnetic Nanoelements*, J. Phys. D, **33**, R1 (2000).
7.44. W.F. Brown, Jr., *Micromagnetics*, Wiley, 1963.
7.45. A. Aharoni, *Introduction to the Theory of Ferromagnetism*, Clarenton Press, 1996.
7.46. J. Shi and S. Tehrani, *Edge-Pinned States in Patterned Submicron NiFeCo Structures*, Appl. Phys. Lett. **77**, 1692 (2000).
7.47. K.J. Kirk, M.R. Scheinfein, J.N. Chapman, S. McVitie, M.F. Gillies, B.R. Ward and J.G. Tennant, *Role of Vortices in Magnetization Reversal of RectangularElements*, J. Phys. D., **34**, 160 (2001).
7.48. J. Shi, S. Tehrani, M.R. Scheinfein, *Geometry Dependence of Magnetization Vortices in Patterned Magnetic Elements*, Appl. Phys. Lett. **76**, 2588 (2000).
7.49. J. Shi, T. Zhu, S. Tehrani, Y.F. Zheng and J.-G. Zhu, *Switching Anomaly and Magnetization Vortices of 200 A Thick NiFeCo Elements in One-Micron Patterned Arrays,* J. Magn. Magn. Mat. **198–199**, 251 (1999).
7.50. J. Shi, S. Tehrani, T. Zhu, Y.F. Zheng and J.-G. Zhu, *Magnetization Vortices and Anomalous Switching in Patterned Submicron Structures*, Appl. Phys. Lett. **74**, 2525 (1999).
7.51. K.J. Kirk, J.N. Chapman, and C.D.W. Wilkinson, *Switching Fields and Magnetostatic Interactions of Thin Film Magnetic Nanoelements*, Appl. Phys. Lett. **71**, 539 (1997).
7.52. R.P. Cowburn, D.K. Koltsov, A.O. Adeyeye, M.E. Welland, D.M. Tricker, *Single-Domain Circular Nanomagnets*, Phys. Rev. Lett. **83**, 1042 (1999).

7.53. R.E. Dddunin-Borkowski, M.R. MaCartney, B. Kardynal, D.J. Smith, M.R. Scheinfein, *Switching Asymmetries in Closely Coupled Magnetic Nanostructure Arrays,* Appl. Phys. Lett.**75**, 2641(1999).
7.54. E. Girgis, J. Schelten, J. Shi, J. Janesky, S. Tehrani, and H. Goronkin, *Switching Characteristics and Magnetization Vortices of Thin-Film Cobalt in Nanometer-Scale Patterned Arrays,* Appl. Phys. Lett. **76**, 3780 (2000).
7.55. T. Shinjo, T. Okuno, R. Hassdorf, K. Shigeto, and T. Ono, *Magnetic Vortex Core Observation in Circular Dots of Permalloy*, Science, **289**, 930 (2000).
7.56. LLG Micromagnetics Simulator is a commercial micromagnetic program. http://llgmicro.home.mindspring.com/.
7.57. A.F. Popkov, L.L. Savchenko, N.V. Vorotnikova, S. Tehrani, and J. Shi, *Edge Pinning Effect in Single- and Three-Layer Patterns*, Appl. Phys. Lett. **77**, 277 (2000).
7.58. T.-N. Fang and J.-G. Zhu, *Switching Fluctuations and Density Limitation of Pseudospin Valve Memory*, J. Appl. Phys. 87, 7061(2000).
7.59. J. Shi, T. Zhu, S. Tehrani, *MRAM with Aligned Magnetic Vectors,* U.S. Patent No. 5,757,695 (1997).
7.60. A. Arrott (private communication).
7.61. T. Zhu, J. Shi, S. Tehrani, M. Durlam and E. Chen, *Switching Characteristics of Submicron Dimension Permalloy Sandwich Films*, IEEE Trans. Magn. **33**, 3601 (1997).
7.62. J. Zhang and R.M. White, *Topological Coupling in Spin Valve Type Mulitlayers*, IEEE Trans. Mang. **32**, 4630 (1996).
7.63. J.M. Slaughter (private communication).
7.64. J. Janesky, N.D. Rizzo, L. Savtchenko, B. Engel, J.M. Slaughter, and S. Tehrani, *Magnetostatic Interactions between Sub-Micrometer Patterned Magnetic Elements,* IEEE Trans. Magn. **37**, 2052 (2001).
7.65. M.C. Abraham, H. Schmidt, T.A. Savas, H.I. Smith, C.A. Ross, and R.J. Ram, *Magnetic Properties and Interactions of Single-Domain Nanomagnets in a Periodic Array*, J. Appl. Phys. 89, 5667 (2001).
7.66. D. Weller and A. Moser, *Thermal Effect Limits in Ultrahigh-Density Magnetic Recording*, IEEE Trans. Magn. 35, 4423 (1999).
7.67. J. Li and S. Tehrani and J. Shi, *Temperature-Dependent Switching Properties in Patterned 200nm NiFe Structures*, Appl. Phys. Lett. **79**, 3821 (2001).
7.68. H.Q. Yin and W.D. Doyle, *Thermal Relaxation of Soft Magnetic Patterned Elements*, to appear in J. Appl. Phys. (2002).
7.69. R.H. Koch, G. Grinstein, G.A. Keefe, Yu Lu, P.L. Trouilloud, W.J. Gallagher, and S.S.P. Parkin, *Thermally Assisted Magnetization Reversal in Submicron-Sized Magnetic Thin Films,* Phys. Rev. Lett. 84, 5419 (2000).

8

Giant Magneto-resistive Random-Access Memories Based on Current-in-Plane Devices

R.R. Katti

8.1 Introduction

A Giant Magneto-resistive Random-Access Memory (GMRAM) is a nonvolatile memory consisting of magnetic memory devices integrated with semiconductor electronics. In GMRAMs, magnetic multi-layer devices that exhibit the giant magneto-resistance (GMR) effect, such as "pseudo-spin-valve" (PSV) and "spin-valve" (SV) devices, are used to store information and to allow the data to be read. PSV and SV devices are current-in-plane (CIP) devices that have served as precursors to more recently developed and higher signal memory devices such as current-perpendicular-to-plane (CPP) magnetic tunnel junction (MTJ) devices. In this chapter, GMR CIP magnetic device operation and characteristics are described that have supported the demonstration of GMRAMs that have passed nonvolatile data retention tests and complex write and read memory pattern tests at write and read cycle times down to approximately 50 nanoseconds. Write and read characteristics of CIP PSV devices are described in terms of write switching, read switching, resistive, and magnetoresistive properties based on individual and statistical ensembles of PSV devices fabricated on bulk Si as well as CMOS (Complementary metal-oxide-semiconductor) underlayer wafers. Based on experimental work and modeling, magnetization reversal has been inferred to be rotational, including irreversible rotations that correspond to switching, reversible rotations that anticipate switching, and reversible rotations that complete reversal from switching to saturation in the opposite direction. Magneto-resistive and magnetic switching properties along with nonvolatility, nondestructive readout, and potentially unlimited cyclability make PSV and SV devices potential options as nonvolatile memory elements for GMRAMs.

The need at this time exists for an ideal nonvolatile memory, in which data are retained even in the absence of supplied power with unlimited write and read cycling, high memory density and capacity, fast cycle times, and low power consumption. A Giant Magneto-resistive Random-Access Memory (GMRAM) is one potential candidate for such an application. A GMRAM uses magnetic multi-layers that exhibit

the giant magneto-resistive (GMR) effect to store data and to read data [8.1–12]. GMR pseudo-spin-valve (PSV) devices and spin-valve (SV) devices are magnetic multi-layers that exhibit the GMR effect. GMRAMs to date have been demonstrated [8.1, 21] that have passed complex memory write and read pattern tests using PSV devices that are described in this chapter. In current-in-plane (CIP) GMR devices the GMR effect that is used is based on in-plane current flow, and currents flow primarily in the plane of the device. In magnetic multi-layers such as magnetic tunnel junctions and stacked magnetic multi-layers, currents flow in a direction primarily perpendicular to the plane of the material (i.e., current perpendicular to plane, or CPP). The GMR effect [8.23] is the pronounced and reversible increase in electrical resistance that occurs in a magnetic multi-layer when the relative direction of magnetization between layers changes from parallel to anti-parallel. Advances in deposition techniques have made it possible to deposit multi-layer metallic films uniformly, in which individual layers are typically up to a few nanometers thick. The GMR effect offers signals that are two to twenty times those produced by the Anisotropic Magneto-resistance (AMR) effect demonstrated in early magnetic random access memories. This emphasis of this article is to describe the operating principles of PSV and SV devices as CIP devices that could be applied to GMRAMs, particularly for the 1R0T (one resistor, zero transistor) cell architecture.

The general attributes of GMRAMs as a nonvolatile random access memory are:

- Nonvolatility (Power is not needed to retain data.)
- No material fatigue mechanisms (potentially unlimited write and read cyclability)
- Nondestructive read
- Reasonably fast write times (less than 50 ns, depending on design)
- Reasonably fast read times (less than 50 ns, depending on design)
- Low write energy.

GMRAMs have been demonstrated [8.21] that support nonvolatile information storage, show nondestructive read-out, have write and read cycle times down to approximately 50 ns, and have passed complex memory pattern tests that require correct write operability, read operability, and immunity from bit disturb effects during both write and read operations. Given the GMRAM attributes demonstrated to date, GMRAMs have the potential to support nonvolatile memory applications, in particular for aerospace applications [8.20–22]. GMRAM technology also has the potential to support embedded chip technology and integrated systems-on-a-chip applications. GMRAMs potentially offer the speed and unlimited cycling of volatile Static Random Access Memories (SRAMs) and Dynamic Random Access Memories (DRAMs) along with the nonvolatility of EEPROM (electronically erasable programmable read-only memory) , Flash, and other nonvolatile memories. GMRAM technology has been under development, in particular for aerospace applications. Shown in Fig. 8.1 is a micrograph of a top view of a GMRAM stand-alone memory chip. GMRAMs result from integrating GMR devices with semiconducting devices. Figure 8.2 shows a cross-section of a GMRAM chip. As shown in Fig. 8.2, magnetic devices are integrated with metallization, dielectrics, and support electronics on silicon to duplicate the functions of static semiconductor random-access memory (RAM) chips.

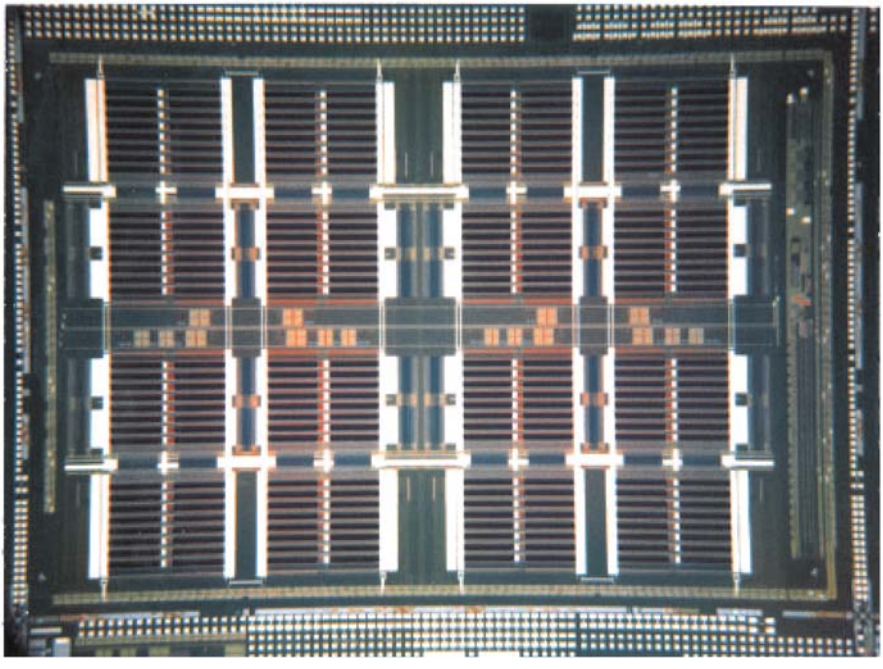

Fig. 8.1. Top-view of a GMRAM chip

The magnetic storage and sense layers in PSV devices are formed by depositing nanometer-thick magnetic and metallic materials including Ni, Fe, Co, and Cu. SV devices include similar layers in the magnetic multi-layer and also include an anti-ferromagnetic layer. Magnetic bits are connected to a sense line to allow selecting and reading bits. Magnetic bits are placed in proximity to a word line to allow selecting, writing, and reading bits. A digit line is placed in proximity to the magnetic bit and parallel to the sense line to help select bits. Because of the magnetic properties of magnetic multi-layers, magnetic storage devices are inherently immune to radiation effects. When coupled with radiation-immune under-layer circuits such as silicon-on-insulator (SOI) CMOS electronics, GMRAMs are also immune to radiation effects. Such GMRAMs are of interest for aerospace nonvolatile memory applications.

In integrated magnetics-on-semiconductor memories, magnetic devices need to provide satisfactory levels of write and read performance. In this work, write and read characteristics of pseudo-spin-valve (PSV) devices, which are current-in-plane devices constructed from patterned magnetic multilayers that exhibit the Giant Magnetoresistive (GMR) effect, are investigated as magnetic devices that can be applied to a magnetics-on-semiconductor memory. Magnetic switching and magneto-resistive properties are used to characterize key PSV device read and write characteristics that are important to a GMRAM.

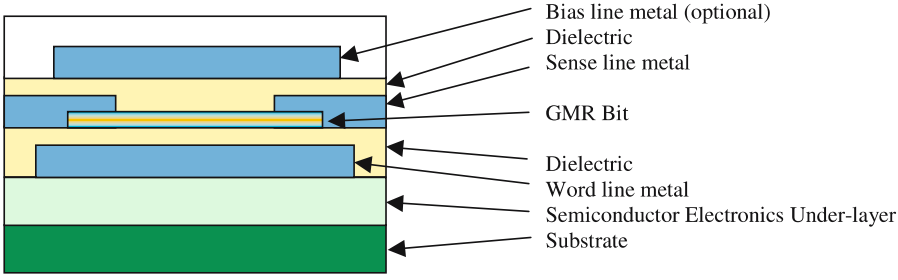

Fig. 8.2. Schematic cross-section of a GMRAM chip

8.2 Magnetic Pseudo-Spin-Valve Device Switching Characteristics, Modeling, and Distributions

In this section, the characteristics of a PSV device for GMRAM applications will be described. Spin valve (SV) devices will be described briefly in a subsequent section. It is noted that SV devices also have widespread application in magnetic recording heads used in magnetic disk drives and also are being evaluated as memory elements in magnetic tunnel junction devices. Even though the name "spin valve" appears more concise than the name "pseudo-spin-valve", the structure of a PSV device is perhaps simpler to describe initially. Both PSV and SV devices have magneto-resistive properties that depend on the relative orientation of magnetization between magnetic layers in their magnetic multi-layers. The resistance properties in PSV and SV devices are a consequence of how the spin of electrons affects the scattering properties of the electrons in such magnetic multi-layers.

The GMR effect [8.23] is the change in resistance in a magnetic multi-layer that occurs with a change in the relative directions of magnetization between layers [8.23]. The dependence of the GMR effect is approximated by:

$$R_{\text{tot}} = R_{\text{min}} + \Delta R_{\text{gmr}} \sin^2 (|0.5\theta|) \tag{8.1}$$

where R_{tot} is the total electrical resistance, R_{min} is the minimum electrical resistance, ΔR_{gmr} is the incremental GMR resistance, and θ, which varies between π and $-\pi$ radians, is the angle between the magnetization directions in the storage and sensing layers. Typical values of R_{tot} are measured in the tens of ohms. The parameter $\Delta R_{\text{gmr}}/R_{\text{min}}$ is a figure of merit called the GMR coefficient, which, at present, can range from a few per cent to greater than 50%.

The GMR effect can be compared to the AMR effect used in early magnetic random access memory technology. The dependence of the AMR effect is given by:

$$R_{\text{tot}} = R_{\text{min}} + \Delta R_{\text{amr}} \cos^2 (\varphi) \tag{8.2}$$

where R_{tot} is the total electrical resistance, R_{min} is the minimum electrical resistance, ΔR_{amr} is the incremental AMR resistance, and φ is the angle between the current flow direction and magnetization direction in the material. The parameter $\Delta R_{\text{amr}}/R_{\text{min}}$ is

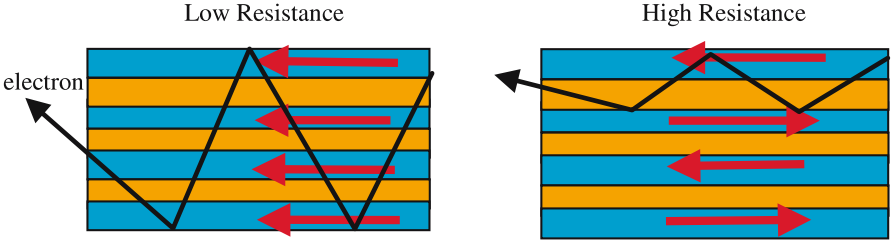

Fig. 8.3. Schematic depictions of spin-dependent scattering in a magnetic multi-layer film. Scattering is shown for parallel and anti-parallel arrangements of magnetization. Propagation of a single spin carrier is shown

a figure of merit called the AMR coefficient, which, at present, can typically range up to 5%. The fact that the magnitude of ΔR_{gmr} is greater than ΔR_{amr} allows read signals from GMR elements to be greater than read signals from AMR elements. This increase in signal is ultimately expected to lead to increases in read speed and reliability and to reductions in power consumption.

The GMR effect is caused by spin-dependent scattering of electrons. As shown in Fig. 8.3a, electron scattering is reduced when the magnetization directions between the storage and sensing layers are parallel. This phenomenon corresponds to an increase in the mean free path of electrons. Since magnetization is oriented in one direction, spin-polarized electrons of one polarity will scatter less than the other polarity. As shown in Fig. 8.3b, electron scattering is then enhanced in a PSV device when the magnetization directions between the storage and sensing layers are anti-parallel. Anti-parallel magnetization increases electrical resistance because of the increased tendency to scatter both polarities of spin-polarized electrons. This phenomenon corresponds to a decrease in the mean free path of electrons. Such scattering can also be viewed as a channeling of electrons within the magnetic multi-layer. Scattering is a consequence of the interfaces as well as the "bulk" regions of the magnetic and non-magnetic layers of magnetic multi-layers, in particular in such structures with nano-scale thicknesses.

Figure 8.4 shows a schematic cross-section of a PSV device. As illustrated, the three essential components of a PSV device are the storage layer, sensing layer, and spacer layer that separates the storage and sensing layers. At present, typical thicknesses of layers in PSV devices are up to several nanometers. In the absence of applied magnetic fields, the magnetization in the magnetic layers of a PSV device is typically uni-axial, or bi-directional. In other words, the magnetization tends to align and to be stable along the magnetic axis, or "easy axis", either parallel or anti-parallel to the axis direction. Binary data are held in the storage layer using the directionality of the magnetization. Magnetizing the storage layer in one direction, along the easy axis, stores, say, a "1". Magnetizing the storage layer in the opposite direction along the easy axis then stores a "0". The magnetization directions for storing binary data in the storage layer are also shown. The storage layer is typically composed of combinations of Ni, Fe, and Co, which are ferromagnetic metal elements.

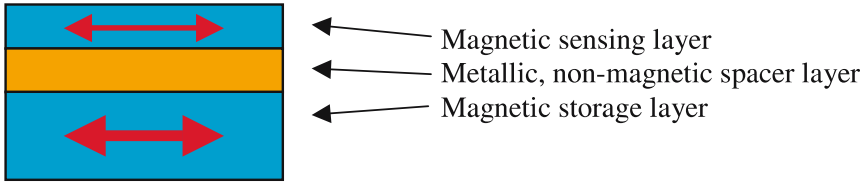

Fig. 8.4. Schematic cross-section of a magnetic pseudo-spin-valve (PSV) device, showing uniaxial orientations of the storage and sensing layers

Also shown in Fig. 8.4 is the sensing layer. The sensing layer, like the storage layer, is also uni-axial, so that its magnetization can align with stability along one direction or the opposite direction. The sensing layer is also typically composed of combinations of Ni, Fe, and Co. A metallic, nonmagnetic spacer, such as Cu, is placed between the storage and sensing layers to allow the two layers to be switched independently and to support the Giant Magneto-resistance (GMR) effect.

Two test systems were used in this work to characterize PSV and SV device performance. First, for measuring electrical magnetoresistive properties, a Magneto-Resistance Wafer (MRW) test system was used to measure resistive, magneto-resistive, and switching characteristics of PSV devices as a function of applied fields and currents using the GMR effect. An in-plane applied magnetic field (H_w) was swept in the easy-axis direction of the PSV device, which is parallel to the major axis and parallel to the word field direction. The desired sense current, I_s, and in-plane hard-axis bias field (H_d, which is perpendicular to H_w) were also applied. The GMR curves allowed extracting the minimum PSV device resistance (R_{min}), PSV device change-in-resistance (dR, where dR is given by the difference between the maximum resistance and the minimum resistance of a PSV device), switching fields of the storage layer in the forward (H_f) and reverse (H_r) easy-axis, i.e., word field, directions. Mean values for R_{min}, dR, H_f, and H_r for specific write and read cases were extracted after cycling each PSV device ten times and measuring PSV devices across the wafer.

Second, an Alternating Gradient Magnetometer (AGM) was used to measure magnetic switching and magnetic hysteresis properties. An AGM measures magnetic moment of the sample as a function of applied field. An AGM therefore allows measuring switching fields and switching field distributions of the devices under test. Magnetic multi-layer films were deposited and test chips were fabricated, as described above, containing arrays of between one million and two million PSV devices. A swept easy-axis field was applied to measure magnetic moment as a function of applied easy-axis field. The switching characteristics of the ensemble of PSV devices was measured with and without a hard-axis bias field, corresponding to selected and unselected device cases. Because the hysteresis loops can be traversed and compared to minor loops that are characterized separately, regions where switching has been completed can be identified within experimental accuracy and necessary conditions on switching windows can be inferred.

Measurements were conducted at laboratory (room) temperature, which was approximately 25 °C. Experimental uncertainty for switching field values is approxi-

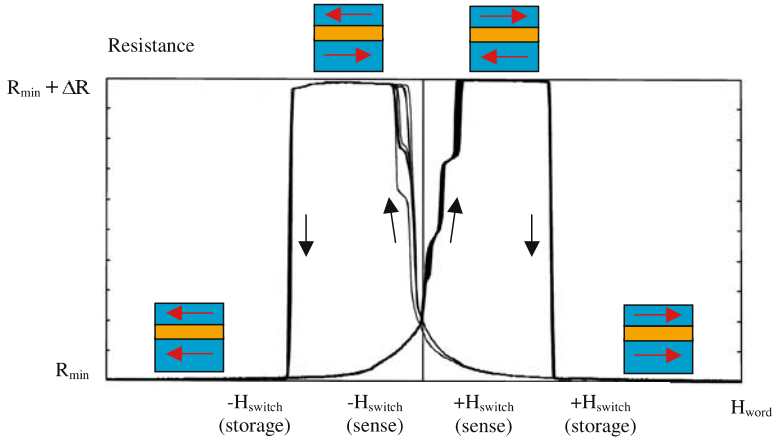

Fig. 8.5. Magneto-resistance characteristics of a PSV device on bulk Si, showing the GMR effect. Directions of magnetization are shown for the storage and sensing layers

mately 2 Oe. Experimental uncertainty for resistance and change-in-resistance values is approximately 1%.

Shown in Fig. 8.5 are magnetoresistive characteristics of a PSV device deposited on a bulk Si wafer. Switching characteristics and magnetic states are shown for the storage and sensing layers. When the sensing layer is magnetized parallel to the storage layer, the electrical resistance of the PSV device is minimized. When the sensing layer is magnetized in a direction opposite, or anti-parallel, to the storage layer, the electrical resistance of the PSV device is maximized. Because the storage layer switches at magnetic fields higher in magnitude than the switching fields for the sensing layer, the sensing layer can be used to determine the direction of magnetization, and hence data state, of the storage layer. The sensing layer can be switched reversibly, without changing the magnetization of the storage layer. As shown in Fig. 8.5, while switching is generally repeatable, a degree of variability in the switching curves is apparent. This variability is associated with slight but measurable deviations in the magnetization reversal process as a function of applied field. This variability will be interpreted further in the micromagnetic modeling discussion.

Figures 8.6a and 8.6b show the dependences, from a PSV device deposited on a bulk Si wafer, of electrical resistance on the magnetization direction of the sense layer for two directions of magnetization for the storage layer. The state of the storage layer can be determined by sampling the resistance for the two sensing layer magnetization states and noting the polarity of the change in resistance relative to the change in magnetization of the thin layer. In this manner, binary “1’s” and “0’s”, for example, can be read. The state of information, held in storage and sensing layers in PSV devices, is retained even when currents and magnetic fields are removed and restored.

Shown in Figs. 8.7–8.9, and 8.10, are results of micromagnetic simulations based on a three-dimensional Landau-Lifshitz-Gilbert solver [8.13] as applied to discretized

Table 8.1. Parameter values used in three-dimensional micromagnetic simulations based on the Landau-Lifschitz-Gilbert equation. $H_{s,eff}$ is the effective magnetic field induced by the sense current

Figure Number	$H_d/H_{w,uns}$	$H_{s,eff}/H_{w,uns}$
7	0	0.01
8	0.5	0.1
9	1	0.1
10	1.5	0.1

PSV devices. Simulated magnetic hysteresis loops are shown in Figs. 8.7a, 8.8a, 8.9a and 8.10a, and corresponding simulated magnetoresistive curves are shown in Figs. 8.7b, 8.8b, 8.9b and 8.10b, each as a function of applied magnetic field in the word direction. The magnetic field conditions used in the micromagnetic simulations are shown in Table 8.1.

Shown in Figs. 8.11a–d are experimental magnetoresistance curves corresponding to the simulated curves shown in Figs. 8.7b, 8.8b, 8.9b, and 8.10b. Similarities are observed of the shapes and features of the experimental and simulated curves. This observed correlation supports using micromagnetic modeling to make inferences about the magnetization reversal process in PSV devices. As the net bias is increased in Figs. 8.7–8.10, greater degrees of rotation are observed. This general increase in rotational effects is qualitatively in agreement with greater amounts of rotation observed in experimental data. Note that write selectivity is observed and read selectivity is apparent in the figures. Write selectivity increases as net bias is increased. Moment parallel to the easy axis decreases as bias is increased, which corresponds to the reduction in maximum change in angle that is observed because of the bias field. This same effect reduces the maximum change in resistance (dR) that is observed in the magneto-resistance curves.

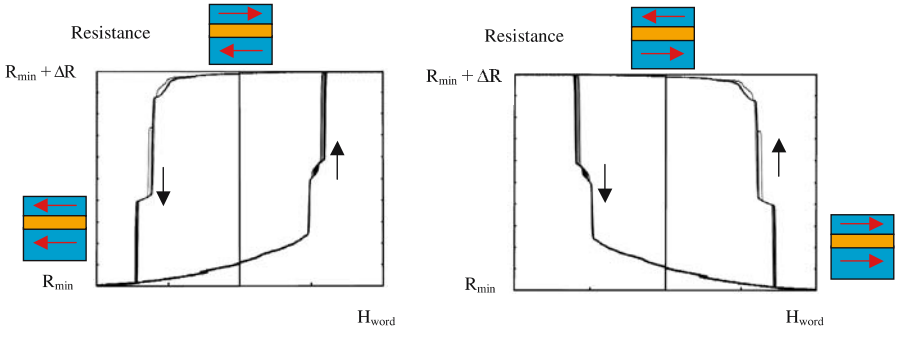

Fig. 8.6. Read characteristics of a PSV device on bulk Si as a consequence of reversible switching of the sensing layer, shown for two orientations of the storage layer

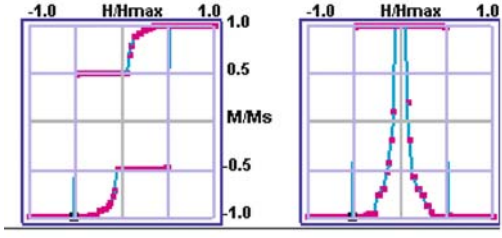

Fig. 8.7. Modeled unselected write condition curves at $H_d = 0$, showing (**a**) magnetization and (**b**) magneto-resistance

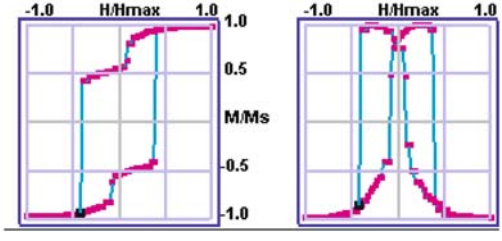

Fig. 8.8. Modeled selected write condition curves at $H_d = 0.5 \times H_{\mathrm{w,wruns}}$, showing (**a**) magnetization and (**b**) magneto-resistance

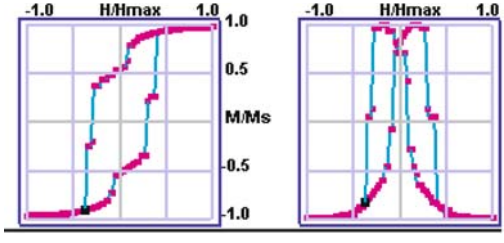

Fig. 8.9. Modeled selected write condition curves at $H_d = 1.0 \times H_{\mathrm{w,wruns}}$, showing (**a**) magnetization and (**b**) magneto-resistance

As shown in Figs. 8.11a–d, as the hard-axis magnetic field is increased, the easy-axis switching field decreases. This characteristic allows the hard-axis field to provide a bias to reduce the easy-axis switching field. This feature has implications regarding applications to memory architectures. A device in a memory array can be "selected", i.e. addressed, by using hard-axis field in conjunction with an easy-axis field. If a hard-axis field is applied to a specific device or to a row of devices, then the easy-axis switching field is correspondingly reduced for that device or row of devices. An easy-axis field can therefore be applied to that device or to a column of devices so that the device that experiences both hard-axis and easy-axis fields switches and is therefore rewritten. All of the other devices in the memory array are unselected, i.e., not addressed, and will not switch and therefore will not be rewritten. The reason for this occurrence is that, uniquely, only the selected device experiences both a hard-axis

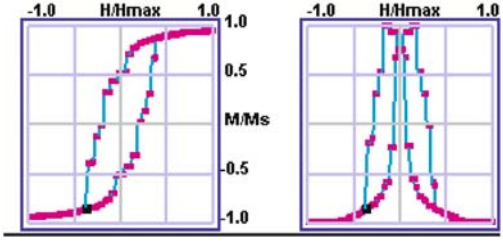

Fig. 8.10. Modeled selected write condition curves at $H_d = 1.5 \times H_{\text{w,wruns}}$, showing (**a**) magnetization and (**b**) magneto-resistance

and easy-axis field that allows the device to experience both a reduction in switching barrier field and a switching field. All of the other devices in the memory array, which are unselected devices, experience either no barrier reduction and/or no switching field of suitable magnitude to effect switching. These unselected devices will not be overwritten as long as the magnitude of the hard-axis and easy-axis fields are chosen correctly and the distributions of the switching characteristics are sufficiently bounded and therefore non-overlapping.

Shown respectively in Figs. 8.12a and 8.12b are AGM hysteresis curves corresponding to switching characteristics with and without a net bias field for an ensemble of between one million and two million PSV devices on a bulk Si wafer. The abscissa shows the word field normalized to the switching threshold field. The ordinate shows easy-axis-directed magnetic moment normalized to the maximum magnetic moment of the hysteresis curve shown without a net bias field. Since the magnetic moment for antiparallel magnetization is one-half of that for parallel magnetization, the storage layer is determined to be three times thicker than the sense layer. The magnetic moment of the hysteresis curve with a net bias has a magnetic moment that is less than that for the hysteresis curve without bias. This reduction in moment is consistent with the magnetization being canted at an angle relative to the easy axis. Selectivity is observed that shows separation of selected-write populations of PSV devices from unselected-write populations. The AGM results are consistent with distribution effects measured from functioning GMRAMs [8.21]. The shapes of the curves shown in Figs. 8.12a and 8.12b correspond respectively to the curves shown in Figs. 8.7a and 8.10a. This correlation between experimental results and simulations suggests, first, that nominal experimental characteristics show physically and theoretically expected behaviors and, second, that simulations can be used to make inferences about magnetization reversal processes.

Figures 8.13a–d show a model for coherent switching in which the patterned sense and storage layers are uniformly magnetized in the absence of a net bias field. Figures 8.13a–d correspond to the four possible magnetization states that can then occur for a PSV device in a GMRAM. As depicted in Figs. 8.13a–d, in the absence of bias and sense fields, the magnetization would align parallel to the easy axis direction. Since neither bias fields nor sense fields are present, switching would occur abruptly and irreversibly at a switching field predicted by the switching astroid

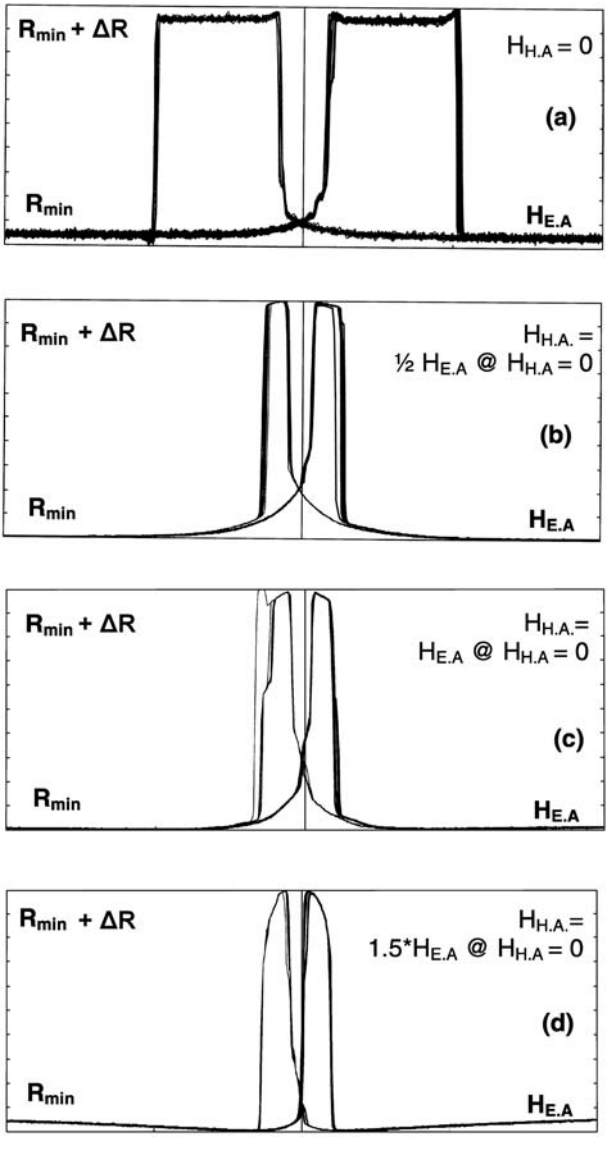

Fig. 8.11. Magneto-resistance curves with a hard-axis bias field equal to (**a**) zero, (**b**) one-half the easy-axis switching field when no hard-axis field is applied, (**c**) the easy-axis switching field when no hard-axis field is applied, and (**d**) one-and-one-half times the easy-axis switching field when no hard-axis field is applied

of the PSV device. The magnetization would be fixed otherwise. These modeled switching characteristics are consistent with the switching characteristics shown in Fig. 8.5 that correspond in particular to the unselected write case.

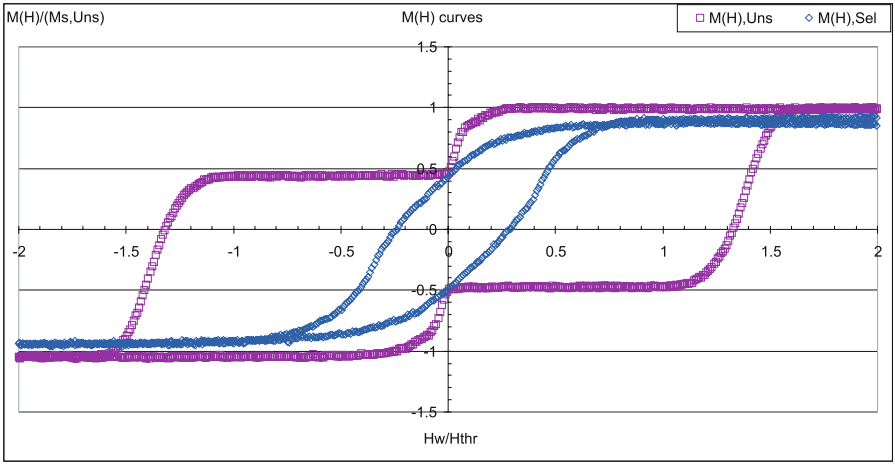

Fig. 8.12. AGM hysteresis curves (**a**) with and (**b**) without a bias field, indicating margins for read and write, for between one million and two million PSV devices fabricated on bulk Si

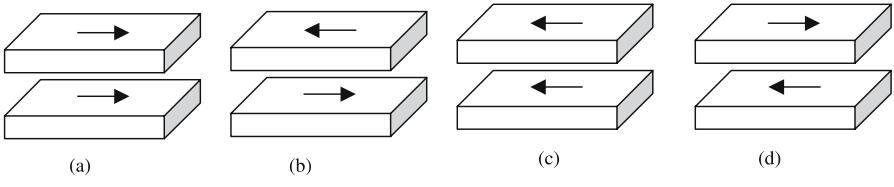

Fig. 8.13. Coupled reversal model for unselected-write switching in a PSV device, as word field is swept, in the absence of a bias field, from (**a**) positive saturation through (**b**) decreasing field, (**c**) negative saturation, and (**d**) increasing field

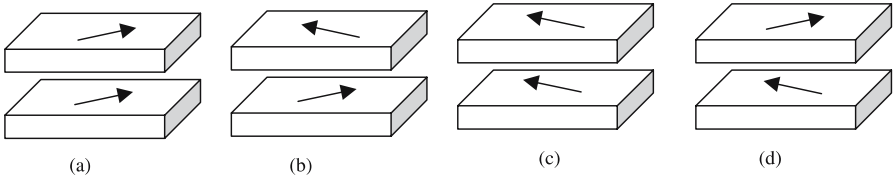

Fig. 8.14. Coupled reversal model for unselected-write switching in a PSV device, as word field is swept, in the presence of a bias field, from (**a**) positive saturation through (**b**) decreasing field, (**c**) negative saturation, and (**d**) increasing field

Figures 8.14a–d show a model for coherent switching in which the patterned sense and storage layers are uniformly magnetized in the presence of a net bias field. Figures 8.14a–d correspond to the four possible magnetization states that can then occur for a PSV device in a GMRAM. As depicted in Figs. 8.14a–d, in the presence of bias and/or sense fields, the magnetization would be canted at some angle to the easy axis direction. Since a net bias field is present, switching would consist of

rotations followed and preceded by abrupt and irreversible switching events predicted by the switching astroid of the PSV device. Reversible switching is defined here to be magnetization reversal that is not hysteretic and that retraces itself when the applied magnetic field changes. Irreversible switching is then defined to be magnetization reversal that is hysteretic and that does not retrace itself when the applied magnetic field is changed. Irreversible easy-axis switching in the presence of a net bias would occur at a switching field less than that in the absence of a net bias, as predicted by the Switching Astroid [8.14] or Stoner-Wohlfarth [8.15] models.

Figure 8.15 shows the reduction in easy-axis switching field when a hard-axis bias is applied, as predicted by the Switching Astroid model. Within the locus of the Switching Astroid, as the hard-axis field is increased in magnitude, the easy-axis field decreases in magnitude. A threshold can be defined for the easy-axis field such that devices with a switching field below the threshold will switch and be rewritten, while devices with a switching field above the threshold will not switch and will not be rewritten. In a memory array, the hard-axis field is used to reduce the easy-axis switching field and therefore help select the device that is to be written. All other devices are unselected and will not be written, rewritten, nor overwritten. Figure 8.16 shows the reduction in easy-axis switching field when a hard-axis bias is applied, as predicted by the Stoner-Wohlfarth model. The square loop characteristic in Fig. 8.16a corresponds to the unselected case and corresponds to easy axis switching in the absence of a hard-axis field. The square loop characteristic switches irreversibly only at $+H_1$ and $-H_1$, as shown in Fig. 8.16a, and otherwise does not exhibit magnetic reversal. The square loop characteristic shown in Fig. 8.16a is consistent with the unselected characteristics shown in Figs. 8.5, 8.7, 8.11a, and 8.12.

The hysteresis loop shown inside the square loop shown Fig. 8.16a corresponds to switching when a hard-axis field is applied. When a hard-axis field is applied, the easy-axis switching field is reduced in magnitude. Irreversible switching now occurs at fields $+H_2$ and $-H_2$, where $|H_2| < |H_1|$. Reversible switching is now observed, as the irreversible switching field events are approached. The rounded loop characteristic is consistent with the selected characteristics shown in Figs. 8.8–8.10, 8.11b–d, and 8.12.

Figures 8.17a–e show details of magnetization reversal in the storage layer of a PSV device based on micromagnetic simulations [8.12] of the reversal process, subject to an easy-axis magnetic field in the presence of a hard-axis magnetic field. Micromagnetic modeling calculates hysteresis loops and magneto-resistance curves that show similarities to experimental data and that are consistent with coherent, Switching Astroid, and Stoner-Wohlfarth models. Details of the micromagnetically calculated reversal process show a sequential reversal process. As observed in Figs. 8.17a–e, magnetization reversal begins with rotation of the bit ends. Magnetization rotation propagates from the bit ends through the central regions of the bit and completes once the edge spins reverse. Since this reversal process has a sequential nature to it, it is noted that variability in the magnetization reversal sequence can be expected. Such variability does appear in experimental work as shown for example in Fig. 8.5.

Figure 8.18 shows magneto-resistance curves for a PSV device deposited on a bulk Si wafer, corresponding to unselected and selected device cases. Note that a field

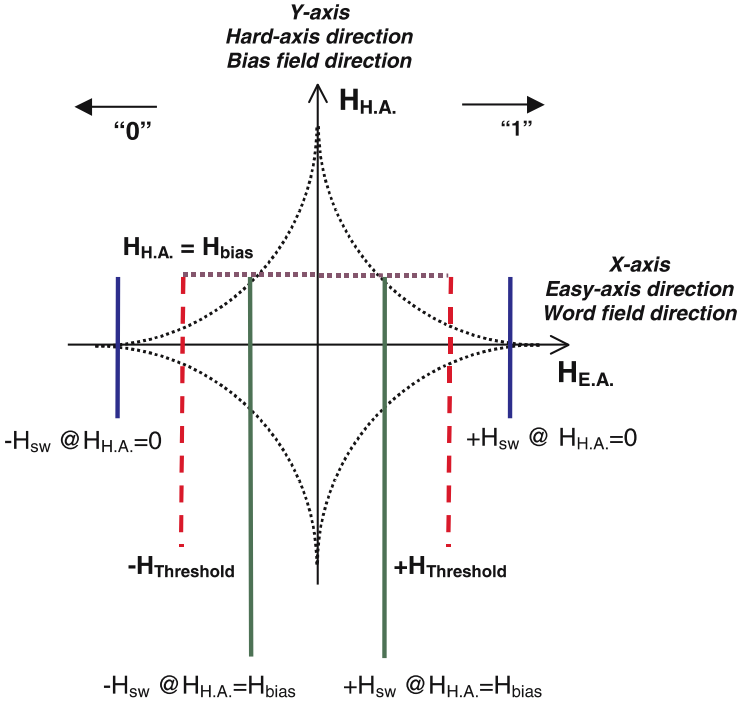

Fig. 8.15. Switching Astroid model switching characteristics, showing reduction of the easy-axis switching field when a hard-axis field is applied. The threshold field shows applied easy-axis field magnitude that switches devices with a hard-axis field applied but does not switch devices with no hard-axis field applied

range, or margin, is observed between the switching fields of the sense and storage layers. The application of a bias field from a selection line reduces the switching field of the selected bit, as shown, allowing the selected bit to be written, while not writing to unselected bits. The reduction in switching field corresponds to the predicted reduction in switching field as shown in the modeled and experimental results in Figs.8.7–8.11, 8.13–8.17a.

Shown in Figs. 8.19 through 8.22 are magnetoresistance characteristics for a PSV device on a CMOS underlayer wafer as a function of applied magnetic field that is in the word field direction, as measured on the MRW test system. The ability to write and to read specific devices without disturbing other devices or device states during write and read is important to the operation of a GMRAM. Figures 8.19 through 8.22 show write and read characteristics that are essential to the operation of a GMRAM and have supported the operation of functional GMRAMs [8.21].

Figure 8.19 shows results that correspond to the unselected write case. In Fig. 8.19, no bias field was applied, and a low sense current was applied that was sufficient to measure magnetoresistance but small enough to have negligible effects on magnetic switching fields. Magnetic switching of the sense layer occurs at positive and negative

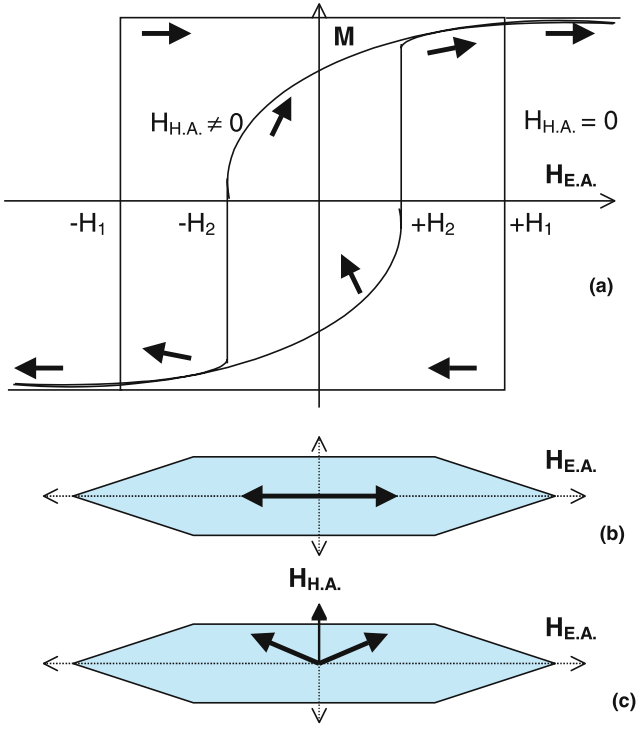

Fig. 8.16. (**a**) Stoner-Wohlfarth model switching characteristics, showing reduction of the easy-axis switching field when a hard-axis field is applied. (**b**) Magnetization showing easy-axis orientation when no hard-axis field is present. (**c**) Magnetization showing canting with respect to the easy-axis when a hard-axis field is applied

fields that are a fraction of the fields needed to switch the storage layer. Figure 8.19 corresponds to an unselected write case for PSV devices that would be in the same word column as the selected PSV device, i.e. for PSV devices that would experience a word field but no sense fields nor bias fields. The switching characteristics show irreversible switching for positive and negative sense and storage switching fields all occurring at the same fields, suggesting that irreversible switching of each layer is occurring coherently. The switching characteristics show switching repeatability. The switching characteristics also show a square shape under unselected write conditions.

Figure 8.20 shows switching characteristics corresponding to the selected write case. The word field sweep range shown in Fig. 8.20 is the same as that in Fig. 8.19. A bias field was applied that was comparable in magnitude to the irreversible switching field under unselected conditions as shown in Fig. 8.19, and the sense current provided an effective bias field that in magnitude was approximately 10% of the bias field. Figure 8.20 corresponds to the selected write case for a PSV device, which corresponds to a PSV device that would experience a columnar word field as well as sense fields and bias fields from a row. In Fig. 8.20, magnetic switching of the

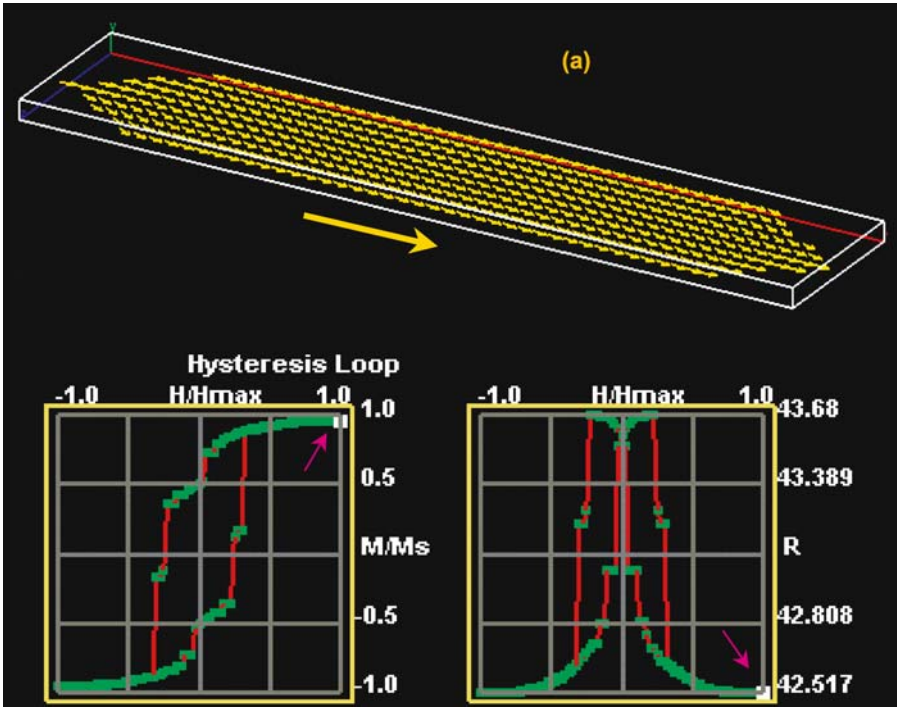

Fig. 8.17a. Micromagnetic simulation showing magnetization in the storage layer of a pseudo-spin-valve device at positive easy-axis saturation, with corresponding hysteresis loops and magneto-resistance curves

sense layer still occurs at positive and negative fields that are a fraction of the fields needed to switch the storage layer. However, the magnetic fields needed to switch the storage layers in Fig. 8.20 are much less than the fields needed to switch the storage layers in Fig. 8.19. The difference in magnitude between the unselected and selected storage-layer switching fields is a measure of write selectivity in a PSV device. Generally, larger values of write selectivity are preferred. The switching characteristics show irreversible switching for positive and negative sense and storage switching fields all occurring at the same fields, suggesting that irreversible switching of each layer is also occurring coherently. The switching characteristics also show switching repeatability. The switching characteristics also show a square shape under selected write conditions, though reversible switching characteristics are observed away from irreversible switching, i.e., at resistance extrema, suggesting the occurrence of magnetization rotation.

Figure 8.21 shows switching characteristics corresponding to the selected read case. The word field sweep range shown in the graph of Fig. 8.21 is the same as that in Figs. 8.19 and 8.20, though the word field sweep range was chosen to show switching of the sense layer without switching the storage layer. No bias field was applied, and a sense current was provided to produce a signal suitable for

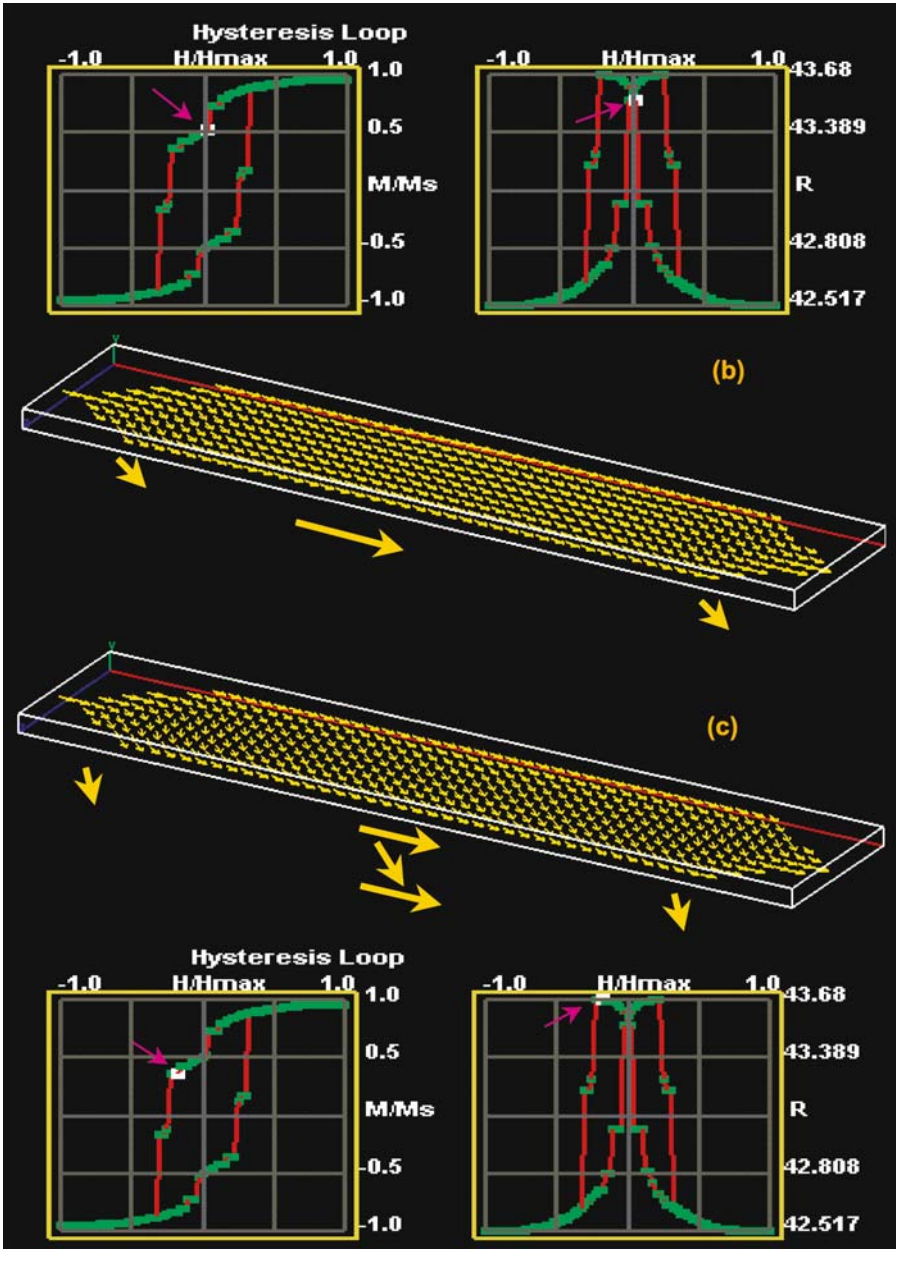

Fig. 8.17. Micromagnetic simulations showing magnetization reversal in the storage layer of a pseudo-spin-valve device, with corresponding hysteresis loops and magneto-resistance curves, (**b**) after sense layer reversal, and (**c**) at onset of storage layer reversal

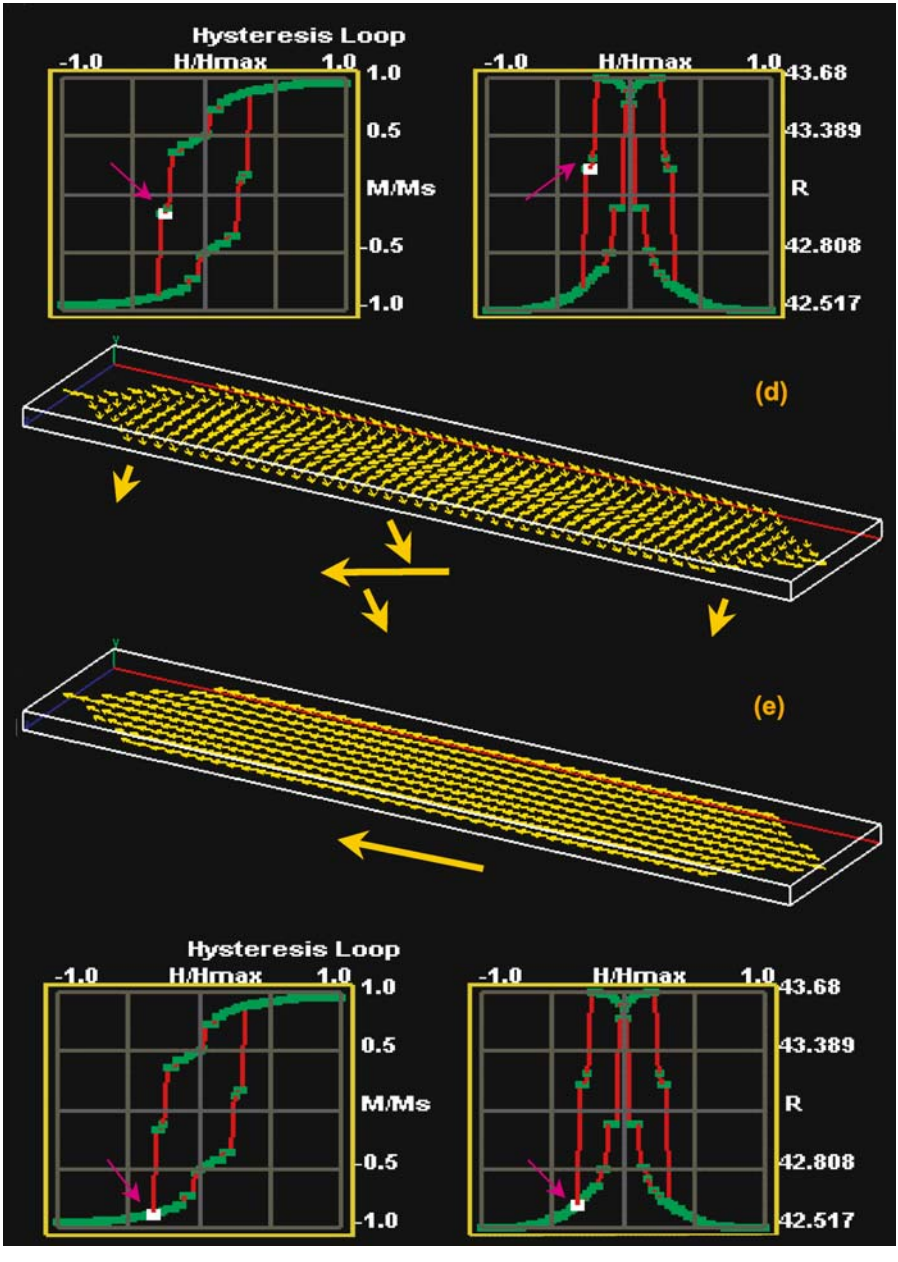

Fig. 8.17. Micromagnetic simulations showing magnetization reversal in the storage layer of a pseudo-spin-valve device, with corresponding hysteresis loops and magneto-resistance curves, (**d**) in the midst of storage layer reversal, and (**e**) at the completion of magnetization reversal

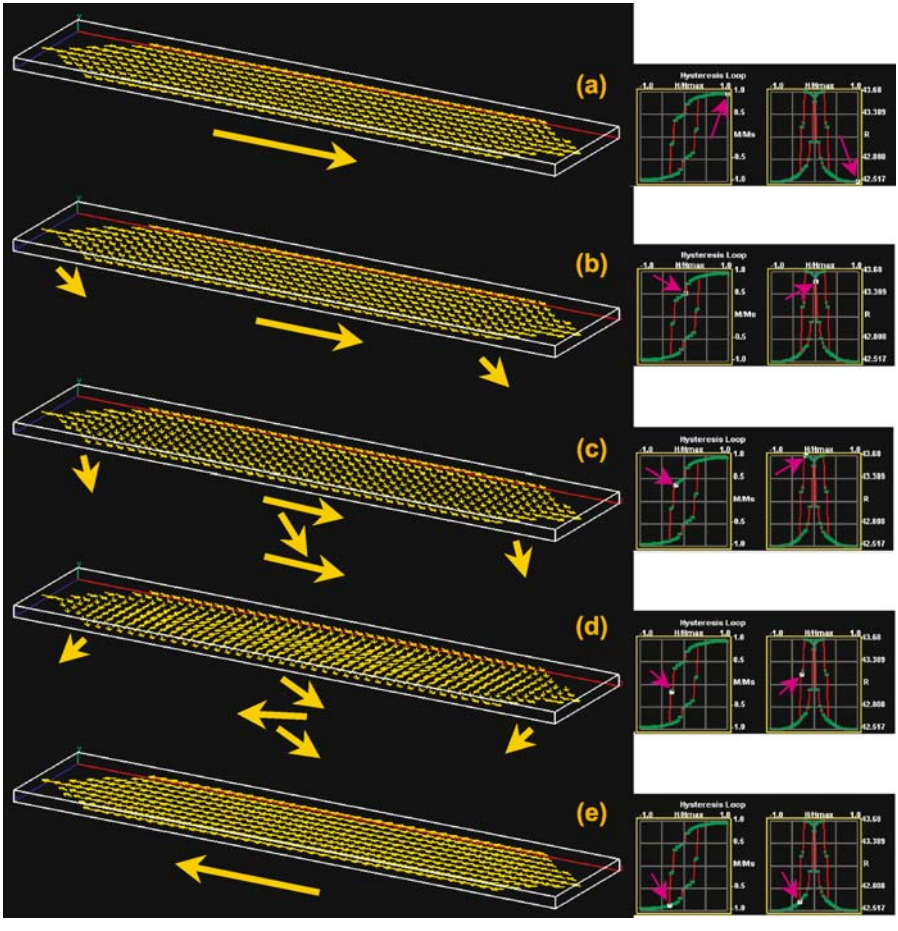

Fig. 8.17. (Composite figure) Micromagnetic simulations showing magnetization reversal in the storage layer of a pseudo-spin-valve device, with corresponding hysteresis loops and magneto-resistance curves, (**a**) at positive easy-axis saturation, (**b**) after sense layer reversal, (**c**) at onset of storage layer reversal, (**d**) in the midst of storage layer reversal, and (**e**) at the completion of magnetization reversal

detection with CMOS electronics. Figure 8.21 corresponds to the selected read case because the PSV device would experience both a word field and a sense field at a given column and row address. Bipolar switching of the sense layer is shown for one orientation of the storage layer, i.e., the storage layer was magnetized in the negative field direction. Magnetic switching of the sense layer occurs at positive and negative fields that are a fraction of the fields needed to switch the storage layers. The switching characteristics show irreversible switching for positive and negative sense switching fields all occurring at the same fields, suggesting that irreversible switching of each layer is also occurring coherently. The switching characteristics also

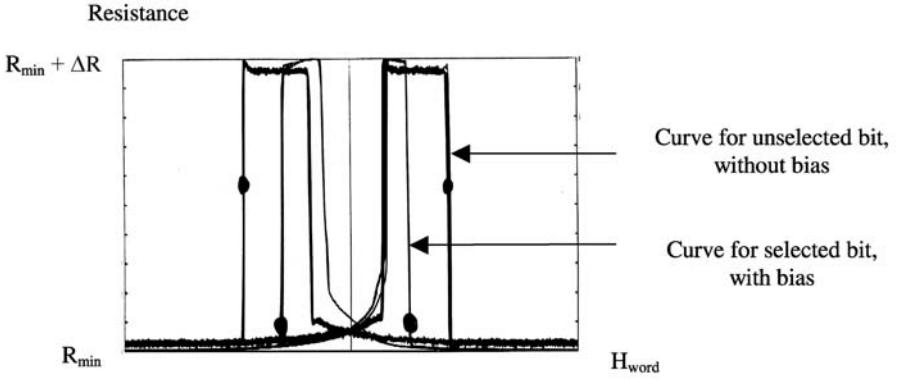

Fig. 8.18. Magneto-resistance characteristics of a PSV device on bulk Si, showing write selectivity between unselected and selected bits through the addition of bias

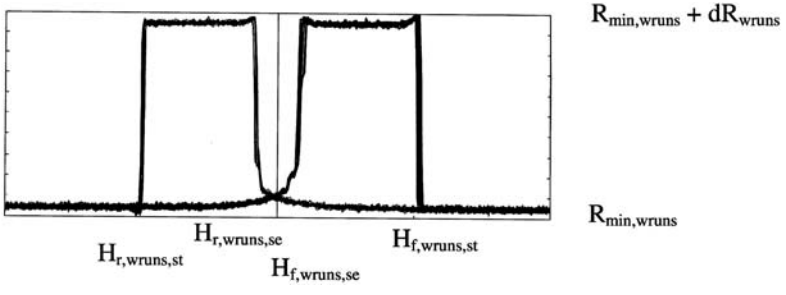

Fig. 8.19. Magneto-resistance curve showing unselected-write characteristics of a PSV device fabricated on CMOS. The horizontal scale is the same in Figs. 8.19, 8.20, 8.21, and 8.22, but the easy-axis field sweep range in Fig. 8.21 is half that in Figs. 8.19, 8.20, and 8.22.

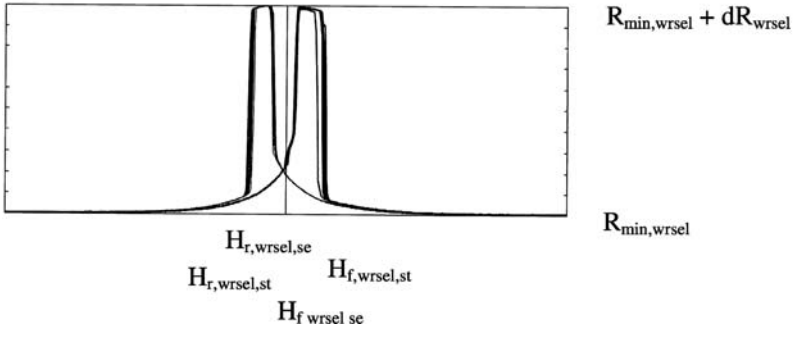

Fig. 8.20. Magneto-resistance curve showing selected-write characteristics of a PSV device fabricated on CMOS. The horizontal scale is the same in Figs. 8.19, 8.20, 8.21, and 8.22, but the easy-axis field sweep range in Fig. 8.21 is half that in Figs. 8.19, 8.20, and 8.22.

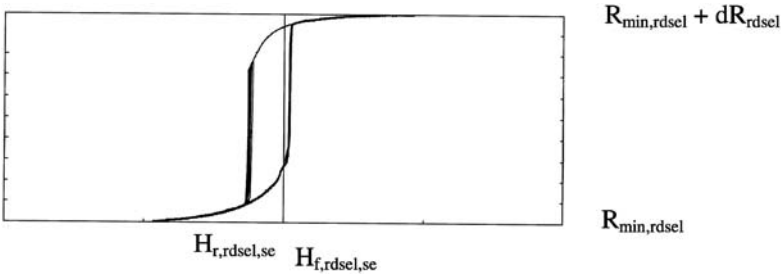

Fig. 8.21. Magneto-resistance curve showing selected-read characteristics of a PSV device fabricated on CMOS. The horizontal scale is the same in Figs. 8.19, 8.20, 8.21, and 8.22, but the easy-axis field sweep range in Fig. 8.21 is half that in Figs. 8.19, 8.20, and 8.22

show switching repeatability. The switching characteristics show reversible switching characteristics away from irreversible switching events, i.e., at resistance extrema, suggesting the occurrence of magnetization rotation. The PSV device signal-to-noise ratio is approximately 60 dB, as calculated from the ratio of the change in resistance to the standard deviation of the measured resistance, in dB.

Figure 8.22 shows switching characteristics corresponding to the unselected read case. The word field sweep range shown in the graph of Fig. 8.22 is the same as that in Figs. 8.19–8.21. However, the word field sweep range was chosen to be the same as in Figs. 8.19 and 8.20 in order to show switching of both the sense and storage layers. No bias field was applied, and a sense current was provided to produce a signal suitable for detection with CMOS electronics. Figure 8.22 corresponds to the unselected read case for a PSV device, i.e. for a PSV device that would experience both a word field and a sense field at a given column and row address and be subject to overwriting. Magnetic switching of the sense layers still occurs at positive and negative fields that are a fraction of the fields needed to switch the storage layers. The magnetic fields needed to switch the storage layers in Fig. 8.22 are slightly less than the fields needed to switch the storage layers in Fig. 8.19 because of the effective selectivity induced by the magnetic field from the sense current. The difference in magnitude between the unselected and selected sense-layer switching fields is a measure of read selectivity in a PSV device. Generally, larger values of read selectivity are preferred. The switching characteristics show irreversible switching for positive and negative sense and storage switching fields all occurring at the same fields, suggesting that irreversible switching of each layer is also occurring coherently. The switching characteristics also show switching repeatability. The switching characteristics also show a square shape under selected write conditions, though reversible switching characteristics are observed away from irreversible switching, i.e., at resistance extrema, suggesting the occurrence of magnetization rotation.

Figures 8.19–8.22 show switching characteristics for sense and storage layers that show irreversible switching at particular critical fields yet otherwise show reversible switching field ranges. Figure 8.13 shows a model for switching in which the patterned sense and storage layers are uniformly magnetized. Figures 8.13a–d correspond to

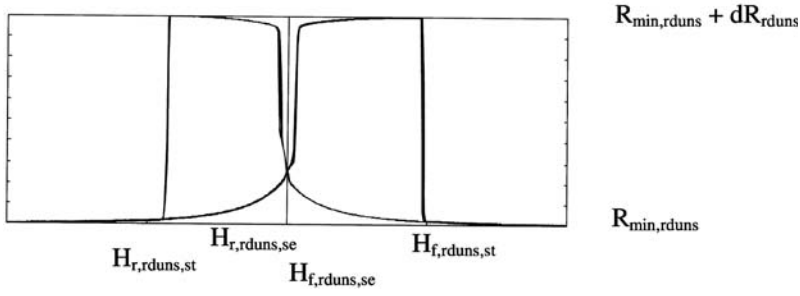

Fig. 8.22. Magneto-resistance curve showing unselected-read characteristics of a PSV device fabricated on CMOS. The horizontal scale is the same in Figs. 8.19, 8.20, 8.21, and 8.22, but the easy-axis field sweep range in Fig. 8.21 is half that in Figs. 8.19, 8.20, and 8.22

the four possible magnetization states that can then occur for a PSV device in a GMRAM. In the absence of bias and sense fields, the magnetization would align parallel to the easy axis direction. Since neither bias fields nor sense fields are present, switching would occur abruptly and irreversibly at a switching field predicted by the switching astroid of the PSV device. The magnetization would be fixed otherwise. These modeled switching characteristics are consistent with the switching characteristics shown in Fig. 8.19 that correspond in particular to the unselected write case. However the simulation results shown in Fig. 8.17a need to be evaluated when considering details of reversal.

Shown in Figs. 8.23 through 8.26 are sample device distributions of key device parameters for GMRAMs. While the statistics presented here are limited, and given that GMRAM write and read functionality has been demonstrated, the results shown in Figs. 8.23 through 8.26 suggest that PSV devices in principle have the potential to support GMRAM functionality at chip capacities up to approximately 1 Mbit [8.21]. Shown in Fig. 8.23 is a distribution of write switching fields for PSV devices fabricated on CMOS underlayers, as measured across a wafer with the MRW test system. The PSV devices were measured under selected-write conditions. The abscissa shows the word field normalized to the write switching threshold field. The ordinate shows the frequency of occurrence as a function of normalized switching field as a percentage. Note that every device tested across the wafer switched with at least a 15% margin below the selected write threshold, and that unselected devices switched with at least a 15% margin above the selected write threshold. These results begin to show a write switching window that could in principle support GMRAM functionality. These electrical device results are consistent with the AGM-measured results described above and have statistical characteristics that are in agreement with the AGM results.

Shown in Fig. 8.24 is a distribution of read switching fields for PSV devices fabricated on CMOS underlayers, as measured across a wafer with the MRW test system. The PSV devices were measured under selected-read conditions. The abscissa shows the word field normalized to the read switching threshold field. The ordinate shows the frequency of occurrence as a function of normalized switching field as a percentage. Note that every device tested across the wafer also switched with at

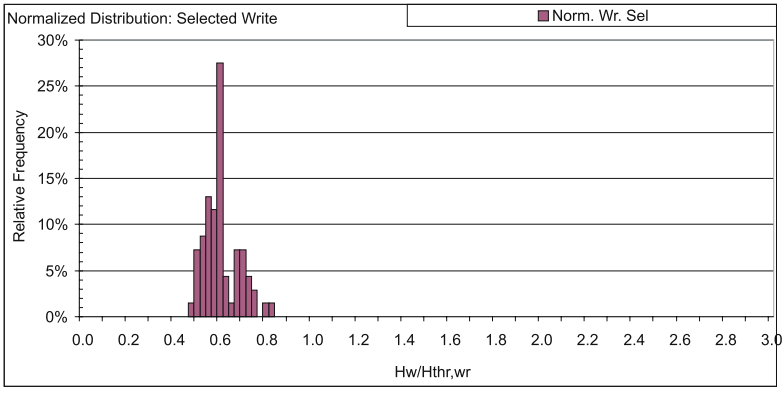

Fig. 8.23. PSV device distributions under selected write conditions showing no device overwriting for fields below the switching threshold set for selected write. These PSV devices were fabricated on CMOS underlayers

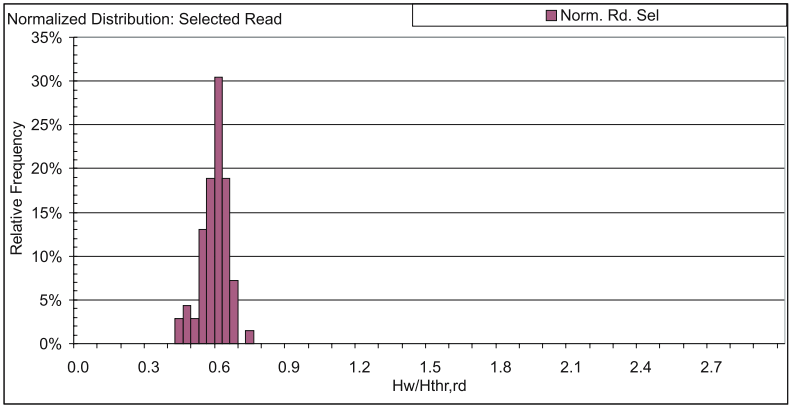

Fig. 8.24. PSV device distributions under selected read conditions showing no device overwriting for fields below the switching threshold set for selected read. These PSV devices were fabricated on CMOS underlayers

least a 15% margin below the selected read threshold, and that unselected devices switched with at least a 15% margin above the selected read threshold. While these statistics are limited, these results indicate a read switching window for PSV devices that is consistent with demonstrated GMRAM functionality [8.21].

Figure 8.25 shows a distribution of maximum change-in-resistance for PSV devices fabricated on CMOS underlayers, as measured across a wafer with the MRW test system. The abscissa shows the maximum change-in-resistance normalized to a minimum change-in-resistance threshold. The ordinate shows the frequency of occurrence as a function of normalized change-in-resistance as a percentage. Note that every device tested across the wafer exhibited at least a 100% margin above

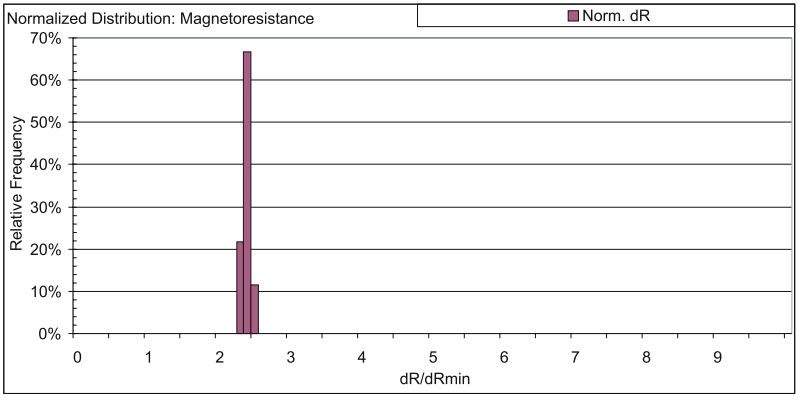

Fig. 8.25. PSV device distributions for maximum PSV device change in resistance (dR) relative to the minimum threshold set for dR. These PSV devices were fabricated on CMOS underlayers

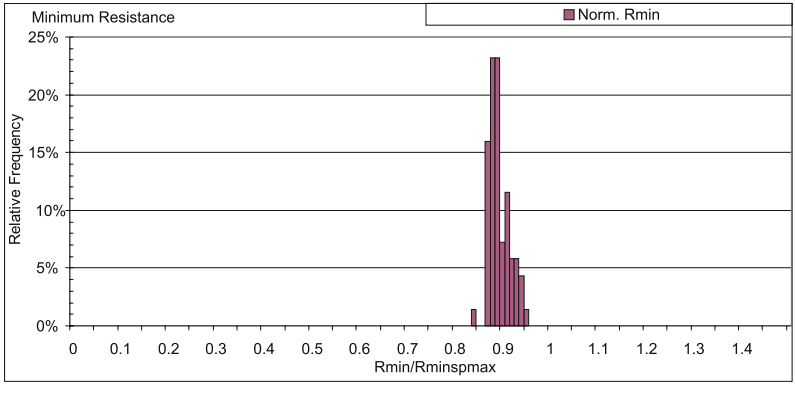

Fig. 8.26. PSV device distributions for minimum resistance relative to the maximum threshold set for minimum resistance. These PSV devices were fabricated on CMOS underlayers

the minimum change-in-resistance threshold. While these statistics are limited, the change-in-resistance offers performance that provides signal levels that support GMRAM operability. Figure 8.26 is a distribution of minimum resistance for PSV devices fabricated on CMOS underlayers, as measured across a wafer with the MRW test system. The abscissa shows the maximum change in resistance normalized to a maximum resistance threshold. The ordinate shows the frequency of occurrence as a function of normalized resistance as a percentage. Note that every device tested across the wafer exhibited at least a 5% margin below the maximum resistance threshold. While these statistics are also limited, the resistance characteristics provide signal levels that support the read process in GMRAMs while keeping resistance low enough to support sense current requirements.

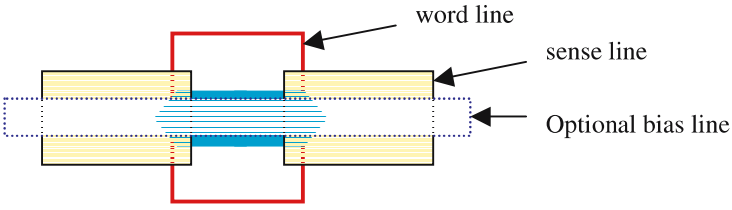

Fig. 8.27. Schematic top-view of a GMRAM cell

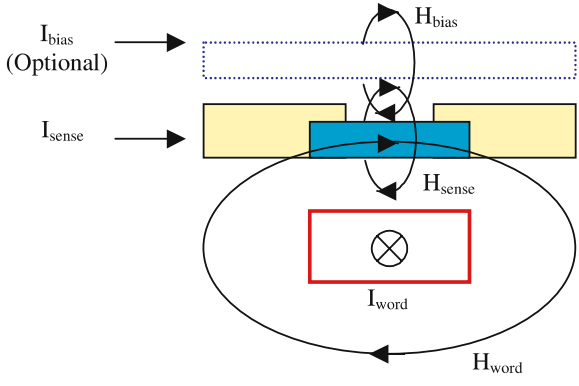

Fig. 8.28. Schematic cross-section of a GMRAM cell

8.3 The 1R0T GMRAM Architecture

A GMRAM cell is formed when a PSV device is integrated with metal lines. Metal lines provide connections to PSV devices that allow sensing the resistance and, hence, information state of PSV devices. Additional metal lines routed in proximity to PSV devices provide magnetic fields that allow switching layers of the PSV device for writing and reading PSV devices. Figure 8.27 shows a GMRAM bit cell. The bit cell includes a PSV device connected in series to a sense line. The PSV device is proximal to a word line that runs perpendicular to the sense line. Optionally, a digit line in addition can be placed in proximity to the PSV device and run parallel to the sense line. The PSV device is the fundamental unit that stores a bit of information and allows the bit of information to be read. The sense, word, and optional digit lines enable the writing and reading processes. Figure 8.28 shows the conventions for the magnetic fields that are produced by sense, word, and digit line currents. Ampere's law can be used to calculate magnetic fields produced by currents in metal lines. Shown in Fig. 8.29 is an array of bit cells in a GMRAM.

Currents in the word line are used to write to the storage layers in PSV devices. Binary "1's" and "0's" are written, depending on the polarity of the word line current. The ability to write to a particular bit is given by the bit cell's property called selectivity. Applying a sense and/or digit line current provides a bias to the storage layer that reduces the switching field of the storage layer. Applying a sufficient

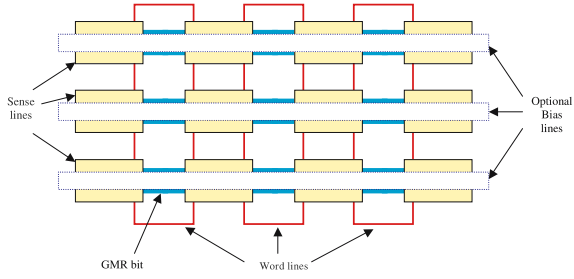

Fig. 8.29. Schematic top-view of a matrix of GMRAM cells

amount of word current, at the desired polarity, produces a magnetic field that writes the selected bit. Bits that have not been selected will not be affected as long as the word current remains below the threshold that writes to unselected bits. The principles of selectivity are shown in Figs. 8.11 through 8.16. As the hard axis, i.e., digit line, magnetic field is increased, the easy-axis, i.e., word line, switching field decreases.

Readback is achieved by applying currents in the sense and word lines. The magnitude of the sense and word currents used during a read are well below values that write to storage layers in PSV devices. When passed through resistive bits, the sense current generates a voltage that can be sensed and amplified. A bipolar word current is used to magnetize the sensing layer in one direction and then the opposite direction, and the voltage is sampled when the sensing layer is in each direction. Because of the GMR effect, the resistance will be increased when the sensing layer is in one of the two directions, as shown in Figs 8.6a and 8.6b. Because the direction of the magnetization in the sensing layer is determined by the word line current during the read process, the state of the storage layer and, therefore, the bit is determined. Because the state of the storage layer is not changed during the read process, the state of the bit is not altered and the read is also said to have occurred non-destructively.

Shown in Fig. 8.30 is a timing diagram for the write and read processes. When writing to a PSV device, the polarity of the word current is used to provide a magnetic field of a given direction. The magnetic field from the word current then magnetizes the storage layer of the PSV device into the desired direction. A particular bit is selected using bias from the sense current. An optional, additional bias field from a bias line can be used to provide a magnetic field that lowers the switching field, either in addition to or instead of the sense current. The bias lowers the switching field of the selected bit while allowing the field of the unselected bits to remain high.

When reading a PSV device, a read current is sent through the PSV device using the sense line. A bipolar word current, with a peak magnitude that allows switching the sensing layer only, is used to set the direction of magnetization of the sensing layer. The sequence of signal polarities produced with the bipolar word current, i.e. high-then-low or low-then-high, indicates the relative orientation of magnetization between the sensing and storage layers. The sequence of signal polarities produced

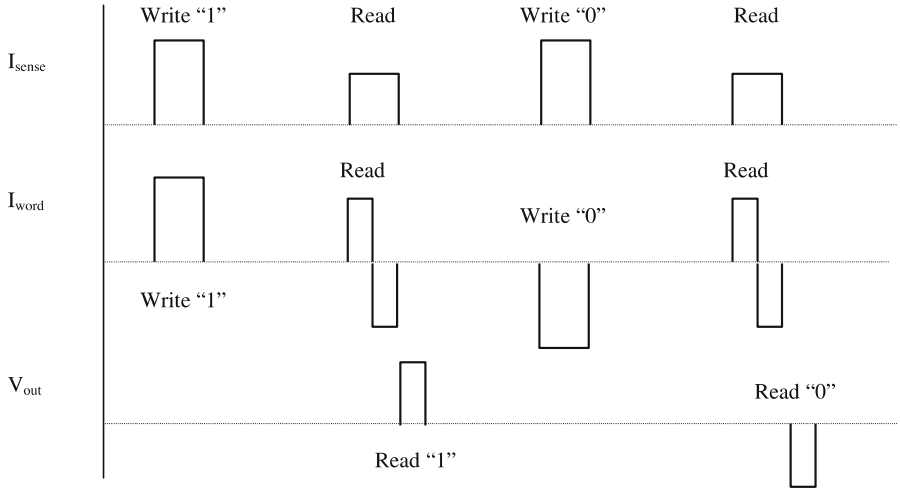

Fig. 8.30. Schematic timing diagram for writing and reading GMRAM cells

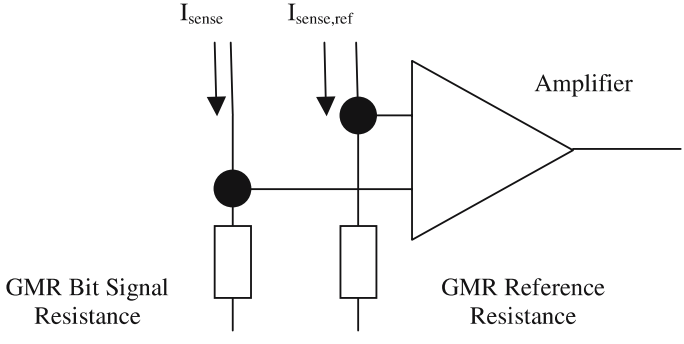

Fig. 8.31. Read method for GMRAM cells

by the GMR effect therefore uniquely determines the information state of the storage layer.

Figure 8.31 shows a schematic diagram that depicts a portion of the read circuit. Two strings of resistors are connected to an amplifier. The first string of resistors comes from the memory and contains bit cells that can exhibit the GMR effect. The second string of resistors is a set of reference resistors that provides common-mode rejection and differential detection. The increment in voltage, which occurs when the sense layer is magnetized in one of two directions, is amplified and detected in a timing window to complete the read process.

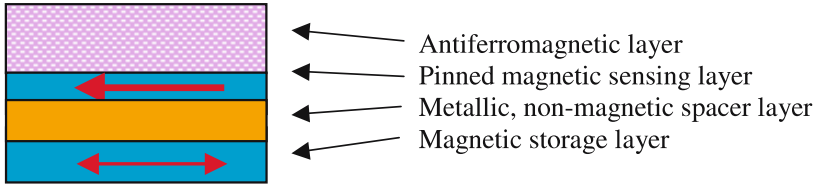

Fig. 8.32. Schematic cross-section of a magnetic spin-valve (SV) device

8.4 Magnetic Spin-Valve Devices for GMRAMs and GMRAM Latch Architectures

Shown in Fig. 8.32 is a schematic cross-section of a magnetic spin-valve (SV) device. The four main components of a SV device are the storage layer, spacer layer, sensing layer, and anti-ferromagnetic (AF) layer. While a PSV device has storage, spacer, and sensing layers, SV devices have these three layers plus the AF layer. In a SV, the sensing layer, which is ferromagnetic, is coupled directly to the anti-ferromagnet layer so that the magnetization of the sensing layer is fixed, or magnetically "pinned", up to some critical temperature and critical magnetic field. At present, the thicknesses of layers in a SV device are measured in nanometers. The storage, spacer, and sensing layers are typically composed of materials similar to those used in PSV devices. Common anti-ferromagnets that are used in SV devices include PtMn, IrMn, CrPtMn, NiMn, and FeMn.

Figure 8.33 shows a SV device deposited on a bulk Si wafer. As is the case for PSV devices which are shown in Figs. 8.5, 8.6a, 8.6b, 8.19–8.22, the electrical resistance of the SV device is minimized when the storage layer is magnetized parallel to the sensing layer. When the storage layer is magnetized in a direction opposite, or anti-parallel, to the sensing layer, the electrical resistance of the PSV is maximized. Magnetic fields that allow switching the magnetization in the storage layer but do not reverse the pinning layer define the operating magnetic field range for the SV device.

A SV device is read by measuring the resistance when the applied magnetic field is zero. For a SV device, the resistance when the applied magnetic field is zero provides a direct measure of the direction of magnetization in the storage layer since the direction of magnetization in the pinned sense layer is determined. The direction of the magnetization in the storage layer is deduced using the GMR effect and the fact that the direction of the magnetization in the sensing layer, by virtue of pinning, is fixed and known.

A SV device is written by setting the magnetization of the storage layer in the desired direction. As shown in Fig. 8.34, a SV device in an array can show switching selectivity in the same way that a PSV device can show selectivity. By applying a sense and/or digit line current as a bias in addition to the word line current, the switching field can be reduced. The bias that is provided reduces the switching field of the selected bit cell. Applying a sufficient amount of word current, at the desired polarity, produces a magnetic field that writes the selected bit. Bits that have not been

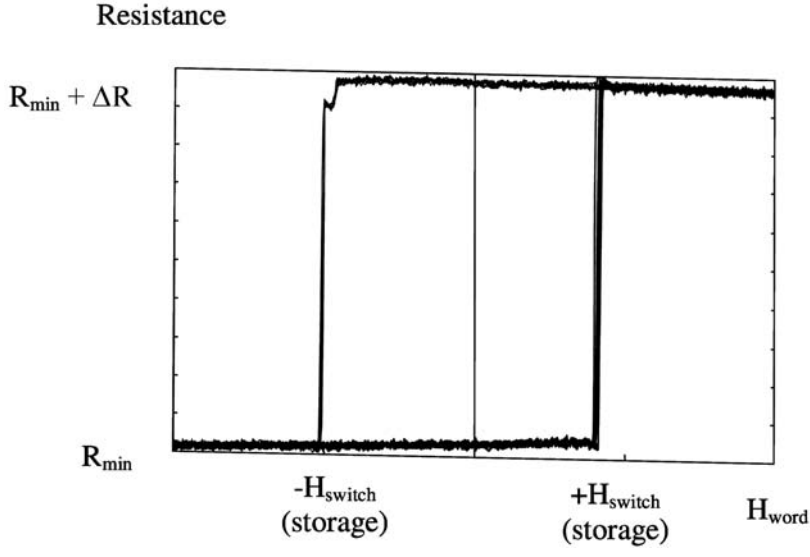

Fig. 8.33. Magneto-resistance characteristics of a SV device on bulk Si. The switching of the storage layer is shown with the GMR effect. At a sufficiently high magnetic field, the magnetization of the pinned layer can be switched reversibly to align with the applied magnetic field

selected will not be affected as long as the word current remains below the threshold that writes to unselected bits.

Similar to results obtained to date from PSV devices, results to date obtained from SV devices indicate that the resistance, magneto-resistance, and switching properties of SV devices are reversible and not obviously subject to degradation. Undesired domain effects can be observed in studies of alternative and sub-optimal materials and devices that have been subjected to sub-optimal processing. Development is underway to show that soft-errors and cyclability limitations are not evident for counts ultimately as high as 10^{15} cycles [8.20, 21]. The information state in storage layers of SV devices is retained even when currents and magnetic fields are removed and restored which supports nonvolatile memory operation. The ability to read the states of storage layers of SV devices can be performed without changing the magnetic states of storage layers in SV devices to support nondestructive readback [8.20, 21]. Switching times of storage layers are on the order of nanoseconds based on reported studies [8.20, 21]. Read cycle times using CIP PSV devices have been demonstrated down to 50 nanoseconds based on present GMRAMs and GMRAM design capabilities, indicating that in principle read cycle times using SV devices can also be 50 nanoseconds or perhaps less [8.20, 21]. Such characteristics in SV devices support desired properties in GMRAMs of potentially unlimited cyclability, nonvolatility, non-destructive readback, fast writing times, and fast reading times that are desired and needed from a nonvolatile memory technology.

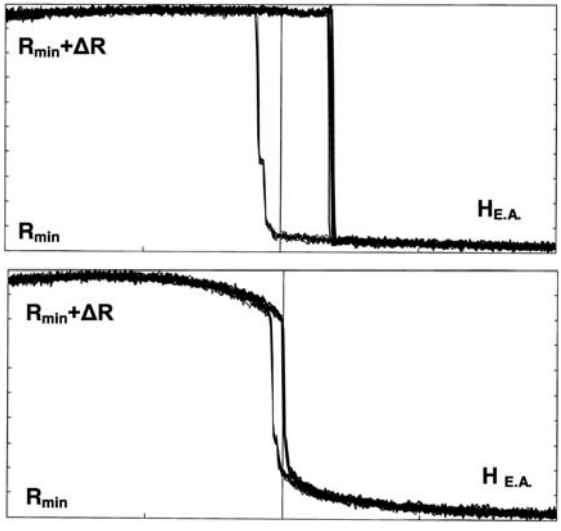

Fig. 8.34. Magneto-resistance characteristics of a SV device on CMOS. The switching of the storage layer is shown with the GMR effect (**a**) without a bias, and (**b**) with a bias. The SV device shows write selectivity. At a sufficiently high magnetic field, the magnetization of the pinned layer can be switched reversibly to align with the applied magnetic field

A 2R2T (two resistor, two transistor) memory architecture that uses SV devices is shown in Fig. 8.35. A latch flip-flop serves as the basis of the active cell. An array of SV devices is used to form a memory array. A complementary pair of SV devices is used to store a bit of information. During a write, a particular pair of SV devices is selected, using address decode logic. A word current is used to magnetize the storage layers in the desired binary state. With a complementary pair of SV devices, one SV device will be in either a low or high resistance state and the other SV device will be in either a high or low resistance state. During a read, a particular pair of SV devices is selected, through address decoding, and connected as load elements to the flip-flop. The relative resistance of the complementary pair of SV devices, either high-low or low-high, then triggers the flip-flop to assert, and therefore read, a corresponding low or high signal. The resulting read is performed non-destructively and is relative fast, limited by the flip-flop's latching time and propagation delays.

8.5 Nonvolatile Memory Comparisons and Potential Applications

GMRAM technology has characteristics that potentially make it attractive as a non-volatile memory technology, in particular for aerospace applications. GMRAM technology is compatible with monolithic integrated circuit technologies in terms of processing capability, device requirements, and design requirements.

A number of solid-state, nonvolatile, random access memory technologies are in existence today and in production, including nonvolatile EEPROMs, and volatile

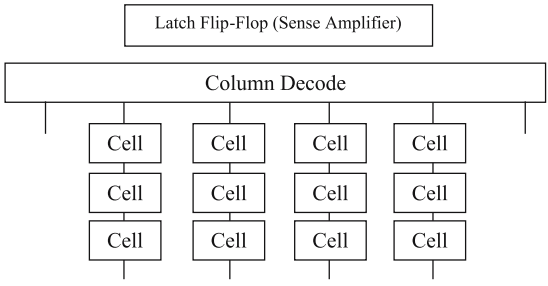

Fig. 8.35. GMRAM Latch-Array Architecture

memories with battery back-up or nonvolatile shadow memory for retaining data during power-down. GMRAM technology potentially offers performance advantages when compared to alternative nonvolatile memory technologies. Factors such is faster write times, faster read times, and greatly improved cyclability are potential attributes of GMRAM technology which have motivated its development. Volatile memories can match the speed of GMRAM, but do require additional hardware and systems integration to achieve nonvolatility.

The state of information, held in storage layers in PSV devices, is retained even when currents and magnetic fields are removed and restored. The ability to reverse the sense layers of PSV devices can be performed without changing the magnetic states of PSV device storage layers. Switching times of storage and sensing layers in magnetic devices are reported to be on the order of nanoseconds [8.20, 21]. Write and read cycle times in demonstration GMRAMs have been shown to reach speeds of approximately 50 nanoseconds [8.20, 21].

An assessment of results to date also indicates that the resistance, magneto-resistance, and switching properties of PSV devices are reversible and are not obviously nor fundamentally subject to degradation. Care must be taken to maintain magneto-resistive and switching performance and avoid soft-error and cyclability limitations through material, device, and process design. Domain states must be carefully controlled. It is not apparent that any practical limitations in cyclability are fundamental.

The following examples provide an indication of the performance opportunities for GMRAM technology. While, for example, EEPROM technology generally offers fast read times and unlimited read cyclability; write cycle times can be relatively slow, around 10 milliseconds for example, write cyclability can be limited, to on the order of 100,000 cycles or so, and high write voltages can be required. In addition to fast read times and unlimited read cyclability, GMRAM technology potentially offers unlimited write cycles, high-speed operation for both writing and readback, and single-supply operation without additional power supply circuitry. Like EEPROM, most Flash EEPROM memories require high voltages for writing and have low write-cycling endurance, typically around a million cycles. At less than 100 µs, the write speed for Flash EEPROM is considerable faster than EEPROM, but still is almost three orders of magnitude slower than DRAM, SRAM, and, potentially,

GMRAM technology. In terms of write speed and cycling endurance, Ferroelectric RAM (FRAM) offers considerable improvement over EEPROM and Flash. FRAM has a cycling endurance of up to 10^{12} cycles and writes as quickly as 150 ns. In addition, high write voltages are generally not required. FRAM, however, generally requires destructive readback, so a write cycle is required with every read, and data retention time can degrade.

Volatile memories can be made to function as nonvolatile memories through system adaptations. With Shadow RAM, a volatile memory such as SRAM can be used as the primary memory, and EEPROM or Flash EEPROM can be used as backup memory when the SRAM is powered down or loses power. With battery-backed RAM, a volatile memory such as SRAM can be used as the primary memory, and a battery or capacitive system can be used to retain data when system power is removed or lost. These approaches provide performance improvements such as high speed, increased cyclability, and nonvolatility, but with added system complexity and system constraints.

While GMR bits and GMR read elements in disk heads and tape heads have some similarities, GMRAM memories differ from magnetic disk and magnetic tape systems. GMRAM technology offers 50 nanosecond to 100 nanosecond write and read cycle times, based on functionality of existing GMRAMs [8.20, 21], whereas disk and tape systems are serial access systems with latency access times ranging from milliseconds to tens of seconds but very high relative storage capacities and data transfer rates. GMRAM technology therefore offers the potential for "instant-on" capabilities for computing applications that enhances or complements the volatile memory and nonvolatile storage data hierarchies which are prevalent today with "reboot" times requiring tens of seconds. GMRAM technology requires greater levels of solid-state integration of magnetics with semiconductor electronics relative to the level of solid-state integration required in mechanically-based disk and tape systems.

The combination of nonvolatility, potentially unlimited cycling endurance for write and readback, and reasonably fast write and read times motivate interest in GMRAM technology, in particular for aerospace applications. Magnetic elements are intrinsically radiation immune and can also be used in wide-temperature-range applications. When the radiation immune properties of magnetic elements are combined with radiation-hardened electronics, a radiation insensitive nonvolatile memory technology is the result. When all of these attributes are combined and considered, GMRAMs have the potential to serve a variety of memory applications, but particularly those in aerospace applications.

8.6 Conclusions

Giant Magneto-resistive Random-Access Memories (GMRAMs) are nonvolatile memories consisting of magnetic memory devices integrated with standard semiconductor electronics. In GMRAMs, magnetic multi-layer devices, such as PSV and SV devices, are made of layers of nanometer-thick materials, and are used to store information and to allow the data to be read. Magneto-resistive and magnetic switching

attributes along with nonvolatility, nondestructive readout, and potentially unlimited cyclability make PSV and SV devices potentially desirable as nonvolatile memory elements for GMRAMs. The 1R0T GMRAM architecture has been described along with GMR CIP PSV device characteristics that have supported the demonstration of GMRAMs that have passed complex pattern tests. In the 1R0T GMRAM technology implementation, a PSV bit is stored by setting the direction of magnetization in the storage layer. A PSV bit is read by determining the orientation of the sense layer with respect to the storage layer using the giant magneto-resistance (GMR) effect that such magnetic multi-layers produce when current flows in the magnetic device. The GMR effect is a magneto-resistive, variable-resistance spin effect in which the resistance depends on the relative magnetization between storage and sense layers in the magnetic multi-layer. In PSV and SV devices, the GMR effect is based on currents flowing in the plane (i.e., current-in-plane, or CIP) and as such, PSV and SV devices are CIP devices. In a magnetic multi-layer that exhibits the GMR effect, resistance is maximized when the relative magnetization between the storage and sense layers is anti-parallel; resistance is minimized when the relative magnetization between the storage and sense layers is parallel. The GMR effect produces a change in resistance that, when excited with a read current, induces a signal that distinguishes between a binary "1" and "0". Write and read characteristics of current-in-plane pseudo-spin-valve (PSV) devices are described in terms of write switching, read switching, resistive, and magnetoresistive properties of individual PSV devices and statistical ensembles of PSV devices fabricated on bulk Si and CMOS underlayers. Based on experimental work and modeling, magnetization reversal has been inferred to be rotational, including irreversible rotations that correspond to switching, reversible rotations that anticipate switching, and reversible rotations that complete reversal from switching to saturation in the opposite direction.

Acknowledgement. Honeywell appreciates the sponsorship of the following government agencies for the development of GMRAM technology and products: Defense Advanced Research Projects Agency (DARPA), Defense Threat Reduction Agency (DTRA), and the U.S. Navy Trident program. Honeywell also appreciates the many contributions of the GMR team and personnel at Honeywell who have and are contributing to GMR technology and products. Comments and suggestions from the reviewers are gratefully acknowledged. This paper has been written on behalf of the GMR team at Honeywell.

References

8.1. R.R. Katti, "Current-in-plane Pseudo-Spin-Valve Device Performance for Giant Magnetoresistive Random Access Memory Applications," *J. Appl, Phys.*, Vol. 91, No. 10, May 15, 2002, pp. 7245–7250.

8.2. R. Katti, A. Arrott, J. Drewes, W. Larson, H. Liu, Y. Lu, T. Vogt, and T. Zhu, "Pseudo-Spin-Valve Device Performance for Giant Magnetoresistive Random Access Memory Applications," *IEEE Transactions on Magnetics*, Vol. 37, No. 4, July, 2001, pp. 1967–1969.

8.3. R. Katti and T. Zhu, “Attractive Magnetic Memories,” *IEEE Circuits and Devices Magazine*, Vol. 17, No. 2, March, 2001, pp. 26–34.
8.4. J. Gadbois, J.-G. Zhu, W. Vavra, and A. Hurst, “The Effect of End and Edge Shape on the Performance of Pseudo-Spin Valve Memories,” *IEEE Transactions on Magnetics*, Vol. 34, No. 4, July, 1998, pp. 1066–1068.
8.5. J. Shi, T. Zhu, M. Durlam, E. Chen, S. Tehrani, Y. Zheng, and J. Zhu, “End Domain States and Magnetization Reversal in Submicron Magnetic Structures,” *IEEE Transactions on Magnetics*, Vol. 34, No. 4, July, 1998, pp. 997–999.
8.6. E.Y. Chen, S. Tehrani, T. Zhu, M. Durlam, and H. Goronkin, “Submicron spin valve magnetoresistive random access memory cell,” *J. Appl. Phys*., **81** (8), 15 April 1997, pp. 3992–3997.
8.7. S. Tehrani, J.M. Slaughter, E. Chen, M. Durlam, J. Shi, and M. DeHerrera, “Progress and Outlook for MRAM Technology,” *IEEE Transactions on Magnetics*, Vol. 35, No. 5, September, 1999, pp. 2814–2819.
8.8. H. Boeve, C. Bruynseraede, J. Das, K. Dessein, G. Borghs, J. De Boeck, R. Sousa, L. Melo, and P. Freitas, “Technology assessment for the implementation of magnetoresistive elements with semiconductor components in magnetic random access memory (MRAM) architectures,” *IEEE Transactions on Magnetics*, Vol. 35, No. 5, September, 1999, pp. 2820–2825.
8.9. M. Johnson, “Magnetoelectronic Memories Last and Last,” *IEEE Spectrum*, February, 2000, pp. 33–40.
8.10. G. Prinz, “Hybrid Ferromagnet Semiconductor Devices,” *Science*, Vol. 250, 1990, pp. 1092–1097.
8.11. S. Tehrani, E. Chen, M. Durlam, M. DeHerrera, J.M. Slaughter, J. Shi, and G. Kerszykowski, “High-Density Submicron Magnetoresistive Random Access Memory,” *J. Appl. Phys*., 85 (8), 15 April 1999, pp. 5822–5827.
8.12. R.R. Katti, “Current-in-Plane Pseudo-Spin-Valve Device Performance for Giant Magnetoresistive Random Access Memory Applications,” Accepted for publication, *J. Appl. Phys*., 2002.
8.13. M. Scheinfein, "LLG Micromagnetics Simulator," Version 1.45, 1998.
8.14. J. K. Watson. “Applications of Magnetism,” John Wiley and Sons, New York, 1980.
8.15. E.C. Stoner and E. P. Wohlfarth. “A Mechanism of Magnetic Hysteresis in Heterogeneous Alloys,” *Phil. Trans. Roy. Soc.*, A240, pp. 599–642, 1948.
8.16. C.D. Mee and E. D. Daniel. “Magnetic Recording Volume I: Technology,” McGraw-Hill Book Company, New York, 1987.
8.17. D. Jiles. “Introduction to Magnetism and Magnetic Materials,” Chapman and Hall, London, 1991.
8.18. S. Chikazumi and S. Charap. “Physics of Magnetism,” Robert E. Kreiger Publishing Company, Malabar, Florida, 1984.
8.19. R.C. O’Handley. “Modern Magnetic Materials: Principles and Applications,” John Wiley and Sons, New York, 2000.
8.20. S. Wolf and D. Treger, eds. Proceedings of the Spins/Spintronics Review, a DARPA-sponsored Program. Long Beach, California, September 3–7, 2001.
8.21. S. Wolf and D. Treger, eds. Proceedings of the Spins/Spintronics Review, a DARPA-sponsored Program. Delray Beach, Florida, September 30–October 4, 2002.
8.22. D. Talbot. “Computing’s New Spin,” *Technology Review*, Cambridge, MA, January/February, 2001, p. 39.
8.23. B. Heinrich and J.A.C. Bland, eds. “Ultrathin Magnetic Structures II,” Springer-Verlag, 1994. Cf. chapter 2.2 by A. Fert and P. Bruno, and chapter 2.4 by S.S.P. Parkin.

Subject Index